

Investigations of magnetic and structural properties of rare earth substituted NdCrO_3

Doctor of Philosophy

By

Pragya Gupta



Department of Physics

Indian Institute of Technology Guwahati

Guwahati-781039, Assam, India

November 2023



Investigations of magnetic and structural properties of rare earth substituted NdCrO_3

*A Thesis submitted in partial fulfillment of the requirements for the
award of the degree of*

Doctor of Philosophy

By

Pragya Gupta



Department of Physics

Indian Institute of Technology Guwahati

Guwahati-781039, Assam, India

November 2023





Dedicated to my beloved parents





INDIAN INSTITUTE OF TECHNOLOGY GUWAHATI
Department of Physics,
Guwahati - 781039

Statement

I hereby declare that this thesis entitled “**Investigations of magnetic and structural properties of rare earth substituted NdCrO_3** ” is the result of my own doctoral research work. This work was carried out under the supervision of **Prof. Dilip Pal** at the Department of Physics, Indian Institute of Technology Guwahati. To the best of my knowledge, the work presented in this thesis has not been submitted to any other Institute/University for the award of any degree.

Date 05/07/2023

Pragya Gupta

Pragya Gupta

Roll No: 176121015

Department of Physics,

Indian Institute of Technology Guwahati,

Guwahati-781039, India





INDIAN INSTITUTE OF TECHNOLOGY GUWAHATI
Department of Physics,
Guwahati - 781039

Certificate

This is to certify that work described in the thesis entitled “**Investigations of magnetic and structural properties of rare earth substituted NdCrO_3** ” by **Pragya Gupta**, a Ph.D. student of Department of Physics, Indian Institute of Technology Guwahati, for the award of degree of Doctor of Philosophy, has been carried out under my supervision. This work has not been submitted elsewhere for the award of any other degree.

Dr. Dilip Pal

Professor

Department of Physics,

Indian Institute of Technology Guwahati,

Guwahati-781039, India

Date 05/07/2023



Acknowledgment

First, I would like to express my profound gratitude to my thesis supervisor, Prof. Dilip Pal, for providing me the opportunity to work under his supervision. This thesis work would have not come to its conclusion without his immense support, precious advice, and valuable suggestions. I must acknowledge him for his patience and for providing the unconditional freedom to work, express my thoughts and keeping faith in my capabilities. Even during any difficult time, he always been soft, encouraging, and constant source of inspiration throughout my research life.

I am grateful to my Doctoral committee members, Prof. S. Ravi, Dr. U. N. Maiti, Prof. Chandan Mukherjee, for their valuable feedback to improve my research work. Their constructive criticism and valuable suggestions helped me to shape this thesis.

I would like to take the opportunity to thank the present Head of Department of Physics, Prof. Perumal Alagarsamy, and former department Heads, Prof. S. Ghosh and Prof. P. Poulouse, for their administrative cooperation. I extend my sincere gratitude to all the faculty members of the Department of Physics, for their support in several ways during my research.

I sincerely thank to the Indian Institute of Technology Guwahati, for allowing me to pursue my dreams and providing great work environment. I would like to thanks Dr. S Sarma, and the technical and non-technical staff of IIT Guwahati for their help and support. I also thank to Heads and technical staff, Central Instrumental Facility (CIF), IIT Guwahati for providing various sophisticated instrument facilities to complete my Ph.D. thesis objectives.

I am thankful to the Ministry of Human Resource and Development (MHRD), Govt. of India, for providing financial assistance for this Ph.D. thesis. Also, I would like to express thanks to the Science and Engineering Research Board (SERB)/Department of Science and Technology (DST) for providing various experimental facilities through research projects [SR/FST/PII-020/2009 and SR/FST/PSII-037/2016]. I would like to extend my thanks to the administration of IIT Guwahati for offering a truly magnificent campus.

I would like to thank my seniors Dr. Ram Kumar and Beenita Dutta for their suggestions and help in learning the basics of the instrument. I am thankful to my lab-mates Gajendra, Kaushik, Joya and Amit, for their support and creating a peaceful environment

in the lab. I also thank other seniors, Dr. Aakansha, Dr. Dolly, batch mates Manisha, Nitu, Madhurima, Ipsita, Dhriti, Debabrat, Devender, Pronoy, juniors Pushpanjali, Shashipriya, friends Juhi, Jaishree for their presence. I am grateful to my friends Subrata and Prajna for their unwavering support and motivation.

Finally, I express my profound gratitude to my family for being there throughout my life and encouraging me to pursue my aspirations. I sincerely thank to my sister (Neha Gupta) for her presence as both a friend and mentor. I am forever indebted to my parents, Maa (Smt. Keerti Gupta) and Papa (Shri Om Prakash Gupta), who always supported me. They have been my ultimate inspiration driving force to achieve whatever I have accomplished in life. Last but not the least, I would like to express deepest gratitude to almighty God for continuously blessing me strength and focus.

-Pragya Gupta



Synopsis

Magnetism and associated phenomena have been a popular subject of study for centuries due to their fundamental significance. Modern technology keeps us surrounded by advanced materials in our everyday lives. One such class is the perovskite oxides, where a number of physical properties result from competitive interactions and coexisting structural features. In particular, the understanding of the family of $R\text{CrO}_3$ (R = rare earth and yttrium) belonging to distorted perovskite structure with octahedrally coordinated B-sites occupied by Cr^{3+} ions and A-sites occupied by R^{3+} ions has been a contested topic. These orthochromites are emerging magnetoelectric multiferroic materials [1] that have recently attracted much interest because of their abundance of magnetic phenomena, including temperature-induced spin reorientation, exchange bias, magnetization reversal [2], and magnetic refrigeration [3], etc. The slight canting of Cr^{3+} spins in these materials arises due to the antisymmetric exchange interactions resulting in weak ferromagnetism. The spin reorientation, in which the direction of Cr^{3+} moments changes from one crystal axis to another, is a fascinating property of some $R\text{CrO}_3$ compounds.

The exchange bias (EB) in oxides is an active research area. The EB is constantly being investigated due to its potential applications in magnetic recording, spin-valve devices, magnetic sensors, and spintronics [4]. Meiklejohn and Bean first introduced EB in the Co/CoO system as shifting of magnetic hysteresis loop along the magnetic field axis [5]. The EB is the phenomenon associated with the exchange anisotropy generated at the interface between the antiferromagnetic (AFM) and ferromagnetic (FM) materials [6]. Further, EB was extended to coexisting magnetic phases with an equal interest in single-phase materials where the mechanism of EB differs from the interfacial systems. Magnetic structures, including magnetic core-shell structures and spontaneously phase-separated systems, were linked to the EB effect in single-phase alloys and compounds [7]. Different orthochromites similar to their isostructural manganites have been reported to illustrate the EB effect [8][9]. However, the role of spin reorientation on the EB effect in orthochromites is not understood. Furthermore, the R -ion dependence of the lattice distortions and magnetic structure corresponds to the phonon parameters and their variations near magnetic ordering temperature [10]. Granado [11] has defined the term spin-phonon coupling due to the phonon modulation of the superexchange integral and there has been a revival of interest

in this direction. Such as the case of $R\text{CrO}_3$, the spin-phonon coupling is observed only for magnetic R -ion [12]. However, no such studies have been reported for Nd-based orthochromite. Moreover, the Raman behavior and structural assignment related to ferroelectricity in orthochromites is a contentious topic [13][14].

Materials with multifunctional properties near room temperature are always desirable for practical uses. In this quest, the NdCrO_3 rare earth chromite can be a promising candidate. The NdCrO_3 crystallizes in an orthorhombic distorted perovskite structure with $Pnma$ symmetry. The magnetic structure of this material is considered as G-type AFM, where the Cr^{3+} moments order antiferromagnetically at $T_N \sim 219$ K [15]. The reorientation of Cr^{3+} spins occurs at $T_{SR} \sim 35$ K due to an abrupt change of spin configuration from high-temperature to low-temperature spin structure [16]. The magnetic ordering of Nd^{3+} ions (T_{RE}) takes place at a much lower temperature ~ 4.2 K [17]. Such complex magnetism mainly arises from the exchange interaction among Cr-Cr, R -Cr, and R - R ions. These interactions offer different magnetic phases and contribute to other properties. The ferroelectricity in NdCrO_3 is reported at $T_C \sim 87$ K which appears well below T_N , unlike other members of $R\text{CrO}_3$ series [18].

Besides such interesting properties, the understanding of NdCrO_3 is confined and less explored than other $R\text{CrO}_3$ members. The correlated structural and magnetic features in pure compound and the substitution effect on Nd site in NdCrO_3 is still lacking. For this work, an effort is made to study the substitution of rare earth elements on A-site. Hence, the Eu, Pr and Ce are chosen to substitute on Nd-site in NdCrO_3 . Here, the ionic radius and magnetic moment of these substituents are different from that of Nd^{3+} ion. From such perturbation of structure, the tuning of orthorhombic distortions and the modification of Cr-Cr and Nd-Cr magnetic interactions is expected. The dc magnetization measurements, low-temperature Raman spectroscopy and low-temperature X-ray diffraction are utilized for understanding of exchange bias feature, spin-lattice interaction, spin-reorientation dynamics, new magnetic states and their correlations to improve the multifunctionality of the material. The following three series of samples were prepared for the thesis work,

1. $\text{Nd}_{1-x}\text{Eu}_x\text{CrO}_3$ with $x = 0.0, 0.05, 0.10, 0.20, 0.50, 0.70, 0.90$ and 1.0
2. $\text{Nd}_{1-x}\text{Pr}_x\text{CrO}_3$ with $x = 0.0, 0.05, 0.10, 0.20$, and 0.30
3. $\text{Nd}_{1-x}\text{Ce}_x\text{CrO}_3$ with $x = 0.0, 0.05, 0.075, 0.10, 0.15$ and 0.175

This thesis is planned in 6 chapters and the brief description of each chapter is given in following section.

Chapter 1 provides various important concepts including fundamentals of magnetism, crystal structure of perovskites, magnetic structure, crystal field, and exchange interactions. The description of exchange bias phenomenon and its occurrence in various magnetic systems starting from interfacial system with special focus on single-phase material is presented. The introduction of rare-earth orthochromites with detailed review on materials is given. The literature survey on perovskite-type NdCrO_3 comprising rich magnetic, magnetoelectric properties, which emphasize the importance of this compound and highlights present research problem. Finally, the description of the motivation to undertake this thesis work is provided.

Chapter 2 outlines several experimental tools with their working principle used to conduct present thesis work. The methodology of sample preparation via a standard solid-state reaction route is discussed. The powder X-ray diffraction (XRD) technique for structural characterization and the Rietveld refinement method utilizing Fullprof software were covered. The introduction Raman scattering spectroscopy was included for detection the structural distortions of the samples. The field emission scanning electron microscope (FESEM) and energy dispersive X-ray (EDX) to analyze microstructure were presented. The X-ray photoelectron spectroscopy (XPS) was also explained to find the valance state. The basic principle of the physical property measurement system (PPMS) equipped with a vibrating sample magnetometer (VSM) to measure the temperature and field-dependent magnetic properties of the samples was described.

Chapter 3 presents synthesis of single-phase $\text{Nd}_{1-x}\text{Eu}_x\text{CrO}_3$ ($x = 0.0-1.0$) samples in polycrystalline form. A detailed study of structural and magnetic properties by means of dc magnetization measurements, temperature-dependent Raman spectroscopy and temperature-dependent X-ray diffraction is provided. The role of complete Eu substitution was discussed in terms of increased structural distortions and decreased antiferromagnetic transition temperature (T_N) and spin-reorientation transition temperature (T_{SR}) for $x = 0.05-1.0$ samples. The T_{SR} exist up to $x = 0.9$ sample and a rich dynamics of T_{SR} appears with Eu^{3+} substitution. The chemical pressure boundary from the structural and magnetic behavior across $x = 0.5$ is observed. The negative exchange bias (EB) effect is obtained, and the EB field decreases with increasing Eu content. For low substitution i.e. up to $x =$

0.2 samples, the non-monotonic behavior of the EB field around T^* is observed and which lies between T_N and T_{SR} temperatures. The strong spin-phonon coupling for $x = 0.0-0.20$ samples are described via the evolution of Raman modes in 80-300 K temperature range. The magnetoelastic coupling was explored by the variation of structural parameters in 3-300 K temperature range. The spin-phonon induced exchange bias around T^* was explained and verified using the density functional theory-based calculations. The maximum entropy method is also utilized to determine the electron density distribution revealing structural reorientation. The study emphasizes lattice modulations around T^* between T_N and T_{SR} for the first time in pure and substituted NdCrO_3 by exploring spin-phonon induced exchange bias and magneto-structural imprints.

Chapter 4 deals with the investigations of $\text{Nd}_{1-x}\text{Pr}_x\text{CrO}_3$ ($x = 0.0-0.30$) composition. In contrast to Eu^{3+} substitution in previous work, here the substituent Pr^{3+} is magnetic with larger ion size. The structural, optical and magnetic properties of $x = 0.0-0.30$ samples are discussed. The dc magnetization measurements provided significantly higher magnetization with slightly increased antiferromagnetic ordering temperature (T_N) through Pr substitution as compared to pure sample. With increasing Pr content, the spin-reorientation transition temperature (T_{SR}) decreases and absence of T_{SR} was seen in $\text{Nd}_{0.7}\text{Pr}_{0.3}\text{CrO}_3$ i.e. $x = 0.3$ sample. The Griffiths-like phase is observed for substituted i.e. $x = 0.05-0.30$ samples, unlike parent sample. The exchange bias effect is observed for all samples. Compared to Eu substitution, here the larger value of exchange bias field (H_{EB}) is achieved. The behavior of EB field below and above T_{SR} with Pr substitution displayed interesting trends linked with structural parameters. The influence of magnetic ordering on the phonon modes suggested spin-phonon coupling up to $x = 0.30$ substitution. The semiconductor behavior of samples was explored by UV-Vis diffuse reflectance spectroscopy. The magnetic phase diagram of the $x = 0.0-0.30$ samples is proposed. The role of tuned spin-reorientation and EB effect in $\text{Nd}_{1-x}\text{Pr}_x\text{CrO}_3$ compounds is discussed in details.

Chapter 5 is dedicated to the systematic structural and magnetic study of $\text{Nd}_{1-x}\text{Ce}_x\text{CrO}_3$ ($x = 0.0-0.175$) compounds for the first time. Compared to two previous chapters, here redox-active Ce is chosen as the final substituent. The presence of mixed Ce^{3+} and Ce^{4+} valency on the A-site and the oxygen vacancies using X-ray photoelectron spectroscopy (XPS) and its influence on NdCrO_3 are discussed. The covalent nature of Cr and O bonds for $x = 0.0-$

0.175 samples is depicted with help of electron density profiles. The antiferromagnetic ordering temperature (T_N) and spin-reorientation transition temperature (T_{SR}) exist for all i.e. $x = 0.05-0.175$ samples and soft nature of spin-reorientation was explained by the field dependence of magnetization. The merging of magnetic hysteresis loop through Ce substitution exhibiting exchange bias effect for $x = 0.05-0.175$ samples is found in different way to parent, Eu^{3+} and Pr^{3+} substituted samples. The observation of negative magnetization below T_N for $x = 0.0-0.175$ sample was discussed. Importantly, a demonstration to obtain different magnitudes of magnetization at same applied field in opposite directions revealing different magnetic states is presented. The discussion on magnetic states by means of normalized magnetic susceptibility and correlated EB feature for the samples are provided.

Chapter 6 is devoted to the summary of the overall research work carried out in the thesis. The influence of different rare-earth substitution on A-site in NdCrO_3 along with fantastic structural and magnetic properties are studied. The scope for future research work has also been included.



List of Publications

Peer Reviewed Journals/conf. proceedings

1. **Pragya Gupta** and D. Pal, Spin induced exchange bias and lattice modulation in $\text{Nd}_{1-x}\text{Eu}_x\text{CrO}_3$, *Journal of Physics: Condensed Matter* 33 (2021) 135806, doi.org/10.1088/1361-648X/abda7d
2. **Pragya Gupta** and D. Pal, Exploration of low field magnetic states in $\text{Nd}_{1-x}\text{Ce}_x\text{CrO}_3$, *Journal of Physics: Condensed Matter* 35 (2023) 345803, doi.org/10.1088/1361-648X/acd7bc
3. **Pragya Gupta** and D. Pal, Interwoven spin-reorientation and exchange bias in $\text{Nd}_{1-x}\text{Pr}_x\text{CrO}_3$, *Journal of Alloys and Compounds*, 969 (2023) 172389, doi.org/10.1016/j.jallcom.2023.172389
4. **Pragya Gupta**, Ram Kumar and D. Pal, Magneto-structural imprints in Eu substituted NdCrO_3 perovskites, *Journal of Superconductivity and Novel Magnetism* (2023) (Under review).
5. **Pragya Gupta** and D. Pal, The correlation between magnetic interactions and lattice distortions in Pr and Eu substituted NdCrO_3 , *Journal of Physics: Conference Series* 2164 (2022) 012066, doi.org/10.1088/1742-6596/2164/1/012066
6. **Pragya Gupta** and D. Pal, Evolution of the spin reorientation temperature of NdCrO_3 by rare-earth substitutions, *JPS Conference Proceedings* 011092 (2023) 1–6, doi.org/10.7566/JPSCP.38.011092

International and National Conference/Workshop/Presentations

1. The Workshop on Characterization of Magnetic Materials, organized by UGC-DAE Consortium for Scientific Research, Mumbai Centre from 27th -29th November 2019 at NIT Nagaland, Dimapur.
2. Online Workshop on Rietveld Refinement Method, organized by UGC-DAE Consortium for Scientific Research, Mumbai Centre, in association with Indore Centre from 22nd – 24th September 2020.
3. Workshop on Software in Mathematics and Statistics (WSMS – 2021), organized by the Department of Mathematics, National Institute of Technology Tiruchirappalli, held in online format from 2nd to 6th August 2021.
4. Best presentation award (\$400) at the Around-the-Clock Around-the-Globe Magnetism Conference (AtC-AtG), 2021, organized by IEEE Magnetism, held in online format on August 30th, 2021.
5. Poster presentation at the International Conference on Strongly Correlated Electron Systems (SCES 2020/2021 Brazil), held online from September 27th to October 02nd, 2021.
6. Poster presentation at the International Conference On Advanced Materials And Mechanical Characterization (ICAMMC-2021), organized by the Department of

Physics and Nanotechnology and Department of Mechanical Engineering, SRM Institute Of Science And Technology, in Virtual Mode, from December 02nd to 4th, 2021.

7. Oral presentation at the National Science Day, organized by the Department of Physics, Indian Institute of Technology Guwahati, held on February 28th, 2022.
8. Poster presentation at the North-East Research Conclave: Sustainable Science and Technology (NERC-2022), organized by the Indian Institute of Technology Guwahati, from May 20th to 22nd, 2022.
9. Poster presentation at the 29th International Conference on Low-Temperature Physics (LT29, 2022, Sapporo, Japan) held online from August 18th to 24th, 2022.



Table of Contents

Chapter 1 : Introduction	1
1.1 Fundamentals of magnetism.....	1
1.2 Crystal structure	4
1.3 Magnetic Structure	7
1.4 Crystal field	8
1.5 Magnetic exchange interactions	9
1.5.1 Direct exchange interaction	9
1.5.2 Superexchange interaction	10
1.5.3 Double exchange interaction.....	11
1.5.4 Ruderman-Kittel-Kasuya-Yosida (RKKY) interaction	12
1.5.5 Dzyaloshinskii-Moriya interaction	12
1.6 Exchange bias effect.....	14
1.7 Rare earth orthochromites	18
1.8 NdCrO ₃ orthochromite	23
1.9 Motivation	28
Chapter 2 : Experimental methods	31
2.1 Sample preparation: Solid State Reaction Method	31
2.2 Characterization Techniques	33
2.2.1 Powder X-ray diffraction	33
2.2.2 Raman spectroscopy	35

2.2.3	Scanning Electron Microscopy	37
2.2.4	X-ray photoelectron spectroscopy	38
2.2.5	Physical Properties Measurement System	40
Chapter 3 : Spin-induced exchange bias, lattice modulation, and magnetostructural imprints in $\text{Nd}_{1-x}\text{Eu}_x\text{CrO}_3$.....		45
3.1	Introduction	45
3.2	Experimental and Computational details	47
3.3	Results and discussions	48
3.3.1	Room temperature Powder X-ray diffraction	48
3.3.2	Microstructural analysis.....	52
3.3.3	Room temperature Raman spectroscopy	54
3.3.4	Magnetic properties	57
3.3.5	Structural properties at low temperatures	66
3.4	Summary	84
Chapter 4 : Interwoven spin-reorientation and exchange bias in $\text{Nd}_{1-x}\text{Pr}_x\text{CrO}_3$.....		87
4.1	Introduction	87
4.2	Experimental details.....	88
4.3	Results and discussions	89
4.3.1	Powder X-ray diffraction	89
4.3.2	Microstructural analysis.....	92
4.3.3	X-ray photoelectron spectroscopy	93

4.3.4	UV-Vis spectroscopy	94
4.3.5	Raman spectroscopy	95
4.3.6	Temperature and field-dependent magnetic properties.....	99
4.4	Summary	107
Chapter 5 : Exploration of low-field magnetic states in Nd_{1-x}Ce_xCrO₃.....		109
5.1	Introduction	109
5.2	Experimental Section	110
5.3	Results and discussions	111
5.3.1	X-ray diffraction (Rietveld refinement and Maximum Entropy Method) .	111
5.3.2	Microstructural analysis.....	115
5.3.3	Raman analysis	116
5.3.4	XPS analysis	118
5.3.5	Magnetic characterization.....	120
5.4	Summary	129
Chapter 6 : Conclusions		131
References.....		145

List of Figures

- Fig. 1-1** Schematics representing different spins arrangement of ferromagnetic, antiferromagnetic, and ferrimagnetic materials.2
- Fig. 1-2** (a) Ideal cubic perovskite structure with general formula ABO_3 (b) The three main distortions of perovskite structure adopted from [126], here circle represents distortions of cation displacement, Jahn-Teller effects, and octahedral tilts using example.4
- Fig. 1-3** The orthorhombic perovskite structure, where yellow, blue and red spheres represent A (R^{3+}) B (Cr^{3+}) and oxygen ions.5
- Fig. 1-4** Schematic presentation of (a) A-type (b) C-type (c) G-type and (d) E-type collinear magnetic structures.7
- Fig. 1-5** The e_g orbitals grouped as dz^2 and $dx^2 - y^2$ orbitals. The t_g orbitals grouped as d_{xy} , d_{yz} and d_{zx} orbitals. The bottom diagram shows the crystal field for octahedral and tetrahedral environment.8
- Fig. 1-6** Schematics for the spin arrangements in (a) the AFM superexchange interaction and (b) the FM superexchange interaction..... 10
- Fig. 1-7** Schematics for Dzyaloshinskii-Moriya interaction..... 13
- Fig. 1-8** Schematics illustrates the spin arrangement of FM-AFM bilayer at various stages of an exchange-biased hysteresis loop. 14
- Fig. 1-9** The effective coercive field and EB field as function of temperature for the rare earth intermetallic $Nd_{0.75}Ho_{0.25}Al_2$ compound. From [68]..... 17
- Fig. 1-10** The variation of Neel temperature (T_N) for Cr^{3+} ordering and rare earth ordering (T_{RE}) with R-ion radii and tolerance factor. From [75]. 18

Fig. 1-11 The spin structures for Pbnm symmetry showing no spin canting in Γ_1 and the spin canting in Γ_2 and Γ_4 configurations. The blue and yellow spheres represent Cr^{3+} (with spin) and R^{3+} ions (without spin). From [76]..... 19

Fig. 1-12 Schematics of t-e hybridization effect on virtual charge transfer for superexchange interaction in RCrO_3 perovskite. From [42]..... 20

Fig. 1-13 The magnetization vs. temperature curves of CeCrO_3 for ZFC and ZFC case at applied magnetic field of 5kOe. From [86]. 20

Fig. 1-14 The EB field vs. temperature plot for various field cooling in the $\text{La}_{0.25}\text{Pr}_{0.75}\text{CrO}_3$ rare earth perovskite compound. From [89]. 21

Fig. 1-15 Temperature effect on the Raman mode associated with octahedral rotations along y-axis out of phase in the YCrO_3 , LuCrO_3 , GdCrO_3 , EuCrO_3 and SmCrO_3 rare earth chromites. From [12]. 23

Fig. 1-16 Magnetic specific heat (C_m) of NdCrO_3 in 0.3 K to 300 K thermal range, which is obtained after subtracting the specific heat of isostructural non-magnetic LaGaO_3 compound shown in inset. From [81]. 24

Fig. 1-17 (Left) The temperature dependent X-ray diffraction patterns of NdCrO_3 where vertical lines below the diffraction data indicate the allowed Bragg reflections at room temperature, From [112]. (Right) The variation of Raman phonon frequency with temperature in LaCrO_3 , From [113]..... 25

Fig. 1-18 The temperature dependence of electric polarization (P) of NdCrO_3 for the poling fields (E) of $\pm 2 \text{ kVcm}^{-1}$ and the inset shows pyroelectric current (I_p) vs. T at $E = +2 \text{ kV cm}^{-1}$. From [18]..... 26

Fig. 1-19 The temperature dependence of exchange bias field in $\text{NdCr}_{0.5}\text{Fe}_{0.5}\text{O}_3$ mixed orthochromite. From [118]..... 27

Fig. 1-20 The coercive field (H_C , closed symbols) and exchange bias field (H_E , open symbols) as the function of temperature for $Dy_{1-x}Nd_xCrO_3$ with $x = 0$ (a), 0.33 (b), 0.67 (c), and 1.0 (d) solid solutions where the peaks in H_C attributes to the onset of H_E that becomes pronounced with the increase of Nd substitution. From [118].	27
Fig. 1-21 Schematics for A-site ionic radius (r_R) and magnetic moment (J) variation in $Nd_{1-x}R_xCrO_3$ ($x = 1.0$ and $R = Eu, Pr$ and Ce).	29
Fig. 2-1 Various steps involved in the sample synthesis procedure via standard solid-state reaction method.	31
Fig. 2-2 Schematic presentation of Bragg's law for X-ray diffraction.	34
Fig. 2-3 Photograph of the X-ray diffractometer (Rigaku, Smart Lab).	34
Fig. 2-4 The energy level diagram for Rayleigh and Raman scattering.	36
Fig. 2-5 Photograph of the Raman spectrometer (Horiba Jobin Yvon, LabRam HR800).	36
Fig. 2-6 Photograph of the field emission scanning electron microscope (Sigma, Zeiss).	37
Fig. 2-7 Photograph of the X-ray photoelectron spectrometer (ESCALAB).	39
Fig. 2-8 Photograph of physical property measurement system (PPMS, DynaCool).	40
Fig. 2-9 The VSM coil set with motor (right) and the block diagram of VSM mode operation of PPMS (left).	41
Fig. 3-1 (a) Rietveld refinement of powder XRD patterns of $Nd_{1-x}Eu_xCrO_3$ ($x = 0.0-1.0$) samples by using the FULLPROF program. The circles are the experimental points, the solid line (black) is refined data, and the bottom green line shows the difference between	

these two. Vertical lines (blue) represent the Braggs position (b) The crystal structure of the $x = 0.10$ sample visualized by VESTA software.48

Fig. 3-2 (a) The cell distortion factor d and orthorhombic strain s as the function of Eu content and (b) The x variation of the tilt angle $\phi[010]$51

Fig. 3-3 FESEM micrograph of $\text{Nd}_{1-x}\text{Eu}_x\text{CrO}_3$, (a) $x = 0.0$ (b) 0.20 (c) 0.70 samples (d) the EDX mapping of $x = 0.05$ sample (e) the grain size distribution of $x = 0.7$ sample and (f) the average grain size as the function of Eu content.....52

Fig. 3-4 (a) Calculated bulk modulus as the function of Eu content and (b) the x dependence of unit cell volume obtained from refinement of $\text{Nd}_{1-x}\text{Eu}_x\text{CrO}_3$ ($x = 0.0-1.0$) samples. ...53

Fig. 3-5 (a) Raman Spectra from 100 to 600 cm^{-1} of $\text{Nd}_{1-x}\text{Eu}_x\text{CrO}_3$ ($x = 0.0-1.0$) samples measured at room temperature and (b)-(c) the x dependence of phonon frequencies of selected Raman modes.54

Fig. 3-6 Temperature-dependent magnetization curves measured in FC mode for the applied field of 100 Oe (b) Temperature dependence of the first derivative of susceptibility curves having peaks at magnetic transition and (c) The variation of T_N and T_{SR} as the function of Eu content for $\text{Nd}_{1-x}\text{Eu}_x\text{CrO}_3$ ($x = 0.0-1.0$) samples.....57

Fig. 3-7 Schematic diagram of the moment arrangements in the temperature regions (a) $T < T_{SR}$ (b) $T_{SR} < T < T^*$, and (c) $T^* < T < T_N$, where M_{Cr} and $M_{|Nd+Eu|}$ indicate the FM component of Cr^{3+} and PM moments of $\text{Nd}^{3+}/\text{Eu}^{3+}$ ions respectively.58

Fig. 3-8 The effect of Eu content on the exchange constants J_1 and J_2 for the $\text{Nd}_{1-x}\text{Eu}_x\text{CrO}_3$ ($x = 0.0$ to 1.0) samples. Inset shows the representation of J_1 and J_2 in the unit cell of the $x = 0.5$ sample.60

Fig. 3-9 (a) Field dependence of magnetization (M-H) loops at 100 K of the $\text{Nd}_{1-x}\text{Eu}_x\text{CrO}_3$ ($x = 0.0-1.0$) system (b) the enlarged portions of exchange biased loop of $x = 0.2-0.9$

samples and (c) The EB field H_{EB} as the function of Eu content at $T = 100$ K of the $Nd_{1-x}Eu_xCrO_3$ ($x = 0.0-1.0$) samples. 62

Fig. 3-10 Temperature dependence of (a) EB field $H_{EB}(T)$, (b) coercive field $H_C(T)$, and (c) the ratio of $H_{EB}(T)$ and $H_C(T)$ extracted from 10 kOe field cooled M-H loops of $Nd_{1-x}Eu_xCrO_3$ ($x = 0.10$ and 0.20) sample, demonstrating the T_{SR} , T^* and T_N 64

Fig. 3-11 Temperature dependence of (a) remanence asymmetry $M_{EB}(T)$ (b) magnetic coercivity $M_C(T)$ and (c) the ratio of $M_{EB}(T)$ and $M_C(T)$ extracted from 10 kOe field cooled M-H loops of $Nd_{1-x}Eu_xCrO_3$ ($x = 0.10$ and 0.20) sample. 65

Fig. 3-12 Raman spectra of $Nd_{1-x}Eu_xCrO_3$ ($x = 0.0$ and 0.10) samples from 100 to 600 cm^{-1} in the temperature range of 80 to 300K. 66

Fig. 3-13 (a)-(d) Temperature dependence of antistretching mode $B_{3g}(3)$ frequencies and (e)-(h) the corresponding linewidths of $Nd_{1-x}Eu_xCrO_3$, ($x = 0.0-0.20$) samples. The red dotted lines show the fitted curves for anharmonic contribution, according to Eq. (3.10), and solid black lines guided to the eye. 67

Fig. 3-14 (a)-(d) The effect of temperature on $A_g(6)$, the bending mode frequencies $Nd_{1-x}Eu_xCrO_3$, ($x = 0.0-0.20$) samples. The red dotted lines are fitted curves for anharmonic contribution, according to Eq. (3.10), and solid black lines guided to the eye. 69

Fig. 3-15 Temperature dependence of phonon frequencies and (e)-(h) the linewidths of $B_{3g}(1)$ mode involving the Nd^{3+}/Eu^{3+} ion vibrations of $Nd_{1-x}Eu_xCrO_3$, ($x = 0.0-0.20$) samples. Solid black lines guided to the eye. 70

Fig. 3-16 Theoretical temperature evolution of (a) $B_{3g}(3)$ and (b) $B_{3g}(1)$ mode frequencies of $Nd_{1-x}Eu_xCrO_3$ ($x = 0.0$) sample, showing the anomaly across the transitions $T_{SR} \sim 37$ K, $T^* \sim 100$ K and $T_N \sim 225$ K. 72

Fig. 3-17 (a) The XRD patterns of $\text{Nd}_{1-x}\text{Eu}_x\text{CrO}_3$ ($x = 0.0$ and 0.2) samples in the 3-300 K temperature range and (b) Rietveld refinement of low-temperature XRD patterns of $x = 0.2$ sample using Pnma space group at selected temperatures.74

Fig. 3-18 The lattice parameters a , b , c , and lattice volume V in the 3-300 K temperature range for $\text{Nd}_{1-x}\text{Eu}_x\text{CrO}_3$ (a) $x = 0.0$ and (b) $x = 0.2$ compositions.75

Fig. 3-19 Temperature dependence of the Cr-O1, Cr-O2 bond lengths, and Cr-O1-Cr, Cr-O2-Cr bond angles of $\text{Nd}_{1-x}\text{Eu}_x\text{CrO}_3$ (a)-(d) $x = 0.0$ and (e)-(h) $x = 0.2$ samples.76

Fig. 3-20 Temperature dependence of (a)-(c) Nd-O1, Nd-O2 bond length and Nd z position for $x = 0.0$ sample (d)-(f) Nd/Eu-O1, Nd/Eu-O2 bond lengths, and Nd/Eu z position for $x = 0.2$ sample.77

Fig. 3-21 The unit cell of $\text{Nd}_{1-x}\text{Eu}_x\text{CrO}_3$ ($x = 0.0$) sample in the a - c plane for Pnma space group at (a) $T = 40$ K ($\sim T_{\text{SR}}$), (b) $T^* = 100$ K, (c) $T = 200$ K ($T < T_{\text{N}}$) and (d) the 3D-ED maps in the xz plane, y -intercept = 0.75 at $T = 40$ K (e) the maximum of ED as the function of temperature of $x = 0.0$ sample.79

Fig. 3-22 The unit cell of $\text{Nd}_{1-x}\text{Eu}_x\text{CrO}_3$ ($x = 0.2$) sample in the a - c plane for Pnma space group at (a) $T = 40$ K ($\sim T_{\text{SR}}$), (b) $T^* = 80$ K, (c) $T = 215$ K ($T \leq T_{\text{N}}$) and (d) the 3D-ED map in the xz plane, y -intercept = 0.75 at $T = 40$ K and (e) the maximum of ED as the function of the temperature of $x = 0.2$ sample.80

Fig. 3-23 The electron density distribution (3D) calculated by the MEM method in the unit cell of $\text{Nd}_{1-x}\text{Eu}_x\text{CrO}_3$ ($x = 0.2$) sample for the Pnma space group using the iso-surface level of $1 \text{ e}/\text{\AA}^3$ at (a) $T = 75$ K (b) $T^* = 80$ K (c) $T = 85$ K and (d)-(f) the corresponding (2D) charge density maps in (010) plane for the $T = 75$ K to 85 K. The contour lines are drawn from 0 to $1 \text{ e}/\text{\AA}^3$ with intervals of $0.1 \text{ e}/\text{\AA}^3$81

Fig. 3-24 Theoretical bulk modulus as a function of temperature for $\text{Nd}_{1-x}\text{Eu}_x\text{CrO}_3$ (a) $x = 0.0$ and (b) $x = 0.2$ samples, showing anomalies at the T_N , T^* , and T_{SR} in the range of 3-300 K.....	82
Fig. 3-25 The distribution of charge density (3D) within the unit cell of $\text{Pna}2_1$ symmetry using the iso-surface level of $1 \text{ e}/\text{\AA}^3$ at (a) $T = 75 \text{ K}$ (b) $T^* = 80 \text{ K}$ (c) $T = 85 \text{ K}$ and (d)-(f) the corresponding (2D) charge density maps in (001) plane from 75 K to 85 K of $\text{Nd}_{1-x}\text{Eu}_x\text{CrO}_3$ ($x = 0.2$) sample using MEM method. Contour lines of charge density are from 0 to $1 \text{ e}/\text{\AA}^3$ with $0.1 \text{ e}/\text{\AA}^3$ intervals.....	83
Fig. 4-1 Rietveld refinement of XRD data for $\text{Nd}_{1-x}\text{Pr}_x\text{CrO}_3$ (a) $x = 0.05$ (b) $x = 0.10$ (c) $x = 0.20$ and (d) $x = 0.30$ samples and (e) The crystal structure of the $x = 0.20$ sample.....	89
Fig. 4-2 FESEM micrograph of $\text{Nd}_{1-x}\text{Pr}_x\text{CrO}_3$ (a) $x = 0.10$ (b) $x = 0.20$ and (c) $x = 0.30$ samples along with their grain size distribution (d) EDX mapping of $x = 0.20$ sample and (e) EDX mapping of $x = 0.30$ sample in a smaller area of $5 \times 5 \mu\text{m}^2$	92
Fig. 4-3 XPS spectra of (a)-(b) the core level Pr 3d spectra (c)-(d) the Cr 2p spectra, and (e)-(f) the O 1s spectra of $x = 0.10$ and 0.30 compounds.	93
Fig. 4-4 (a) UV-Vis DRS spectrum of $\text{Nd}_{1-x}\text{Pr}_x\text{CrO}_3$ ($x = 0.0-0.3$) samples in the range of 250 to 850 nm. (b) Estimation of bandgap E_g from Tauc plots for each sample.....	94
Fig. 4-5 Room temperature Raman spectra acquired for the $\text{Nd}_{1-x}\text{Pr}_x\text{CrO}_3$ ($x = 0.0-0.3$) samples in the 100 to 600 cm^{-1} wavenumber range.....	95
Fig. 4-6 Effect of temperature on (a)-(b) antisymmetric stretching mode frequency $B_{3g}(3)$ and (c)-(d) corresponding linewidth of $\text{Nd}_{1-x}\text{Pr}_x\text{CrO}_3$ ($x = 0.10, 0.30$) composition. The dotted lines (red) represent fitted curves for anharmonicity by Eq.4.2 and solid lines (black) guide to the eye.	97

Fig. 4-7 Temperature dependence of phonon mode $A_g(6)$ for bending of CrO_6 octahedra of $\text{Nd}_{1-x}\text{Pr}_x\text{CrO}_3$ (a) $x = 0.10$ and (b) $x = 0.30$ compound. The dotted lines (red) represent fitted curves for anharmonicity by Eq.4.2, and solid lines (black) guide to the eye.....98

Fig. 4-8 Temperature dependence of magnetization for field cooled condition under 100 Oe applied field for $\text{Nd}_{1-x}\text{Pr}_x\text{CrO}_3$ ($x = 0.0-0.3$) compositions.....99

Fig. 4-9 Temperature dependence of FC magnetization under different applied magnetic field of 100 Oe, 1 kOe and 10 kOe for $\text{Nd}_{1-x}\text{Pr}_x\text{CrO}_3$ (a) $x = 0.0$ and left inset shows M-T curve under 50 kOe (b) $x = 0.05$ (c) $x = 0.10$ (d) $x = 0.20$ and (e) $x = 0.30$ samples. The right inset of (a)-(e) shows the derivative of magnetic susceptibility vs. temperature exhibit peaks at T_N and T_{SR} for the corresponding samples. 100

Fig. 4-10 (a) The inverse magnetic susceptibility ($1/\chi$) vs. temperature (T) of $\text{Nd}_{1-x}\text{Pr}_x\text{CrO}_3$ ($x = 0.0-0.30$) samples at the 100 Oe field and the inset shows the CW analysis for $x = 0.0$ sample. The $1/\chi$ vs T plots at different applied magnetic fields of 100 Oe, 1kOe and 10 kOe for (b) $x = 0.10$ (c) $x = 0.30$ samples showing the deviation from CW law at low field and (d) Log-log plot of inverse susceptibility as a function of temperature following Eq.4.3, where the red line is linear fit in the PM and GP regime..... 102

Fig. 4-11 The evolution of different phases through magnetic phase diagram of $\text{Nd}_{1-x}\text{Pr}_x\text{CrO}_3$ samples. 103

Fig. 4-12 (a) The M-H loops measured at $T = 5$ K ($T < T_{SR}$) for $\text{Nd}_{1-x}\text{Pr}_x\text{CrO}_3$ ($x = 0.0-0.30$) samples. The enlarged portion of the loops for (b) $x = 0.05$ (c) $x = 0.10$ (d) $x = 0.20$ and (f) $x = 0.30$ samples. The variation of (g) the coercive field H_C , (h) the exchange bias field H_{EB} and (i) the cell distortion factor with Pr substitution..... 104

Fig. 4-13 (a) The M-H loops at $T = 100$ K ($T > T_{SR}$) for $\text{Nd}_{1-x}\text{Pr}_x\text{CrO}_3$ ($x = 0.0-0.30$) samples. The enlarged portion of the loops for (b) $x = 0.05$ (c) $x = 0.10$ (d) $x = 0.20$ and (f)

x = 0.30 samples. The variation of (g) the coercive field H_C , (h) the exchange bias field H_{EB} and (i) the Cr-O2 bond length with Pr substitution..... 105

Fig. 4-14 Temperature dependence of (a) the coercive field $H_C(T)$ and (b) the exchange bias field $H_{EB}(T)$ extracted from FC M-H loops of $Nd_{1-x}Pr_xCrO_3$ (x = 0.30) sample. 106

Fig. 5-1 The Rietveld refinement fitting of XRD data of the $Nd_{1-x}Ce_xCrO_3$ (a) x = 0.05 (b) x = 0.10 and (c) x = 0.175 compositions. 111

Fig. 5-2 The MEM charge density map of $Nd_{1-x}Ce_xCrO_3$ (a) x = 0.05 and (b) 0.175 samples at the iso surface level of $1 \text{ eA}^{\circ-3}$. The charge density distribution of (c) x = 0.05 and (d) x = 0.175 samples for the (100) section. The contour range is from 0 to $1 \text{ eA}^{\circ-3}$ with $0.1 \text{ eA}^{\circ-3}$ intervals. 114

Fig. 5-3 FESEM images of the $Nd_{1-x}Ce_xCrO_3$ (a) x = 0.05 and (b) x = 0.15 composition (c) Average grain size as the function of Ce concentration and the inset shows the grain size distribution of x = 0.15 sample (d) EDX spectrum and (e) elemental mapping of x = 0.15 composition showing the presence of Nd, Ce, Cr, and O elements..... 115

Fig. 5-4 Raman spectra acquired from the $Nd_{1-x}Ce_xCrO_3$ (x = 0.05-0.175) compositions. 116

Fig. 5-5 The wavenumbers as a function of Ce content of selected phonon modes and (b) Fitting of Raman spectra of $Nd_{1-x}Ce_xCrO_3$ (x = 0.05 to 0.175) compositions in 490 to 590 cm^{-1} wavenumber range illustrating additional hump as compared to the undoped sample. 117

Fig. 5-6 The XPS results of $Nd_{1-x}Ce_xCrO_3$ for (a)-(c) The core-level Ce 3d of x = 0.05, 0.10 and 0.15 (d) The core-level Cr 2p spectra of x = 0.05 and (e)-(f) The O 1s spectra of x = 0.05 and 0.15 samples..... 118

- Fig. 5-7** (a) FC magnetization vs. temperature under an applied magnetic field of 100 Oe of $\text{Nd}_{1-x}\text{Ce}_x\text{CrO}_3$ ($x = 0.05-0.175$) samples (b) The value of T_N and T_{SR} as the function of Ce content where insets show extended $d\chi/dT$ vs. T curves of present samples (c) Temperature variation of the magnetic susceptibility times temperature (χT) using 100 Oe FC magnetization curves, demonstrating the magnetic phases and (d) Inverse susceptibility vs. temperature curves and the solid red lines are fit to the Curie-Weiss law for selected samples..... 120
- Fig. 5-8** (a) Field dependence of magnetization (M-H) of $\text{Nd}_{1-x}\text{Ce}_x\text{CrO}_3$ ($x = 0.05-0.175$) samples in -90 to +90 kOe field sweep at 100 K (b)-(e) Expanded view of exchange biased M-H loops of $x = 0.0, 0.05, 0.10,$ and 0.15 samples and (f) The variation of EB field (H_{EB}) and coercive field (H_C) with Ce content. 123
- Fig. 5-9** The Magnetic susceptibility as the function of temperature, measured in ZFC mode (χ_{ZFC}) (solid line) and FC mode (χ_{FC}) (scatter line) at the magnetic field of (a) $H = +500$ Oe and (b) $H = -500$ Oe for the $\text{Nd}_{1-x}\text{Ce}_x\text{CrO}_3$ ($x = 0.05, 0.10$ and 0.15) samples. The arrow indicates the χ_{ZFC} direction for the positive and negative fields, respectively..... 124
- Fig. 5-10** Temperature dependence of magnetic susceptibility measured in ZFC mode (χ_{ZFC}) under the applied field of (a) ± 250 Oe (b) ± 500 Oe (c) ± 750 Oe (d) ± 1000 Oe (e) ± 1500 Oe (f) ± 2800 Oe and (g) ± 3500 Oe for the $\text{Nd}_{1-x}\text{Ce}_x\text{CrO}_3$ ($x = 0.0, 0.05$ and 0.15) compositions. Here, χ_+ (solid line in blue shades) is the ZFC susceptibility under the positive applied magnetic field, and χ_- (solid line in red shades) is the ZFC susceptibility under the negative applied magnetic field. 125
- Fig. 5-11** Magnetic field dependence of Zeeman energy for the $\text{Nd}_{1-x}\text{Ce}_x\text{CrO}_3$ ($x = 0.0, 0.05,$ and 0.15) samples..... 126

Fig. 5-12 The Temperature dependence of EB field (H_{EB}) for $Nd_{1-x}Ce_xCrO_3$ (a) $x = 0.05$ and (b) 0.15 samples. Temperature dependence of ZFC magnetic susceptibility difference normalized by FC susceptibility $\frac{(\chi_+ - \chi_-)/2}{\chi_{FC}}$ for (c) $x = 0.05$ and (d) 0.15 samples under the applied field of 250 Oe to 3500 Oe..... 127



List of Tables

Table 1-1 General atomic positions for rare earth orthochromites with Pnma space group.	6
Table 3-1 Lattice parameters a, b, c, unit-cell volume V, bond lengths Nd-O1 and Cr-O2, and bond angle Cr-O1-Cr obtained from Rietveld refinement of Nd _{1-x} Eu _x CrO ₃ (x = 0.0 to 1.0) samples.	49
Table 3-2 Experimental phonon modes wavenumbers of Nd _{1-x} Eu _x CrO ₃ (x = 0.0-1.0) samples, theoretical wavenumber, and their assignment for x = 0.0 and 1.0 sample calculated at 300 K.....	56
Table 4-1 The lattice parameters a, b, and c, cell volume (V), bond lengths Cr-O1, Cr-O2, and bond angles Cr-O1-Cr, Cr-O2-Cr from Rietveld refinement of Nd _{1-x} Pr _x CrO ₃ (x = 0-0.3) samples. The tolerance factor (t), orthorhombic strain (S _{ac}), and cell distortion factor (d) are obtained from crystallographic parameters.	90
Table 4-2 The Raman mode frequencies of the Nd _{1-x} Pr _x CrO ₃ (x = 0.0-0.3) samples at room temperature.	96
Table 5-1 The lattice parameters a, b, and c, cell volume (V), orthorhombic strain (S _{ac}), Cr-O1-Cr bond angle, Cr-O1 bond length, position coordinates, site occupancies obtained from Rietveld refinement and the electron charge density at the Cr-O1 bond mid and at central O1 atom obtained from MEM analysis.....	113
Table 5-2 The Ce ions percentage in 3+, 4+ oxidation states for the Nd _{1-x} Ce _x CrO ₃ (x = 0.05, 0.10, and 0.15) compositions.	119

List of Symbols and Abbreviations

m	Meter	L	Orbital angular momentum number
cm	Centimeter	S	Spin angular momentum number
μm	Micrometer	μ_{eff}	Effective paramagnetic moment
nm	Nanometer	μ_B	Bohr magneton
\AA	Angstrom	N	Avogadro number
GPa	Gigapascal	k_B	Boltzmann constant
$^{\circ}\text{C}$	Centigrade (degree)	M	Magnetization
T	Temperature	H	Magnetic field
K	Kelvin	χ	Magnetic susceptibility
Oe	Oersted	ZFC	Zero field cooled
T	Tesla	FCC	Field cooled cooling
FM	Ferromagnetic	FC/FC	Field cooled warming
AMF	Antiferromagnetic	W	
FIM	Ferrimagnetic	$M-T$	Temperature dependent magnetization
C	Curie constant	$M-H$	Field dependent magnetization
T_C	Curie temperature	EB	Exchange bias
T_N	Néel temperature	H_{EB}	EB field
J_{ij}	Superexchange integral	H_C	Coercive field
S_i	Magnetic moment	M_R	Remanence
NN	Nearest neighbors	H_{FC}	Cooling field
NNN	Next nearest neighbors	T_{SR}	Spin reorientation transition
g	Lande g-factor	T_{comp}	Compensation temperature
J	Total angular momentum number		

M_s Saturation magnetization

M_R Remanent magnetization

$FC M-H$
 H Field cooled M-H

J Exchange constant

ω Wavenumber

ρ Electron scattering density

F_{hkl} Structure factor

V Volume

Other parameters

XRD X-ray diffraction

d_{hkl} Inter planar spacing

θ Diffraction angle

λ Wavelength

χ^2 Chi-square

R_{Bragg} Bragg factor

R_f Profile factor

RT Room temperature

h Hours

a, b, c Lattice parameters of orthorhombic unit cell

FESEM Field emission scanning electron microscopy

EDX Energy dispersive X-ray spectroscopy

XPS X-ray photoelectron spectroscopy

VSM Vibrating sample magnetometer

PPMS Physical Properties Measurement System



Chapter 1 : Introduction

The magnetism and associated phenomenon have been an avid subject of study for centuries due to their fundamental significance. The technological advancement in magnetic materials keep everyday life surrounded by information storage, medical equipment, electrical machines and aviation industry, robotics and many more. The discovery of intriguing giant magnetoresistance (GMR) [19][20], high temperature superconductors [21][22], colossal magnetoresistance (CMR) [23], exchange bias (EB) [4], magnetic refrigeration [24], topological insulators [25] and skyrmions [26] has generated remarkable interest in research community. Primarily, the spin degree of freedom in addition to charge degree of freedom unlocked the field of spintronics [27], where the EB effect shows a very important role in spintronic devices [28]. For improved functionality, one can also think of enabling lattice degree of freedom. For instance, we can opt for materials having more than one ferroic order i.e. multiferroics [29]. In one such class, the magnetic and ferroelectric ordering coexist and can be controlled by one another due to magnetoelectric (ME) coupling. The multiferroics offer a large number of potential applications in the forms of thin films like tunnel magnetoresistance, spin-valves, and multiple-state memory, as well as in bulk forms like magnetic field sensors, filters, oscillators, and phase-shifters [30][31]. In addition to that, few others aspects like gas sensing, photovoltaic effect and issues related to symmetry breaking has maintained sufficient scientific attention over the years [32]. In order to customize the material for practical applications, it is crucial to comprehend its essentials.

1.1 Fundamentals of magnetism

The magnetic phenomena in solid materials are mainly perceived from the spin degree of freedom. An ordered magnetic state occurs in magnetic material below a characteristic

temperature known as transition temperature. The foundation of magnetism lies in the presence of unpaired electrons. These unpaired electrons give rise to localized moments that interact with each other through magnetic exchange interactions. The magnetic ordering below the transition temperature is attributed to the dominance of exchange interaction energy over thermal energy.

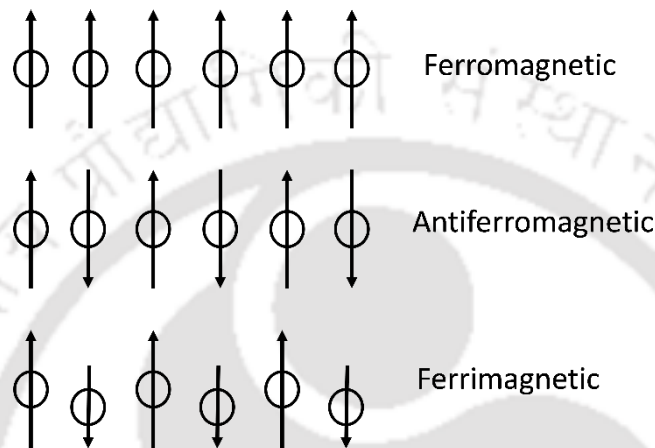


Fig. 1-1 Schematics representing different spins arrangement of ferromagnetic, antiferromagnetic, and ferrimagnetic materials.

The classification of magnetic materials, namely ferromagnetic (FM), antiferromagnetic (AFM), and ferrimagnetic (FIM), is based on their microscopic arrangements of moments, as illustrated in **Fig. 1-1**. In FM materials, the adjacent moments align in parallel, even without an external field, resulting in a spontaneous magnetization below a specific temperature called the Curie temperature (T_C). In AFM materials, the neighboring moments align in opposite directions, leading to a zero net magnetic moment below a temperature called the Neel temperature (T_N). Ferrimagnetic (FIM) materials can be considered as a distinct type of antiferromagnetic (AFM) materials. They possess two magnetic sublattices with varying magnetic moments, leading to a net magnetization that resembles ferromagnetic (FM) materials. Weiss theory [33] explains that the internal molecular field within these materials strives to align the magnetic moments either in parallel or antiparallel

orientations, resulting in the emergence of magnetic ordering. Consequently, magnetic materials exhibit a spontaneous moment below T_C due to the strong internal field, even in the absence of an external magnetic field. The magnetic exchange energy is expressed by the equation according to Heisenberg theory [33],

$$E = - \sum J_{ij} \mathbf{S}_i \cdot \mathbf{S}_j \quad (1.1)$$

Here, the \mathbf{S}_i and \mathbf{S}_j are neighbouring spins and the J_{ij} is exchange integral and the summation is over all nearest neighbours. The positive and negative signs of J_{ij} indicate parallel (FM) and antiparallel (AFM) arrangement of the moments, respectively. When the thermal energy dominates the exchange energy above magnetic ordering temperature (T_C or T_N), the moments become disordered and the paramagnetic state occurs in most of the FM, AFM and FIM systems. The molar susceptibility of the material in the paramagnetic region is governed by the Curie-Weiss law [34],

$$\chi = \frac{C}{T - \Theta} \quad (1.2)$$

Here, C is Curie constant and defined by the relation $C = N\mu_{eff}^2/3k_B$, where N , k_B and μ_{eff} are the Avogadro number, Boltzmann constant and effective paramagnetic moment of free ions and the Θ is Curie-Weiss temperature. The positive value of Θ attributes the FM interactions such as in the pure metals Fe ~ 1043 K, Ni ~ 1394 K and Co ~ 631 K [35]. On the other hand, the negative Θ corresponds to AFM interactions in transition metal oxides MnO [36], Fe₂O₃ [37] Cr₂O₃ [38] and perovskites [39] etc. The eq. (1.2) shows that the paramagnetic susceptibility follows inverse relation with temperature and the experimental value of μ_{eff} can be obtained from fitting of $\chi(T)$. Using the relation, $\mu_{eff} = \sqrt{J(J+1)}$, the theoretical effective paramagnetic moment can be estimated in Bohr magnetons. In

transition metal oxide compounds, the strong crystal field quenches the orbital moment i.e. $L = 0$ and $J = S$. In this case, the experimental value of μ_{eff} follows the theoretical one obtained from spin only contribution of magnetic ion. However, this scenario is not clear in heavier ions ($4d$ and $5d$ series) due to large spin-orbit coupling and its comparable strength with crystal field. Moreover, in the inter-metallic compounds, no orbital quenching is observed due to the stronger spin-orbit coupling. Therefore, the good agreement of experimental μ_{eff} with the theoretical value calculated from both spin and orbital contribution is seen [40]. In few materials the Curie-Weiss law does not hold well [41,42] and the generalized Weiss theory is used for the temperature dependence of the paramagnetic susceptibility.

1.2 Crystal structure

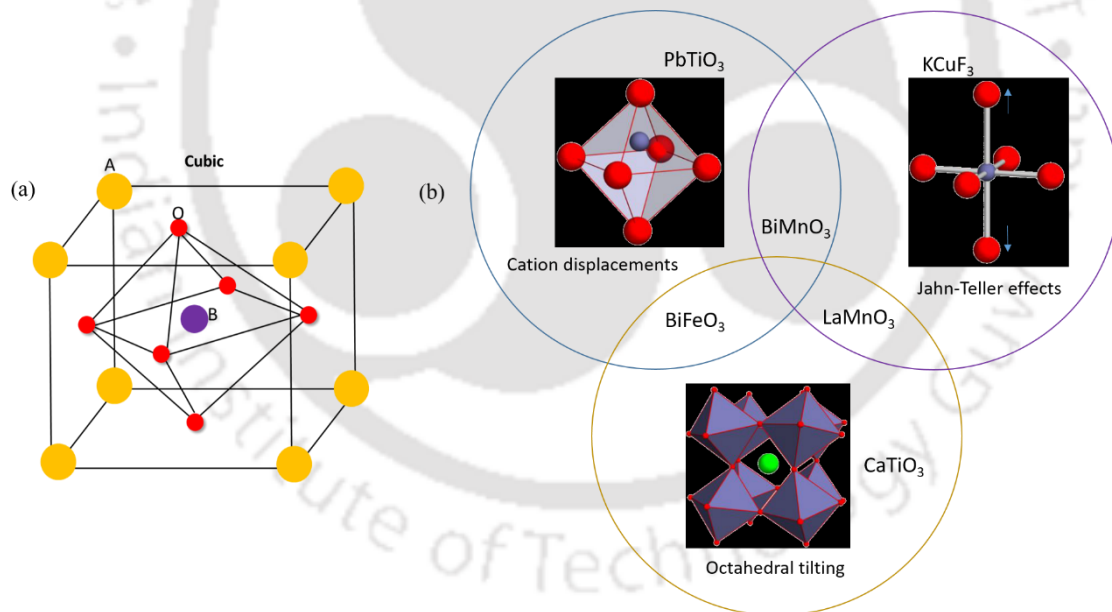


Fig. 1-2 (a) Ideal cubic perovskite structure with general formula ABO_3 (b) The three main distortions of perovskite structure adopted from [126], here circle represents distortions of cation displacement, Jahn-Teller effects, and octahedral tilts using example.

A range of interesting physical phenomena observed in perovskite oxides is due to simple structural characteristics. The ideal perovskite ABO_3 compounds (eg. $SrTiO_3$ [43]) have a

cubic structure, where the A site ions occupy the corners (0, 0, 0), the B site ion occupy the body centre position ($\frac{1}{2}, \frac{1}{2}, \frac{1}{2}$), the O ions are at six face centered positions ($\frac{1}{2}, \frac{1}{2}, 0$) of cubic unit cell as depicted in **Fig. 1-2(a)**. Here, the BO_6 octahedra is formed with the B-O-B angle of 180° .

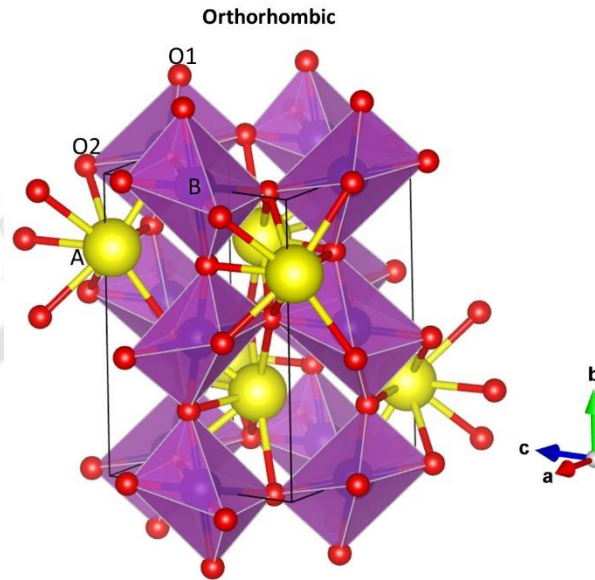


Fig. 1-3 The orthorhombic perovskite structure, where yellow, blue and red spheres represent A (R^{3+}) B (Cr^{3+}) and oxygen ions.

The degree of deviation in ideal perovskite can be obtained by using Goldschmidt's tolerance factor, given by the following relation [44],

$$t = \frac{(r_A + r_O)}{\sqrt{2}(r_B + r_O)} \quad (1.3)$$

where r_A , r_B are the A, B cation ionic radii and r_O is the O anion ionic radius. The value of t is 1 for a cubic structure and the decrease of t give rise to the change from cubic symmetry to orthorhombic or rhombohedral. For distorted perovskites, the value of t ranges from 0.75 to 1.0 [44]. Although t does not provide structural information like space group, it is a reliable indicator of deviation. The three main types of structural distortions in perovskite

structure are displayed in **Fig. 1-2(b)** with examples. The first is the cation displacements from their central position within the local coordination environment. The distortion of the octahedra themselves is another possibility when the central position is occupied by an Jahn-Teller active ion. The most common type is the tilting of BO_6 octahedra, which has a prominent effect on structural symmetry and unit cell. Their combinations are also observed in perovskite materials.

We are particularly interested in the family of RCrO_3 (R = rare earth or yttrium) belonging to distorted perovskite-type structure [45]. **Fig. 1-3** shows a typical crystal structure of the RCrO_3 compound with orthorhombic structure. It has $Pnma$ space group (No. 62) with four formulas per unit cell. **Table 1-1** presents the general atomic positions in $Pnma$ setting for RCrO_3 compound. The Cr^{3+} ions occupy B -sites (centre of the octahedra surrounded by O ions) and R^{3+} ions occupy the A -sites.

Table 1-1 General atomic positions for rare earth orthochromites with $Pnma$ space group.

Atom	Site	Point symmetry	Atomic position
R	$4c$	m	$(x, \frac{1}{4}, z)$
Cr	$4b$	$\bar{1}$	$(0, 0, \frac{1}{2})$
O1	$4c$	m	$(x, \frac{1}{4}, z)$
O2	$8d$	1	(x, y, z)

These materials are governed by different structural distortions, such as the tilt of CrO_6 octahedra, R -ion displacements, and octahedral distortions [46]. Depending on rare earth ions, these perovskite-type compounds exhibit intriguing magnetic properties.

1.3 Magnetic Structure

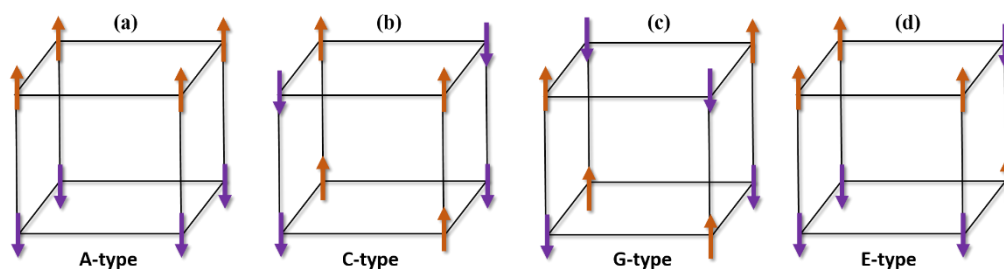


Fig. 1-4 Schematic presentation of (a) A-type (b) C-type (c) G-type and (d) E-type collinear magnetic structures.

The arrangement of ordered spins associated with each atom in unit cell refers the magnetic structure. The magnetic structure of perovskites depends on A and B-sites [47]. **Fig. 1-4** shows the schematics of the A, C, G and E-type AFM structures, possible in perovskites. In A-type structure, the spins align parallel in each (001) plane and opposite in the alternate planes as shown in **Fig. 1-4(a)**. Here, the intra plane coupling is FM and the inter plane coupling is AFM, one such example is LaMnO_3 [48]. **Fig. 1-4(b)** represents the C-type structure with parallel alignment of spins in (101) and $(1 \bar{1} 0)$ planes. Here, the intra plane coupling is AFM and the inter plane coupling is FM. In G-type structure, each spin align antiparallel to all six nearest neighbors as shown in **Fig. 1-4(c)**. Here, both intra plane and inter plane coupling is AFM, for example RCrO_3 [16]. **Fig. 1-4(d)** shows the E-type structure where two spins align in one direction and next two align in other direction i.e. zigzag chains, for example HoMnO_3 [49]. The $Pnma$ (or $Pbnm$) crystal structure of these perovskite allow the spin canting perpendicular to spin easy axis for any of three (C, G and E) magnetic collinear orders described in Fig. 1.4, which results in a FM component and thus the net magnetization [50].

1.4 Crystal field

The electric produced by neighbouring atoms in crystal is called crystal field. The nature of crystal field effect is dependent on the symmetry of local environment [34]. In general, the d -orbital consist five degenerate energy levels, which are classified into two types as shown in **Fig. 1-5**.

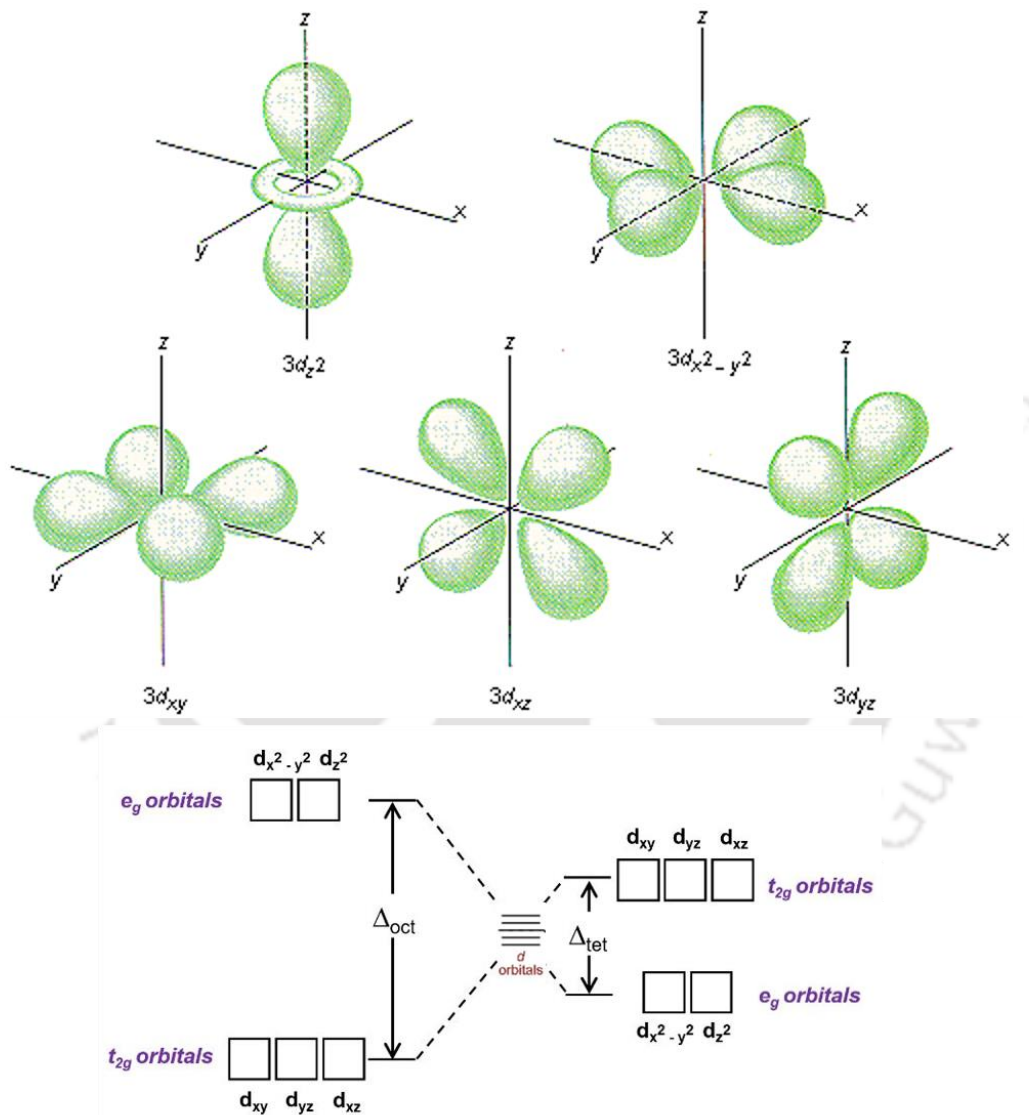


Fig. 1-5 The e_g orbitals grouped as d_{z^2} and $d_{x^2-y^2}$ orbitals. The t_g orbitals grouped as d_{xy} , d_{yz} and d_{zx} orbitals. The bottom diagram shows the crystal field for octahedral and tetrahedral environment.

The t_{2g} orbitals point in between the x , y , and z -axes (namely d_{xy} , d_{yz} and d_{zx} orbitals). The e_g orbitals point along these axes (namely d_{z^2} or $d_{z^2-r^2}$ and $d_{x^2-y^2}$ orbitals). The transition metal compounds like ABO_3 -type perovskites, the crystal field for octahedral environment originates from electrostatic repulsion from electrons in the oxygen orbitals. In octahedral environment, the overlapping of e_g orbitals of transition metal ion occurs with the p -orbitals (p_x , p_y and p_z) of oxygen ion. This overlapping is predominant as compared to that of t_{2g} orbital electrons. Hence, the energy of e_g orbitals rises. As a result, the degeneracy of d -orbitals is lifted up by rising energy of e_g levels as compared to t_{2g} levels and such splitting is shown in the bottom of **Fig. 1-5**. However, in tetrahedral environment, the t_{2g} levels are lifted up with respect to e_g levels. The energy difference (Δ) between two sets of orbitals, such as e_g and t_{2g} , represents the crystal field in their respective environments [35]. The octahedral crystal field typically exhibits a higher magnitude compared to the tetrahedral crystal field.

1.5 Magnetic exchange interactions

The magnetic interactions allow the magnetic dipoles inside a material to interact with each other and align in particular arrangements to minimize the total energy of that material. These are quantum mechanical effects governed by the electrostatic interaction and the Pauli's exclusion principle. At microscopic scale, different magnetic interactions attribute the long range magnetic ordering and few of them are briefly described as follows.

1.5.1 Direct exchange interaction

The interaction of the electrons of the neighboring magnetic atoms without the intermediate non-magnetic ion is called the direct exchange interaction. However, the existence of such simple interaction in real physical system is very rare. This interaction is usually observed in antiparallel spin configuration as the Pauli's exclusion principle maintains the electrons

with parallel spins apart. Due to small overlapping of neighboring magnetic orbitals, the direct exchange interaction is weak and insignificant to describe the magnetic properties of the materials. Hence, the indirect type of exchange interactions are required.

1.5.2 Superexchange interaction

It is an indirect exchange interaction between two next nearest neighbor magnetic cation through an intermediate non-magnetic anion. These are long-range interaction and the mechanism related to superexchange interaction is as follows.

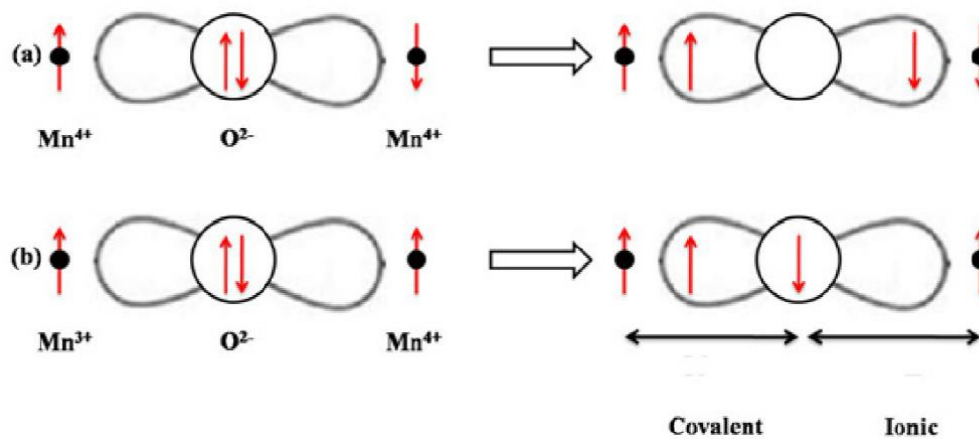


Fig. 1-6 Schematics for the spin arrangements in (a) the AFM superexchange interaction and (b) the FM superexchange interaction.

When the antiparallel alignment of the core spins of magnetic cations via non-magnetic intermediate ion like oxygen occurs, it results in the antiferromagnetic interaction due to strong Hund's coupling. The spin up electron of oxygen anion shared with the cation having up spin configuration whereas the spin down electron of oxygen anion shared with the cation having down spin configuration to satisfy the Hund's rule. Thus, net cation-cation interaction becomes antiferromagnetic but the cation-anion pair show ferromagnetic spin alignment. This process for $Mn^{4+}-O^{2-}-Mn^{4+}$ pair is demonstrated in **Fig. 1-6(a)**. Here we

observe oxygen-mediated exchange interaction and the overall interaction between two Mn^{4+} ions becomes antiferromagnetic.

According to Goodenough [51], when covalent bonding is one side while the ionic bonding on other side i.e. the asymmetric cation-anion-cation interaction, then superexchange interaction can attribute to ferromagnetism. **Fig. 1-6(b)** displays such scenario for Mn^{3+} - O^{2-} - Mn^{4+} pair. On left, the covalent bonding is present for the spin up electron of O^{2-} and spin up electron of Mn^{3+} ion. However, the ionic bond is formed between the spin down electron of O^{2-} and spin up electron of Mn^{4+} ion on right side. Thus, the overall interaction becomes ferromagnetic between Mn^{3+} and Mn^{4+} ions. Hence, the superexchange interaction via the networks like Cr^{3+} - O^{2-} - Cr^{3+} , Fe^{3+} - O^{2-} - Fe^{3+} , Mn^{3+} - O^{2-} - Mn^{3+} and Mn^{4+} - O^{2-} - Fe^{4+} give antiferromagnetism, whereas the network Mn^{3+} - O^{2-} - Mn^{4+} with mixed valency shows ferromagnetism. The AFM ordering in $R\text{CrO}_3$ is related to the Cr^{3+} - O^{2-} - Cr^{3+} superexchange interaction that has the influence of R -ion radii.

1.5.3 Double exchange interaction

This exchange interaction takes place between magnetic ions with different oxidation states. Zener first proposed the concept of double exchange [52], which predicts the ease with which an electron can be exchanged between two species. This phenomenon holds significance in ferromagnetic (FM), antiferromagnetic (AFM) materials, or spiral magnetism. For example, the Mn-O-Mn interaction, in which one of the Mn ions has more electrons than other does and the e_g orbitals of Mn are directly interacting with $2p$ orbitals of O ion. In ground state, the electrons of Mn ions are aligned according to Hund's rule. If O ion transfers its spin-up electron to Mn^{4+} ion, an electron from Mn^{3+} ion can then occupy the vacant orbital. An electron is moved between the neighbouring metal ions while maintaining its spin which is known as double exchange interaction. This exchange is

similar to superexchange. In double-exchange, the interaction one atom has an additional electron relative to the other.

1.5.4 Ruderman-Kittel-Kasuya-Yosida (RKKY) interaction

When the exchange interaction between the magnetic ions is mediated via conduction electrons, this indirect exchange called RKKY interaction. For example, in rare-earth inter-metallic compounds, the f -shell electrons tend to be highly localized around the nucleus and are surrounded by a sea of conduction electrons. The spatial extent of the 4f orbitals is relatively small compared to the inter-ionic distance. In this context, the interaction between rare-earth ions occurs through the intermediation of the conduction electrons. In general, the coupling between the magnetic moments at large distance r is given by the exchange interaction [34],

$$J_{RKKY}(r) \propto \frac{\cos(2k_F r)}{r^3} \quad (1.4)$$

Where, $J_{RKKY}(r)$ is r dependent exchange interaction and k_F is the radius of spherical Fermi surface. This long-range interaction can FM or AFM depending on separation between the magnetic moments and its nature is oscillatory.

1.5.5 Dzyaloshinskii-Moriya interaction

In 1958-60, Dzyaloshinskii and Moriya [53][54] proposed an antisymmetric exchange interaction known as Dzyaloshinskii-Moriya (DM) interaction. The DM interaction causes the canting of the magnetic moments of antiparallel spins toward each other, which results in the net magnetic moment. For such canted spin arrangement, the crystal symmetry needs to be same as the initial antiparallel spin arrangement. Under above condition, one term favors canted spin arrangement over antiferromagnetic one and is essential to the weak ferromagnetism. This term in Hamiltonian is written as,

$$H_{DM} = \mathbf{D}_{ij} \cdot (\mathbf{S}_i \times \mathbf{S}_j) \quad (1.5)$$

where $\mathbf{S}_i, \mathbf{S}_j$ are two neighboring spins of magnetic ions i and j , and \mathbf{D}_{ij} is DM vector. The vector \mathbf{D}_{ij} is proportional to $\mathbf{R} \times \mathbf{r}_{ij}$ where vector \mathbf{R} is displacement of oxygen and \mathbf{r}_{ij} is unit vector along the axis connecting magnetic ions as shown in **Fig. 1-7**.

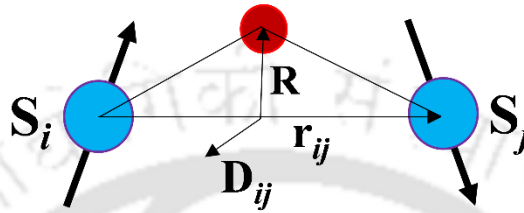


Fig. 1-7 Schematics for Dzyaloshinskii-Moriya interaction.

The DM interaction in perovskite is determined by the octahedral tilting of oxygen. For M-O-M bond (M is B-site ion and O is oxygen) the octahedral tilting moves the oxygen anion perpendicularly away from the midpoint between NN B-site cations [55]. Due to symmetry argumentation, the \mathbf{D}_{ij} vector lies perpendicular to the M_i -O- M_j bond (see **Fig. 1-7**). If the crystal field has an inversion symmetry (with respect to the centre point connecting two magnetic ions), \mathbf{D}_{ij} vector vanishes. The DM interaction tries to align the two spins at right angle to each other in a plane perpendicular to DM vector. The microscopic origin of spin canting can be explained by the anisotropic superexchange interaction, which consider the superexchange interaction along with spin-orbit coupling. Originally, this antisymmetric interaction was argued to be responsible for the weak ferromagnetism in the AFM crystals like α - F_2O_3 , MnCO_3 , CoCO_3 and Cr_2O_3 [56][57]. The weak ferromagnetism in the $R\text{CrO}_3$ perovskites also arises from the DM interaction. Recently, the DM interaction has been proven relevant for the generation magnetic skyrmions [58] and explains magnetoelectric effects in multiferroic perovskites.

1.6 Exchange bias effect

Exchange bias refers to the occurrence of exchange anisotropy that arises at the interface between antiferromagnetic (AFM) and ferromagnetic (FM) substances [6]. In 1956, Meiklejohn and Bean made the discovery of the exchange bias (EB) effect during their examination of FM Co particles incorporated within AFM CoO oxide [5].

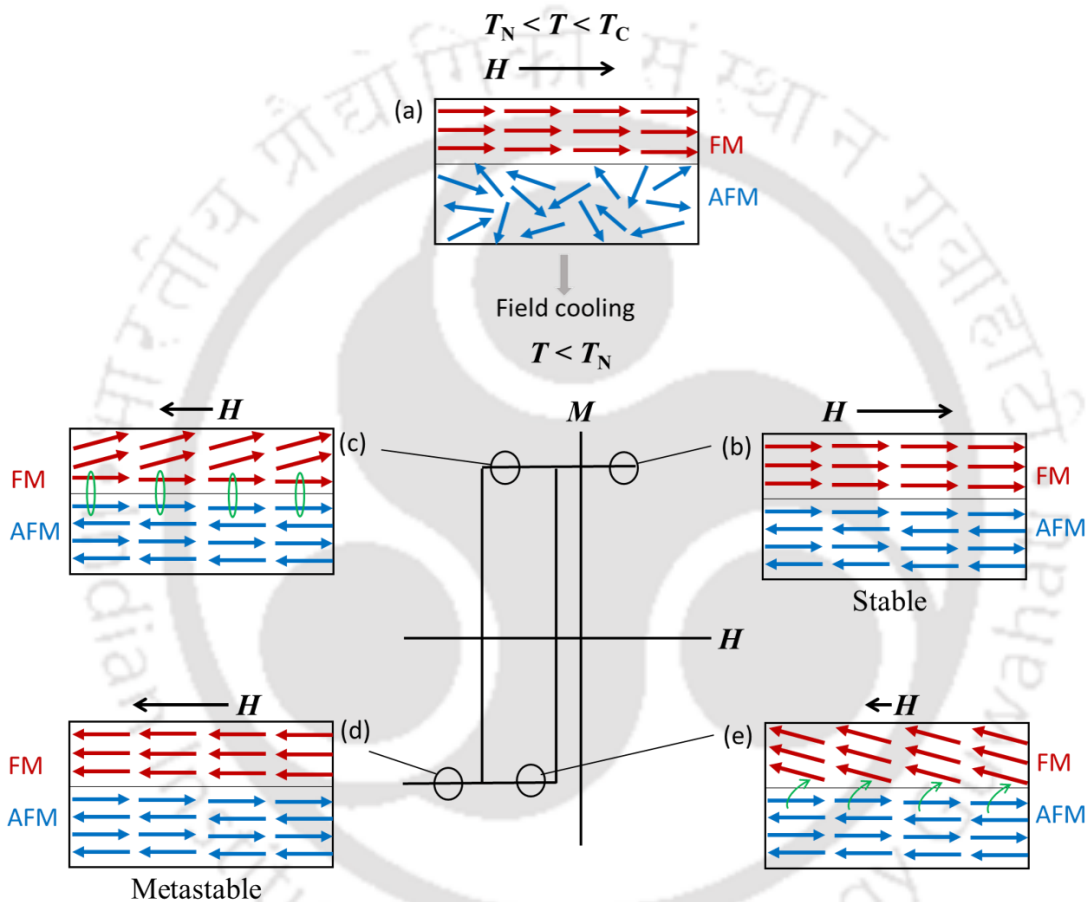


Fig. 1-8 Schematics illustrates the spin arrangement of FM-AFM bilayer at various stages of an exchange-biased hysteresis loop.

Upon cooling this system in a static applied magnetic field from a temperature higher than the T_N of the CoO material, an observed shift of the magnetization (M - H) loops occurred along the axis of the magnetic field. The additional anisotropy responsible for this shift in

the M - H loop can be accurately represented in terms of the exchange bias field (H_{EB}) using the following equation,

$$H_{EB} = \frac{H_+ + H_-}{2} \quad (1.6)$$

and the coercive field is given by,

$$H_C = \frac{H_+ - H_-}{2} \quad (1.7)$$

where, H_+ and H_- stand for the positive and negative coercive field values for the M - H loop. The simple phenomenological model illustrated in **Fig. 1-8** explains the mechanism of EB. In this model, there is contact between AFM (magnetic ordering T_N) and FM (magnetic ordering T_C) materials. In the $T_N < T < T_C$ temperature range, as we applied the magnetic field, the spins of the FM material align with the field direction, while the spins of the AFM material remain random due to their paramagnetic behavior, as depicted in **Fig. 1-8(a)**. Once the system is cooled to a temperature lower than T_N while a field is present, the adjacent spins of the AFM material align in a parallel manner (ferromagnetically) to the spins of the FM material at the AFM-FM interface. The remaining spins of the AFM material maintain their AFM ordering, as shown in **Fig. 1-8(b)**. During the M - H measurement, as the field is decreased and reversed, the spins of the FM material begin to rotate in the direction of the field. However, the spins of the AFM material remain unaffected due to their substantial AFM anisotropy. The AFM spins at the interface between the AFM and FM materials oppose the rotation of the ferromagnetically coupled FM layers at the interface, as illustrated in **Fig. 1-8(c)**.

Alternatively, microscopic torque is exerted by the AFM spins on the FM spins at the interface, ensuring that their alignment remains FM at the interface. As a result, the pinning of few layers of FM spins to the AFM spins occur at the interface. The FM spins possess a single stable configuration that results in unidirectional anisotropy. Consequently, an additional field is required to rotate these pinned spins and counteract the effects of the unidirectional anisotropy. Nevertheless, when the field reaches a sufficient magnitude to saturate the FM moments, all FM spins align in the direction of the field, as shown in **Fig. 1-8(d)**. As the field is subsequently decreased to complete the *M-H* loop, the FM spins rotate with ease. This is facilitated by the torque exerted by the AFM spins in the same direction as the field, as depicted in **Fig. 1-8(e)**. Consequently, there will be a difference in the magnetic energy needed to rotate the FM spins in the negative and positive field directions. This behavior gives the impression of an internal biasing field within the material, resulting in a shift of the *M-H* loop along the field axis. This phenomenon is commonly referred to as exchange bias. The extent of the shift observed in the *M-H* loop depends on the level of pinning within the FM material and the variation of anisotropy in the AFM material. As mentioned earlier, the coupling at the interface is ferromagnetic, leading to the shifting of *M-H* loop along the negative field axis. However, it is also possible to observe shifted *M-H* loop toward the positive field axis when the coupling at the interface between the FM and AFM layers is antiferromagnetic [6].

Although the EB effect was originated as the interfacial phenomenon for the AFM-FM interface, later on this effect has been found in homogeneous materials namely, core-shell nanostructures, spin-glass and magnetically phase separated systems [59] [60] [61]. Different bulk materials like Heusler alloys, intermetallic compounds as well as oxide materials are known to exhibit EB [7]. Technological importance of EB effect was revealed by the practical use of FM-AFM multilayers in read/write heads of magnetic recording

devices [4][62]. Thereafter it has found many other applications like magnetic field sensors [63], permanent magnets [64], magnetoresistive random access memories [65]. In FeF₂/Fe bilayers [66] and Co/Pt multilayers [67] the sign reversal of EB field was also observed by changing external parameters.

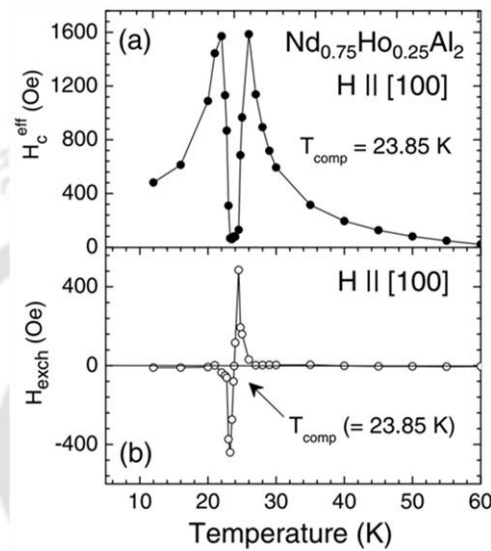


Fig. 1-9 The effective coercive field and EB field as function of temperature for the rare earth intermetallic $Nd_{0.75}Ho_{0.25}Al_2$ compound. From [68].

Fig. 1-9 displays the sign change of EB field across $T_{comp} \sim 24$ K in the single crystal of $Nd_{0.75}Ho_{0.25}Al_2$ rare earth intermetallic compound. The EB effect in this intermetallic compound was attributed to different kinds of exchange coupling between the moments corresponding to the conduction electron polarization and two different rare earth atom [68]. Varieties of single-phase compounds exhibit the EB behavior. Such as the spinels $CoCr_2O_4$ [69][70] and perovskites like rare earth manganites $YMnO_3$, $NdMnO_3$ [71][72][73], chromites $TmCrO_3$ [74], $YbCrO_3$ [75], cobalites $Nd_{1-x}Sr_xCoO_3$ [76] and double perovskites Pr_2CoMnO_6 [77], $LaSrCoFeO_6$ [78]. The mechanism of EB in single-phase compounds differs from the interfacial systems, which will be discussed later.

1.7 Rare earth orthochromites

The rare earth orthochromites with general formula $R\text{CrO}_3$ (R = rare earth or yttrium) are emerging the class of multiferroic materials [79][80], similar to isostructural manganites [81] and ferrites [82]. In particular, the interplay of two different magnetic sublattices in orthochromites $R\text{CrO}_3$ arises the magnetoelectricity, spin-reorientations, magnetization switching, magnetocaloric effect etc. [83][84][85], which has stimulated significant attention in recent years. In this section, we will discuss some noble properties of these compounds. The $R\text{CrO}_3$ members undergo magnetic transitions in a broad temperature range upon cooling from paramagnetic phase. These magnetic properties are basically governed by the $\text{Cr}^{3+}\text{-Cr}^{3+}$, $R^{3+}\text{-Cr}^{3+}$ and $R^{3+}\text{-R}^{3+}$ exchange interactions. First, the Cr-sublattice orders antiferromagnetically at T_N , which decreases monotonically with rare earth ionic radius from 288 K in LaCrO_3 to 109 K in LuCrO_3 [86] as depicted in **Fig. 1-10**. Further, the reorientation of Cr spins in few $R\text{CrO}_3$ occurs at $T_{\text{SR}} \sim 35$ K to 7 K. At very low temperature ~ 2 K to 15 K, the R -sublattice orders in some species as shown in **Fig. 1-10**.

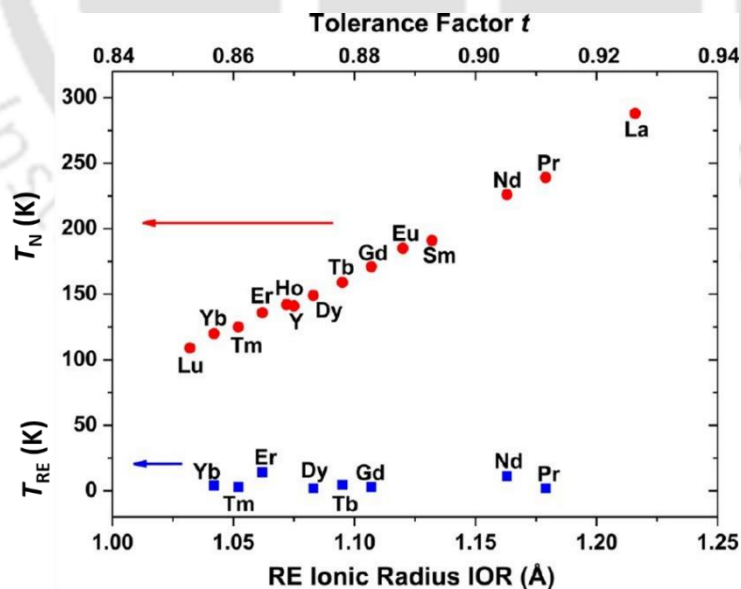


Fig. 1-10 The variation of Neel temperature (T_N) for Cr^{3+} ordering and rare earth ordering (T_{RE}) with R -ion radii and tolerance factor. From [75].

Furthermore, **Fig. 1-11** shows three G-type AFM spin configurations $\Gamma_1(A_x, G_y, C_z)$, $\Gamma_2(F_x, C_y, G_z)$ and $\Gamma_4(G_x, A_y, F_z)$ for $R\text{CrO}_3$ materials, following the Bertaut's notation [1][17]. The absence of canting does not allow the weak ferromagnetism in Γ_1 configuration. However, the slightly canted Γ_2 and Γ_4 magnetic structures have weak ferromagnetism along the x and z directions, respectively. For non-magnetic R -ions, the ground state remains weakly ferromagnetic with Γ_4 structure. The high temperature spin structure can be Γ_4 or Γ_2 below T_N for magnetic R -ion. Interestingly, few $R\text{CrO}_3$ members exhibit the spin-reorientation transition at low temperatures, where magnetic structure changes from

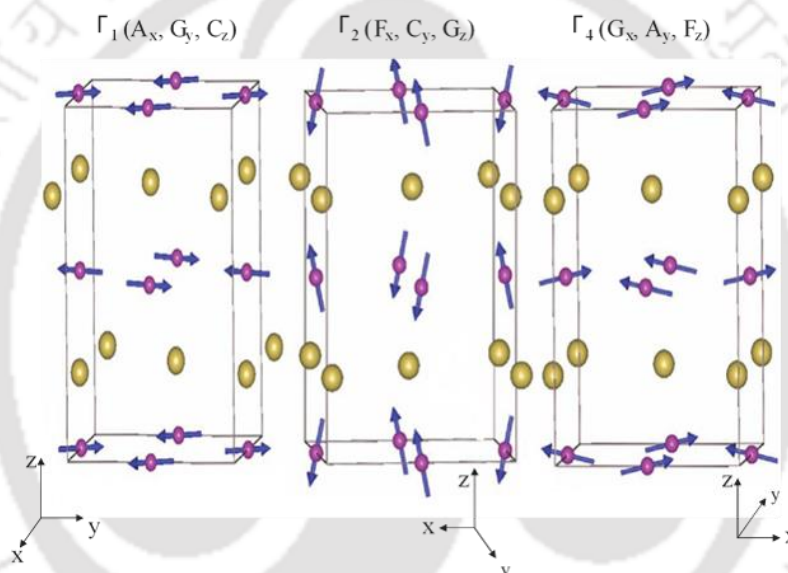


Fig. 1-11 The spin structures for $Pbnm$ symmetry showing no spin canting in Γ_1 and the spin canting in Γ_2 and Γ_4 configurations. The blue and yellow spheres represent Cr^{3+} (with spin) and R^{3+} ions (without spin). From [76].

Γ_2 to Γ_1 ($T_{\text{SR}} \sim 35$ K for NdCrO_3 [87]), Γ_4 to Γ_1 ($T_{\text{SR}} \sim 22$ K for ErCrO_3 [15]) and Γ_4 to Γ_2 ($T_{\text{SR}} \sim 34$ K for SmCrO_3 [88] and $T_{\text{SR}} \sim 7$ K for GdCrO_3 [89]). Moreover, in $R\text{CrO}_3$, the $3d^3$ electrons of Cr^{3+} are half-filled in the t_{2g} orbitals only. J.S. Zhou *et al.* [90] has explained

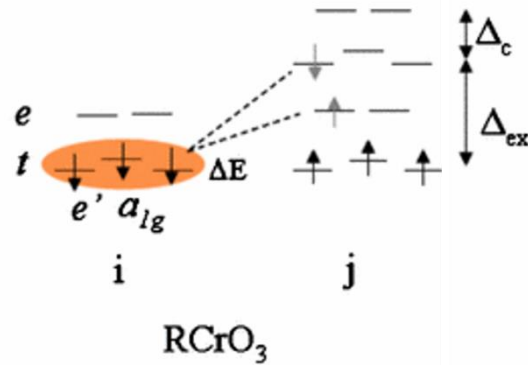


Fig. 1-12 Schematics of t - e hybridization effect on virtual charge transfer for superexchange interaction in RCrO_3 perovskite. From [42].

the superexchange interaction between two adjacent transition-metal ions via virtual charge transfer (VCT). **Fig. 1-12** shows the t - e hybridization where the VCT to the empty e orbital on site j i.e. superexchange interaction t^3 -O- e^0 gives FM coupling whereas superexchange interaction t^3 -O- t^3 gives the AF coupling. Such effect of t - e hybridization was due to the structural distortions, which is responsible for dramatic variation in T_N values for RCrO_3 family. The magnetic behavior of the orthochromites and its reliance on rare earth ionic radii or structural distortions make these systems intriguing.

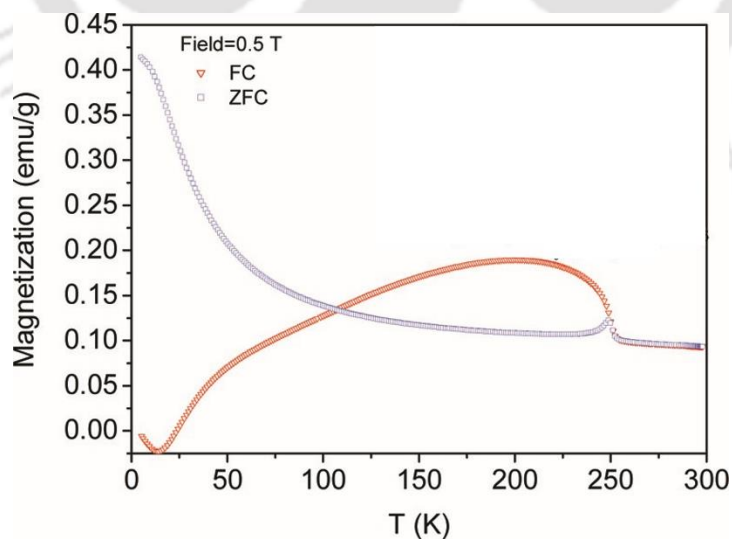


Fig. 1-13 The magnetization vs. temperature curves of CeCrO_3 for ZFC and FC case at applied magnetic field of 5kOe. From [86].

The $R\text{CrO}_3$ compounds exhibit a variety of properties that mainly originate from complex magnetic interactions. The temperature-induced magnetization reversal has been reported in $R\text{CrO}_3$ compounds, which has potential application for information storage. In TmCrO_3 , the first magnetization reversal occurs at ~ 28 K ascribed to antiparallel coupling between Tm^{3+} and Cr^{3+} moments and second reversal takes place at lower temperature ~ 6 K related to rotation of magnetic moments [91]. Other compounds like YbCrO_3 [92] and Nd substituted LaCrO_3 [93] etc. show similar magnetization reversal. Apart from this, the CeCrO_3 displays magnetic compensation transition at larger temperatures more than 100 K as shown in **Fig. 1-13** [94] and further explained by the Ce^{3+} and Cr^{3+} moments antiparallel coupling [2]. However, literature shows the lack of Ce-based rare earth perovskites as compared to other members.

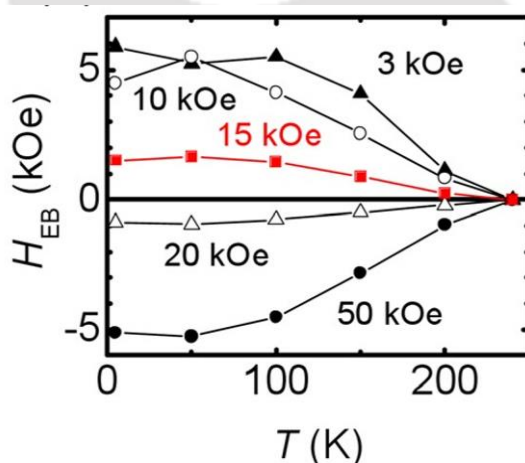


Fig. 1-14 The EB field vs. temperature plot for various values of field cooling in the $\text{La}_{0.25}\text{Pr}_{0.75}\text{CrO}_3$ rare earth perovskite compound. From [89].

The EB effect in correlated oxides is an active research area and this feature has been continuously reported for several rare earth chromites. The EB in single-phase compounds can be described one way using the core-shell structure consisting of an AFM core with Cr^{3+} and R^{3+} spins and the disordered shell having uncompensated spins explaining the magnetization reversal and EB effect in $\text{La}_{0.2}\text{Ce}_{0.8}\text{CrO}_3$ nanoparticles [95]. In other way,

the coexistence of AFM and FM ordering arising from the competing interactions between transition metal ions and magnetic rare earth ion [8]. **Fig. 1-14** The EB field vs. temperature plot for various values of field cooling in the $\text{La}_{0.25}\text{Pr}_{0.75}\text{CrO}_3$ rare earth perovskite compound. From [89]. The graph depicts the temperature variation of the EB field in $\text{La}_{1-x}\text{Pr}_x\text{CrO}_3$ substituted chromite, where the sign of the EB field changes with the change in cooling magnetic field and is explained in terms of the orientation of Pr^{3+} moment and canted Cr^{3+} moments [8]. The SmCrO_3 [96], $\text{LuFe}_{0.5}\text{Cr}_{0.5}\text{O}_3$ [9] and $\text{Yb}_{1-x}\text{Pr}_x\text{CrO}_3$ [75] orthochromites are some of recent examples. Therefore, the investigations of new materials is desired to explore the EB feature.

In addition, the $R\text{CrO}_3$ shows semiconductor behavior in the visible frequency range, which provides advantage of over conventional TiO_2 and makes it attractive for application in solar energy harvesting and photocatalytic activity [97–99][94]. For example, the dc conductivity measurements of PrCrO_3 disclose semiconductor behavior at room temperature and transition to metal at ~ 400 K [100]. Further, the effect of the external pressure give rise to structural distortions modifying band structure and leads to interesting magnetic properties [101].

Furthermore, the coexistence of ferroelectric and magnetic ordering in magnetoelectric systems is appealing to scientific community [29][102]. The reports shows magnetoelectric coupling in some $R\text{CrO}_3$ members [79,103,104] and indicate they are type-II multiferroics [3]. B. Rajeswaran *et.al* [1] has reported the field-induced switchable polarization ~ 0.2 to $0.8 \mu\text{C}/\text{cm}^2$ below T_N in $R\text{CrO}_3$ for magnetic R -ions. In such systems, the causes of ferroelectricity is different from conventional ferroelectrics that is an ongoing topic of debate [13]. Their roots lies in the improper character related with the spin-lattice interaction observed in isostructural orthomanganites [105].

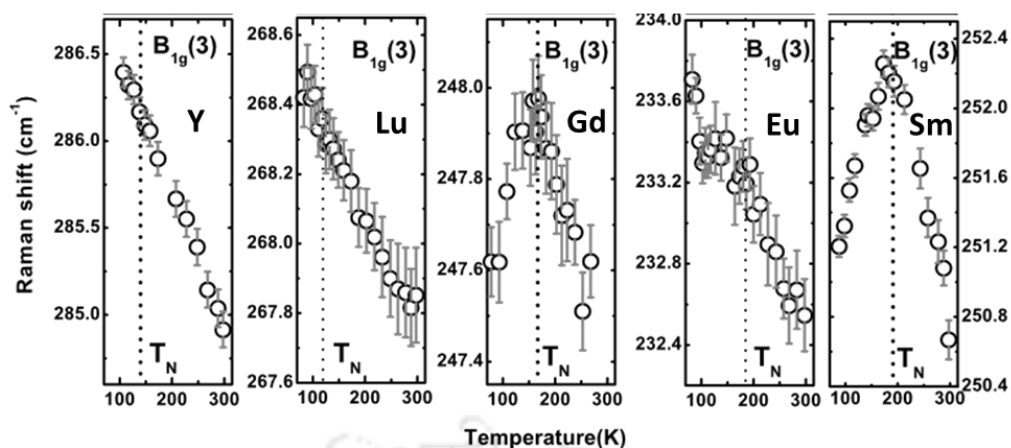


Fig. 1-15 Temperature effect on the Raman mode associated with octahedral rotations along y-axis out of phase in the $YCrO_3$, $LuCrO_3$, $GdCrO_3$, $EuCrO_3$ and $SmCrO_3$ rare earth chromites. From [12].

The R -ion dependence of the lattice distortions and magnetic structure corresponds with the phonon parameters and their variations near magnetic ordering temperature [10]. Granado et al [11] has defined the term spin-phonon coupling due to the phonon modulation of the superexchange integral and there has been a revival of interest in direction [106] [107,108]. **Fig. 1-15** demonstrate temperature dependence of Raman mode for $RCrO_3$ ($R = Y, Lu, Gd, Eu, Sm$) which confirms the spin-phonon coupling only for magnetic R -ions [12]. Further, this coupling is observed in few mixed chromites $DyFe_{0.5}Cr_{0.5}O_3$ [104] and $HoCr_{1-x}Fe_xO_3$ [109]. However, no such studies related to local structure and spin-phonon coupling is reported for Nd based orthochromite.

1.8 $NdCrO_3$ orthochromite

Materials with multifunctional properties near room temperature are always desirable for practical uses. In this quest, the $NdCrO_3$ rare earth chromite can be a promising candidate. The $NdCrO_3$ crystalizes in orthorhombic distorted perovskite structure with $Pnma$ symmetry. The magnetic structure of this material is considered as G-type AFM, where the Cr^{3+} moments order antiferromagnetically at $T_N \sim 219$ K [15]. The isotropic, antisymmetric,

and anisotropic exchange interaction among the Cr^{3+} - Cr^{3+} , Cr^{3+} - Nd^{3+} and Nd^{3+} - Nd^{3+} moments comprise multiple magnetic transitions in these materials [84]. For example, the canting of Cr^{3+} spins related to DM interactions leads to the weak ferromagnetism below T_N [110]. Further, the spin-reorientation transition occurs at $T_{SR} \sim 35$ K where the abrupt change of Cr^{3+} spin configuration from high temperature $\Gamma_2(F_x, C_y, G_z)$ to low temperature $\Gamma_1(A_x, G_y, C_z)$ spin structure were observed using Neutron diffraction measurements [16]. Further, the Nd^{3+} ordering takes place at much lower temperature $T_{RE} \sim 4.2$ K, which is induced by Cr^{3+} sublattice [17]. **Fig. 1-16** displays the magnetic specific heat of NdCrO_3 compound [111]. The different magnetic contribution to specific heat in NdCrO_3 provided

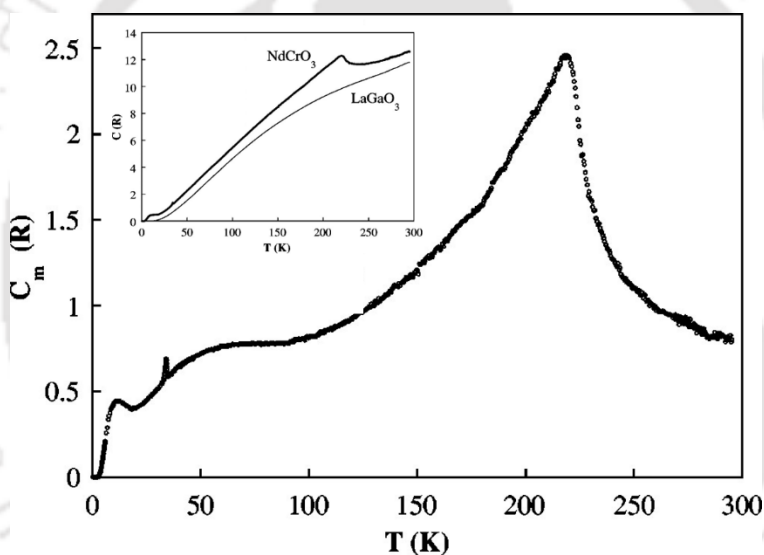


Fig. 1-16 Magnetic specific heat (C_m) of NdCrO_3 in 0.3 K to 300 K thermal range, which is obtained after subtracting the specific heat of isostructural non-magnetic LaGaO_3 compound shown in inset. From [81].

four main outcomes, which were described as the hyperfine contribution below 1 K, the Schottky contribution from thermal depopulation of the ground $^4I_{9/2}$ multiplet of Nd from 2 K to high temperatures, the spin reorientation peak at ~ 35 K and the lambda peak centered at antiferromagnetic ordering ~ 219 K. It has also been found that the Nd-Cr interaction in the NdCrO_3 is stronger by a factor ~ 2.6 than Nd-Fe in isostructural NdFeO_3 orthoferrite

due to different superexchange Nd- M (M transition metal) paths and extremely strong coupling of Nd^{3+} and Cr^{3+} moments [87][111]. These reports suggest the NdCrO_3 exhibits complex magnetic phases in a large temperature window.

Furthermore, the perovskites with one or two magnetic sublattices exhibit interesting structural chemistry and physical properties. The temperature and pressure dependent X-ray diffraction or Raman spectroscopy are well known tools for such characterization. The high temperature XRD data has been reported for the NdCrO_3 compound [112]. As shown in left panel of **Fig. 1-17**, no appearance or disappearance of any diffraction peaks occurs in 323-823 K range. This study confirmed no structural phase transition in NdCrO_3 up to

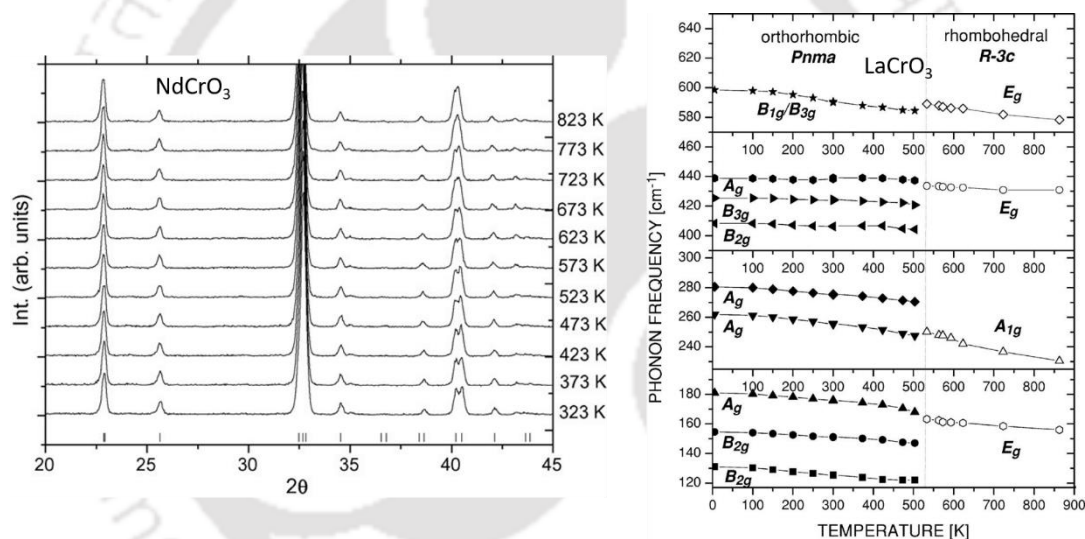


Fig. 1-17 (Left) The temperature dependent X-ray diffraction patterns of NdCrO_3 where vertical lines below the diffraction data indicate the allowed Bragg reflections at room temperature, From [112]. (Right) The variation of Raman phonon frequency with temperature in LaCrO_3 , From [113].

823 K, which was different from LaCrO_3 [113] that exhibits orthorhombic to rhombohedral phase transition near 529 K seen in temperature variation of Raman modes (see right panel of **Fig. 1-17**). However, detailed low-temperature structural behavior of NdCrO_3 based compounds is not explored.

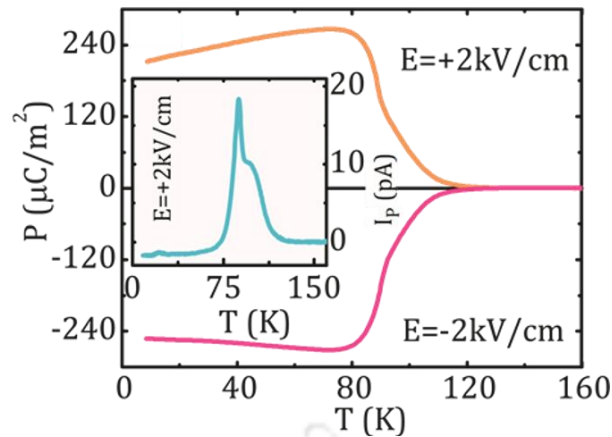


Fig. 1-18 The temperature dependence of electric polarization (P) of NdCrO_3 for the poling fields (E) of $\pm 2 \text{ kVcm}^{-1}$ and the inset shows pyroelectric current (I_p) vs. T at $E = +2 \text{ kV cm}^{-1}$. From [18].

Unlike other members of the $R\text{CrO}_3$ series, the ferroelectricity in NdCrO_3 is reported at $T_C \sim 87 \text{ K}$ that appears well below $T_N \sim 225 \text{ K}$ [18]. **Fig. 1-18** shows the temperature variation of electric polarization (P) for NdCrO_3 where the polarization occurred well below T_N and ferroelectricity was observed at $T_C \sim 87 \text{ K}$. The inset of **Fig. 1-18** shows the thermal variation of pyroelectric current (I_p) having peak around T_C . The value of P ($260 \mu\text{C m}^{-2}$ at 74 K for $E = 2 \text{ kVcm}^{-1}$) was reasonably high and the switching of P with opposite poling fields verified ferroelectricity. The strong influence of magnetic field on the P below T_C suggest large magnetoelectric coupling in NdCrO_3 .

In spite of such interesting observations, the correlated properties in pure compound and the substitution effect on Nd or Cr-site in NdCrO_3 is still lacking. For instance, the variation in CrO_6 tilting and the dilution of the Nd^{3+} and Cr^{3+} moments observed upon doping of Sr^{2+} at Nd site in $\text{Nd}_{1-x}\text{Sr}_x\text{CrO}_3$ [114]. The presence of Ca^{2+} increases the density, electrical conductivity and thermal expansion coefficient in $\text{Nd}_{1-x}\text{Ca}_x\text{CrO}_3$ for possible interconnect applications in solid oxide fuel cells [115]. On other hand, the doping of La^{3+} increases the energy level splitting of Cr^{3+} and Nd^{3+} and suppress Cr–Nd interaction confirmed by Schottky anomaly and mean-field interaction parameters in $\text{Nd}_{1-x}\text{La}_x\text{CrO}_3$ [116].

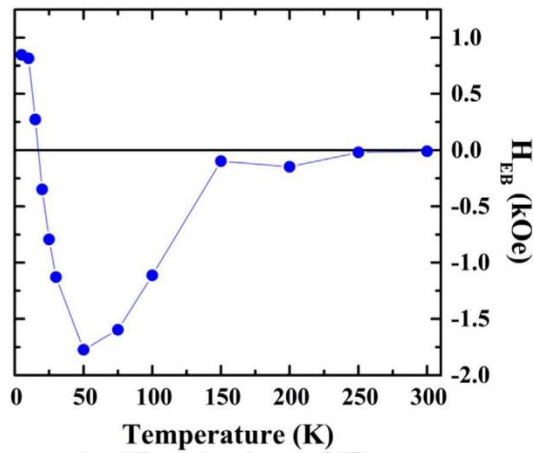


Fig. 1-19 The temperature dependence of exchange bias field in $\text{NdCr}_{0.5}\text{Fe}_{0.5}\text{O}_3$ mixed orthochromite. From [118].

In polycrystalline $\text{NdCr}_{0.5}\text{Fe}_{0.5}\text{O}_3$ [117], the Cr-site substitution by Fe^{3+} ion resulted in magnetization reversal and switching of exchange bias. **Fig. 1-19** shows the negative exchange bias field until 16 K and small positive exchange bias for temperatures below 16 K, which corresponds to magnetic compensation (T_{comp}). The tunable exchange bias was explained on the basis of magnetization reversal. According to that when the net magnetization is opposite to the applied field, it requires larger positive field to bring the magnetization to zero, which causes EB effect.

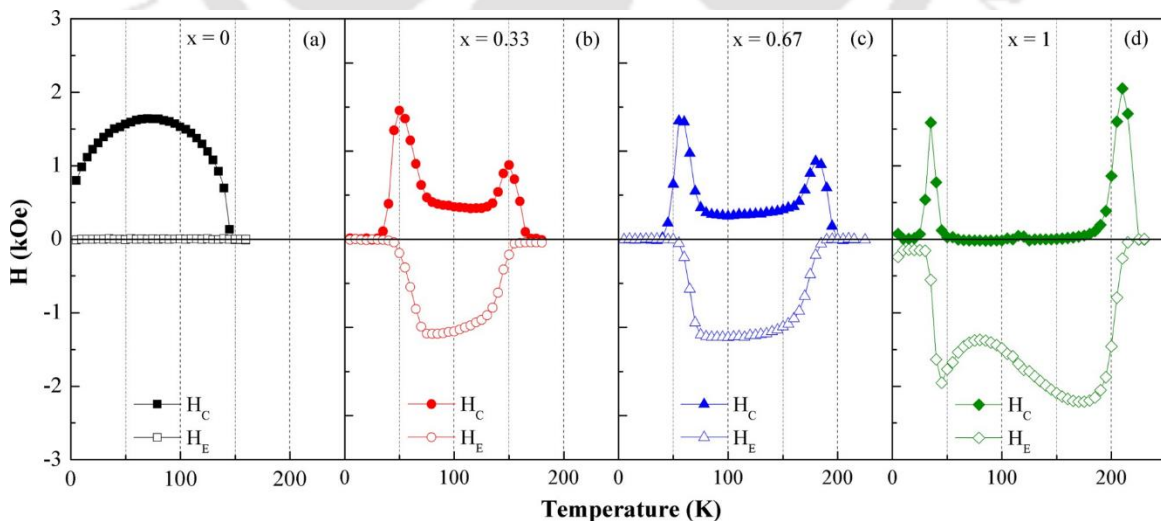


Fig. 1-20 The coercive field (H_C , closed symbols) and exchange bias field (H_E , open symbols) as the function of temperature for $\text{Dy}_{1-x}\text{Nd}_x\text{CrO}_3$ with $x = 0$ (a), 0.33 (b), 0.67 (c), and 1.0 (d) solid solutions where the peaks in H_C attributes to the onset of H_E that becomes pronounced with the increase of Nd substitution. From [118].

Recently, the exchange bias effect is reported in $\text{Dy}_{1-x}\text{Nd}_x\text{CrO}_3$ single-phase solid solution with the $x = 0.33, 0.67,$ and 1.0 doping corresponds to increased T_N values ~ 175 K, 200 K and 225 K. Most importantly, the presence of Nd^{3+} in these materials induced the spin-reorientation transition at $T_{\text{SR}} \sim 48$ K, 58 K, and 38 K and resulted in the onset on exchange bias field. Thus, a negative exchange bias effect was observed in temperature range of T_{SR} and T_N for Nd substituted samples, whereas no such exchange bias was seen in the parent compound (see **Fig. 1-20**) [118]. This study consider the canted antiferromagnetism to be essential feature for exchange bias in multiple sublattice magnetic system, but the exact mechanism is not explained. Even though the tenability of the EB effect has been the subject of extensive study, the origin of the EB without reversal and the role of spin-reorientation are not understood.

1.9 Motivation

The pristine NdCrO_3 is a member of the $R\text{CrO}_3$ family with an orthorhombic structure occupying the R^{3+} ion on the A-site and the Cr^{3+} ion on the octahedral B-site, respectively. The interesting magnetic behavior with canted antiferromagnetic ordering of Cr^{3+} spins below T_N and the reorientation of Cr^{3+} spins below T_{SR} were observed in NdCrO_3 . However, the exact structural assignments for magnetoelectric effect in orthochromites is controversial. The distinctive properties of this system mainly comes from the superexchange interactions among A and B sites with two magnetic sublattices. For $R\text{CrO}_3$, many reports are available about the magnetic properties for the Cr-site substitution but the substitution effect at R-site especially in NdCrO_3 is limited. The substitution of different R on Nd-site can influence the strong coupling between Nd^{3+} and Cr^{3+} spins. Furthermore, a new dimension can be added to the technological importance of exchange bias effect by exploring its correlations in these materials.

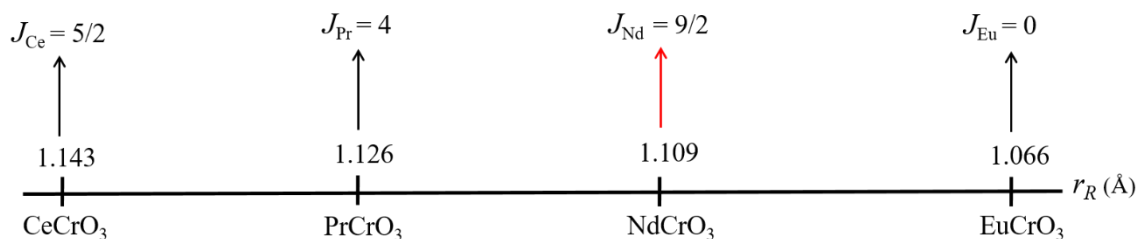


Fig. 1-21 Schematics for A-site ionic radius (r_R) and magnetic moment (J) variation in $Nd_{1-x}R_xCrO_3$ ($x = 1.0$ and $R = Eu, Pr$ and Ce).

The present thesis consist two goals. At first, an effort is made to study the substitution effect of rare earth elements on A-site (Nd-site) altering cross talk of $4f$ electrons of Nd-ion and $3d$ electrons of Cr ion. Therefore, we have chosen Eu, Pr and Ce to substitute on Nd-site for the first time. The ionic radius (r_R) and magnetic moments (J) of these substituents are different from that of Nd^{3+} ion as shown in **Fig. 1-21**, where one can expect the fine-tuning of distortion, antiferromagnetic ordering and spin-reorientation transition with substitution. The Eu^{3+} ion with smaller ionic radius may exert higher chemical pressure on the parent compound as compared to the Pr^{3+} ion with larger ionic radius. It would also be interesting to study the role of mixed Ce^{3+} and Ce^{4+} valency on the A-site due to Ce substitution.

From such perturbation of structure, we can expect the modification of Cr-Cr and Nd-Cr magnetic interactions resulting interesting magnetic properties in a wide temperature range.

The following three series of samples were prepared for this thesis work,

1. $Nd_{1-x}Eu_xCrO_3$ with $x = 0.0, 0.05, 0.10, 0.20, 0.50, 0.70, 0.90$ and 1.0
2. $Nd_{1-x}Pr_xCrO_3$ with $x = 0.0, 0.05, 0.10, 0.20$, and 0.30
3. $Nd_{1-x}Ce_xCrO_3$ with $x = 0.0, 0.05, 0.075, 0.10, 0.15$ and 0.175

Secondly, the involvement of the low-temperature Raman spectroscopy and the low-temperature X-ray diffraction along with the low-temperature magnetization measurements will allow the direct probing of lattice modulations in magnetically ordered phase, which is unknown for the pure and substituted NdCrO_3 . This will also provide a comprehensive understanding of noble phenomena of exchange bias effect, spin-phonon coupling, spin reorientations, and magnetic states to improve the multifunctionality of the material. A systematic investigation of these fascinating features in rare earth substituted neodymium orthochromite is presented in this thesis.



Chapter 2 : Experimental methods

This chapter delves into the synthesis method of sample preparation, offering an in-depth exploration of the basic principles behind a range of instruments used for experimental data recording and analysis. Additionally, the chapter undertakes a comprehensive examination of the structural and magnetic properties of the studied compounds to facilitate the physical characterization of the samples.

2.1 Sample preparation: Solid State Reaction Method

In general, a polycrystalline material can be synthesized using two basic methods; solid-state reaction and sol-gel method. For the present thesis work, we have opted the solid-state reaction method to prepare polycrystalline samples. It is known that the solid-state reaction method is a versatile and widely used method for synthesizing bulk samples [119].

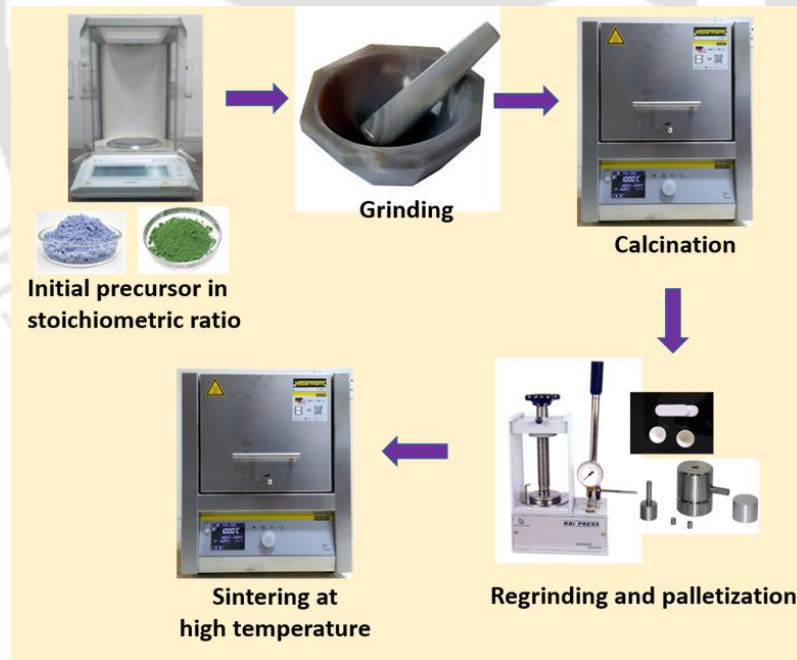


Fig. 2-1 Various steps involved in the sample synthesis procedure via standard solid-state reaction method.

This method provides the advantage of using a variety of starting materials like high-purity oxides, carbonates, acetates, etc. The two main steps involved in this method are the uniform mixing of starting material for homogeneity and the heat treatment for phase formation. Hence, the stoichiometric amounts of starting materials are mechanically mixed, and the repeated cycles of grinding and heating process provide the solid-state reaction among the constituted powders. As the solids cannot react to each other at ambient temperatures. Therefore, the heating is crucial for the ions to diffuse across their kinetic barrier. Thus, calcination and sintering are important processes in the solid-state reaction method. Calcination removes volatile components, such as water, carbon dioxide, and organic matter, from the material, transforming it into a more stable and reactive form and helping to initiate solid-state reactions. Further, sintering is a process that follows calcination and involves heating materials to a high temperature below their melting point. The sintering process involves several stages, including particle rearrangement, neck formation, and grain growth. The temperature and duration of sintering are critical parameters that need to be carefully controlled to achieve the desired properties while avoiding excessive grain growth or melting. For this, the high-temperature furnace (Naberthem Sintering Furnace HTCT 01/16, temperature range 30 °C to 1500 °C) is utilized. A typical reaction time of a few days is required to overcome the diffusion barrier. For a better sintering process, the kinetics of the reaction is also dependent on the heating or cooling temperature rate. Good contact between the surfaces of the reactants can improve the reaction rate. Thus, several hours of grinding is important for homogeneity and the reduction in the particle size of reactants that corresponds to the increase in surface area.

In the present thesis, Eu, Pr, and Ce substituted NdCrO_3 polycrystalline samples are synthesized by a standard solid-state reaction route (**Fig. 2-1**). The required amount of

high-purity starting materials (in oxide form) is calculated by stoichiometric equation and weighed using an electronic balance (Mettler Toldo, ME204, accuracy ~ 0.1 mg). The stoichiometric ratio of these oxides was thoroughly ground in an organic medium (acetone or methanol) using an agate mortar pestle for several hours to obtain the homogenous mixture of the particular compound. The dried homogenous mixture was placed in an alumina crucible and calcined at 1000 °C for 12h (in the air atmosphere). The calcined powder was further ground and pressed into cylindrical discs of 10 mm in diameter and nearly 1 mm in thickness with the help of a KBr hydraulic press (Technosearch Instruments, M-15). Finally, these pellets were sintered at 1300 °C for 12 h (or more hours) to achieve desired single-phase polycrystalline compound.

2.2 Characterization Techniques

2.2.1 Powder X-ray diffraction

Powder X-ray diffraction (XRD) is a versatile and non-destructive technique for determining phase purity and structural information of the materials. We know the wavelength of X-ray is comparable to the inter-planar spacing of the atoms of the order of few Å. When the beam of monochromatic X-ray is incident on the set of parallel atomic planes in a crystal lattice, the X-rays are diffracted, as shown in **Fig. 2-2**. The constructive interference of diffracted X-rays occurs if Bragg's law is satisfied. Bragg's law is given the relation [120],

$$2d_{hkl} \sin\theta = n\lambda \quad (2.1)$$

where d_{hkl} is inter-planer spacing, θ is the angle of incidence/diffraction, n is the order of the diffraction, and λ is the wavelength of the X-ray. The maximum intensity peak is observed if different planes are exposed while changing the angle of incidence. Thus, the XRD pattern as the function of 2θ for all possible (h, k, l) planes is obtained.

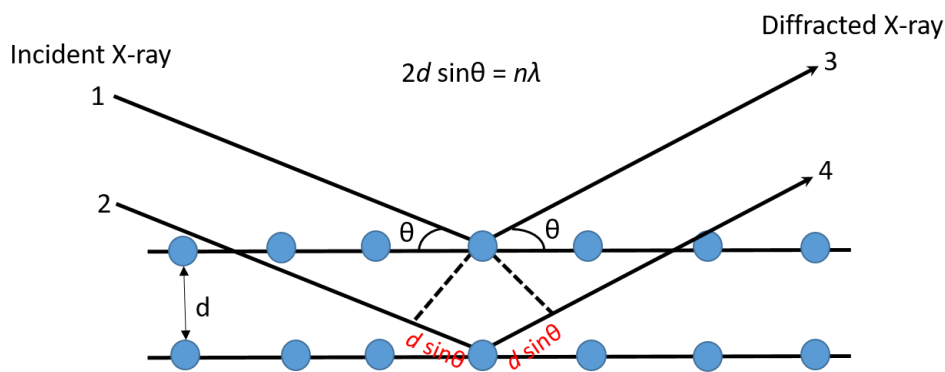


Fig. 2-2 Schematic presentation of Bragg's law for X-ray diffraction.

In this thesis, the X-ray diffractometer (Rigaku, Smart Lab, 9 kW) with Cu-K α radiation ($\lambda = 1.5406 \text{ \AA}$) was employed for the structural characterization of prepared polycrystalline samples. **Fig. 2-3** shows the typical photographic view of the X-ray diffractometer used for the present work.



Fig. 2-3 Photograph of the X-ray diffractometer (Rigaku, Smart Lab).

The instrument is based on the principle of Bragg-Brentano geometry in which the X-ray generator and detector are placed at equidistance from the sample holder. The system consists of the PhotonMax high-flux 9kW rotating anode X-ray source, which is coupled with HyPix-3000 high-energy resolution 2D multidimensional semiconductor detector. This detector allows all applications to be handled with a single detector and used to obtain 2D powder diffraction patterns. A high-resolution θ/θ goniometer drive system with an in-plane diffraction arm is incorporated to the system. For the measurement, the voltage and current of the X-ray generator were kept at 50 kV and 180 mA. The XRD patterns were measured with the scanning step size of 0.02° between the 2θ range of $10-90^\circ$. The structural investigation of the samples was done by analyzing the XRD patterns by Rietveld refinement technique using the Fullprof software [121]. The experimentally observed XRD pattern was fitted with the theoretical pattern using the phases obtained from the crystallographic database in which user-selected parameters were refined to minimize the difference between the experimentally observed pattern and the calculated pattern. We can find important information about the crystalline structure through refinement analysis, such as lattice parameters, atomic positions, site occupancies, bond lengths, bond angles, *etc.*

2.2.2 Raman spectroscopy

In 1928, C. V. Raman first discovered the famous Raman effect as the inelastic scattering of light from molecules [122]. Raman spectroscopy is a sensitive tool that detects vibrational or low-frequency modes to study structural properties like crystalline phases, bonding, chemical composition, strain, defects, *etc.*, of the material. In Raman spectroscopy, when the monochromatic laser beam falls to the sample, it interacts with the molecular vibrations, and most of the light gets scattered elastically (Rayleigh scattering).

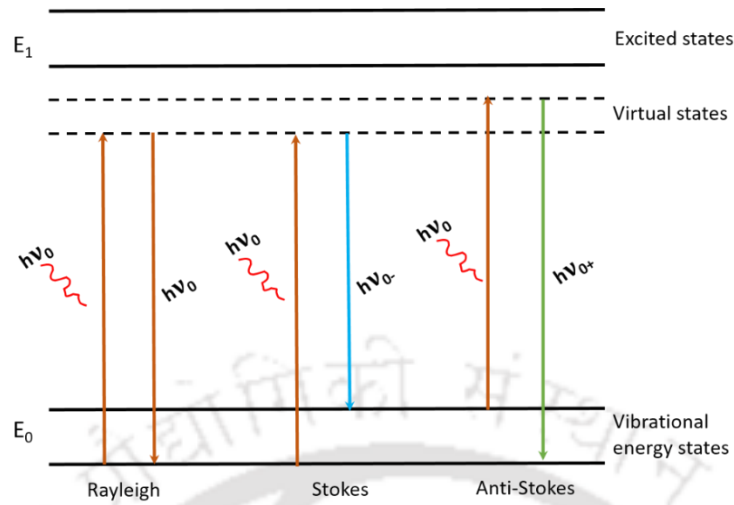


Fig. 2-4 The energy level diagram for Rayleigh and Raman scattering.

The small fraction of scattered light has a different wavelength than the incident wavelength due to inelastic scattering and comprises the main feature of Raman spectra. The scattered lines are known as the Stokes line if the scattered wavelength is shorter and the anti-stokes line if the scattered wavelength is longer as compared to the incident wavelength (see **Fig. 2-4**). In conventional Raman spectrometers, the Stokes shifted Raman bands are measured, as they are more intense than anti-Stokes shifted Raman bands and corresponds to the

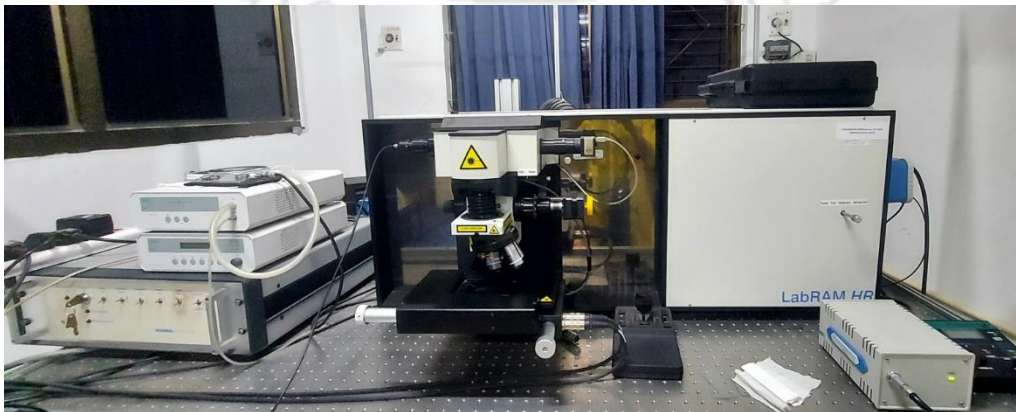


Fig. 2-5 Photograph of the Raman spectrometer (Horiba Jobin Yvon, LabRam HR800).

molecular transition from lower to higher vibrational energy levels. The fluorescing specimen causes interference with Stokes bands, and there anti-Stokes bands are measured.

Fig. 2-5 depicts the photographic view of the micro-Raman spectrometer (Horiba Jobin Yvon, LabRam HR800) used for the Raman spectra of prepared samples for the present work. The excitation of the photon is obtained with the monochromatic laser source (Ar-ion) of wavelength of 514 nm. The backscattered geometry with 50× objective, edge filter, and Peltier-cooled charge-coupled device detector are used for the recording spectra. For temperature-dependent Raman spectroscopy, the heating/cooling sample stage (Linkam, THMS600) is attached to the instrument. The instrument has a spectral resolution of 1 cm^{-1} , and the 1800 mm^{-1} grating was fixed during the temperature-dependent measurement for positional accuracy.

2.2.3 Scanning Electron Microscopy

In the present thesis, a Scanning electron microscope (SEM, Leo 1430VP) equipped with a field-emission scanning electron microscope (FESEM, Sigma-300 Zeiss) and energy dispersive X-ray spectrometer (EDX, Sigma) were used for the morphological and elemental composition study of prepared samples.



Fig. 2-6 Photograph of the field emission scanning electron microscope (Sigma, Zeiss).

In SEM, the scanning of the surface of the material is done by the thermionically emitted high-energy electrons that are accelerated towards an anode with sufficient kinetic energy and focused by two successive condenser lenses into a beam with a narrow spot size (50 Å). Similarly, in FESEM, the electrons are emitted from field emission. The image magnification of $\sim 10^5$ times is provided by the shorter wavelength of electrons. The deflection of the beam over the area of the sample surface occurs with scanning coils near the objective lens. Depending on the interaction between electrons and the sample, different signals like secondary electrons, backscattered electrons, and characteristic X-rays are generated, and the detectors collect their intensity. The secondary electrons are used to analyze the sample's surface topography, and the backscattered electrons provide information of the sample composition. The photographic view of the field emission scanning electron microscope is shown in **Fig. 2-6**. Furthermore, the energy dispersive X-ray spectroscopy (EDX) is quite useful for the elemental characterization of the specimen. The EDX spectrum generally consists of the peak related to the energy levels for which most of the X-rays are received. Each of these peaks in the spectrum is unique to an atom and corresponds to a particular element.

2.2.4 X-ray photoelectron spectroscopy

X-ray photoelectron spectroscopy (XPS) is a surface science technique that is used to determine the quantitative elemental composition and oxidation state. Usually, the XPS can probe to the depth of 1-10 nm on the surface of a specimen. When the sample is irradiated with monochromatic X-rays, it results in the emission of photoelectrons whose energies are the characteristics of the elements. The XPS spectra obtained by the number of electrons and their binding energy allow the identification of the element inside the material.



Fig. 2-7 Photograph of the X-ray photoelectron spectrometer (ESCALAB).

The kinetic energy of core electrons ejected by the incident X-ray is given by the following equation [123],

$$E_k = h\nu - E_b - \phi \quad (2.2)$$

where, E_k is the kinetic energy of the photoelectron, $h\nu$ is the energy of an incident photon, E_b is the binding energy of the electron, and ϕ is the work function. In general, the XPS instrument has different components. When the X-rays (typically the Al K_α and Mg K_α) hit the sample, the electron leaves the surface with a range of energies and directions. The ultrahigh vacuum system ($< 10^{-9}$ Torr) is required due to the relatively low energy of the emitted photoelectrons. The portion of these photoelectrons is collected by the set of multielement lenses and transferred to the hemispherical analyzer. The electrostatic field

within the analyzer allows the electrons with specific energy to reach the detector. The XPS data are compared to archives of experimentally determined XPS data of standard reference materials. For the present thesis work, the used X-photoelectron spectrometer (Thermo Fisher Scientific, ESCALAB Xi+) is displayed in **Fig. 2-7**.

2.2.5 Physical Properties Measurement System

The physical property measurement system (PPMS) is a sensitive and adaptable tool for the highly precise measurement of a wide range of physical properties as a function of magnetic field or temperature, including magnetization, electrical resistivity, heat capacity, thermal conductivity, etc. Therefore, after structural analysis, the single-phase polycrystalline samples were further studied, and the dc magnetization measurements were performed to investigate the magnetic properties of the compounds.



Fig. 2-8 Photograph of physical property measurement system (PPMS, DynaCool).

The details of the measurements are discussed in this section. In the present thesis, a PPMS (DynaCool, Quantum Design) equipped with a vibrating sample magnetometer (VSM) is used for the magnetization measurements. In this instrument, the measurement options can be operated in a wide range of temperatures of 2 to 325 K with the applied magnetic fields up to 9T. **Fig. 2-8** shows the photographic view of PPMS with a dewar that has a 9T conduction-cooled superconducting switchless magnet, pump setup, lock-in amplifier, and a power source. The integrated cryo pump evacuates the sample chamber to less than 10^{-4} Torr. The sophisticated MultiVu software controls the system and helps it operate during the experiment.

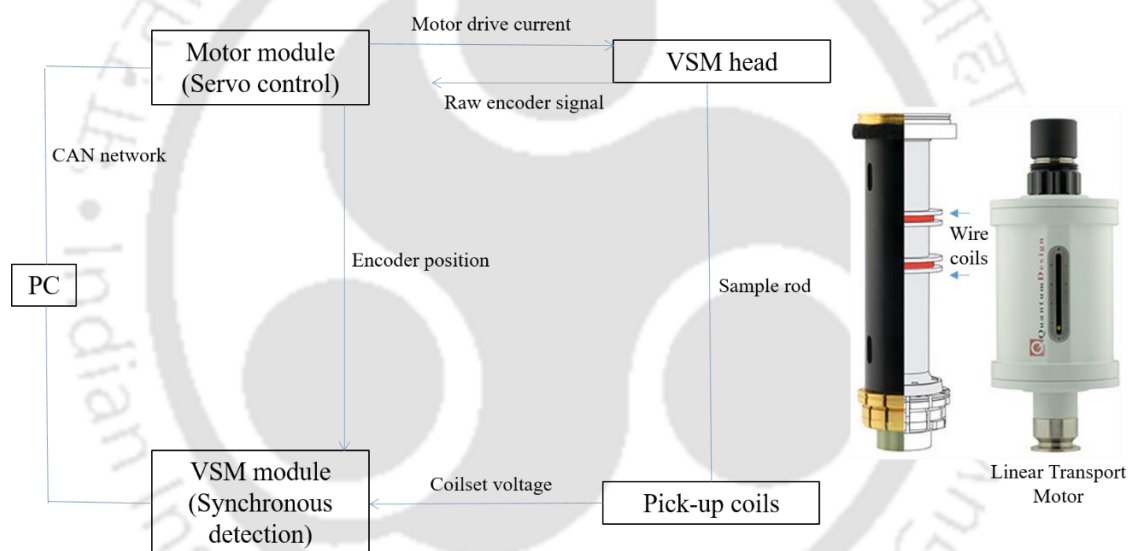


Fig. 2-9 The VSM coil set with motor (right) and the block diagram of VSM mode operation of PPMS (left).

For temperature and field-dependent magnetic properties, the VSM configuration is used. The VSM option employs a puck-based first-order gradiometer coil set and high-resolution linear transport motor (see **Fig. 2-9**), which transforms the PPMS into a sensitive DC magnetometer for faster data recording. The major components of the VSM option are the VSM linear motor transport/head with centering accuracy ± 0.04 mm for vibrating the

sample, the detection coil set puck, the electronics for operating the linear motor transport and detecting the response from the pickup coils, and the computer interface. The VSM can perform measurements up to the maximum field available from the PPMS magnet, as the sensitivity of the detection coils is unaffected by large magnetic fields. A temperature sensor integrated within the coil set provides the thermometry of the sample through exchange gas coupling. The VSM measures the static or dc magnetic moment of the sample as the function of temperature or applied field. The single crystal, thin film, polycrystalline pieces, and loose powders can be measured with standard sample holders, including low-background quartz paddle, brass half-tube spacer, and polycarbonate capsules.

The working principle of VSM is based on Faraday's law that changing magnetic flux can induce a voltage in the pickup coil. The induced voltage is given by the relation,

$$V = \frac{d\phi}{dt} = \left(\frac{d\phi}{dz}\right) \left(\frac{dz}{dt}\right) \quad (2.3)$$

Here, ϕ is the magnetic flux related to the pickup coil, z is the sample's vertical position with respect to the coil, and t is the time. The output voltage for a vibrating sample may be expressed as,

$$V = 2\pi f C m A \sin(2\pi f t) \quad (2.4)$$

Here, C , m , A , and f are the coupling constant, magnetic moment, amplitude of oscillation, and frequency, respectively. The basic measurement is done by oscillating the sample near a detection (pickup) coil and simultaneously detecting induced voltage. Several steps involved in VSM operation are shown by the block diagram in **Fig. 2-9**. The analyzed sample is attached to the end of a sample rod, which is driven sinusoidally. The center of oscillation is positioned at the vertical center of the gradiometer pickup coil by centering the sample. The precise position and amplitude of oscillation are controlled by the VSM

linear motor module. The VSM detection module uses the position encoder signal as a reference for synchronous detection. This encoder signal is obtained from the VSM motor module, which interprets the raw encoder signals from the VSM linear motor transport. The VSM detection module detects the in-phase and quadrature-phase signals from the encoder and from the amplified voltage from the pickup coil. These signals are averaged and sent over the CAN bus to the VSM application running on the PC. By using a compact gradiometer pickup coil configuration, a typical oscillation amplitude of 2 mm, and a frequency of 40 Hz, the system is able to resolve magnetization change of less than 10^{-6} emu at the data rate of 1 Hz. To conduct temperature-dependent dc-magnetization measurements, different modes are described as,

(1) Zero-field-cooling (ZFC): In this mode, the sample was cooled from room temperature or the paramagnetic region to the lowest temperature of measurement in the absence of any magnetic field. Data were recorded during the subsequent heating cycle after applying a constant magnetic field.

(2) Field-cooled cooling (FCC): In this mode, the sample was cooled from room temperature or the paramagnetic region to the lowest temperature of measurement while maintaining a constant applied magnetic field. Data were recorded during the same cooling cycle.

(3) Field-cooled warming (FCW): Similar to the FCC mode, the sample was cooled from room temperature or the paramagnetic region to the lowest temperature of measurement with a constant applied magnetic field (same as the FCC case). However, data were recorded during the subsequent heating cycle of the measurement. Generally, FCW is commonly referred to as FC.



Chapter 3 : Spin-induced exchange bias, lattice modulation, and magnetostructural imprints in $Nd_{1-x}Eu_xCrO_3$

3.1 Introduction

The family of rare earth chromites $RCrO_3$ (R = rare earth and yttrium) belongs to an orthorhombic space group $D_{2h}^{16} - Pnma$ with four formula units per unit cell with octahedrally coordinated B-sites occupied by Cr^{3+} ions and A-sites occupied by R^{3+} ions [45]. For practical applications, materials with multifunctional properties close to room temperature are more acceptable. A promising candidate in this search may be the perovskite-type $NdCrO_3$ with an orthorhombic $Pnma$ structure. The magnetic structure of $NdCrO_3$ is known to be G-type antiferromagnetic. The Cr^{3+} spins exhibit the antiferromagnetic ordering at $T_N \sim 219$ K and the weak ferromagnetism below T_N . The reorientation of Cr^{3+} spins takes place because of the transition from a weak ferromagnetic phase to an antiferromagnetic phase at spin-reorientation transition $T_{SR} \sim 35$ K [15,87]. The magnetic ordering of Nd^{3+} ions (T_{RE}) exhibits at a much lower temperature (~ 4.2 K) induced by the Cr^{3+} sublattice [16]. Similarly, $EuCrO_3$ has $T_N \sim 180$ K with a canted antiferromagnetic structure. Based on magnetization or neutron diffraction studies, the ordering of Eu moments is not known, but the contribution of Eu^{3+} ions to magnetism has been described by the Van Vleck-type temperature-dependent Eu moments [14,124]. In recent years, the exchange bias (EB) effect is under intense investigation due to its utilization in sensors, spintronic devices, and magnetic recording devices [4,6,125]. Initially, the EB effect was observed due to exchange anisotropy generated at the interface between antiferromagnetic (AFM)-ferromagnetic (FM) layers [6]. The EB effect in single-

phase alloys and compounds was associated with magnetic structures such as spontaneously phase-separated systems and magnetic core-shell structures [7]. In order to demonstrate the *EB* effect through various mechanisms, different orthochromites similar to their isostructural manganites have been recently reported [71] [74][118].

The interaction between the moments of *R* and Cr offers not only several magnetic phases but also other properties. Such as the case of $RCrO_3$ the spin-phonon coupling is observed only for magnetic *R*-ion [12], and Raman behavior and ferroelectricity below T_N are topic of debate [107][126][13]. The presence of magnetoelastic distortions in $EuCrO_3$ is examined with temperature variation of lattice parameters, thermal expansions, and dielectric measurements [14]. However, the analysis of electron density distribution as the function of temperature linked to the crystal structure and atomic displacement has not been reported in $RCrO_3$ so far. We find that the understanding of $NdCrO_3$ is confined to individual properties, which still requires the study of phonon modes as a function of temperature and its correlations with magnetic properties. Further, there is a requisite for the evolution of the chemical pressure induced by Eu^{3+} ions on the structure and magnetism of $NdCrO_3$. To improve the multifunctionality of the material will, therefore, be interesting and technologically significant. For this, the orthorhombic distortions can be tuned by substituting the R^{3+} of different ionic sizes that may give the various magnetic properties and the spin-lattice coupling through the magnetic transitions.

This chapter deals with the synthesis of $Nd_{1-x}Eu_xCrO_3$ ($x = 0.0$ to 1.0) samples and the study of its structural and magnetic properties. The chemical pressure-induced magnetostructural effects through Eu substitution are examined. The possibility of a significant *EB* effect in the weak ferromagnetic state and the detailed temperature-dependent Raman study. The magnetoelastic coupling is studied via the structural parameters at low temperatures. The DFT based calculations are involved to support the findings. The

experimental electron density distribution of the samples is investigated using the maximum entropy method.

3.2 Experimental and Computational details

The polycrystalline samples of $Nd_{1-x}Eu_xCrO_3$ ($x = 0.0, 0.05, 0.10, 0.20, 0.50, 0.70, 0.90,$ and 1.0) were synthesized by the standard solid-state reaction method. The stoichiometric ratio of the starting compounds Nd_2O_3 (99.9%), Eu_2O_3 (99.9%), and Cr_2O_3 (99.6%) was weighed and mixed into the agate mortar pestle in the acetone medium. These finely mixed powders were pressed into pellets ~ 10 mm in diameter using a hydraulic press and put in the alumina crucibles. After intermediate grinding and heating steps, all the pellets were finally sintered at 1300°C for 12 h, followed by slow cooling in the air at a rate of $3^\circ\text{C}/\text{min}$. The structural characterization was performed using the X-ray diffractometer (Rigaku, Smart Lab, 9kW) with Cu-K α radiation ($\lambda = 1.5406 \text{ \AA}$). Low-temperature XRD measurements were performed at selected temperatures in the 3-300 K range using the Rigaku SmartLab machine equipped with a low-temperature attachment. Raman spectra were recorded with a Raman spectrometer (Horiba Jobin Yvon, LabRam HR) having an excitation wavelength of 514 nm at room temperature to confirm the phase purity. The samples were kept in a Linkam (THMS600) Stage for temperature-dependent Raman spectroscopy in the temperature range of 80-300 K. The morphology and the homogeneity were examined by field emission scanning electron microscope (FE-SEM) (Zeiss, Sigma 300) and energy dispersive X-ray (EDX) (Sigma), respectively. Magnetization measurements were carried out using a physical property measurement system (PPMS) (Quantum Design, DynaCool) in the temperature range of 3-300 K and up to a maximum field of 9T.

The calculations with density-functional theory (DFT) and density-functional perturbation theory (DFPT) were performed using the Quantum-ESPRESSO package [127]. The simulations utilized the experimentally derived lattice parameters and were conducted using 20 atoms cells (four Nd, four Cr, and twelve O). We replaced each of these four Nd sites with Eu in one supercell, and the difference in the result was minimal. Thus, the average result of the above four configurations has been taken. The Perdew-Burke-Ernzerhof function for exchange-correlation energy is used. The self-consistent field (SCF) run was executed on the $4 \times 4 \times 4$ k -point mesh with the kinetic energy cutoff of 50 Ry for wavefunctions and 500 Ry for charge density. The energy convergence accuracy of 10^{-8} Ry is used for the SCF calculations.

3.3 Results and discussions

3.3.1 Room temperature Powder X-ray diffraction

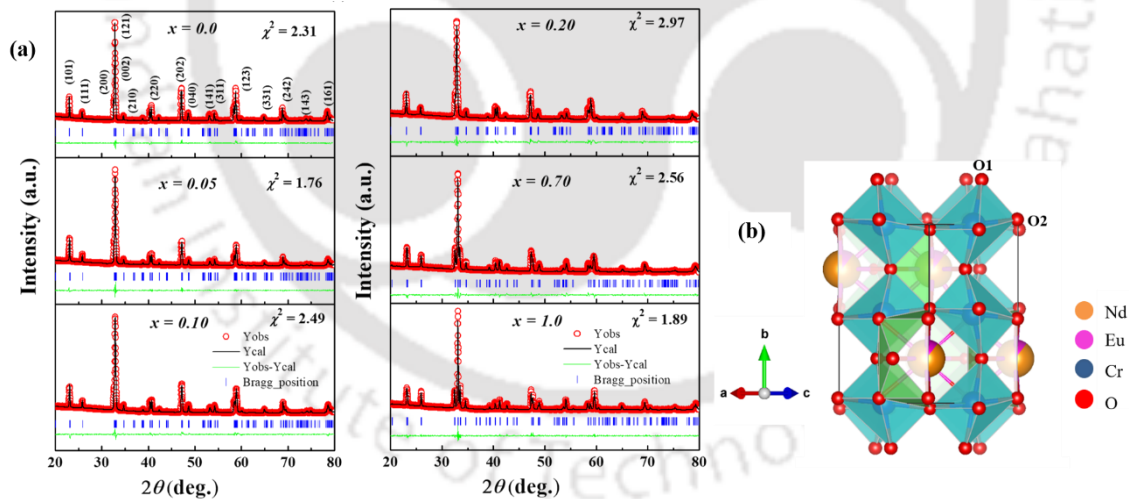


Fig. 3-1 (a) Rietveld refinement of powder XRD patterns of $Nd_{1-x}Eu_xCrO_3$ ($x = 0.0-1.0$) samples by using the FULLPROF program. The circles are the experimental points, the solid line (black) is refined data, and the bottom green line shows the difference between these two. Vertical lines (blue) represent the Bragg position (b) The crystal structure of the $x = 0.10$ sample visualized by VESTA software.

The phase purity and the crystal structure of the greenish samples were confirmed by performing a powder X-ray diffraction (XRD) experiment on polycrystalline $Nd_{1-x}Eu_xCrO_3$ ($x = 0.0-1.0$) samples. The typical XRD pattern, together with the Rietveld refinement, is shown in **Fig. 3-1(a)**. The obtained XRD peaks were well matched with the ICSD Card No. 01-083-0261, suggesting no sign of any impurity phases. For further confirmation, the Rietveld refinement of the XRD patterns was carried out using the FULLPROF program. The refinement confirms the formation of single-phase samples having the space group *Pnma* (No.62) with an orthorhombic structure. The goodness of the fit (χ^2) values confirms the quality of fitting. It is found that all the substituted samples crystallize in single-phase with the orthorhombic crystal structure having the *Pnma* space group. The refinement is used to calculate the lattice parameters, bond lengths, and bond angles. The unit cell parameters for all the samples are given in **Table 3-1**. The lattice parameters of the present $x = 0.0$ sample are in good agreement with the previous report [46].

Table 3-1 Lattice parameters a , b , c , unit-cell volume V , bond lengths $Nd-O1$ and $Cr-O2$, and bond angle $Cr-O1-Cr$ obtained from Rietveld refinement of $Nd_{1-x}Eu_xCrO_3$ ($x = 0.0$ to 1.0) samples.

x	a (Å°)	b (Å°)	c (Å°)	V (Å°) ³	Nd-O1 (Å°)	Cr-O2 (Å°)	Cr-O1-Cr (deg.)
0.0	5.482	7.689	5.418	228.37	2.395	1.939	156.5
0.1	5.484	7.688	5.415	228.30	2.31	1.901	153.2
0.2	5.488	7.686	5.413	228.39	2.381	2.092	154.4
0.5	5.498	7.667	5.385	227.03	2.353	2.045	153.9
0.7	5.496	7.633	5.354	224.67	2.317	2.037	151.78
0.9	5.506	7.626	5.344	224.44	2.319	1.982	152.12
1.0	5.512	7.626	5.342	224.58	2.343	1.993	152.39

The doping of Eu^{3+} ions brings the increase in lattice parameter a , reduction in b , c , and lattice volume V , attributed to the lattice contraction arising from the difference in the ionic radii of Nd^{3+} (1.109\AA) and Eu^{3+} (1.066\AA). The crystal structure obtained from the refinement of $x = 0.10$ sample is displayed in **Fig. 3-1(b)**, where the Nd^{3+}/Eu^{3+} ions (yellow/pink spheres) occupy the A-site, and the Cr^{3+} ions (blue spheres) occupy the octahedral B-site. Oxygen ions O1 and O2 (red spheres) connect the CrO_6 octahedra along the b -axis and the a - c plane. The unit cell is outlined. The distorted perovskite-type structure shows the in-phase tilting of the CrO_6 octahedra along the b -axis. The distortion of cell edges of the $Nd_{1-x}Eu_xCrO_3$ system from ideal cubic symmetry is tested using different factors. We found that Goldschmidt's tolerance factor $t = (r_{|Nd+Eu|} + r_o)/\sqrt{2}(r_{Cr} + r_o)$ [44], decreases from 0.883 ($x = 0.0$) to 0.868 ($x = 1.0$). In addition, the cell distortion factor d is defined by the equation [128],

$$d = 10^6 \left[\frac{\left(\frac{a}{\sqrt{2}} - a_p\right)^2 + \left(\frac{b}{2} - a_p\right)^2 + \left(\frac{c}{\sqrt{2}} - a_p\right)^2}{3a_p^2} \right] \quad (3.1)$$

where, $a_p = \frac{\left(\frac{a}{\sqrt{2}} + \frac{b}{2} + \frac{c}{\sqrt{2}}\right)}{3}$ is the average cubic lattice parameter. We observed the d increases sharply with increasing Eu content from ~ 24 ppm ($x = 0.0$) to 172 ppm ($x = 1.0$), as illustrated in **Fig. 3-2(a)**.

Further, the orthorhombic strain s along the b -axis is calculated using the relation [129],

$$s = 2(a + c - \sqrt{2}b)/(a + c + \sqrt{2}b) \quad (3.2)$$

The doping of the Nd-site with Eu^{3+} ions increases the s (in order of 10^{-3}) from 2.51 ($x = 0.0$) to 6.59 ($x = 1.0$), shown in Fig. 2(a).

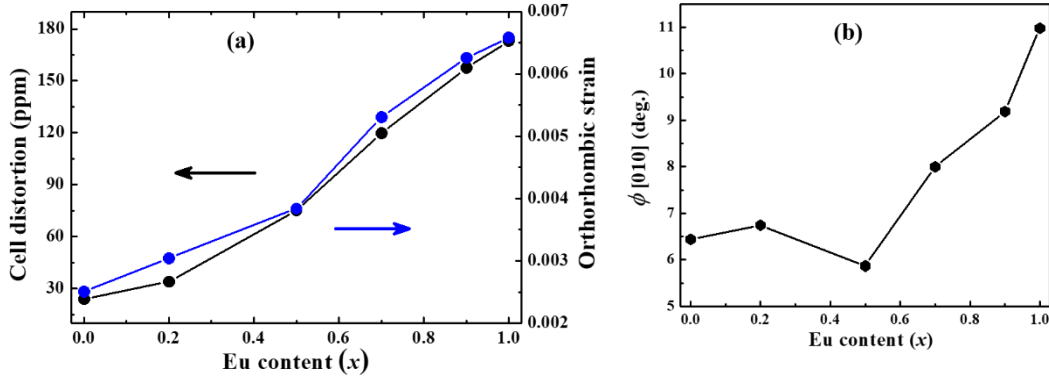


Fig. 3-2 (a) The cell distortion factor d and orthorhombic strain s as the function of Eu content and (b) The x variation of the tilt angle $\phi[010]$.

Here, we noticed both d and s show some ambiguity at the $x = 0.5$ sample; however, no such trend is seen directly in the cell parameters. Furthermore, the internal crystallographic parameters such as Nd/Eu-O1, Cr-O2 bond length, and the Cr-O1-Cr bond angle obtained from refinement are listed in **Table 3-1**, exhibit the significant modifications related to the structural distortions. In order to calculate the in-phase octahedral tilt angle $\phi[010]$, the following expression is used [130],

$$\cos\phi = \frac{\cos[\{180 - \langle Cr - O2 - Cr \rangle\}/2]}{\sqrt{\cos[\{180 - \langle Cr - O1 - Cr \rangle\}/2]}} \quad (3.3)$$

Fig. 3-2(b) shows the decrease in the ϕ value for $x \leq 0.5$ and the rapid increase for $x > 0.5$ samples. According to the calculation of the tilt angle $\phi[010]$ from atomic positions by Weber *et al.* [46], the decrease of ionic radii of R -ion can increase the ϕ value. However, present results deviate from this behavior at $x = 0.5$, suggesting the possible non-monotonic increase of structural distortion by substituting Nd^{3+} with Eu^{3+} ions in the $Nd_{1-x}Eu_xCrO_3$ system.

3.3.2 Microstructural analysis

3.3.2.1 FESEM and EDX

The FESEM micrographs of $Nd_{1-x}Eu_xCrO_3$ ($x = 0.0-0.70$) and the EDX mapping of the $x = 0.05$ sample are displayed in **Fig. 3-3(a)-(d)**. The surface morphology of the bulk samples shows a uniform grain formation with considerable porosity. The elemental mapping for $x = 0.05$ sample confirms the uniform distribution of elements. The average grain size is calculated using the linear intercept method by image-J software. The grain size distribution for $x = 0.7$ sample is displayed in **Fig. 3-3(e)**. The estimated grain size is found to be in the range of 0.648 to 0.858 μm for $x = 0$ to 1.0 samples as shown in the **Fig. 3-3(f)**. We noticed the trend of grain size changes across $x = 0.5$ composition similar to the d , s , and $\phi[010]$ observed from XRD analysis, showing possible influence of non-monotonic structural distortions on the surface morphology.

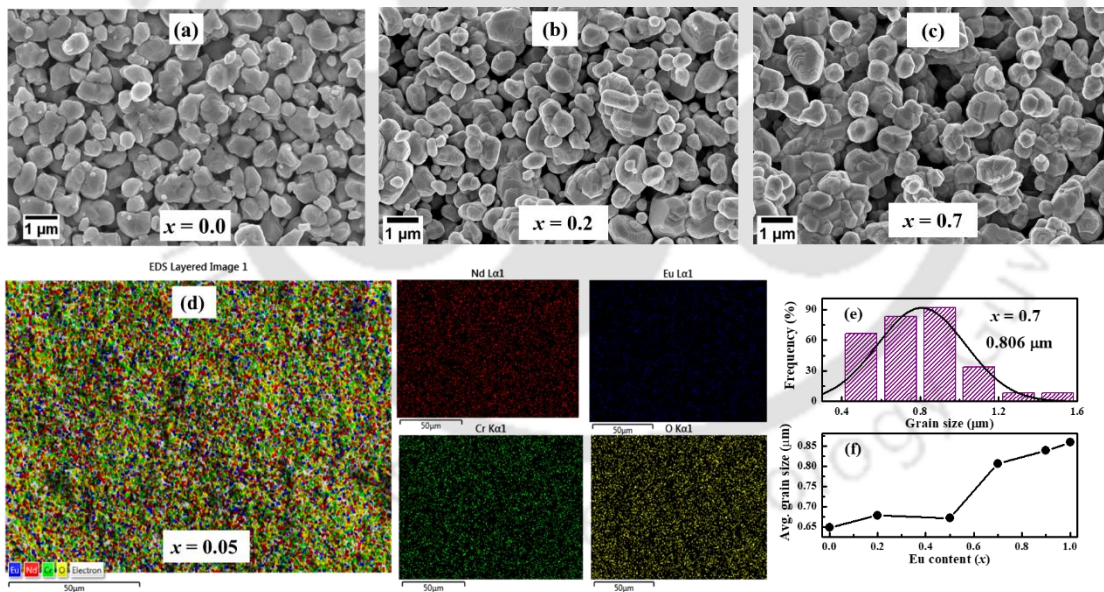


Fig. 3-3 FESEM micrograph of $Nd_{1-x}Eu_xCrO_3$, (a) $x = 0.0$ (b) 0.20 (c) 0.70 samples (d) the EDX mapping of $x = 0.05$ sample (e) the grain size distribution of $x = 0.7$ sample and (f) the average grain size as the function of Eu content.

3.3.2.2 Bulk modulus

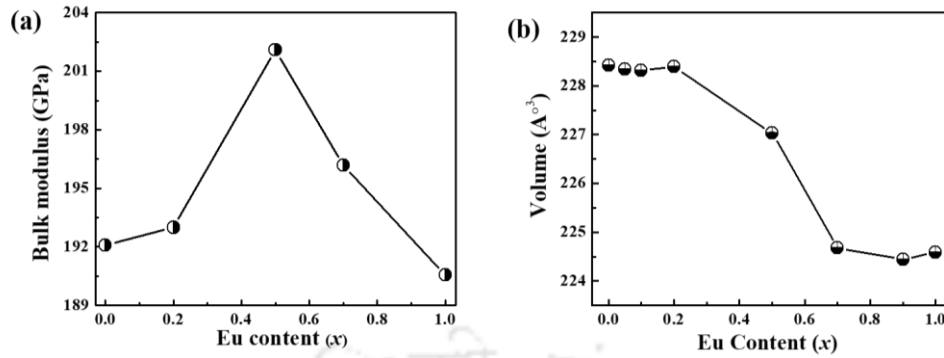


Fig. 3-4 (a) Calculated bulk modulus as the function of Eu content and (b) the x dependence of unit cell volume obtained from refinement of $Nd_{1-x}Eu_xCrO_3$ ($x = 0.0-1.0$) samples.

For a clear understanding, we have also investigated the bulk modulus of these compounds. The experimental value of bulk modulus is usually obtained by fitting a second-order Birch-Murnaghan equation of state to the pressure dependence of unit cell volume [131]. In this work, we employed the DFT-based calculations to find the bulk modulus of the $Nd_{1-x}Eu_xCrO_3$ ($x = 0.0$ to 1.0) compositions, as depicted in **Fig. 3-4(a)**. It is observed that the bulk modulus increases with increasing Eu content, showing a maximum value of ~ 202.17 GPa across $x = 0.5$ sample. The further increase of Eu substitution resulted in a sharp decrease of bulk modulus up to $x = 1.0$ sample. The value of bulk modulus for $x = 0.0$ compound is comparable with the theoretical value ~ 192 GPa of cubic $NdCrO_3$ [132] and experimental results of other perovskites such as $GdFeO_3 \sim 182$ GPa and $GdAlO_3 \sim 191$ GPa [133]. The increase of bulk modulus with Eu substitution may be due to the decrease of the average A-site radii as the ionic radii of Eu^{3+} (1.066 \AA) is comparably smaller than Nd^{3+} (1.109 \AA). The pressure effect on $RCrO_3$ suggest the experimental value of bulk modulus increases with decreasing ionic radii of the R -ion [112,131,134][135]. However, our result deviates from this behavior for higher Eu content and shows the least compressibility for $x = 0.5$ composition. These observations are associated with the volume or structural change. The x dependence of volume (see **Fig. 3-4(b)**) shows the decrease of

volume (V) as it should be the case with Eu substitution. However, the V for $x = 0.0-0.20$ sample is in the range of $\sim 228 \text{ \AA}^3$ and it decrease to the range of 224 \AA^3 for $x = 0.70-1.0$ sample. Thus, the V is not gradually decreasing with the gradual increase of Eu content, but the maximum change near $x = 0.50$. Further, the x dependence of selected Raman modes showed the similar behavior that will be discussed in upcoming section. Thus, it seems the chemical pressure induced by Eu substitution increases for $x \leq 0.5$ and decreases for $x > 0.5$ samples suggesting some boundary at $x = 0.5$ concentration. The effect of chemical pressure boundary is evident from the observed structural properties of present samples.

3.3.3 Room temperature Raman spectroscopy

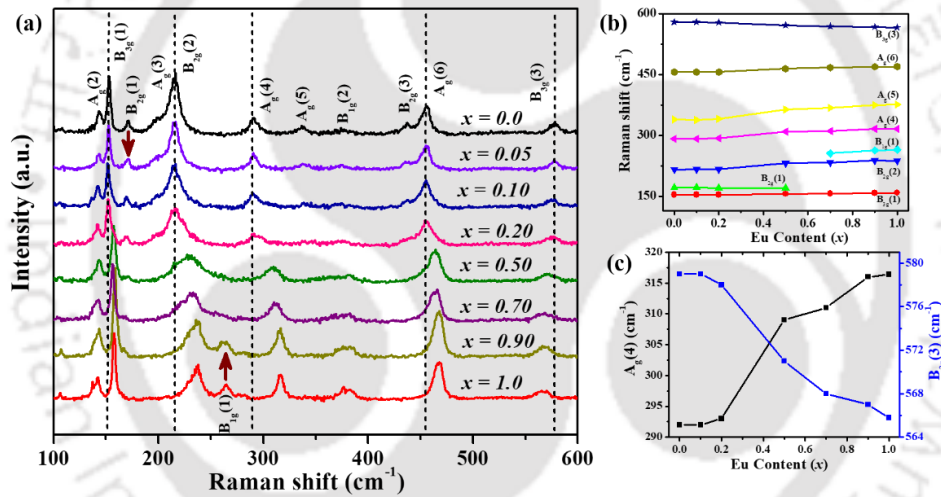


Fig. 3-5 (a) Raman Spectra from 100 to 600 cm^{-1} of $Nd_{1-x}Eu_xCrO_3$ ($x = 0.0-1.0$) samples measured at room temperature and (b)-(c) the x dependence of phonon frequencies of selected Raman modes.

Raman scattering spectroscopy is always a powerful and sensitive tool for detecting local structural distortions by the evolvement of phonons. According to group theory, $RCrO_3$ compounds belonging to the orthorhombic crystal structure with the $Pnma$ space group show a total of 24 Raman active phonon modes [136].

$$\Gamma_{\text{Raman, Pnma}} = 7A_g + 5B_{1g} + 7B_{2g} + 5B_{3g} \quad (3.4)$$

Raman spectra of $Nd_{1-x}Eu_xCrO_3$ for $x = 0.0-1.0$ samples at room temperature are displayed in **Fig. 3-5(a)**, in which the $x = 0.0$ sample is consistent with the previous study [116]. For each measured spectrum, Lorentzian functions were used to obtain the exact peak position by decomposing the fitted curves into individual Lorentzian components. We are getting 11 prominent Raman active modes. Lattice dynamics calculations using DFPT have been involved in assigning exact Raman modes, which are in good match with our experimental modes and comparable with an earlier report on $LaCrO_3$ [137]. The experimental and calculated Raman modes with their assignment for $x = 0.0-1.0$ samples are presented in **Table 3-2**. It is clear that the substitution of Eu^{3+} ions significantly changes the phonon frequencies. The Raman wavenumber is related to the bond length (l) by $1/(l)^{1/2}$ and changes in the bond length of the particular atoms involved in the mode vibrations can give changes in mode positions [109].

It is observed that the movement of Nd/Eu atoms affects the modes below 200 cm^{-1} reflected in the shift of the $A_g(2)$ mode toward low wavenumber (red shift). However, the higher wave number shift of $B_{3g}(1)$ mode and a notable decrease in $B_{2g}(1)$ mode intensity is observed. It results in the merging of $B_{2g}(1)$ mode to the intense $B_{3g}(1)$ mode and becomes a shoulder-like feature for $x \geq 0.5$ compositions. This can be further linked to the absence of theoretical $B_{2g}(1)$ mode for the $x = 1.0$ sample, mentioned in **Table 3-2**. The modes from 200 to 500 cm^{-1} (except $B_{1g}(1)$ mode) exhibit the shift towards higher wavenumber (blue shift) due to the decrease of A-site ionic radii. We noticed the mode $B_{1g}(1)$ appears for $x > 0.5$ (higher substituted) compositions, which is consistent with the present calculation related to R and O motion. Above 500 cm^{-1} , the modifications in antisymmetric stretching of O atom inside CrO_6 octahedra result in the red shift of $B_{3g}(3)$ mode. The phonon frequencies in **Fig. 3-5(b)-(c)** shows the maximum change near the $x = 0.5$ composition which confirm the aforementioned structural behavior.

Table 3-2 Experimental phonon modes wavenumbers of $Nd_{1-x}Eu_xCrO_3$ ($x = 0.0-1.0$) samples, theoretical wavenumber, and their assignment for $x = 0.0$ and 1.0 sample calculated at 300 K.

Assignment	x = 0.0 Calc.	x = 0.0	x = 0.10	x = 0.2	x = 0.5	x = 0.7	x = 0.9	x = 1.0	x = 1.0 Calc.	Symmetry
R(z)	127	144	144	144	143	142	141	141.2	120.8	$A_g(2)$
R(y)	129	154	154	154	156	157	158	158.6	122.2	$B_{3g}(1)$
R(x)	183	172	172	171	171	no mode	no mode	no mode	no mode	$B_{2g}(1)$
In-phase y rotation of CrO_6 octahedra	194	200	202	201	218	221	230	230.1	227.7	$A_g(3)$
R(z), O1(z)	205	216	217	217	232	233	238	237.5	230.9	$B_{2g}(2)$
R(y), O2(y)	no mode	no mode	no mode	no mode	no mode	256	263	264.6	279.4	$B_{1g}(1)$
O1(x), R(-x)	250	292	292	293	309	311	316	316.4	316	$A_g(4)$
Out of phase x rotation of CrO_6 octahedra	325	339	338	341	364	368	375	376	356.9	$A_g(5)$
Out of phase y rotation of CrO_6 octahedra	373	376	376	375	382	382	384	383.1	360.3	$B_{1g}(2)$
Out of phase z rotation of CrO_6 octahedra	423	438	440	438	453	462	464	464.9	444	$B_{2g}(3)$
Out of phase bending of CrO_6 octahedra	464	456	456	456	464	467	469	469.2	467.6	$A_g(6)$
Antistretching of CrO_6 octahedra	572	579	579	578	571	568	567	565.8	547.1	$B_{3g}(3)$

3.3.4 Magnetic properties

3.3.4.1 Temperature and field-dependent magnetization

The temperature dependence of magnetization (M - T) under the field cooled (FC) conditions with an applied field of $H = 100$ Oe and the first derivative of magnetic susceptibility, ($d\chi/dT$) as a function of temperature (T) for $Nd_{1-x}Eu_xCrO_3$ ($x = 0.0-1.0$) samples are shown in **Fig. 3-6**. We see the magnetic ordering exhibits at $T_N = 225.4$ K associated with AFM ordering of Cr^{3+} and $T_{SR} = 37.1$ K due to spin reorientation of Cr^{3+} spins for $x = 0.0$ sample, which is in agreement with the previous report [111].

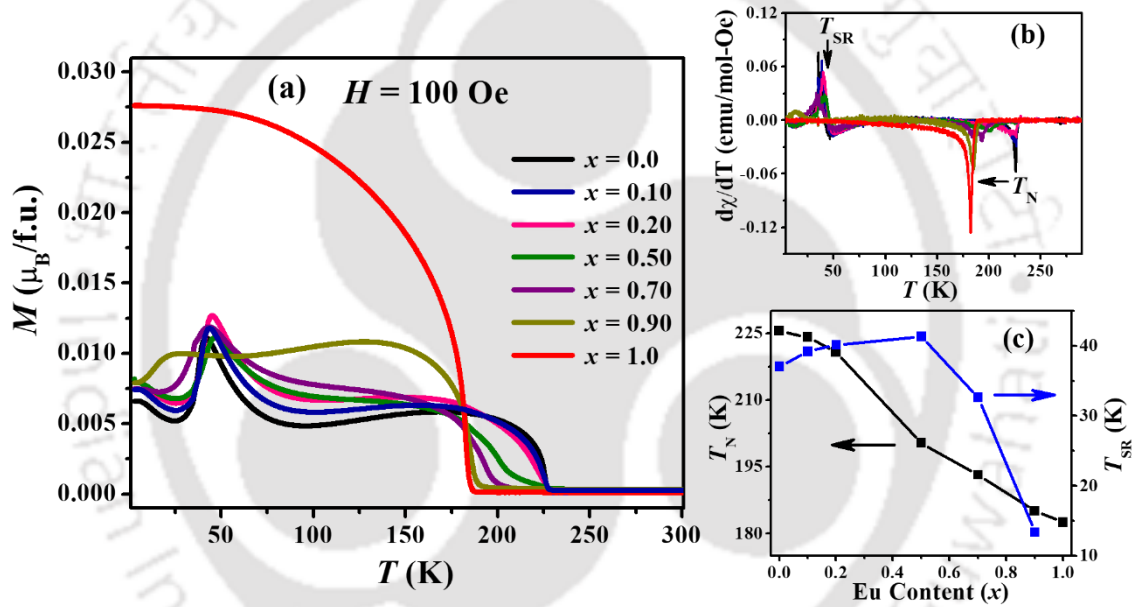


Fig. 3-6 Temperature-dependent magnetization curves measured in FC mode for the applied field of 100 Oe (b) Temperature dependence of the first derivative of susceptibility curves having peaks at magnetic transition and (c) The variation of T_N and T_{SR} as the function of Eu content for $Nd_{1-x}Eu_xCrO_3$ ($x = 0.0-1.0$) samples.

The x dependence of T_N and T_{SR} is plotted in **Fig. 3-6(c)**, which shows the substantial decrease in T_N values from 224.1 K ($x = 0.10$) to 182.5 K ($x = 1.0$). On the other hand, the T_{SR} first increases to 41.3 K ($x = 0.5$) and then decreases to 13.3 K ($x = 0.9$) such that no spin-reorientation is observed for the $x = 1.0$ composition. Present $x = 1.0$ sample is found to be

in agreement with the report [12]. It is expected that the contraction of lattice parameters causes a sufficient decrease in T_N values. However, the changes observed in T_{SR} can be related to the non-uniform structural behavior through Eu substitution. By the help of the neutron diffraction of $NdCrO_3$, it is known that the Cr^{3+} spin system exhibits the weak FM phase (Γ_2) below T_N and AFM phase (Γ_1) below T_{SR} [16]. As observed from the x variation of T_{SR} in **Fig. 3-6(c)**, the lower Eu substitution ($x \leq 0.50$) slightly increases the T_{SR} value because of the similar magnetic phases as the parent compound. However, the decrease of the AFM phase up to $x = 0.90$ results the sharp decrease in T_{SR} . The samples with higher Eu content possibly contain a mixed weak FM phase (Γ_2 and Γ_4) below T_N and the AFM phase below T_{SR} . We expect the strong interaction between Nd^{3+}/Eu^{3+} and Cr^{3+} moments resulting in spin-reorientations up to 90 % Eu substituted samples. However, the presence of only weak FM phase (Γ_4) for $x = 1.0$ compound [15] drastically increases magnetization and vanishes T_{SR} . It is in accordance with the $EuCrO_3$ report showing no spin-reorientation transition [124].

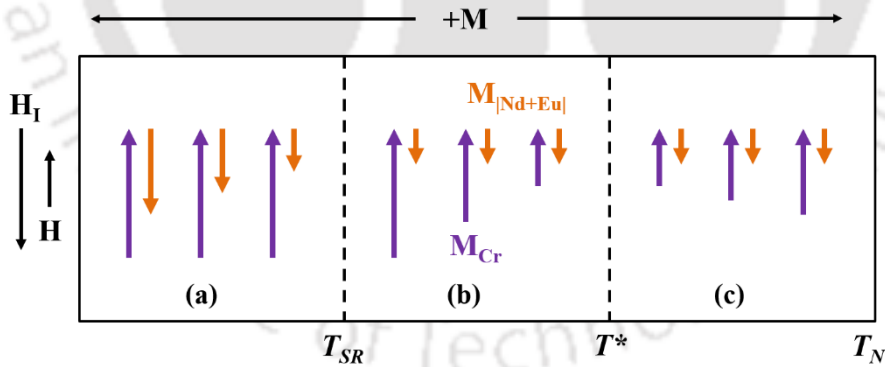


Fig. 3-7 Schematic diagram of the moment arrangements in the temperature regions (a) $T < T_{SR}$ (b) $T_{SR} < T < T^*$, and (c) $T^* < T < T_N$, where M_{Cr} and $M_{[Nd+Eu]}$ indicate the FM component of Cr^{3+} and PM moments of Nd^{3+}/Eu^{3+} ions respectively.

The FC M - T curve in **Fig. 3-6(a)** shows that as we decrease T , first magnetization (for $x < 0.5$) increases to its maximum at $T \sim 170$ K and then drops to give a minimum around T^*

~ 90 K, below which it rises sharply to a maximum at $T \sim 39$ K. The magnetic behavior of the $Nd_{1-x}Eu_xCrO_3$ system below T_N can be explained in terms of the Cr sublattice and $|Nd+Eu|$ sublattice, such that their moment aligns opposite but not exactly equal in magnitude to fully compensate each other, giving the minimum magnetization at T^* . The canting of magnetically ordered Cr^{3+} ions results in a weak ferromagnetic moment (M_{Cr}), whereas the paramagnetic moment of Nd^{3+}/Eu^{3+} ions ($M_{|Nd+Eu|}$) experiences a negative internal field (H_I) due to the AFM ordered Cr^{3+} ions. The schematic diagram in **Fig. 3-7** presents the coupling scheme of weak ferromagnetic Cr^{3+} moments and paramagnetic Nd^{3+}/Eu^{3+} moments. We observed that the M_{Cr} due to canting of Cr^{3+} spins depends on the chemical substitution. The strong Nd/Eu-Cr exchange interaction results in spin-reorientation for the samples. The increase of the M_{Cr} minimizes the reorientation of Cr^{3+} spins after $x = 0.7$ compound and finally vanishes the reorientation for $x = 1.0$ composition showing the saturation of magnetization at lower temperatures.

3.3.4.2 Exchange constants

At sufficiently high temperatures ($T > T_N$), the magnetic susceptibility (χ) follows a Curie-Weiss law according to,

$$\chi_{mol} = \frac{C}{(T - \Theta)} = \frac{N_A \mu_{eff}^2}{3k_B(T - \Theta)} \quad (3.5)$$

where C is the Curie constant, can be written in terms of the Avogadro number N_A , the Boltzmann constant k_B , the effective magnetic moment μ_{eff} , and Θ is the Curie temperature. The following relation is used to calculate effective magnetic moment values for the samples,

$$\mu_{eff}^{Th} = \sqrt{[(1 - x) \mu_{Nd}^2 + x \mu_{Eu}^2 + \mu_{Cr}^2]} \quad (3.6)$$

where μ_{Nd} , μ_{Eu} , and μ_{Cr} indicate the spin magnetic moments of Nd^{3+} , Eu^{3+} , and Cr^{3+} ions, respectively. The Curie Weiss fitting using Eq.(3.5) results in the experimental value of effective moments $\mu_{eff} \sim 5.73 \mu_B$ ($x = 0.0$) to $6.21 \mu_B$ ($x = 1.0$). These values are relatively higher than calculated μ_{eff} values varying from $5.29 \mu_B$ ($x = 0.0$) to $5.15 \mu_B$ ($x = 1.0$). The μ_{eff} values show the Cr^{3+} in a high spin state ($\mu_{Cr} = 3.87 \mu_B$). With substituting less magnetic Eu^{3+} ions ($\mu_{Eu} = 3.4 \mu_B$) on Nd-site ($\mu_{Nd} = 3.62 \mu_B$) the decrease in the μ_{eff} values was expected. However, the increase in μ_{eff} values suggests the Van Vleck-contributions arising due to Eu^{3+} moments [14]. The increase of negative Curie-Weiss temperature $\Theta \sim -215$ K ($x = 0.0$) to -466 K ($x = 1.0$) samples shows enhanced antiferromagnetic interactions. Further, the considerable difference (in magnitude) of Néel temperature T_N and Curie-

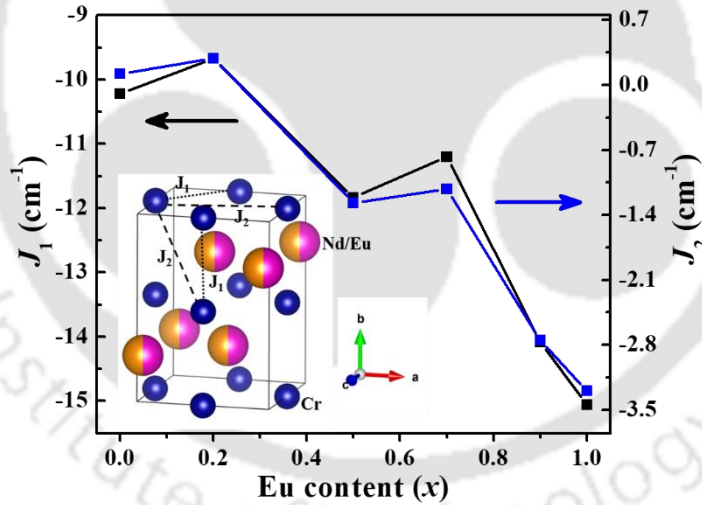


Fig. 3-8 The effect of Eu content on the exchange constants J_1 and J_2 for the $Nd_{1-x}Eu_xCrO_3$ ($x = 0.0$ to 1.0) samples. Inset shows the representation of J_1 and J_2 in the unit cell of the $x = 0.5$ sample.

Weiss temperature Θ provides the two exchange constants J_1 and J_2 for the $Nd_{1-x}Eu_xCrO_3$ system described by molecular field relations [138].

$$J_1 = \frac{k_B(\Theta - T_N)}{8S(S+1)} \text{ cm}^{-1} \quad (3.7)$$

$$J_2 = \frac{k_B(\theta + T_N)}{16S(S+1)} \text{ cm}^{-1} \quad (3.8)$$

where, $S = 3/2$ for Cr^{3+} spins, J_1 and J_2 stand for the mean of two exchange constants along the $(a \pm c)$ and b axes for six nearest neighbors (NN), and the mean of three exchange constants for twelve next nearest neighbors (NNN) Cr ions, respectively, as demonstrated in the inset of **Fig. 3-8**. The x dependence of exchange constants in **Fig. 3-8** shows the maximum value of $J_1 = -15.06 \text{ cm}^{-1}$ and $J_2 = -3.29 \text{ cm}^{-1}$ for the $x = 1.0$ compound, which is higher than the exchange constants of $YCrO_3$ [107]. It is noticed that the trend of J_1 and J_2 changes at $x = 0.5$, suggesting the modification of the $Cr^{3+}-Cr^{3+}$ interaction. As octahedral tilting of CrO_6 (explained in **Fig. 3-2(b)**) brings the two facing O^{2-} ions closer, which helps the electron hopping via $Cr^{3+}-O^{2-}-O^{2-}-Cr^{3+}$ path between NN and NNN Cr^{3+} ions for such exchange interactions.

3.3.4.3 Exchange bias

Magnetization as the function of the applied field of ± 90 kOe at $T = 100$ K ($T_{SR} < T < T_N$) after cooling from the paramagnetic state with the cooling field of +10 kOe for the $Nd_{1-x}Eu_xCrO_3$ ($x = 0.0-1.0$) compositions is displayed in **Fig. 3-9(a)**. From the graph, we found a significant increase of coercive field $H_C \sim 12.6$ kOe and remanent magnetization $M_R \sim 25.3 \times 10^{-3} \mu_B/\text{f.u.}$ for $x = 1.0$ sample. This indicates the increase of weak ferromagnetic contributions (in accordance with observed $M-T$ behavior) for higher doped $Nd_{1-x}Eu_xCrO_3$ samples. Furthermore, the shift of the $M-H$ loops toward the negative applied field axis at $T = 100$ K in **Fig. 3-9(b)** is the fingerprint of the EB effect in the $Nd_{1-x}Eu_xCrO_3$ system. The shift is due to genuine EB and not corresponding to any minor loop [139] is confirmed

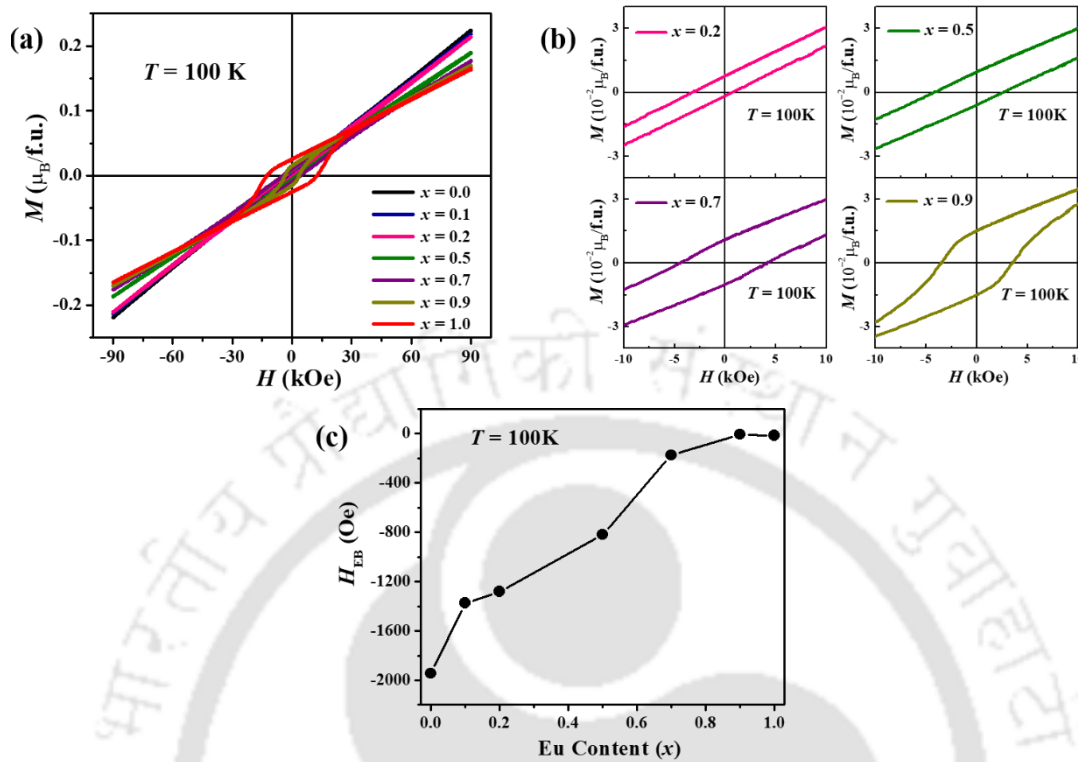


Fig. 3-9 (a) Field dependence of magnetization (M - H) loops at 100 K of the $Nd_{1-x}Eu_xCrO_3$ ($x = 0.0-1.0$) system (b) the enlarged portions of exchange biased loop of $x = 0.2-0.9$ samples and (c) The EB field H_{EB} as the function of Eu content at $T = 100$ K of the $Nd_{1-x}Eu_xCrO_3$ ($x = 0.0-1.0$) samples.

by the M - H measurements with the maximum field (± 90 kOe) and closed loops up to +50 kOe. We know that the EB effect arises due to the exchange anisotropy at the interface of AFM and FM moments. This additional anisotropy for the asymmetric M - H loop can be given by the EB field $H_{EB} = (H_+ + H_-)/2$ and coercive field $H_C = (H_+ - H_-)/2$, here H_+ and H_- are the ascending and descending branch field values at $M = 0$ for the hysteresis loop. Initially, such negative EB at 30 K for low cooling fields was reported in isostructural $NdMnO_3$ [71]. Also, the only negative H_{EB} has obtained for $Dy_{1-x}Nd_xCrO_3$ shows the EB effect without any magnetic reversal [118]. The dependence of H_{EB} on Eu content at 100 K for the $x = 0.0-1.0$ samples are presented in **Fig. 3-9(c)**, which shows the H_{EB} decreases

with increasing x and vanishes for $x > 0.5$ samples. The competing AFM interaction between the weak FM component of canted Cr^{3+} moments (M_{Cr}) and the paramagnetic moment of Nd^{3+}/Eu^{3+} ions ($M_{Nd/Eu}$) below T_N are responsible for the EB effect. With increasing Eu substitution, the decrease of EB field at 100 K is observed. It is in accordance with $EuCrO_3$ report showing no EB effect around 100 K [140]. Thus, the presence of mixed magnetic phases and lattice distortions for higher Eu substituted samples influence the Cr^{3+} spin canting such that the exchange anisotropy due to AFM coupled M_{Cr} and $M_{Nd/Eu}$ decreases, which leads to the decrease of EB field for higher Eu substituted samples.

Therefore, we have discussed the temperature dependence of the EB effect for $x = 0.1$ and 0.2 compounds in detail. The temperature variation of EB field $H_{EB}(T)$ along with the coercive field $H_C(T)$ are shown in **Fig. 3-10**. We obtain the $H_{EB} \sim -209$ Oe ($x = 0.10$) and -319 Oe ($x = 0.20$) around 5 K that reaches its minimum value across T_{SR} . After that, the $H_{EB}(T)$ starts increasing sharply with increasing T and attains the maximum value of EB field $H_{EB} \sim -1297$ Oe ($x = 0.10$) and -1322 Oe ($x = 0.20$) at $T^* \sim 90$ K and 80 K, respectively. A dissimilar trend is observed for $H_C(T)$, showing maximum value across T_{SR} and the minima around T^* . To analyze the T window of having maximum $H_{EB}(T)$ and the concurrent minima of $H_C(T)$, the field ratio H_{EB}/H_C , as the function of T is plotted in **Fig. 3-10**. The quantity H_{EB}/H_C is the normalized H_{EB} with respect to H_C that can reduce the complications due to the consecutive changes in H_C [141]. The $|H_{EB}/H_C|$ value is found to be high ~ 1.3 at T^* , indicating that the large H_C is not always necessary for getting the large H_{EB} value [142]. This result is different from the general observations where the large EB effect was involved with the large coercivity, and the value of H_{EB}/H_C is usually $\ll 1$ [7].

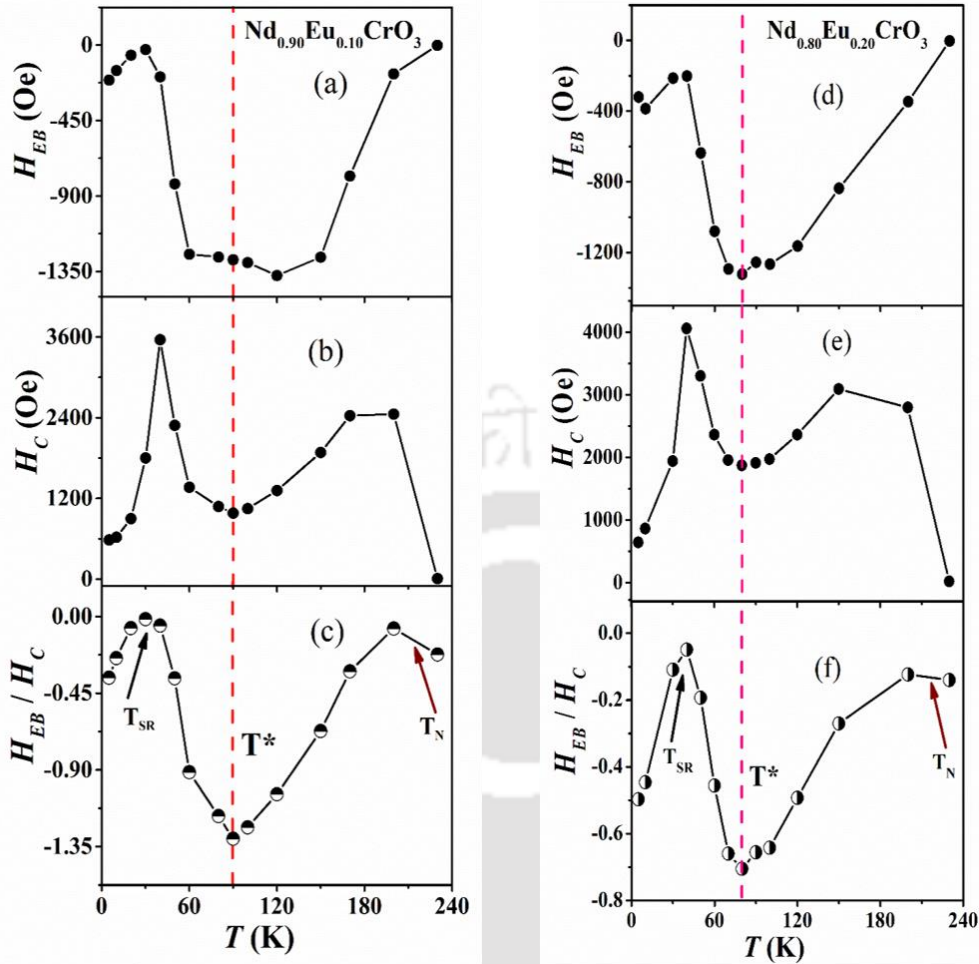


Fig. 3-10 Temperature dependence of (a) EB field $H_{EB}(T)$, (b) coercive field $H_C(T)$, and (c) the ratio of $H_{EB}(T)$ and $H_C(T)$ extracted from 10 kOe field cooled M - H loops of $Nd_{1-x}Eu_xCrO_3$ ($x = 0.10$ and 0.20) sample, demonstrating the T_{SR} , T^* and T_N .

From the enlarged portions in **Fig. 3-9(b)**, we observe that there is not only a horizontal shift of exchange-biased M - H loop but also a vertical shift at $H = 0$ Oe. Therefore, the EB characteristics can also be defined using the quantities remanence asymmetry $M_{EB} = (M_+ + M_-)/2$ and magnetic coercivity $M_C = (M_+ - M_-)/2$, where M_+ and M_- are the remanent magnetizations i.e. magnetization values at $H = 0$ Oe for descending and ascending branches of the loop, respectively. The temperature dependence of the M_{EB} and M_C are plotted in **Fig. 3-11**. The nature of $M_{EB}(T)$ and $M_C(T)$ is similar to $H_{EB}(T)$ and $H_C(T)$, which is expected from the equivalence between M_{EB} and H_{EB} [59]. The quantity

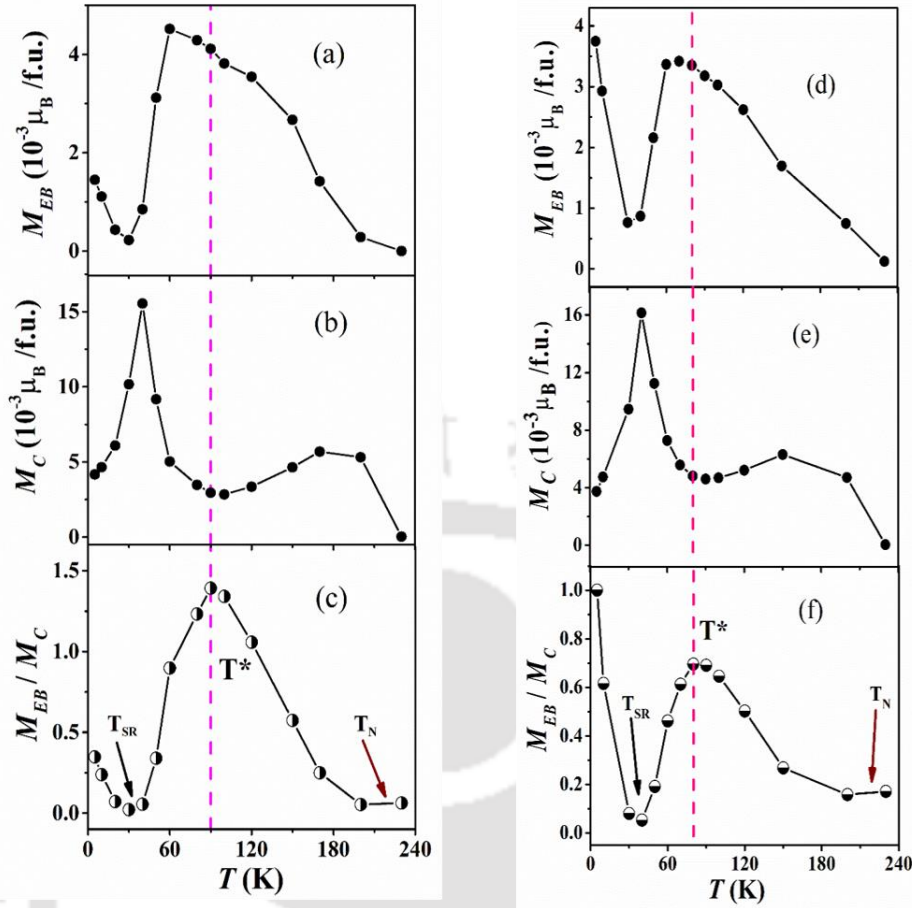


Fig. 3-11 Temperature dependence of (a) remanence asymmetry $M_{EB}(T)$ (b) magnetic coercivity $M_C(T)$ and (c) the ratio of $M_{EB}(T)$ and $M_C(T)$ extracted from 10 kOe field cooled M - H loops of $Nd_{1-x}Eu_xCrO_3$ ($x = 0.10$ and 0.20) sample.

$M_{EB}(T)$ as the measure of EB effect has been reported recently for the $YbCrO_3$ [74] and $LuFe_{0.50}Cr_{0.50}O_3$ [9]. The ratio M_{EB}/M_C as the function of temperature displayed the highest ratio value ~ 1.39 at $T^* \sim 90$ K, similar to the H_{EB}/H_C , which confirms that the EB effect is occurring with the low coercivity. The EB effect from the shift of field cooled M - H loops along the H - and M - axis for $Nd_{1-x}Eu_xCrO_3$ ($x = 0.10$ and 0.20) system suggests one more magnetic phase across T^* lies between the T_N and T_{SR} and consistent with the schematic spin-diagram. However, it would need further neutron studies to be confirmed. Therefore, to find the physical significance of T^* , the temperature-dependent Raman spectroscopy and low-temperature power XRD measurements are carried out in the upcoming section.

3.3.5 Structural properties at low temperatures

3.3.5.1 Temperature-dependent Raman spectroscopy

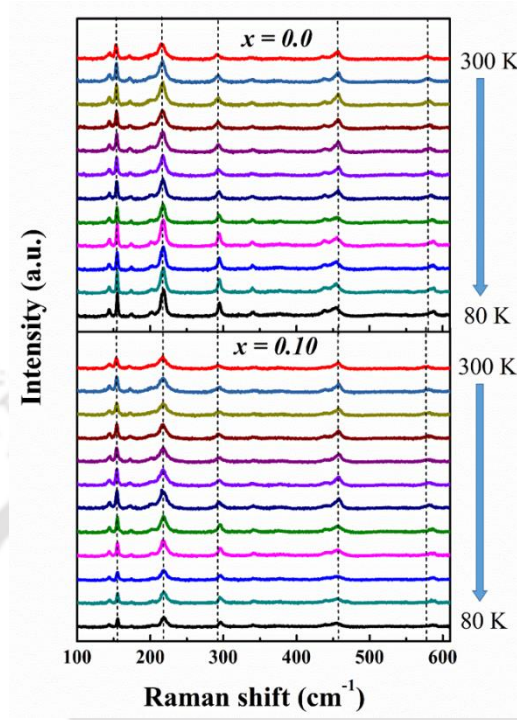


Fig. 3-12 Raman spectra of $Nd_{1-x}Eu_xCrO_3$ ($x = 0.0$ and 0.10) samples from 100 to 600 cm^{-1} in the temperature range of 80 to 300 K.

Moreover, the study of low-temperature Raman spectra for $x < 0.5$ sample is also involved and the temperature-dependent Raman spectra are recorded in the range of 80 - 300 K. The Raman spectra at a few temperatures for $x = 0.0$, and 0.10 samples are shown in **Fig. 3-12**. We observed that no new phonon modes are emerging in the temperature range of 80 - 300 K, ruling out the occurrence of any structural phase transitions. Therefore, the temperature dependence of line shape parameters of $x = 0.0$ - 0.10 samples has investigated to understand the subtle structural distortions in terms of the interaction between lattice and spin degrees of freedom such as spin-phonon coupling. The wavenumber of a phonon mode as a function of temperature in magnetic materials is given by Granado *et al.*[11]

$$\Delta\omega(T) = (\Delta\omega)_{latt} + (\Delta\omega)_{ren} + (\Delta\omega)_{anh} + (\Delta\omega)_{s-ph} \quad (3.9)$$

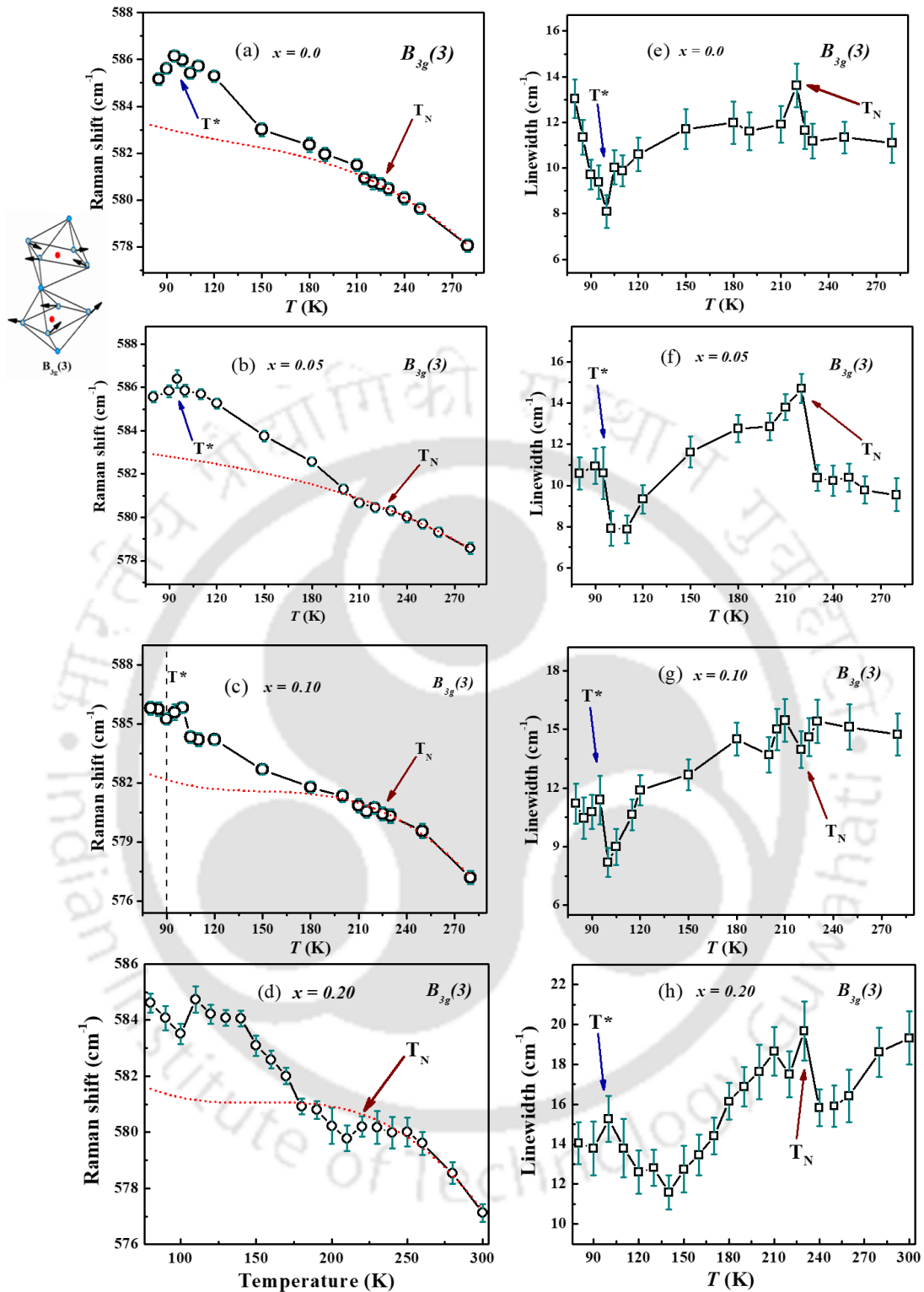


Fig. 3-13 (a)-(d) Temperature dependence of antistretching mode $B_{3g}(3)$ frequencies and (e)-(h) the corresponding linewidths of $Nd_{1-x}Eu_xCrO_3$, ($x = 0.0-0.20$) samples. The red dotted lines show the fitted curves for anharmonic contribution, according to Eq. (3.10), and solid black lines guided to the eye.

where, $(\Delta\omega)_{latt}$ is the lattice expansion due to anharmonicity or contraction due to magnetostriction. The term $(\Delta\omega)_{ren}$ gives the renormalization of the electronic states that may occur near the spin ordering temperature. The $(\Delta\omega)_{anh}$ represent anharmonic frequency shift at constant volume known as the intrinsic anharmonic effect. The last term $(\Delta\omega)_{s-ph}$ is the spin-phonon effect, caused by the modulation of the exchange integral by lattice vibrations. The first term is attributed to the isotropic change in volume, which is not applicable here. Also, the second term can be neglected in case of low carrier concentration. Balkanski *et al.* have been proposed the purely anharmonic contribution to the temperature-dependent phonon frequency of Raman modes can be understood by the following relation [143],

$$\omega_{anh}(T) = \omega(0) + A \left[1 + \frac{2}{e^x - 1} \right] + B \left[1 + \frac{3}{e^y - 1} + \frac{3}{(e^y - 1)^2} \right], \quad (3.10)$$

where, $x = \frac{\hbar\omega(0)}{2k_B T}$, $y = \frac{\hbar\omega(0)}{3k_B T}$ and $\omega(0)$, A, and B are adjustable parameters optimized for the fitting of the experimental data above T_N .

The temperature evolution of $B_{3g}(3)$ mode of the $Nd_{1-x}Eu_xCrO_3$, $x = 0.0-0.20$ samples are shown in **Fig. 3-13**. The antisymmetric stretching mode shows a clear deviation from anharmonicity (red dotted line) given by eq.(3.10) below T_N , indicating there might be another factor apart from anharmonicity giving hardening of the mode for the samples displayed in **Fig. 3-13(a)-(d)**. Similar behavior of anti stretching mode is also observed in $GdCrO_3$ [13] and $HoCrO_3$ [109]. Such hardening may contribute to the magnetostriction caused by the changes in the unit cell volume. Therefore, the temperature dependence of the corresponding linewidths is plotted in **Fig. 3-13(e)-(h)**. The linewidths are related to phonon lifetime and unaffected by magnetostriction. The anomaly observed in linewidths

below T_N confirms spin-phonon coupling in $Nd_{1-x}Eu_xCrO_3$ ($x = 0.0-0.20$) systems, which can be explained by different magnetic interactions of Nd^{3+}/Eu^{3+} and Cr^{3+} moments.

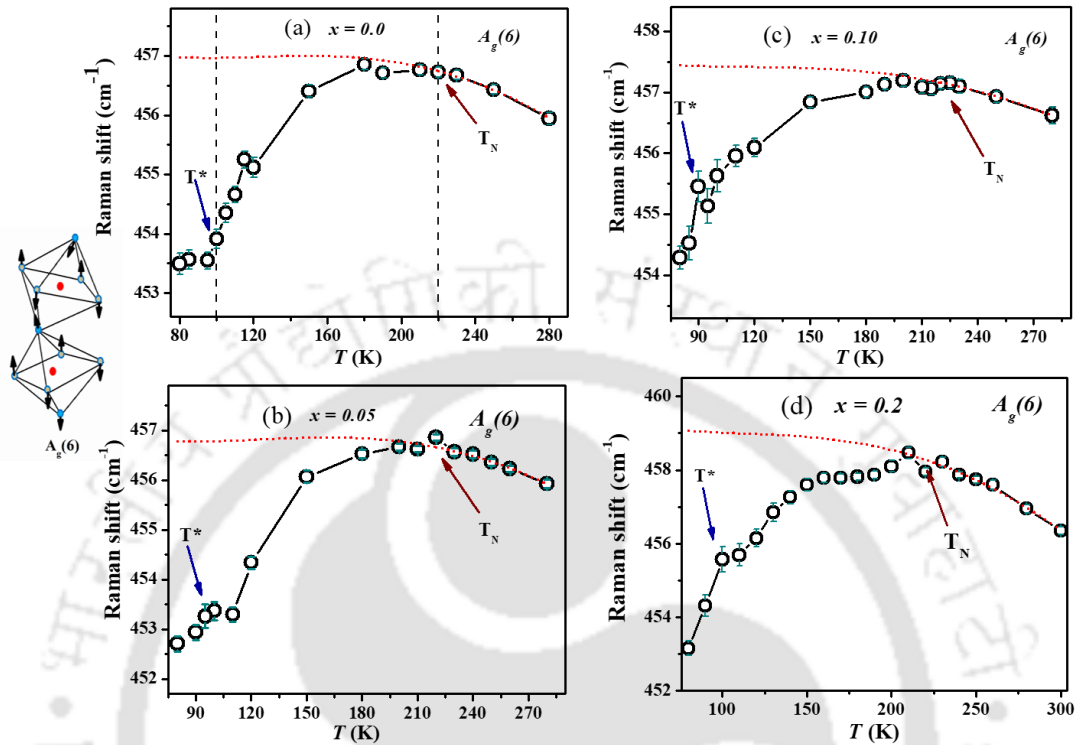


Fig. 3-14 (a)-(d) The effect of temperature on $A_g(6)$, the bending mode frequencies $Nd_{1-x}Eu_xCrO_3$, ($x = 0.0-0.20$) samples. The red dotted lines are fitted curves for anharmonic contribution, according to Eq. (3.10), and solid black lines guided to the eye.

The temperature-dependent phonon frequencies of out of phase bending mode $A_g(6)$ are displayed in **Fig. 3-14(a)-(d)**. The anomalous softening of mode frequencies below T_N is observed for $x = 0.0-0.20$ samples, showing a clear spin-phonon coupling in these systems. The softening of bending mode has been initially observed in isostructural $RMnO_3$ [10] and magnetic $RCrO_3$ ($R = Gd, Sm$) [12]. The softening could be associated with the weak ferromagnetism due to the canting of Cr^{3+} spins resulting in the strong spin-phonon coupling. The mode $B_{3g}(1)$ corresponds to pure R -ion (Nd^{3+}/Eu^{3+}) vibration. The hardening of the modes and the anomaly in the linewidths are shown in **Fig. 3-15(a)-(h)**.

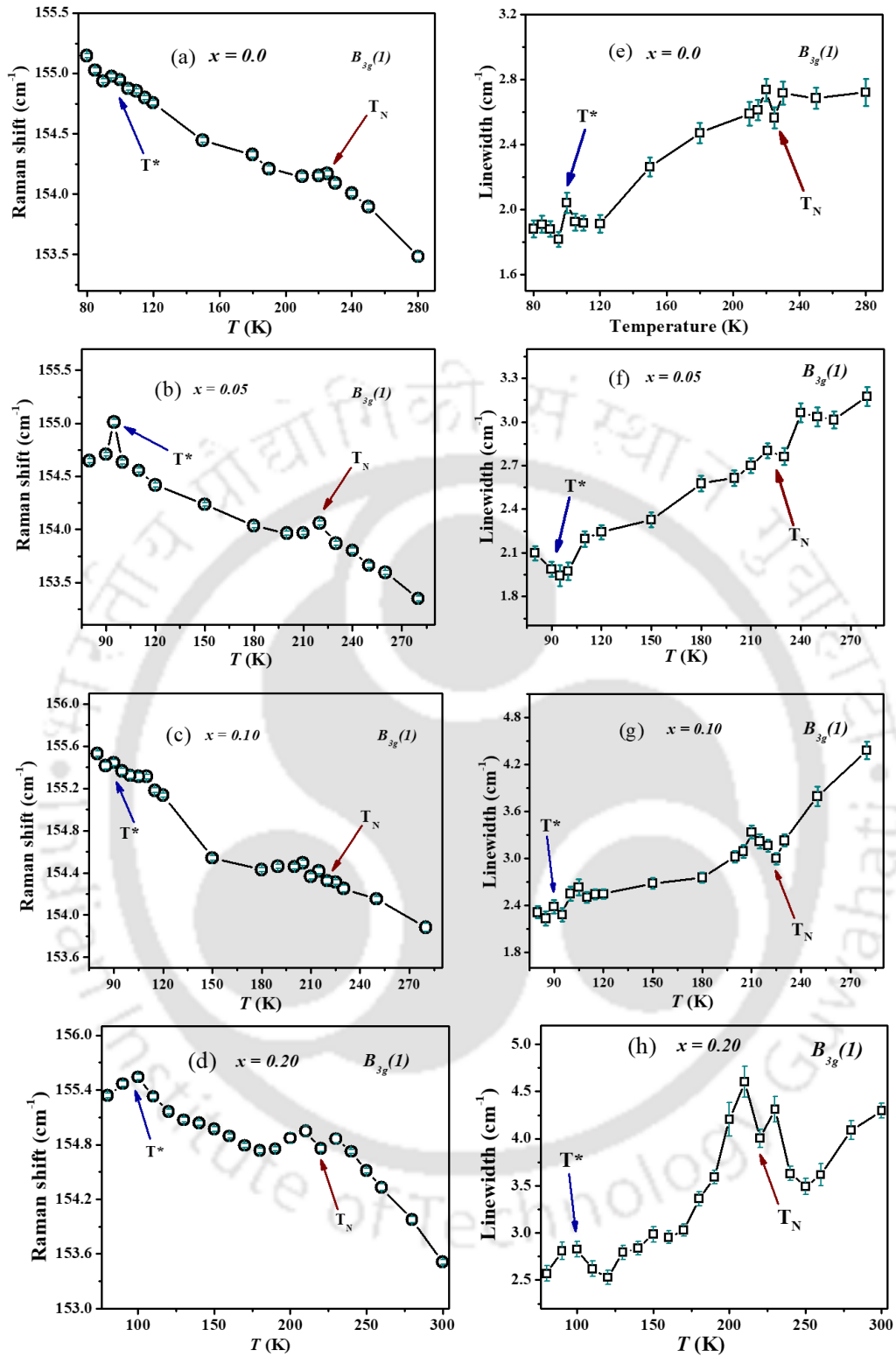


Fig. 3-15 Temperature dependence of phonon frequencies and (e)-(h) the linewidths of $B_{3g}(1)$ mode involving the Nd^{3+}/Eu^{3+} ion vibrations of $Nd_{1-x}Eu_xCrO_3$, ($x = 0.0-0.20$) samples. Solid black lines guided to the eye.

Bhadram et al. have proposed the displacement of magnetic R^{3+} ions can induce the spin-phonon coupling for low-frequency mode [12]. Thus, the possible movement of Nd^{3+}/Eu^{3+} ions also contributes to the spin-phonon coupling in $Nd_{1-x}Eu_xCrO_3$ ($x = 0.0-0.20$) system. Since the phonon coupling to $Cr^{3+}-Cr^{3+}$ and $Nd^{3+}-Cr^{3+}$ magnetic exchange interactions below T_N induces strong spin-phonon coupling. Thus the modification of these exchange due higher Eu substitution decrease the spin-phonon coupling beyond the $x = 0.20$ system. This is in accordance with reports on $EuCrO_3$, which shows no spin-phonon coupling [12]. In addition to the spin-phonon coupling below the AFM ordering temperature (T_N), we can notice the existence of one more anomaly near T^* in the mode frequencies as well as linewidths. It indicates that with increasing Eu content, the nature of spin-phonon is changing in the vicinity of T^* , which is well below T_N .

3.3.5.2 Spin-induced lattice modulations

The experimentally observed spin-phonon coupling from the temperature-dependent phonon modes and linewidths suggests the behavior of these modes sharply changes at lower temperatures. Therefore, the crystal structure of the $x = 0.0$ system is stimulated with the experimental lattice constants. The lattice dynamics calculation (DFPT) is employed to relax the internal atomic positions and generate the theoretical Raman modes. In **Fig. 3-16(a)-(b)**, the effect of magnetic ordering on the phonon frequencies is predicted for the modes related to anti stretching CrO_6 octahedra $B_{3g}(3)$ and Nd^{3+}/Eu^{3+} ion displacement $B_{3g}(1)$ for $x = 0.0$ sample at lower temperatures. The phonon modes show the first anomaly for magnetically ordered phase below T_N , afterward, the phonon frequencies sharply decrease to give minima across $T^* \sim 100$ K, which further confirms the involvement of strong spin-phonon coupling in the vicinity of T_N and T^* as discussed in **Fig. 3-13** and **Fig. 3-15**.

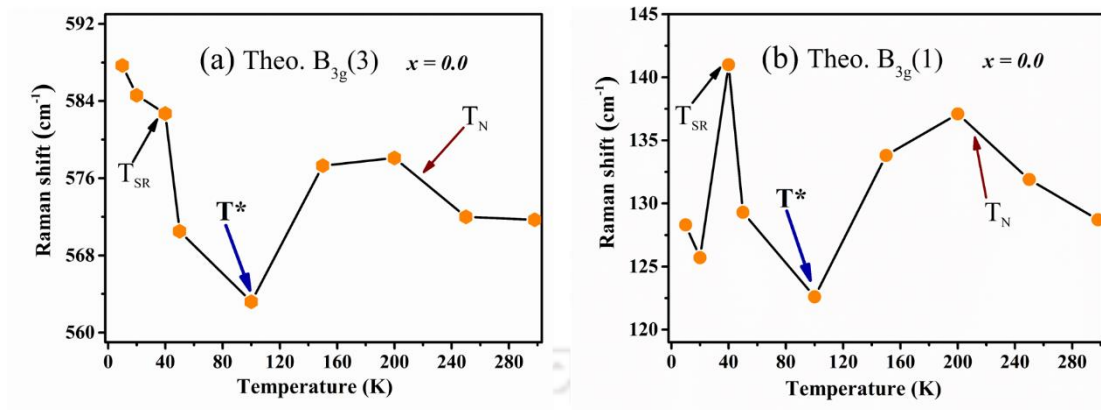


Fig. 3-16 Theoretical temperature evolution of (a) $B_{3g}(3)$ and (b) $B_{3g}(1)$ mode frequencies of $Nd_{1-x}Eu_xCrO_3$ ($x = 0.0$) sample, showing the anomaly across the transitions $T_{SR} \sim 37$ K, $T^* \sim 100$ K and $T_N \sim 225$ K.

With decreasing temperature, the increase in phonon frequencies results in the anomaly corresponding to the spin-reorientation transition T_{SR} . Thus, the lattice dynamics calculations allow us to analyze the phonon-mediated magnetic interaction not only at T_N and T^* but also at T_{SR} .

We have searched some of the studies for the possible origin of the additional phonon anomaly. In $YFe_{1-x}Mn_xO_3$, the magnetodielectric effect is found at T_{SR} , and T_N with the ferroelectric ordering at T_C has related to the spin-phonon coupling [144]. Also, Indra *et al.*[18] have reported the ferroelectricity at $T_C \sim 88$ K for $NdCrO_3$ using a synchrotron X-ray diffraction and dielectric measurements. In $SmCrO_3$ and $GdCrO_3$, the ferroelectricity exhibits well below T_N due to local symmetry breaking [108][13]. Therefore, it is possible that the anomaly around T^* observed in our Raman results may correspond to the *FE* transitions across T^* in the $Nd_{1-x}Eu_xCrO_3$ system.

The magnetic correlations of the phonon anomaly at T^* are possible from the nature of the *M-T* curve and the negative *EB*, showing the minima of magnetization and the high values of H_{EB}/H_C and M_{EB}/M_C across T^* , as discussed in **Fig. 3-6** and **Fig. 3-10**. We can describe

the negative EB in $Nd_{1-x}Eu_xCrO_3$ ($x = 0.10$) system by taking into account the exchange anisotropy due to canted Cr^{3+} ions resulting in the weak ferromagnetic moment (M_{Cr}) and the paramagnetic moment of Nd^{3+}/Eu^{3+} ions ($M_{|Nd+Eu|}$) below T_N . As we apply the external field, M_{Cr} aligns in the direction of the applied field, and $M_{|Nd+Eu|}$ becomes antiparallel to M_{Cr} but along the direction of the negative internal field H_I as shown in the schematic diagram (**Fig. 3-7**). For the temperature $T^* < T < T_N$, the antiferromagnetically coupled Cr^{3+} and Nd^{3+}/Eu^{3+} ions are organized in a way that gives a net positive magnetization due to the dominance of M_{Cr} over $M_{|Nd+Eu|}$. To bring the magnetization towards zero, an extra negative applied field is needed, which shifts the loop to the negative field axis, resulting in negative EB . The neutron diffraction studies on parent $NdCrO_3$ have disclosed a sharp transition from $\Gamma_2 (F_x, C_y, G_z)$ phase to $\Gamma_1 (A_x, G_y, C_z)$ phase at T_{SR} , and the ordering of Nd^{3+} moments at $T < T_{SR}$ [16]. Therefore, for the temperature $T_{SR} < T < T^*$, we can expect the high rate of change of Cr^{3+} spin canting angle, which favors the lattice distortions arising from the distortion of CrO_6 octahedra along with Nd^{3+}/Eu^{3+} ion vibrations as discussed in the section of Raman analysis. It can enhance the M_{Cr} but weaken the pinning force introduced by $M_{|Nd+Eu|}$, causing a decrease in EB for this temperature range. At $T \sim T_{SR}$, the system got completely distorted, resulting in nearly zero EB . Whereas for the temperature $T < T_{SR}$, the negative EB starts building up again, attributed to the pinning mechanism of the magnetically ordered $|Nd+Eu|$ and Cr sublattice. Thus, the effect of lattice distortions on the EB effect is found in the $Nd_{1-x}Eu_xCrO_3$ system.

3.3.5.3 Temperature-dependent Powder X-ray diffraction

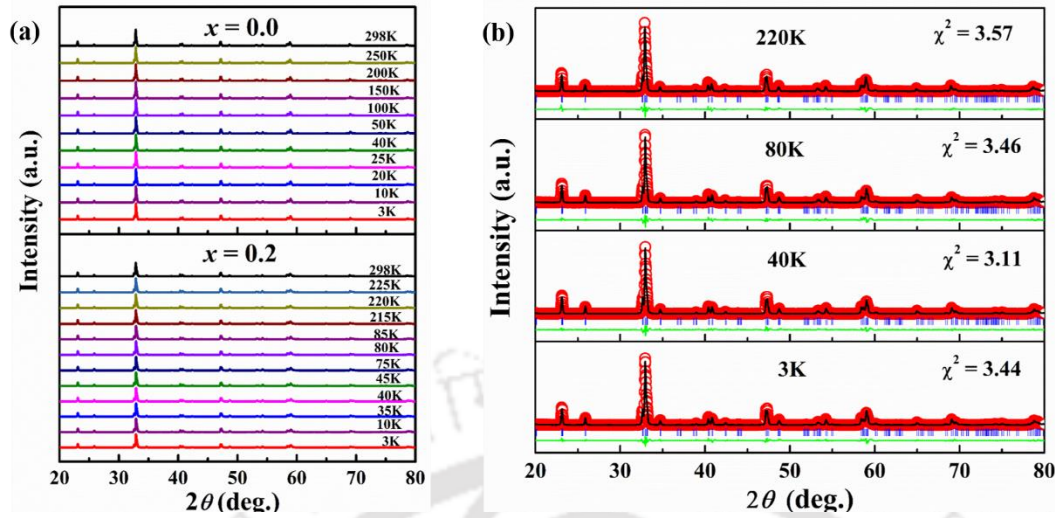


Fig. 3-17 (a) The XRD patterns of $Nd_{1-x}Eu_xCrO_3$ ($x = 0.0$ and 0.2) samples in the 3-300 K temperature range and (b) Rietveld refinement of low-temperature XRD patterns of $x = 0.2$ sample using $Pnma$ space group at selected temperatures.

The structural properties of the $Nd_{1-x}Eu_xCrO_3$ ($x < 0.5$) samples are further probed with the powder XRD in the temperature range of 3-300 K, as depicted in **Fig. 3-17(a)**. No additional reflections were detected in the entire temperature range for $x = 0.0$ and 0.20 samples ruling out any structural phase transition. The Rietveld refinement of XRD patterns of $x = 0.2$ sample at selected temperatures is presented in **Fig. 3-17(b)**. We refine the XRD patterns using the $Pnma$ space group in the entire temperature range with a distribution of Nd/Eu, Cr, O1, and O2 atoms at $4c(x, 0.25, z)$, $4b(0,0, 0.5)$, $4c(x, 0.25, z)$ and $8d(x, y, z)$ sites. In a few rare-earth chromites, the preferred structure is noncentrosymmetric, resulting in the polar phase to elucidate the improper ferroelectricity [36]. Nevertheless, we have opted for a centrosymmetric structure as the $Pnma$ space group can provide the average structural characteristics for the magnetoelastic coupling below magnetic ordering [13]. The temperature dependence of the lattice parameters a , b , and c and the unit cell volume V of the $x = 0.0$ and 0.2 samples are depicted in **Fig. 3-18(a)-(b)**. The lattice parameters decrease with decreasing temperature, but the slight change in slope below T_N is observed. The thermal variation of lattice parameters $b(T)$ and $c(T)$ is similar to the cell volume $V(T)$,

unlike the thermal variation of lattice parameters $a(T)$, for both $x = 0.0$ and 0.2 samples, respectively.

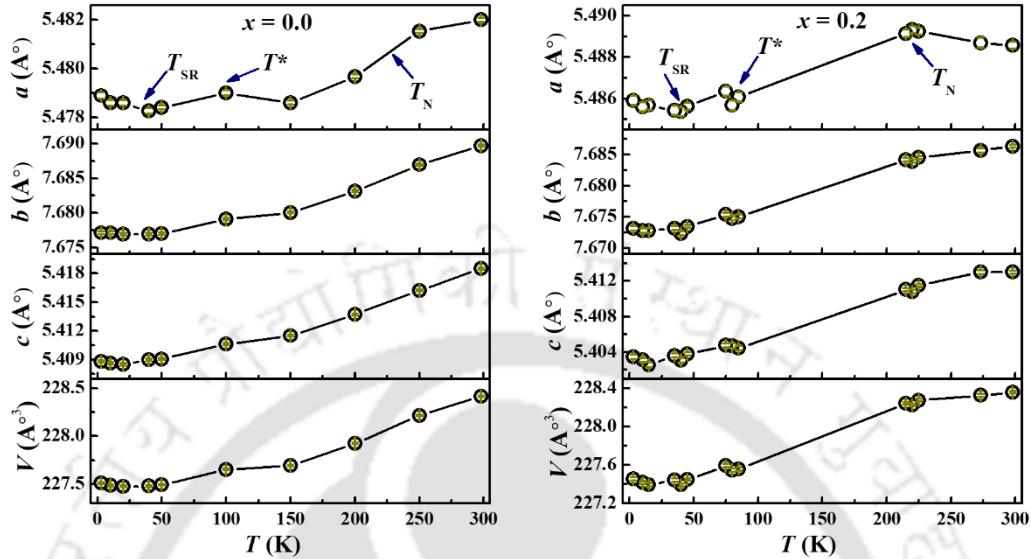


Fig. 3-18 The lattice parameters a , b , c , and lattice volume V in the 3-300 K temperature range for $Nd_{1-x}Eu_xCrO_3$ (a) $x = 0.0$ and (b) $x = 0.2$ compositions.

The deformations of CrO_6 octahedra are also possible as we go down in temperature, therefore, the temperature dependence of the bond lengths Cr-O1, Cr-O2, and the bond angles Cr-O1-Cr, Cr-O2-Cr for $x = 0.0$, and 0.2 systems are displayed in **Fig. 3-19(a)-(h)**, that shows the significant x dependence and anomalies for magnetically ordered phase. In the 3-300 K range, the Cr-O1 and Cr-O2 lengths exhibit enough thermal variation, which increases with x content. The maximum Cr-O1 length variation is about 0.04 \AA for $x = 0.0$ (see **Fig. 3-19(a)**), whereas for $x = 0.2$ sample, its value is about 0.08 \AA (see **Fig. 3-19(e)**). The change in Cr-O2 length ranges from 0.04 \AA ($x = 0.0$) to 0.10 \AA ($x = 0.2$) as shown in **Fig. 3-19(b),(f)**. In general, the anomalous behavior at magnetic transitions T_N and T_{SR} with an additional anomaly at T^* is revealed by either change in slope or sudden steps observed from the temperature dependence of the Cr-O1 and Cr-O2 bond lengths. Further, the thermal variation of the Cr-O1-Cr angle shows that with decreasing T , the angle decreases

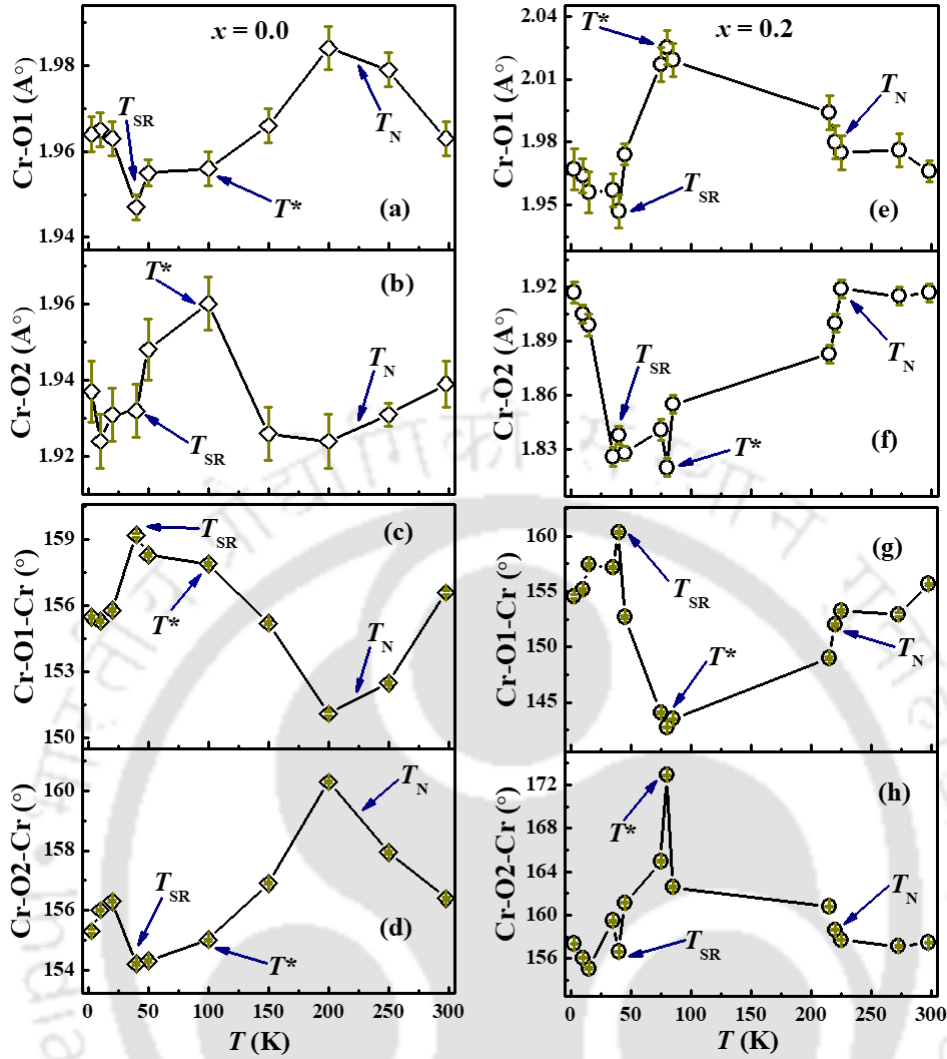


Fig. 3-19 Temperature dependence of the Cr-O1, Cr-O2 bond lengths, and Cr-O1-Cr, Cr-O2-Cr bond angles of $Nd_{1-x}Eu_xCrO_3$ (a)-(d) $x = 0.0$ and (e)-(h) $x = 0.2$ samples.

to give a minimum around T_N with the slope change at T^* attaining the maximum at T_{SR} for $x = 0.0$ (see **Fig. 3-19(c)**). For the $x = 0.2$ sample, the Cr-O1-Cr angle has the anomaly at T_N , which becomes prominent to give minimum at T^* and maximum at T_{SR} (see **Fig. 3-19(g)**). The change in Cr-O1-Cr angle increases with x content, such as its value is about 8° for $x = 0.0$ and 17° for $x = 0.2$ sample. In **Fig. 3-19(d)**, the Cr-O2-Cr angle increases as T decreases, showing a maximum around T_N , reaching the minimum at T_{SR} with the slope change at T^* for $x = 0.0$ sample. Also, the temperature dependence of the Cr-O2-Cr angle

for $x = 0.2$ sample in **Fig. 3-19(h)** clearly shows a peak across T^* with the anomalies at T_N and T_{SR} . The amplitude of the Cr-O2-Cr angle anomaly varies from 6° ($x = 0.0$) up to 18° ($x = 0.2$). The variations observed in the present orthochromite system are relatively higher than in the isostructural orthomanganite [145] and orthoferrites [146].

The rare-earth ions also marked changes in their bonds and positions as the temperature decreased. The Nd/Eu-O1 length variation in **Fig. 3-20(a),(d)** lies between 0.14 \AA ($x = 0.0$) to 0.24 \AA ($x = 0.2$). Similarly, **Fig. 3-20(b),(e)** shows the Nd/Eu-O2 length variation of 0.10 \AA for $x = 0.0$ and 0.27 \AA for $x = 0.2$ sample. We found that the Nd/Eu-O bond length variation is larger than the Cr-O bond length variations. In addition, the Nd

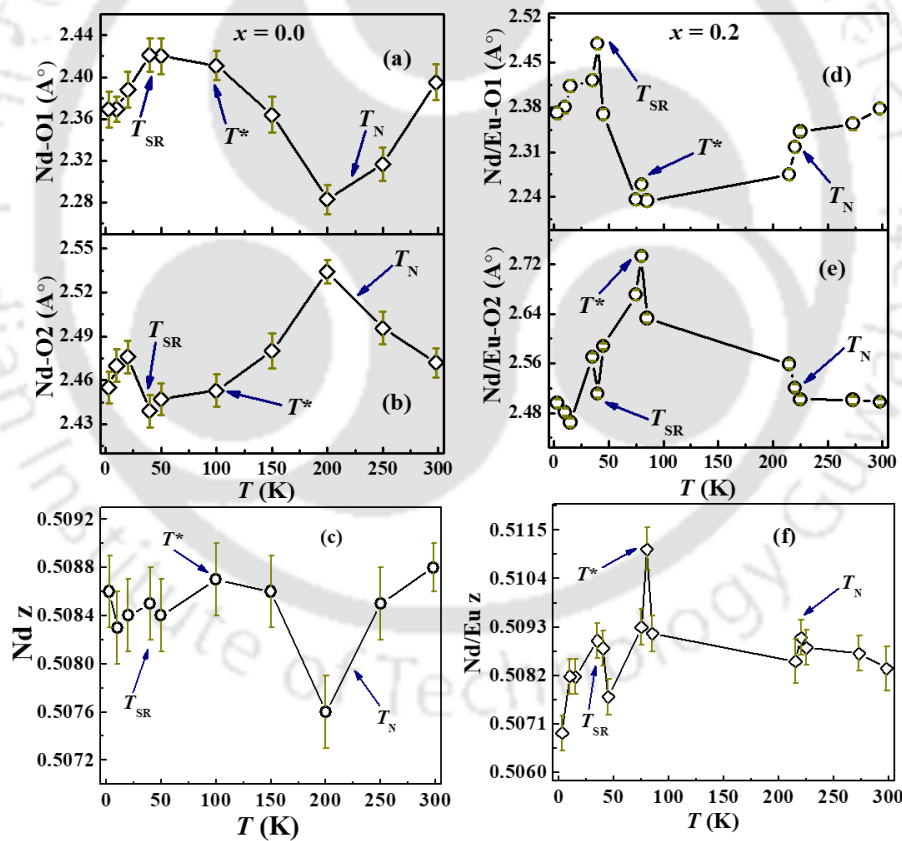


Fig. 3-20 Temperature dependence of (a)-(c) Nd-O1, Nd-O2 bond length and Nd z position for $x = 0.0$ sample (d)-(f) Nd/Eu-O1, Nd/Eu-O2 bond lengths, and Nd/Eu z position for $x = 0.2$ sample.

displacement of 0.001 \AA° ($x = 0.0$) increases to 0.004 \AA° ($x = 0.2$) with Eu substitution as shown in **Fig. 3-20(c),(f)**. Overall, the anomalies mentioned in the temperature dependence of the lattice parameters, CrO_6 octahedral deformations, and Nd/Eu ions position across magnetic transitions confirm that the magnetic order and lattice are strongly coupled, yielding the strong magnetoelastic coupling in the present compounds. However, the large anomaly at T^* seems to have a different origin. For the physical interpretation of T^* , the experimental electron density distribution is investigated using both inverse Fourier transform and maximum entropy methods in the upcoming section.

3.3.5.4 Electron density distribution

The magnetic interactions between the Nd/Eu-Cr and Cr-Cr ions can leave an imprint on the electron density (ED) maps as it undergoes magnetic transitions. Therefore, we attempt to understand the atomic interaction of the $Nd_{1-x}Eu_xCrO_3$ system through the ED maps derived from the Rietveld refinement of LT-XRD patterns. The information of the ED can be retrieved by applying inverse Fourier transform to the structure factors defined by [147],

$$\rho(x, y, z) = \sum_{hkl} \frac{F_{hkl} e^{[-2\pi i(hx+ky+lz)]}}{V} \quad (3.11)$$

where $\rho(x, y, z)$ is the electron scattering density, F_{hkl} is the structure factor, h , k , and l are the Miller indices, and V is the unit cell volume. In a few $RFeO_3$ [148] [149], the ED maps have been used as the tool for probing magnetic interaction and spin-reorientation. However, this is the first attempt to discuss the temperature evolution of the crystal structure and the ED map in orthochromite. Here, **Fig. 3-21** is the plot of the crystal structure and the ED maps for the parent $x = 0.0$ sample. The crystal structure of $x = 0.0$ sample at three temperatures $T = 40 \text{ K}$, $T^* = 100 \text{ K}$, and $T = 200 \text{ K}$, are displayed in **Fig. 3-21(a)-(c)**. The dashed rectangle shows the highlighted part of the structure in **Fig. 3-21(a)-(c)**, where the Nd ions connect the two adjacent layers of the CrO_6 octahedra.

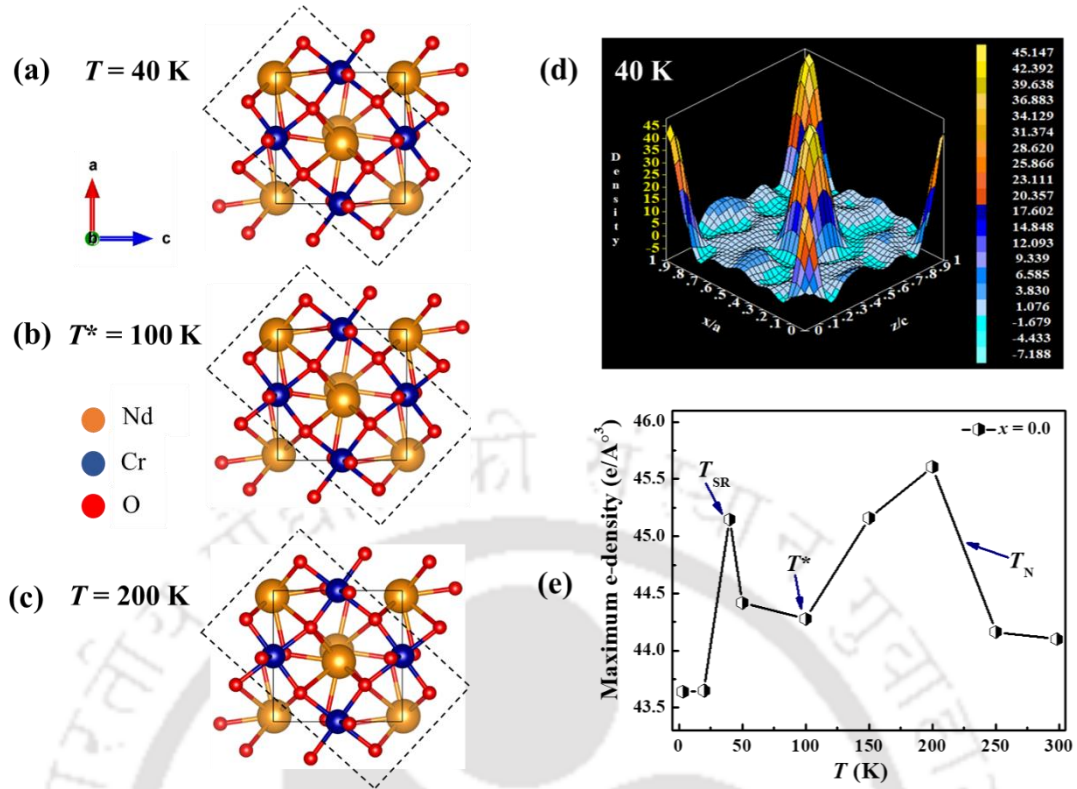


Fig. 3-21 The unit cell of $Nd_{1-x}Eu_xCrO_3$ ($x = 0.0$) sample in the a - c plane for $Pnma$ space group at (a) $T = 40$ K ($\sim T_{SR}$), (b) $T^* = 100$ K, (c) $T = 200$ K ($T < T_N$) and (d) the 3D-ED maps in the xz plane, y -intercept = 0.75 at $T = 40$ K (e) the maximum of ED as the function of temperature of $x = 0.0$ sample.

It is important to note that the orientation of this highlighted structure is invariant for all three temperatures. The 3D map of the ED for the $x = 0.0$ sample depicted in **Fig. 3-21(d)** shows the peaks corresponding to the maximum ED ~ 45.14 $e/\text{\AA}^3$ at 40 K arising due to Nd ions. This maximum of ED obtained from such ED maps at different temperatures is plotted in **Fig. 3-21(e)**. The temperature variations of this maximum of ED show non-monotonic behavior. The earlier observed values of T_{SR} , T^* and T_N derived from the temperature-dependent magnetization and XRD measurements are marked in **Fig. 3-21(e)**. We find definitely that any change in the magnetic transition/interaction is imprinted on this ED plot.

The crystal structure of $x = 0.2$ sample at $T = 40$ K, $T^* = 80$ K, and $T = 215$ K are shown in **Fig. 3-22(a)-(c)**. Similar to **Fig. 3-21**, we have highlighted the portion where Nd/Eu ions are connected to the adjacent layers of the CrO_6 octahedra. We observe that the orientation of highlighted portion for $T \sim T_{SR}$ and $T \leq T_N$ is the same but different for T^* . This is in contrast with the parent compound, where such reorientation of the highlighted structure is not noticed. The 3D map of ED at 40 K for the $x = 0.2$ sample is illustrated in **Fig. 3-22(d)**. It shows that the Eu substitution on the Nd-site increases the maximum of ED to ~ 52.95 $e/\text{\AA}^3$ compared to that of the parent compound. The temperature dependence of the maximum of the ED for $x = 0.2$ sample plotted in **Fig. 3-22(e)** indicates the clear peaks at T_{SR} and T_N but a sudden jump in the ED values in T^* region.

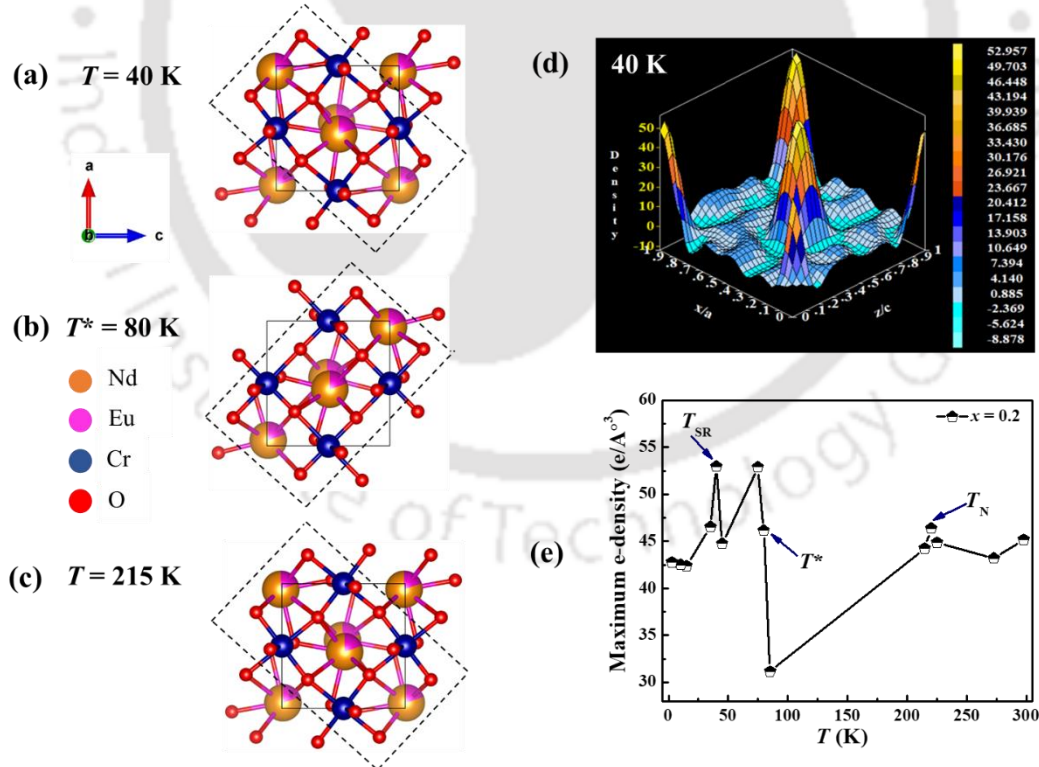


Fig. 3-22 The unit cell of $Nd_{1-x}Eu_xCrO_3$ ($x = 0.2$) sample in the a - c plane for $Pnma$ space group at (a) $T = 40$ K ($\sim T_{SR}$), (b) $T^* = 80$ K, (c) $T = 215$ K ($T \leq T_N$) and (d) the 3D-ED map in the xz plane, y -intercept = 0.75 at $T = 40$ K and (e) the maximum of ED as the function of the temperature of $x = 0.2$ sample.

Therefore, further investigation is carried out by employing more sophisticated XRD charge density analysis methods, such as the Maximum Entropy Method (MEM) [150][151]. The MEM involves the structure factors extracted from the Rietveld refinement and is well known for its accuracy in charge density determination [152]. Hence, the refinements and MEM computations were performed with the help of JANA2006 [153] and Dysnomia programs [154]. The partition of the unit cell into $48 \times 72 \times 48$ pixels was used at each temperature. In **Fig. 3-23(a)-(c)**, we represent the 3D MEM charge density of $x = 0.2$ sample for the $Pnma$ space group using the iso-surface level of $1 \text{ e}/\text{\AA}^3$ from $T = 75$ -85 K. The MEM analysis shows the sudden reorientation of electron density distribution indicated by dashed rectangle.

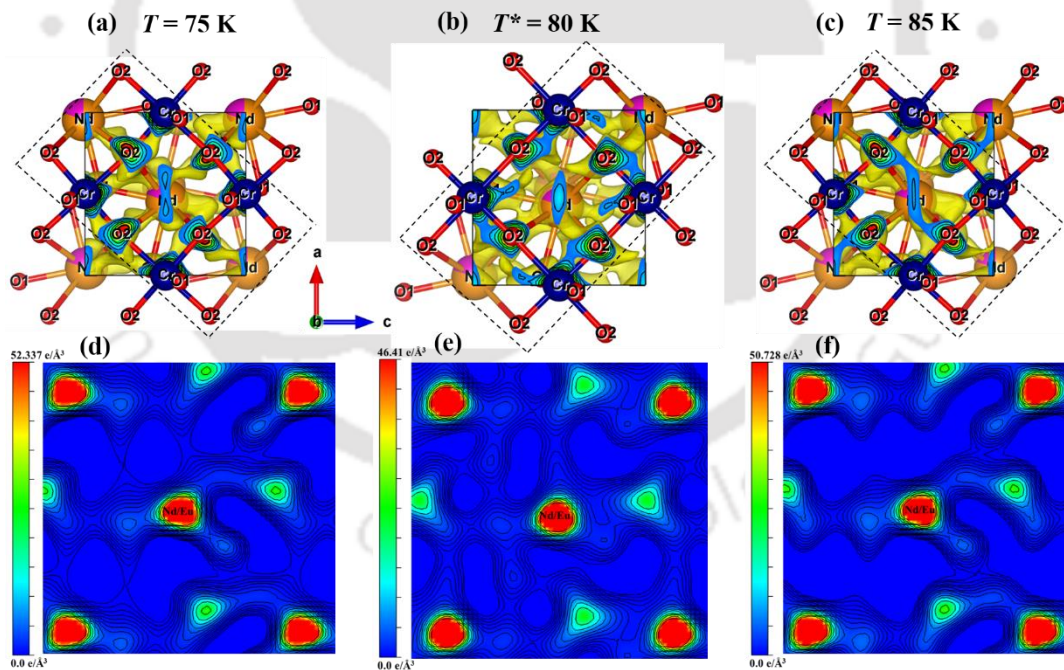


Fig. 3-23 The electron density distribution (3D) calculated by the MEM method in the unit cell of $Nd_{1-x}Eu_xCrO_3$ ($x = 0.2$) sample for the $Pnma$ space group using the iso-surface level of $1 \text{ e}/\text{\AA}^3$ at (a) $T = 75 \text{ K}$ (b) $T^* = 80 \text{ K}$ (c) $T = 85 \text{ K}$ and (d)-(f) the corresponding (2D) charge density maps in (010) plane for the $T = 75 \text{ K}$ to 85 K . The contour lines are drawn from 0 to $1 \text{ e}/\text{\AA}^3$ with intervals of $0.1 \text{ e}/\text{\AA}^3$.

Furthermore, a sharp decrease in electron density is observed from the 2D charge density map around T^* depicted in **Fig. 3-23(d)-(f)**. We infer from the reorientation of highlighted structure (dashed rectangle) that the nonpolar $Pnma$ space group is insufficient to explain the crystal structure of the $Nd_{1-x}Eu_xCrO_3$ system across T^* in detail. This result is further corroborated by the bulk modulus predicted by the calculations for $x = 0.0$ and 0.2 samples at different temperatures, as shown in **Fig. 3-24**. Similar to the maximum of the ED vs. T plot, the bulk modulus vs. T plot also shows the influence of magnetic ordering at T_N and T_{SR} . In the region of T^* , we observed the largest bulk modulus of ~ 215.6 GPa for $x = 0.2$ composition. From the calculations, it is also found that the pressure acting on the unit cell of the $x = 0.2$ system is quite high ~ 6.7 GPa near T^* .

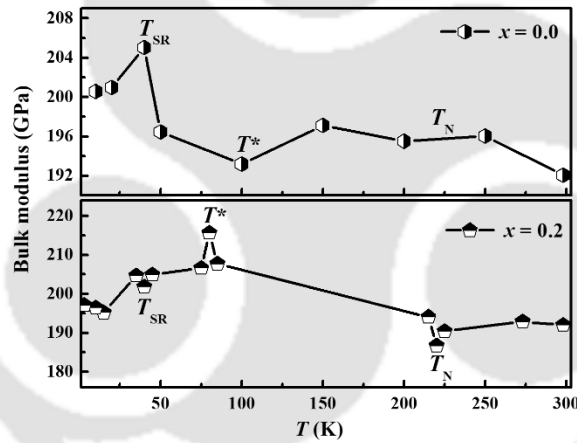


Fig. 3-24 Theoretical bulk modulus as a function of temperature for $Nd_{1-x}Eu_xCrO_3$ (a) $x = 0.0$ and (b) $x = 0.2$ samples, showing anomalies at the T_N , T^* , and T_{SR} in the range of 3-300 K.

This is sufficiently large to displace the atoms, as depicted in **Fig. 3-20(f)**, where the Nd/Eu atoms are displaced by an amount of ~ 0.004 Å at T^* . Such displacement can cause an utmost change in the Nd/Eu-O length ~ 0.27 Å around T^* (see **Fig. 3-20(e)**). Therefore, we attempt to look at the closely related crystal structure and MEM charge density for the $x = 0.2$ sample using the $Pna2_1$ symmetry, as shown in **Fig. 3-25**.

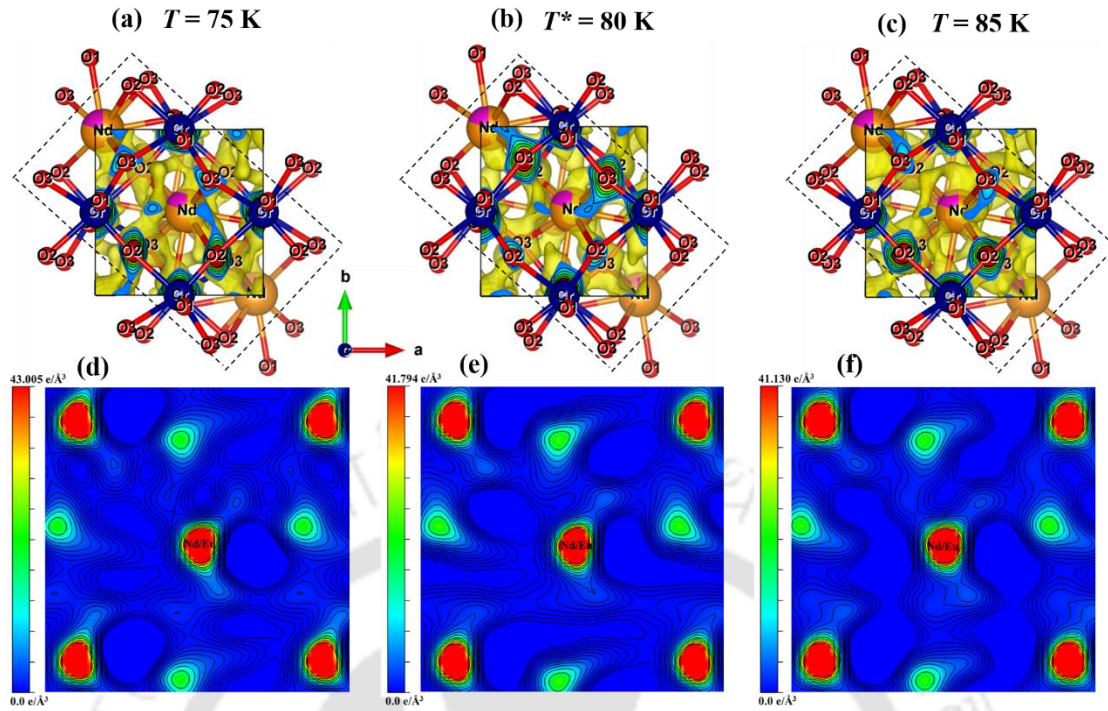


Fig. 3-25 The distribution of charge density (3D) within the unit cell of $Pna2_1$ symmetry using the iso-surface level of $1 \text{ e}/\text{\AA}^3$ at (a) $T = 75 \text{ K}$ (b) $T^* = 80 \text{ K}$ (c) $T = 85 \text{ K}$ and (d)-(f) the corresponding (2D) charge density maps in (001) plane from 75 K to 85 K of $Nd_{1-x}Eu_xCrO_3$ ($x = 0.2$) sample using MEM method. Contour lines of charge density are from 0 to $1 \text{ e}/\text{\AA}^3$ with $0.1 \text{ e}/\text{\AA}^3$ intervals.

We noticed that the highlighted 3D charge density map (dashed rectangle) does not reorient across T^* in **Fig. 3-25(a)-(c)**. Also, the ED of Nd/Eu ions $\sim 43 \text{ e}/\text{\AA}^3$ to $41.13 \text{ e}/\text{\AA}^3$ for $T = 75 \text{ K}$ to 85 K is obtained from the 2D-ED map shown in **Fig. 3-25(d)-(f)**. Such distribution of the ED indicates the stability across the temperature window of T^* . Thus, we propose the structure of the $Nd_{1-x}Eu_xCrO_3$ compound cannot be explained entirely by the nonpolar ($Pnma$) phase as atomic displacement arises in the vicinity of T^* , which is stabilized by the polar ($Pna2_1$) phase, resulting in the anomalous structural and magnetic properties in this region.

3.4 Summary

We synthesized the single-phase $Nd_{1-x}Eu_xCrO_3$, ($x = 0.0-1.0$) samples by solid-state reaction method where the Nd has been gradually replaced with Eu, and this induces a gradual change in the chemical pressure in these samples. The room temperature X-ray diffraction and Raman analysis confirm increased structural distortions with Eu substitution. The microstructural analysis showed the good quality of homogenous bulk samples. The calculated maximum bulk modulus ~ 202 GPa across $x = 0.5$ sample. A significant decrease in T_N values from ~ 225.4 K ($x = 0.0$) to 182.5 K ($x = 1.0$) with Eu substitution is observed. The T_{SR} exhibits for $x = 0.0-0.9$ samples in ~ 37.1 K to 13.3 K temperature range. The x dependence of J_1 and J_2 indicates the modification of Cr-Cr interactions. The chemical pressure boundary from the structural and magnetic behavior across $x = 0.5$ is observed. The negative EB effect is obtained, and the H_{EB} decreases from ~ -1945 Oe ($x = 0.0$) to -15 Oe ($x = 1.0$) with increasing Eu content. The non-monotonic behavior of the EB field with maximum H_{EB} across T^* between the T_N and T_{SR} is observed for $x = 0.10$ and 0.20 sample. The competing AFM interaction between the weak ferromagnetic component of canted Cr^{3+} moments and the paramagnetic moment of Nd^{3+}/Eu^{3+} ions with the lattice distortions could be responsible for the EB effect. The temperature dependence of phonon modes related to anti-stretching and bending of CrO_6 octahedra and Nd^{3+}/Eu^{3+} ion vibration below T_N confirms the strong spin-phonon coupling up to $x = 0.20$ sample. The T^* found from the non-monotonicity of the EB is imprinted with the additional phonon anomaly. The Raman results are also verified using density functional theory-based calculations. Furthermore, the strong magnetoelastic coupling below T_N up to $x = 0.2$ sample was confirmed by the temperature dependence of the lattice parameters, CrO_6 deformations, and Nd/Eu positions. The MEM analysis of electron density distribution shows the centrosymmetric ($Pnma$) phase is insufficient to explain the crystal structure of

the $Nd_{1-x}Eu_xCrO_3$ system near $T^* \sim 80$ K in between T_N and T_{SR} . The structural reorientation across T^* resolves the anomalous ED jump of Nd/Eu ions for the $Pnma$ structure and provides a stable ED ~ 41.79 e $^\circ$ A 3 for the $Pna2_1$ structure. However, further microscopic studies are needed to confirm this proposition. The work reports the lattice modulations around T^* between T_N and T_{SR} for the first time in pure and substituted $NdCrO_3$ by exploring spin-phonon induced exchange bias and magneto-structural imprints.





Chapter 4 : Interwoven spin-reorientation and exchange bias in $Nd_{1-x}Pr_xCrO_3$

4.1 Introduction

The $RCrO_3$ has witnessed huge attention due to its unique physical properties [1,83,137]. The $RCrO_3$ are mostly G-type canted antiferromagnets and exhibit weak ferromagnetism due to Dzyaloshinskii-Moriya interaction [15][155]. Further, the spin reorientation from magnetic symmetry to another is an intriguing phenomenon [156]. The three spin configurations $\Gamma_1(A_x, G_y, C_z)$, $\Gamma_2(F_x, C_y, G_z)$, $\Gamma_4(G_x, A_y, F_z)$ are found in orthochromites [16] and the continuous or abrupt nature of spin-reorientation transition is dependent on R -ion [89] [87]. In $NdCrO_3$, the antiferromagnetic ordering of the Cr^{3+} sublattice starts at $T_N \sim 225$ K [111], and the spin-reorientation transition of the Cr^{3+} moment occurs at $T_{SR} \sim 35$ K [16]. Meanwhile, in $PrCrO_3$, the antiferromagnetic ordering of the Cr^{3+} sublattice exhibits at $T_N \sim 237$ K [157]. The high Neel temperature, as compared to other $RCrO_3$ compounds, is appealing for room temperature applications. Furthermore, substituting Nd or Cr-site in $NdCrO_3$ offers various interesting properties. For instance, the presence of non-magnetic Ca^{2+} increases the density, electrical conductivity, and thermal expansion coefficient in $Nd_{1-x}Ca_xCrO_3$ [115]. In our recent study, the low field magnetic states were found in Ce substituted $NdCrO_3$ [158]. Other than this, the dc conductivity measurements of $PrCrO_3$ disclose semiconductor behavior at room temperature and transition to metal at ~ 400 K [100]. Furthermore, the Pr substitution leads to large negative magnetization below the compensation temperature of ~ 230 K in $La_{1-x}Pr_xCrO_3$ solid solutions [159]. A certain doping percentage in $Yb_{1-x}Pr_xCrO_3$ showed Yb^{2+} and Pr^{4+} valence states and further exchange bias effect [75].

This literature motivated us to carry out a detailed study of the Pr substitution in NdCrO₃. Despite the fact that both Nd³⁺ and Pr³⁺ are magnetic ions, the NdCrO₃ comprises sharp spin reorientation, whereas no spin reorientation transition exists in the PrCrO₃ orthochromite. Hence, the major modification of spin-reorientation is expected with Pr³⁺ ion substitution in NdCrO₃. Moreover, the interaction between Nd³⁺ and Cr³⁺ moments in NdCrO₃ is very strong. The regulation at Nd-site with Pr doping will directly influence the Nd³⁺-Cr³⁺ interaction keeping the Cr³⁺-Cr³⁺ interaction less affected. In this way, studying exchange bias in such systems would be beneficial.

In this work, we present a comprehensive understanding of the structural and magnetic properties of Nd_{1-x}Pr_xCrO₃ (0.05 ≤ x ≤ 0.30) single-phase samples through X-ray diffraction, X-ray photoelectron spectroscopy, temperature, and field-dependent dc magnetization and Raman scattering measurements. The evolution of spin-reorientation, induction of Griffiths-like phase, and improvement of exchange bias field in correlation with structural behavior are observed with Pr substitution in present compounds.

4.2 Experimental details

The Nd_{1-x}Pr_xCrO₃ (x = 0.05, 0.10, 0.20, and 0.30) compounds were synthesized by the standard solid-state reaction method. The stoichiometric ratio of Nd₂O₃ (99.9%), Pr₆O₁₁ (99.9%), and Cr₂O₃ (99.6%) powders were taken and ground using an agate mortar pestle in the acetone medium. The uniform mixture was calcined at 1000 °C for 12 h, and the calcined powder was pressed in pellets using a hydraulic press. The final sintering was done at 1300 °C for 24 h in an air atmosphere. The phase purity of these compounds was analyzed by the X-ray diffractometer (Rigaku, Smart Lab) using Cu-K_α radiation of the wavelength λ = 1.5406 Å. Microstructural analysis was done using the field emission scanning electron microscope (FESEM) (Zeiss, Sigma 300) and energy-dispersive X-ray (EDX). Raman spectrometer (Horiba Jobin Yvon, LabRam HR, 514 nm) was used to collect the Raman

spectra. The valance state of compounds was confirmed by High-resolution X-ray photoelectron spectroscopy (XPS) with the help of an X-ray photoelectron spectrometer (ESCALAB Xi+, Thermo Fisher). Temperature and field-dependent magnetization measurements were carried out using the physical property measurement system (PPMS, Quantum Design).

4.3 Results and discussions

4.3.1 Powder X-ray diffraction

The XRD patterns of the $Nd_{1-x}Pr_xCrO_3$ ($x = 0.05-0.3$) samples were recorded, and the diffraction peaks of the substituted samples were well matched with parent $NdCrO_3$ (ICSD card No. 01-083-0261) compound. The XRD data of the $Nd_{1-x}Pr_xCrO_3$ ($x = 0.05-0.3$) samples is analyzed by the Rietveld refinement method using the FULLPROF program.

Fig. 4-1(a)-(d) demonstrates the Rietveld refinement of the $x = 0.05-0.3$ compositions.

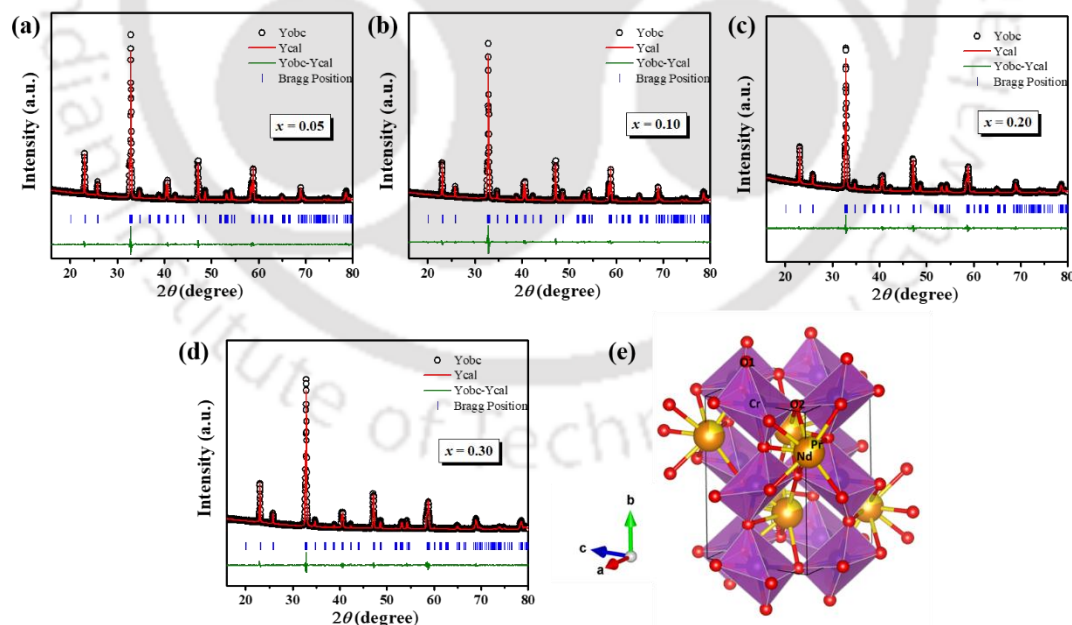


Fig. 4-1 Rietveld refinement of XRD data for $Nd_{1-x}Pr_xCrO_3$ (a) $x = 0.05$ (b) $x = 0.10$ (c) $x = 0.20$ and (d) $x = 0.30$ samples and (e) The crystal structure of the $x = 0.20$ sample.

Here, the XRD patterns are fitted well to the orthorhombic structure ($Pnma$ space group), confirming the single-phase nature of all the samples. Furthermore, the **Fig. 4-1(e)** represents the distorted perovskite crystal structure of the $x = 0.2$ compound, which clearly shows the Pr^{3+} substitution at the Nd-site and six O^{2-} ions (apical oxygen O1 and equatorial oxygen O2) around Cr^{3+} ion form the CrO_6 octahedra.

Table 4-1 The lattice parameters a , b , and c , cell volume (V), bond lengths $Cr-O1$, $Cr-O2$, and bond angles $Cr-O1-Cr$, $Cr-O2-Cr$ from Rietveld refinement of $Nd_{1-x}Pr_xCrO_3$ ($x = 0-0.3$) samples. The tolerance factor (t), orthorhombic strain (S_{ac}), and cell distortion factor (d) are obtained from crystallographic parameters.

	$x = 0.0$	$x = 0.05$	$x = 0.10$	$x = 0.20$	$x = 0.30$
a (Å)	5.4821(1)	5.4814(1)	5.4805(3)	5.4795(2)	5.4786(4)
b (Å)	7.6896(3)	7.6903(2)	7.6904(1)	7.6924(1)	7.6971(2)
c (Å)	5.4184(2)	5.4201(4)	5.4195(2)	5.4221(3)	5.4279(1)
V (Å ³)	228.41(6)	228.44(5)	228.45(4)	228.55(7)	228.89(5)
$Cr-O1$ (Å)	1.963(3)	1.972(1)	1.981(2)	1.988(4)	1.994(3)
$Cr-O2$ (Å)	1.999(4)	2.013(3)	2.055(1)	2.025(1)	2.009(3)
$Cr-O1-Cr$ (°)	156.57(1)	154.18(8)	152.23(4)	150.57(7)	149.56(5)
$Cr-O2-Cr$ (°)	156.30(4)	156.19(2)	156.43(1)	157.18(3)	157.07(3)
t	0.8838	0.8841	0.8844	0.8850	0.8856
S_{ac}	0.0117	0.0113	0.0111	0.0105	0.0093
d	23.96	22.32	22.03	19.49	15.30

The lattice parameters and cell volume for $x = 0.0-0.3$ samples obtained from the refinement are mentioned in Here, the XRD patterns are fitted well to the orthorhombic structure ($Pnma$ space group), confirming the single-phase nature of all the samples. Furthermore, the **Fig. 4-1(e)** represents the distorted perovskite crystal structure of the $x = 0.2$ compound, which clearly shows the Pr^{3+} substitution at the Nd-site and six O^{2-} ions (apical oxygen O1 and equatorial oxygen O2) around Cr^{3+} ion form the CrO_6 octahedra.

Table 4-1, where the $x = 0.0$ sample agrees with the report [112]. With Pr doping, the lattice parameter a decreases and b , c , volume V increases which are attributed to the increase in

average A-site ionic radius with the substitution of larger Pr^{3+} (1.126 Å) ions at Nd^{3+} (1.109 Å) site, resulting in the lattice expansion. The corresponding changes in Cr-O bond length and Cr-O-Cr bond angles with Pr substitution are observed (see **Table 4-1**). The substitution of larger ions can decrease the distortion in the lattice, which is analyzed by different factors and listed in Here, the XRD patterns are fitted well to the orthorhombic structure ($Pnma$ space group), confirming the single-phase nature of all the samples. Furthermore, the **Fig. 4-1(e)** represents the distorted perovskite crystal structure of the $x = 0.2$ compound, which clearly shows the Pr^{3+} substitution at the Nd-site and six O^{2-} ions (apical oxygen O1 and equatorial oxygen O2) around Cr^{3+} ion form the CrO_6 octahedra.

Table 4-1 It is found that the Goldschmidt's tolerance factor $t = (r_{|Nd+Pr|} + r_o)/\sqrt{2}(r_{Cr} + r_o)$ and the orthorhombic strain, $s = 2(a-c)/(a+c)$ decreases with Pr substitution. Furthermore, the cell distortion factor (d) is estimated using the relation,

$$d = 10^6 \left[\frac{\left(\frac{a}{\sqrt{2}} - a_p\right)^2 + \left(\frac{b}{2} - a_p\right)^2 + \left(\frac{c}{\sqrt{2}} - a_p\right)^2}{3a_p^2} \right] \quad (4.1)$$

where, $a_p = \frac{\left(\frac{a}{\sqrt{2}} + \frac{b}{2} + \frac{c}{\sqrt{2}}\right)}{3}$ stands for the average cubic lattice parameter. A noticeable decrease in d values ~ 23.96 ppm ($x = 0.0$) to 15.30 ppm ($x = 1.0$) is observed with Pr substitution, which indicates less deviation of cell edges from the ideal cubic perovskite structure.

4.3.2 Microstructural analysis

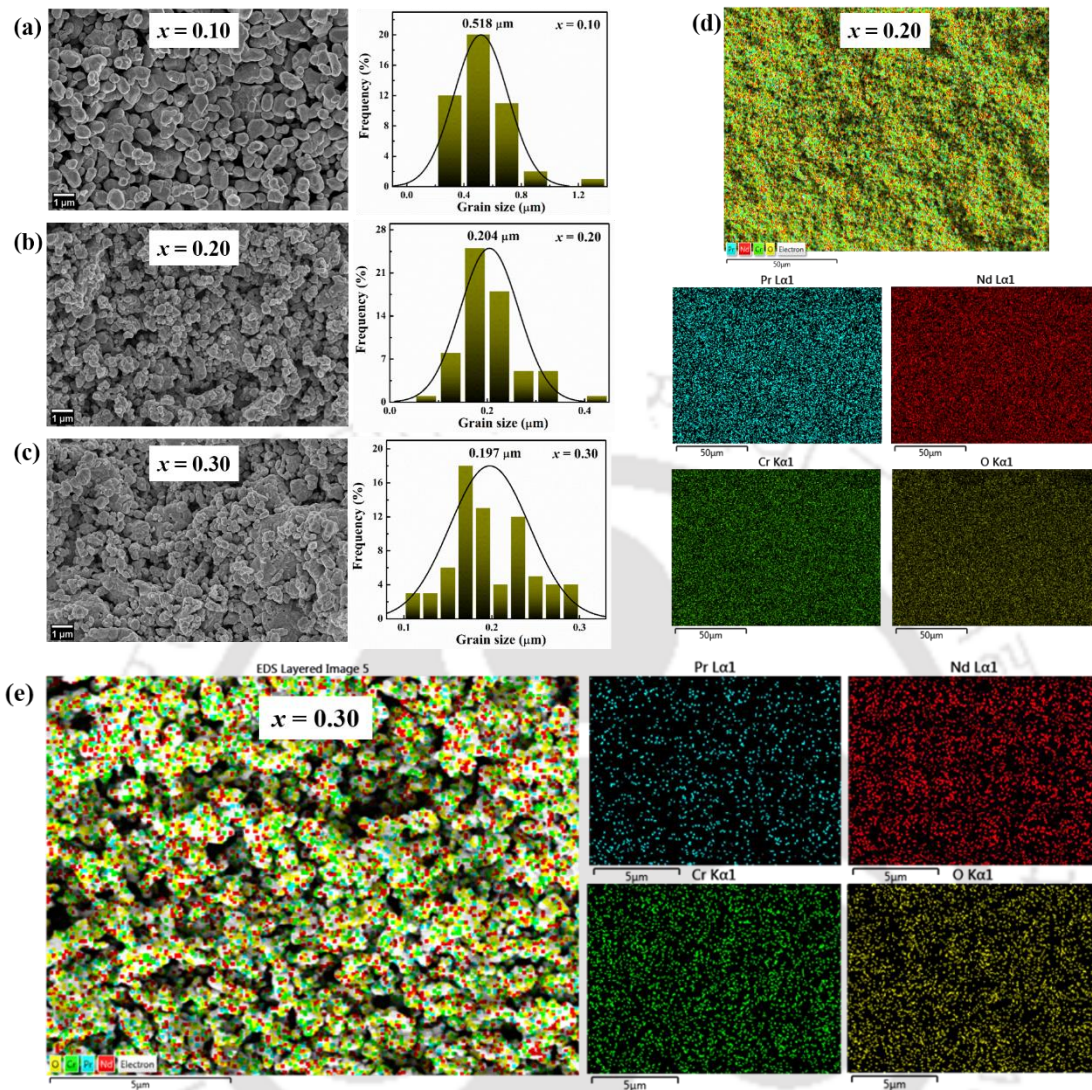


Fig. 4-2 FESEM micrograph of $Nd_{1-x}Pr_xCrO_3$ (a) $x = 0.10$ (b) $x = 0.20$ and (c) $x = 0.30$ samples along with their grain size distribution (d) EDX mapping of $x = 0.20$ sample and (e) EDX mapping of $x = 0.30$ sample in a smaller area of $5 \times 5 \mu m^2$.

In **Fig. 4-2(a)-(c)**, the FESEM micrographs of the $Nd_{1-x}Pr_xCrO_3$ ($x = 0.1, 0.2,$ and 0.3) samples display uniform grain formation. The average grain size of the samples was found using the linear intercept method (Image-J software). The grain size distribution for $x = 0.1-0.3$ samples shows the value of the average grain size varies from $\sim 0.518 \mu m$ to $0.197 \mu m$. With increasing Pr concentration, the average grain size decreases, which might be related to the decrease of grain surface energy [160]. Furthermore, the EDX mapping

displayed in **Fig. 4-2(d)** for the $x = 0.20$ sample shows the presence of O, Cr, Nd, and Pr elements. **Fig. 4-2(e)** represents the EDX mapping of the $x = 0.30$ sample in a smaller $5 \times 5 \mu\text{m}^2$ area, showing uniform elemental distribution without segregation in Pr-rich samples.

4.3.3 X-ray photoelectron spectroscopy

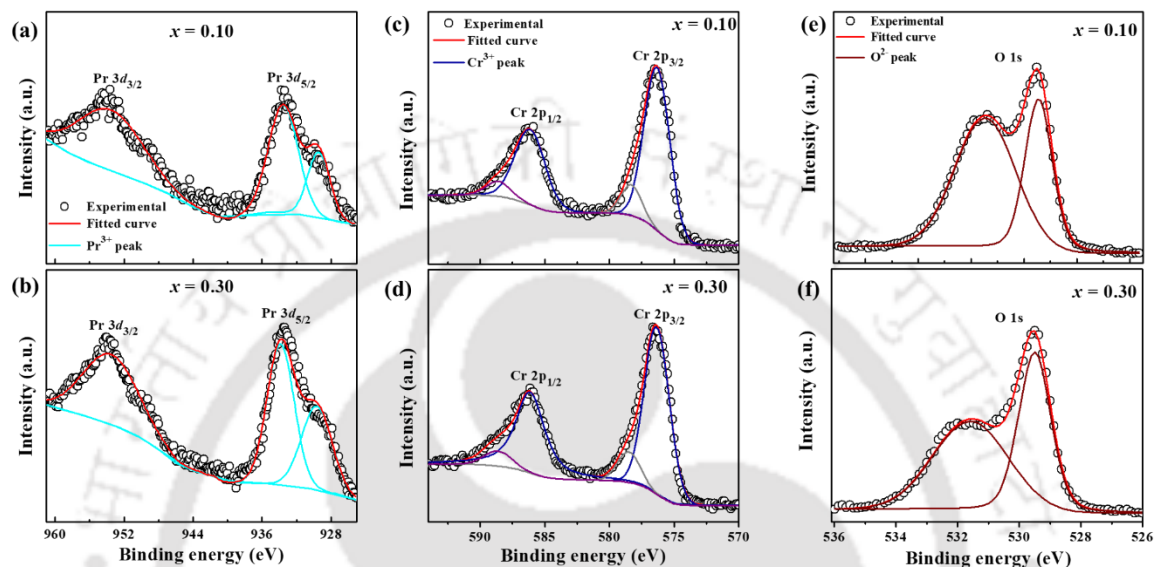


Fig. 4-3 XPS spectra of (a)-(b) the core level Pr 3d spectra (c)-(d) the Cr 2p spectra, and (e)-(f) the O 1s spectra of $x = 0.10$ and 0.30 compounds.

High-resolution XPS data are used to find the valency of constituent ions. Here, **Fig. 4-3(a)-(b)** shows the Pr 3d spectra for $x = 0.10$ and 0.3 composition. The spin-orbit resolved peaks of Pr $3d_{5/2} \sim 933.4$ eV and Pr $3d_{3/2} \sim 953.5$ eV ($x = 0.30$) confirm the Pr^{3+} ($J = 4$) ions [161]. The deconvoluted peaks at 929.2 eV indicate the Pr^{3+} ion in the product [162]. In addition, **Fig. 4-3(c)-(d)** shows the XPS spectra of Cr 2p and O 1s for substituted samples. The binding energies ~ 576.3 eV and ~ 586.1 eV ($x = 0.30$) indicate the Cr^{3+} ($S = 3/2$) ion due to the splitting of 2p level into $2p_{3/2}$ and $2p_{1/2}$ peaks [163]. Moreover, the O 1s XPS spectra in **Fig. 4-3(e)-(f)** are resolved at binding energies ~ 529.5 eV and 531.5 eV ($x = 0.30$), describing the lattice oxygen.

4.3.4 UV-Vis spectroscopy

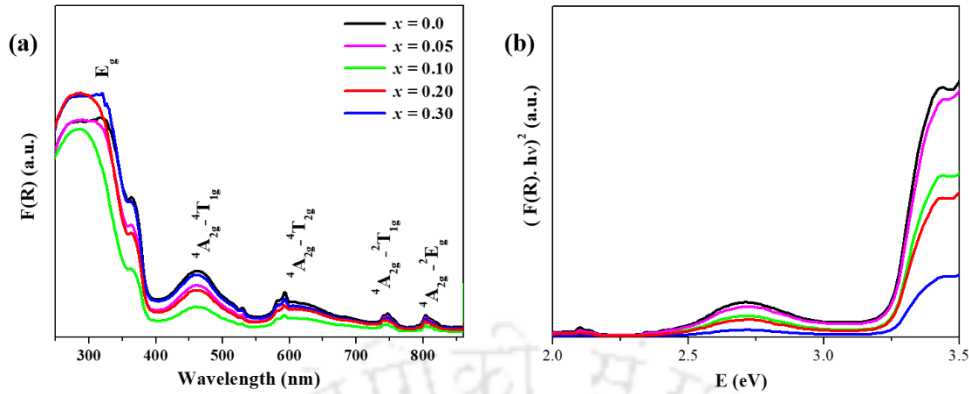


Fig. 4-4 (a) UV-Vis DRS spectrum of $Nd_{1-x}Pr_xCrO_3$ ($x = 0.0-0.3$) samples in the range of 250 to 850 nm. (b) Estimation of bandgap E_g from Tauc plots for each sample.

The optical behavior of the samples is investigated by the UV-Vis diffuse reflectance spectroscopy technique. The UV-Vis spectrum of the samples is analyzed by optical absorption, i.e., Kubelka-Munk (KM) function $F(R)$, which can be expressed as $F(R) = (1-R)^2/2R$, where R is the diffuse reflectance of the sample. From $F(R)$ versus wavelength plot in **Fig. 4-4(a)**, we see a multiband electronic structure consisting of the filled O $2p$ band and partially filled Cr $3d^3$ and Nd $4f^4$ orbitals. The broad absorption band located around 250-390 nm is attributed to bandgap E_g of the material due to O $2p$ to Cr $3d$ transitions. The other two intense absorption bands at about 463 nm and 593 nm correspond to the $^4A_{2g}$ to $^4T_{1g}$ and $^4A_{2g}$ to $^4T_{2g}$ transition. The two weak transitions at 748 nm and 804 nm correspond to the $^4A_{2g}$ to $^2T_{1g}$ and $^4A_{2g}$ to 2E_g transitions. These transitions are related to the octahedral crystal field splitting of Cr^{3+} d-orbitals that allow the corresponding $d(Cr)-d(Cr)$ transitions.

The optical energy band gap can be calculated from the Tauc relation $F(R)hv = B(hv - E_g)^n$. The value of n depends on the direct ($n = 1/2$) or indirect ($n = 2$) band gap of the material. The Tauc plot of $(F(R).hv)^2$ versus (hv) is used to determine the direct band gap (E_g) as shown in **Fig. 4-4(b)**, which shows the samples have the bandgap $E_g = 3.23$ eV (x

= 0.0) and 3.29 eV ($x = 0.3$) lies in the visible region. We have also utilized the Density functional theory (DFT) with the quantum ESPRESSO suite to calculate the fermi energy of the system. The obtained fermi energy values are $E_F \sim 14.41$ eV ($x = 0.3$). The substitution of Pr on the Nd-site may influence the Cr-O overlap integral, which can also modify the structural distortion via the distortion of the CrO_6 octahedra, resulting in a change in the optical bandgap and fermi energy.

4.3.5 Raman spectroscopy

Raman spectroscopy is an important tool for identifying subtle structural distortions. The group theory suggests 24 Raman active modes for $RCrO_3$ compounds as given by the relation, $\Gamma = 7A_g + 5B_{1g} + 7B_{2g} + 5B_{3g}$ [46].

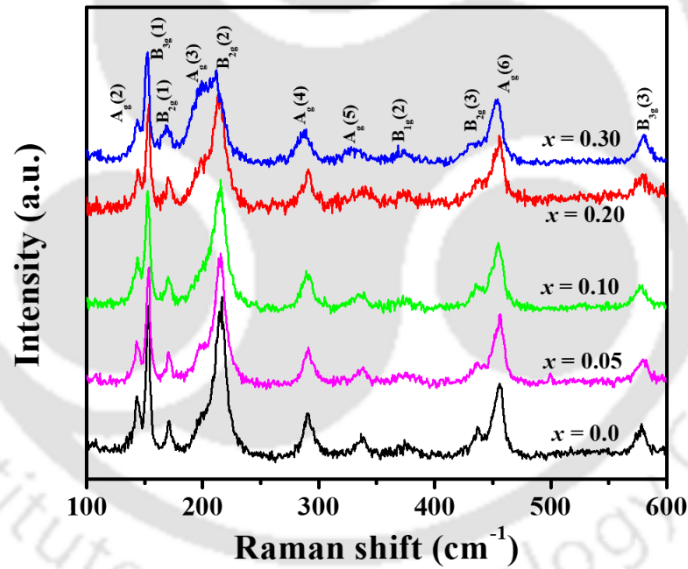


Fig. 4-5 Room temperature Raman spectra acquired for the $Nd_{1-x}Pr_xCrO_3$ ($x = 0.0-0.3$) samples in the 100 to 600 cm^{-1} wavenumber range.

Fig. 4-5 shows the room temperature Raman spectra of $Nd_{1-x}Pr_xCrO_3$ ($x = 0.0-0.3$) composition where 11 Raman active modes are detected. **Table 4-2** consists of the phonon frequencies of these samples obtained by fitting the Lorentzian function. The Raman modes (below 200 cm^{-1}) related to R-ion vibration exhibit a slight shift to low wavenumber, which can be attributed to the average A-site ionic radii increase through Pr substitution. Further,

the modes from 200 to 500 cm^{-1} mark the low wave number shift and the mode above 500 cm^{-1} exhibits the high wave number shift. These changes may be related to the change in A-site atomic mass and CrO_6 octahedral distortion with Pr substitution.

Table 4-2 The Raman mode frequencies of the $Nd_{1-x}Pr_xCrO_3$ ($x = 0.0-0.3$) samples at room temperature.

Symmetry	x = 0.30	x = 0.20	x = 0.10	x = 0.05	x = 0.0	Assignment
$A_g(2)$	143.4	144.1	143.0	143.3	144.2	$R(z)$
$B_{3g}(1)$	151.8	152.5	153.1	153.0	153.8	$R(y)$
$B_{2g}(1)$	169.7	170.8	170.8	170.9	172.2	$R(x)$
$A_g(3)$	198.1	198.6	199.2	198.8	199.7	CrO_6 in phase rotation (y)
$B_{2g}(2)$	212.7	214.1	213.9	215.0	216	$R(z)$, $O1(z)$
$A_g(4)$	289.8	290.5	290.3	290.9	291.8	$O1(x)$, $R(-x)$
$A_g(5)$	335.9	336.4	337.4	337.0	338.6	CrO_6 out of phase rotation (x)
$B_{1g}(2)$	373.7	374.7	374.3	375.7	376.1	CrO_6 out of phase rotation (y)
$B_{2g}(3)$	434.4	435.8	438.0	437.0	438.2	CrO_6 out of phase rotation (z)
$A_g(6)$	453.6	454.5	455.1	455.5	456.2	CrO_6 out of phase bending
$B_{3g}(3)$	580.0	579.2	579.1	579.1	578.9	CrO_6 anti stretching

Moreover, the study of low-temperature Raman spectra for $x = 0.10$ and 0.30 samples is also involved in the investigation of the lattice distortions in correlation with the magnetic behavior of the $Nd_{1-x}Pr_xCrO_3$ system. The phonon frequency as the function of temperature for purely anharmonic phonon-phonon scattering is given by the equation [36],

$$\omega_{anh}(T) = \omega(0) + A \left[1 + \frac{2}{e^x - 1} \right] + B \left[1 + \frac{3}{e^y - 1} + \frac{3}{(e^y - 1)^2} \right] \quad (4.2)$$

here, $x = \frac{\hbar\omega(0)}{2k_B T}$, $y = \frac{\hbar\omega(0)}{3k_B T}$ and $\omega(0)$, A, and B are adjustable parameters for fitting the experimental data above T_N .

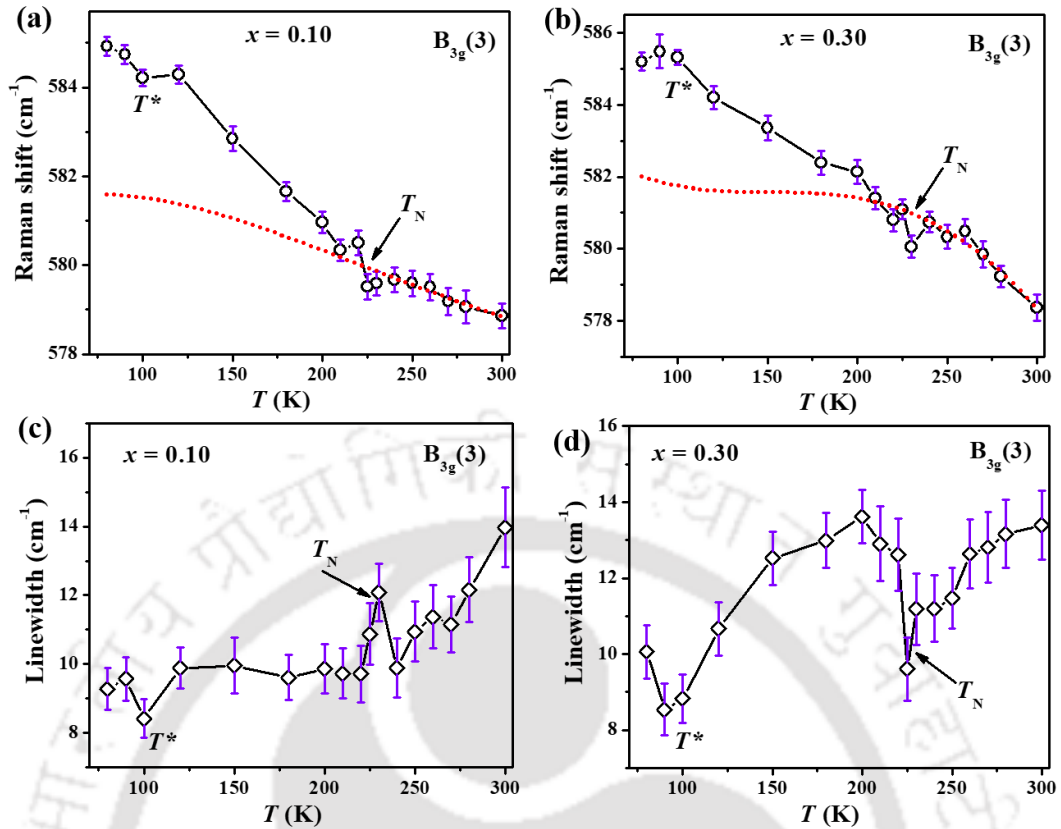


Fig. 4-6 Effect of temperature on (a)-(b) antisymmetric stretching mode frequency $B_{3g}(3)$ and (c)-(d) corresponding linewidth of $Nd_{1-x}Pr_xCrO_3$ ($x = 0.10, 0.30$) composition. The dotted lines (red) represent fitted curves for anharmonicity by Eq.4.2 and solid lines (black) guide to the eye.

Further, the temperature variation of the mode $B_{3g}(3)$ related to antisymmetric stretching of CrO_6 octahedra for $x = 0.10$ and 0.30 samples in **Fig. 4-6** Effect of temperature on (a)-(b) antisymmetric stretching mode frequency $B_{3g}(3)$ and (c)-(d) corresponding linewidth of $Nd_{1-x}Pr_xCrO_3$ ($x = 0.10, 0.30$) composition. The dotted lines (red) represent fitted curves for anharmonicity by Eq.4.2 and solid lines (black) guide to the eye. **Fig. 4-6(a)-(b)** exhibit hardening with the deviation from an anharmonic contribution below T_N . The report shows similar anti-stretching mode behavior in a few orthochromites with magnetic R -ion [13][109]. Further, the corresponding linewidths also decrease with T shown in **Fig. 4-6(c)-(d)**, giving the anomaly at T_N and the peak at T^* for both modes. This anomalous behavior of phonon frequencies caused by phonon modulation of exchange integral [11] is attributed

to a spin-phonon coupling that changes phonon lifetime and corresponds to the anomaly in linewidths. Thus, different $Nd^{3+}/Eu^{3+}-Cr^{3+}$ and $Cr^{3+}-Cr^{3+}$ interactions below T_N induce the spin-phonon coupling in these samples.

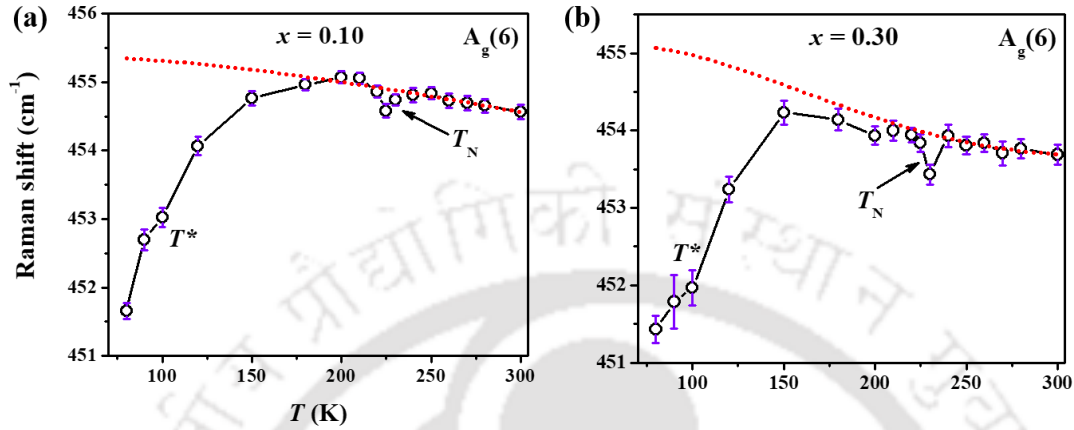


Fig. 4-7 Temperature dependence of phonon mode $A_g(6)$ for bending of CrO_6 octahedra of $Nd_{1-x}Pr_xCrO_3$ (a) $x = 0.10$ and (b) $x = 0.30$ compound. The dotted lines (red) represent fitted curves for anharmonicity by Eq.4.2, and solid lines (black) guide to the eye.

Fig. 4-7(a)-(b) represents the thermal variation of phonon frequencies of $A_g(6)$ mode related to the out of phase bending of CrO_6 octahedra. The clear sign of spin-phonon coupling is observed for $x = 0.10$ and 0.30 samples through anomalous softening of the Raman mode below T_N . Initially, such softening of the mode was observed in $RMnO_3$ [10] and few $RCrO_3$ [12], which is associated with weak ferromagnetism of Cr^{3+} spins, causing spin-phonon coupling.

4.3.6 Temperature and field-dependent magnetic properties

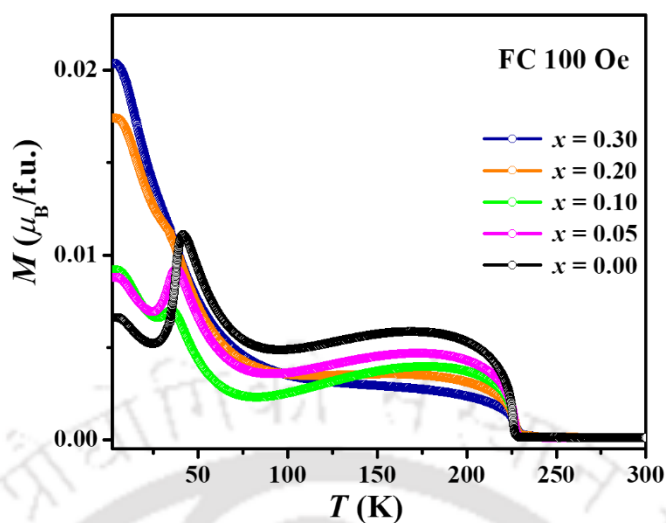


Fig. 4-8 Temperature dependence of magnetization for field cooled condition under 100 Oe applied field for $Nd_{1-x}Pr_xCrO_3$ ($x = 0.0-0.3$) compositions.

Fig. 4-8 demonstrates the M - T curves of the $Nd_{1-x}Pr_xCrO_3$ ($x = 0.0-0.30$) samples in field cooled (FC) mode under the applied field of 100 Oe. We noticed the substitution of Pr^{3+} gives rise to interesting magnetic behavior. The FC magnetization first decreases for $x = 0.05$ to 0.10 substitution, and further increases of Pr content up to $x = 0.30$ provide higher magnetization $\sim 0.02 \mu_B/f.u.$ as compared to pristine compound. The report suggests the coupling between Nd^{3+} and Cr^{3+} in $NdCrO_3$ is very strong [87], and the Pr^{3+} substitution can play an important role by influencing this coupling. Therefore, the temperature dependence of FC magnetization under different applied fields of 100 Oe, 1 kOe and 10 kOe for $x = 0.0-0.30$ samples are analyzed as shown in **Fig. 4-9(a)-(e)**. The inset of **Fig. 4-9(a)** shows the derivative of magnetic susceptibility (dy/dT) vs. temperature curve, where the first peak near $T_N \sim 225.4$ attributes to the antiferromagnetic ordering and the second peak near $T_{SR} \sim 37.1$ K represents spin-reorientation transition for $x = 0.0$ sample in accordance with reports [111][17]. At lower temperatures ~ 11 K, the Nd^{3+} ordering may be induced by the Cr^{3+} sublattice [16]. The incorporation of Pr slightly increases T_N up to

227.5 K for $x = 0.3$ sample, which is related to the lattice expansion with Pr doping. The magnetization curves for $x = 0.05$ and $x = 0.10$ samples in **Fig. 4-9(b)-(c)** show the decrease in magnetization below T_N followed by the decrease in the T_{SR} up to ~ 33.6 K.

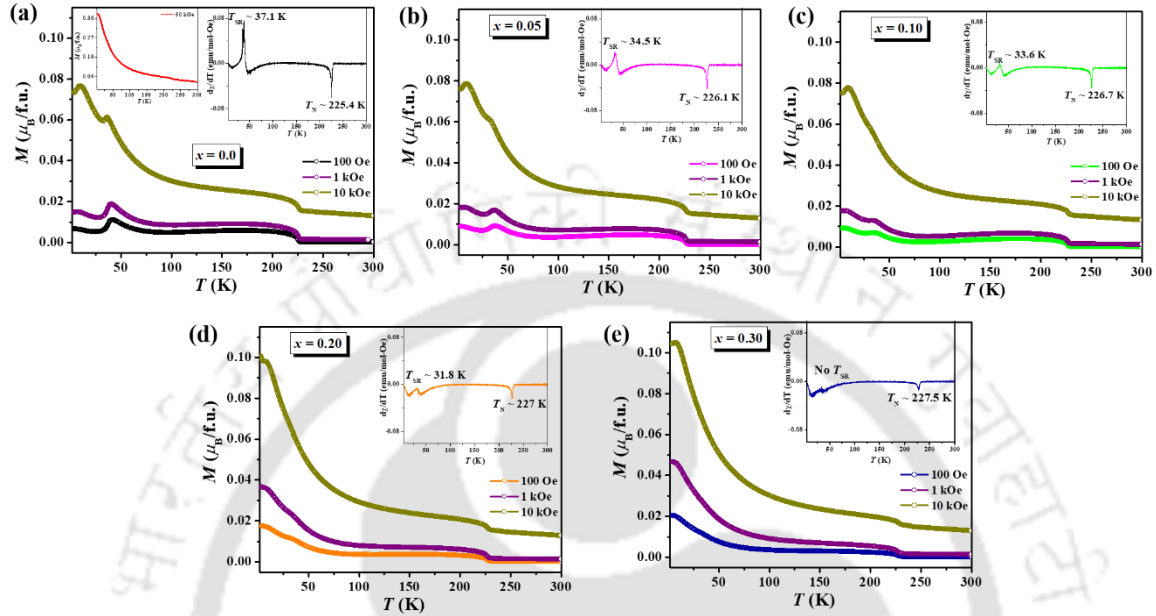


Fig. 4-9 Temperature dependence of FC magnetization under different applied magnetic field of 100 Oe, 1 kOe and 10 kOe for $Nd_{1-x}Pr_xCrO_3$ (a) $x = 0.0$ and left inset shows M - T curve under 50 kOe (b) $x = 0.05$ (c) $x = 0.10$ (d) $x = 0.20$ and (e) $x = 0.30$ samples. The right inset of (a)-(e) shows the derivative of magnetic susceptibility vs. temperature exhibit peaks at T_N and T_{SR} for the corresponding samples.

For the parent compound, the Cr^{3+} moments exhibit the weak ferromagnetic $\Gamma_2(F_x, C_y, G_z)$ phase at high temperatures and the antiferromagnetic $\Gamma_1(A_x, G_y, C_z)$ phase at low temperatures [16]. It is possible that the Pr substitution ($x = 0.05$ to 0.10) decreases both phases resulting decrease in magnetization and reorientation of Cr^{3+} spins. The further increase of $x = 0.20$ to 0.30 sharply increases the magnetization, but the T_{SR} starts vanishing after $x = 0.2$ as shown in **Fig. 4-9(d)-(e)**. Consequently, no spin reorientation is observed for the $x = 0.3$ sample due to the presence of only weak ferromagnetic (Γ_2) phase. Thus, a maximum 30% Pr substitution may significantly enhance the Cr^{3+} - Cr^{3+} superexchange interactions but dilute the Nd^{3+} - Cr^{3+} superexchange interactions, which leads to no spin-

reorientation for the $Nd_{0.7}Pr_{0.3}CrO_3$ system. These results are in accordance with the $PrCrO_3$ reports, which shows no spin-reorientation transition in this compound [157]. Further, the ordering of rare-earth sublattice in the antiferromagnetic arrangement may be possible due to Nd/Pr spins around 15 K [164]. The temperature dependence of magnetization under different applied fields reveals the spin reorientation of Cr^{3+} spins possesses strong magnetic field dependence. We found T_{SR} is suppressed under the 10 kOe magnetic field for higher Pr substitution. But the strong coupling of Nd^{3+} and Cr^{3+} moments maintains the T_{SR} in $x \leq 0.10$ samples even under the field of 10 kOe, which requires a high field of 50 kOe to vanish T_{SR} (see inset of **Fig. 4-9(a)**).

Thus, the increase of Pr^{3+} substitution improves Cr^{3+} - Cr^{3+} interactions and softens Nd^{3+} - Cr^{3+} interactions in $Nd_{1-x}Pr_xCrO_3$ samples, resulting in no spin-reorientation for maximum Pr content. The observed variation of T_{SR} in these systems is in accordance with the end composition of the series $PrCrO_3$ which exhibits no spin-reorientation of Cr^{3+} moments [157]. Such behavior of present samples seems to be opposite to other orthochromites where T_{SR} was induced by Pr doping [165].

Furthermore, the inverse susceptibility ($1/\chi$) vs. temperature (T) plots for $x = 0.0$ - 0.30 samples derived from 100 Oe magnetization measurements are shown in **Fig. 4-10(a)**. From these curves, it is observed that the linear fitting in the paramagnetic region ($T > T_N$) for all the samples follows Curie-Weiss (CW) law. However, the $1/\chi$ begins to deviate from linear behavior and drops downward at the characteristic temperature (T_G) for the substituted samples, as shown in **Fig. 4-10(b)-(c)**. Such magnetic behavior in disordered magnets is a signature of Griffith's phase (GP), which was characterized by the formation of finite-size ferromagnetic clusters within the paramagnetic matrix above Curie temperature [166,167]. The Pr-based doped manganites are known to exhibit GP singularity [168,169], however, it has also been reported in doped orthochromites recently [170,171].

The downward deviation of $1/\chi$ vanishes with an increasing magnetic field, as depicted in **Fig. 4-10(b)-(c)**, which is the sign of GP singularity. In the GP region, the low field magnetic susceptibility follows the power law behavior [169],

$$\chi^{-1}(T) \propto (T - T_C^R)^{1-\lambda} \quad (4.3)$$

where, T_C^R is the critical temperature of random FM. The λ ($0 \leq \lambda < 1$) is the susceptibility exponent, which describes the degree of deviation from CW behavior.

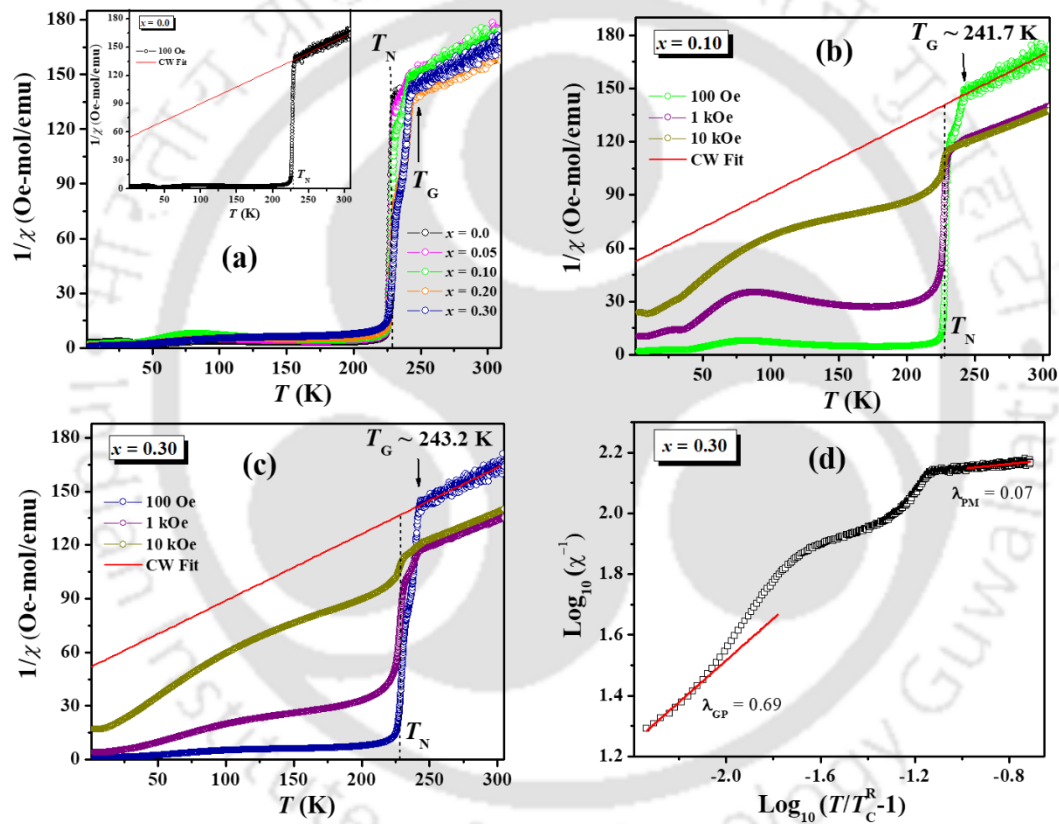


Fig. 4-10 (a) The inverse magnetic susceptibility ($1/\chi$) vs. temperature (T) of $Nd_{1-x}Pr_xCrO_3$ ($x = 0.0-0.30$) samples at the 100 Oe field and the inset shows the CW analysis for $x = 0.0$ sample. The $1/\chi$ vs T plots at different applied magnetic fields of 100 Oe, 1kOe and 10 kOe for (b) $x = 0.10$ (c) $x = 0.30$ samples showing the deviation from CW law at low field and (d) Log-log plot of inverse susceptibility as a function of temperature following Eq.4.3, where the red line is linear fit in the PM and GP regime.

Fig. 4-10(d) shows the plot of χ^{-1} vs $(T/T_C^R - 1)$ on log scale for $x = 0.3$ sample and the λ is obtained by the straight line fit in the GP regime. We found the value of λ is ~ 0.688

for $x = 0.30$, which signifies the GP possibly induced by Pr substitution. In the high-temperature region, the $\lambda \sim 0.07$ shows the system enters to complete the PM phase. Thus,

Fig. 4-11 shows the proposed magnetic phase diagram of the $Nd_{1-x}Pr_xCrO_3$ samples.

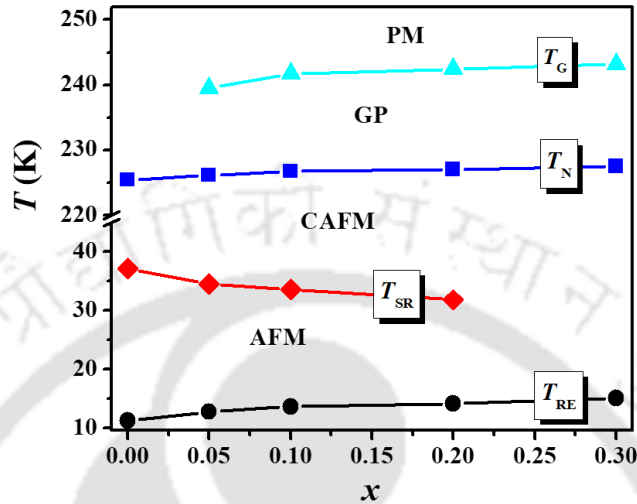


Fig. 4-11 The evolution of different phases through magnetic phase diagram of $Nd_{1-x}Pr_xCrO_3$ samples.

Magnetization as the function of the field after cooling from the paramagnetic state with the cooling field of 10 kOe for $x = 0.0-0.30$ samples at 5 K is plotted in **Fig. 4-12(a)**. The enlarged portion of the hysteresis loop for $x = 0.05-0.30$ samples in **Fig. 4-12(b)-(e)** demonstrate the significant increase in the coercive field (H_C) ~ 1224 Oe ($x = 0.05$) to 6186 Oe ($x = 0.30$) as the indication of increased weak ferromagnetic contributions with increasing Pr doping (see **Fig. 4-12(f)**). In addition, the shift of the $M-H$ loops toward the negative field axis signs the negative exchange bias (EB) effect. The exchange anisotropy at the ferromagnetic/antiferromagnetic interfaces describes the EB effect, and the analysis of the coercive field and EB field were carried out using $H_C = (H_+ - H_-)/2$ and $H_{EB} = (H_+ + H_-)/2$ where H_+ and H_- are the right and left coercive field values. Here, **Fig. 4-12(g)** illustrates the variation of H_{EB} as the function of Pr content at 5 K. We found that the value of H_{EB} increases from ~ -418.5 Oe to -1285.8 Oe for $x = 0.05$ to 0.30 Pr substitution. The

variation of H_{EB} at 5 K is similar to the variation of the cell distortion factor (d) obtained from XRD analysis (see **Fig. 4-12(h)**), which shows the maximum EB field for $x = 0.3$ sample having minimum cell distortion.

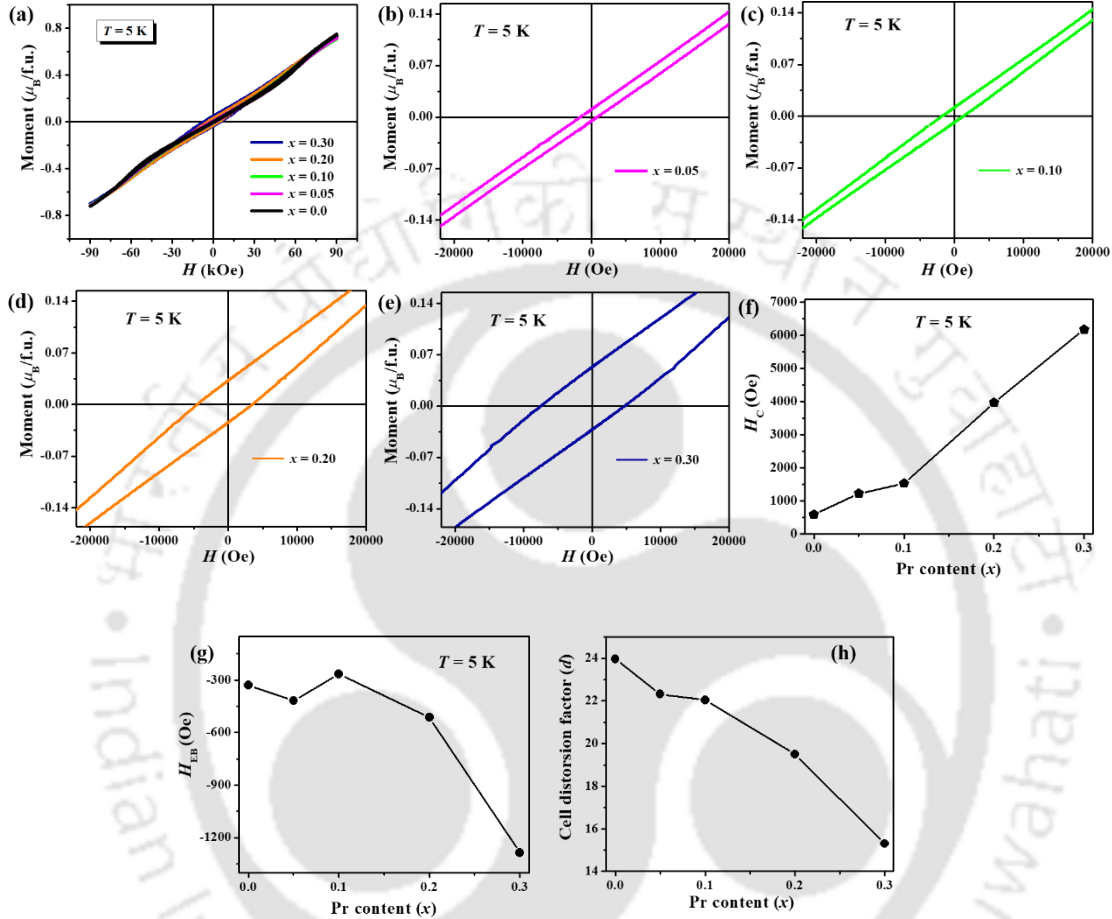


Fig. 4-12 (a) The M - H loops measured at $T = 5$ K ($T < T_{SR}$) for $Nd_{1-x}Pr_xCrO_3$ ($x = 0.0$ - 0.30) samples. The enlarged portion of the loops for (b) $x = 0.05$ (c) $x = 0.10$ (d) $x = 0.20$ and (e) $x = 0.30$ samples. The variation of (g) the coercive field H_c , (h) the exchange bias field H_{EB} and (i) the cell distortion factor with Pr substitution.

Furthermore, we have plotted the FC M - H loops for $x = 0.0$ - 0.30 samples in **Fig. 4-13(a)** at the $T = 100$ K which is above T_{SR} and below T_N . The enlarged portion of the M - H loop for $x = 0.05$ - 0.30 samples at 100 K in **Fig. 4-13(b)-(e)** shows the prominent left shift and significant negative EB for each sample. Similar to 5K, the coercive field (H_c) increases ~ 378 Oe ($x = 0.05$) to 1494.94 Oe ($x = 0.30$) at 100 K with increasing substitution (see **Fig.**

4-13(f)). However, the variation of H_{EB} as the function of Pr content at 100 K depicted in Fig. 4-13(g) is different from that of 5K. Here, the EB field first decreases from -1942.4 Oe ($x = 0.0$) to -746.4 Oe ($x = 0.10$) and then increases up to -1368.2 Oe ($x = 0.30$) with the increase of Pr substitution. It is important to note the trend of the EB field at 100 K is analogous to the variation of Cr-O2 bond length, as shown in Fig. 4-13(h).

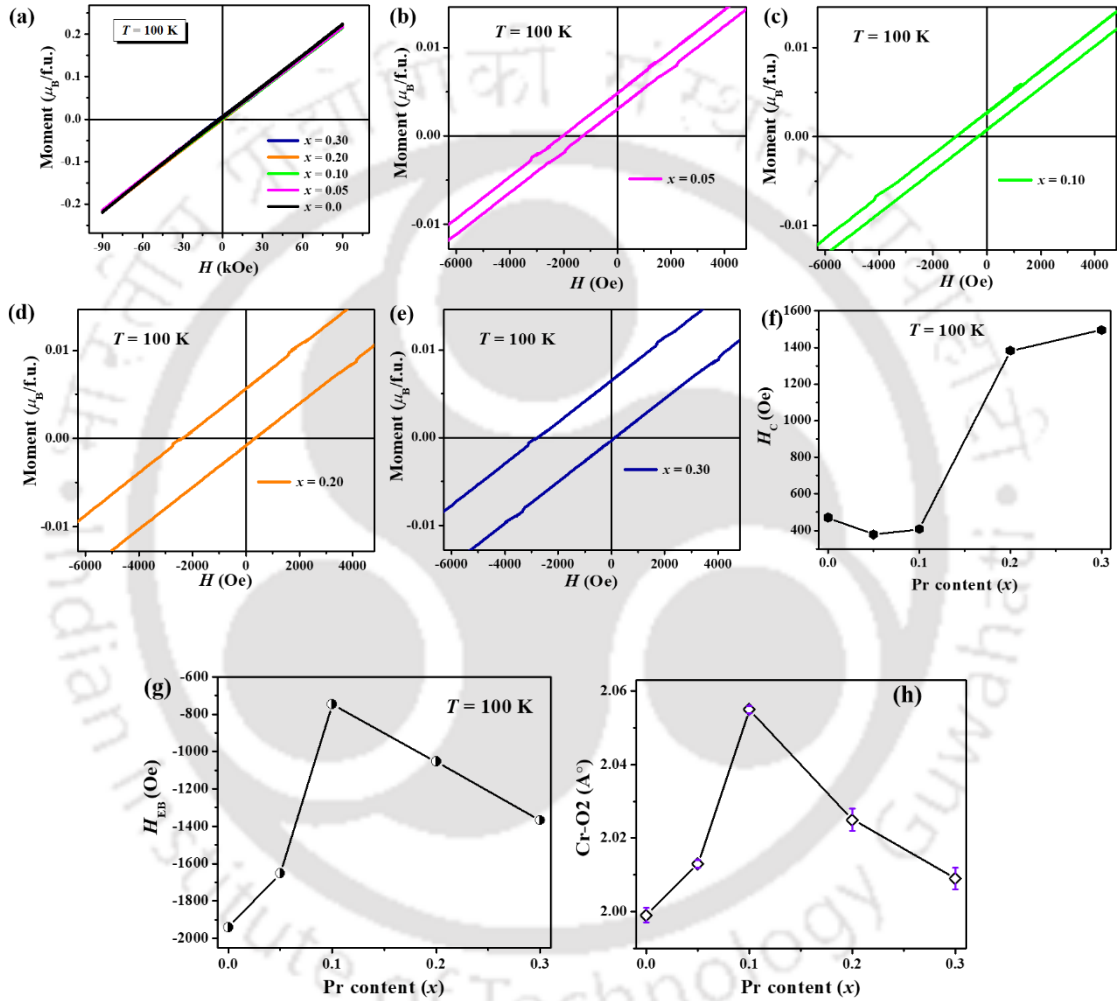


Fig. 4-13 (a) The M-H loops at $T = 100$ K ($T > T_{SR}$) for $Nd_{1-x}Pr_xCrO_3$ ($x = 0.0-0.30$) samples. The enlarged portion of the loops for (b) $x = 0.05$ (c) $x = 0.10$ (d) $x = 0.20$ and (f) $x = 0.30$ samples. The variation of (g) the coercive field H_c , (h) the exchange bias field H_{EB} and (i) the Cr-O2 bond length with Pr substitution.

The clear correspondence is obtained from the anomalous Raman behavior near 100 K for the modes related to anti-stretching and bending of CrO_6 octahedra in Fig. 4-6 and Fig.

4-7 validates the role of coupled structural features for the occurrence of EB effect in the present system. Furthermore, **Fig. 4-14(a)-(b)** shows the temperature dependence of coercive field $H_C(T)$ and the EB field $H_{EB}(T)$ extracted from FC M - H loops of $\text{Nd}_{1-x}\text{Pr}_x\text{CrO}_3$ ($x = 0.30$) sample. The H_C increases monotonically below T_N and attains a minimum value near 5 K. However, the non-monotonic behavior of the EB field shows significant H_{EB} in the temperature region below T_N with a maximum value of ~ -1991.8 Oe. The EB in present samples is explained in terms of the weak ferromagnetism of canted Cr^{3+} moments and rare-earth paramagnetic moment and their competing AFM interaction. The large H_{EB} at lower temperatures is attributed to the vanishing nature of T_{SR} , which can be related to less change of the Cr^{3+} spin canting angle.

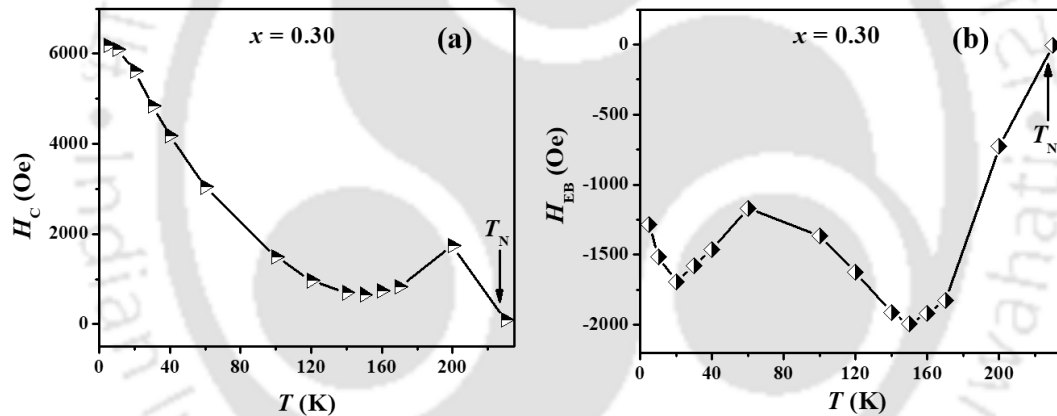


Fig. 4-14 Temperature dependence of (a) the coercive field $H_C(T)$ and (b) the exchange bias field $H_{EB}(T)$ extracted from FC M - H loops of $\text{Nd}_{1-x}\text{Pr}_x\text{CrO}_3$ ($x = 0.30$) sample.

From the magnetization measurements, we can expect Cr^{3+} spins to be in weak ferromagnetic condition for $x = 0.30$ sample with reduced distortions which maintains the EB effect at lower T . Such behavior of Pr^{3+} ($J = 4$) substitution in NdCrO_3 is different from the Eu^{3+} ($J = 0$) substitution where the EB field vanishes in the T_{SR} region [172]. These results indicate the spin reorientation and EB effect are significantly influenced by Pr substitutions.

4.4 Summary

We synthesized single-phase $Nd_{1-x}Pr_xCrO_3$ ($x = 0.05-0.30$) samples with an orthorhombic structure. The Rietveld refinement and Raman analysis show the unit cell expansion and reduced structural distortions with increasing Pr concentration. The EDX and FESEM images display the homogenous polycrystalline samples with smaller grain sizes due to Pr doping. The UV-Vis spectroscopy reveals the semiconductor behavior of the samples. The XPS analysis confirmed the presence of Pr ions in desired (3+) valance states. The dc magnetization measurements show higher magnetization and the increase in T_N up to ~ 227.5 K. Furthermore, the Pr doping increases the weak ferromagnetic phase by diluting antisymmetric Nd/Pr and Cr interactions, which gradually decreases the T_{SR} up to ~ 31.8 K and finally attributes to no spin-reorientation in $x = 0.30$ sample. In addition, the Griffiths-like phase is observed in $x = 0.05-0.30$ samples due to the presence of short-range weak ferromagnetic clusters above T_N . The shift of $M-H$ loops evidences the exchange bias effect for all samples. For the temperatures below T_{SR} , the significant increase of coercive field ~ 6186 Oe and EB field ~ -1285.8 Oe is marked with Pr substitution. The maximum EB field of ~ -1991.8 Oe is noted for $x = 0.3$ sample for $T = 150$ K. Importantly, in the temperature region above T_{SR} , the behavior EB field of $x = 0.0-0.30$ samples is matched with the trend of the Cr-O2 bond length. The anomalous softening of the CrO_6 bending mode and hardening of the anti-stretching mode indicate spin-phonon coupling. The present finding shows the coupling of structural and magnetic parameters in $Nd_{1-x}Pr_xCrO_3$ compounds to optimize multifunctional properties near liquid nitrogen temperature for various applications.



Chapter 5 : Exploration of low-field magnetic states in $Nd_{1-x}Ce_xCrO_3$

5.1 Introduction

In particular, the interplay of two different magnetic sublattices in $RCrO_3$ emerges the appealing multiferroicity, spin reorientation, magnetization switching, magnetocaloric effect, and improper electric polarization [2][177][178][88], which has stimulated significant attention in recent years. In these materials, the AFM ordering of Cr^{3+} ($S = 3/2$) spins occur below T_N with weak ferromagnetism [15] along the a or c unit cell axis depending upon the R ion. An intriguing phenomenon in $RCrO_3$ is the spin reorientation transition (T_{SR}), where the direction of moments changes from one crystal axis to another [161] and has found importance for topological spintronics in other materials [26]. Among the $RCrO_3$ compounds, both $NdCrO_3$ and $CeCrO_3$ possess magnetic R -ion ($J = 9/2$ and $5/2$) with larger $T_N \sim 220$ K and 260 K values suited for practical uses. In addition, a prominent T_{SR} at ~ 35 K exhibits in $NdCrO_3$ due to the evolution of weak ferromagnetic Cr^{3+} spins [111]. On the other hand, the $CeCrO_3$ shows a magnetic compensation at ~ 133 K where the magnetization becomes zero due to antiparallel coupled Cr^{3+} and Ce^{3+} spins [2]. In general, the substitution on A or B sites can change the distinctive properties of $RCrO_3$, which mainly originate from the cross-talk of $4f$ and $3d$ electrons [106]. For instance, the presence of nonmagnetic La^{3+} increases the energy level splitting of Cr^{3+} and Nd^{3+} indicated by low-temperature Schottky anomaly in $Nd_{(1-x)}La_xCrO_3$ [173]. Moreover, the spin-phonon induced EB has been found recently in $Nd_{(1-x)}Eu_xCrO_3$ via thermal variation of Raman modes [172]. Further, the magnetic Pr^{3+} ion triggers the spin reorientation followed by magnetization reversal and EB in the $Y_{(1-x)}Pr_xCrO_3$ [165]. The literature suggests the EB effect exhibiting no moment reversal is less studied in orthochromites. Furthermore,

substantial changes in the magnetic coercivity and linear field dependence of magnetization were observed in $La_{1-x}Ce_xCrO_3$ [174]. However, the evidence of ordered Ce^{3+} moments around 100 K using an extra peak in neutron diffraction data [128] is still a contentious topic. In addition, the redox-active Ce [175] promotes oxygen vacancy, enhancing the functionality of perovskite-type multiferroics by radically changing magnetic exchange interactions [176]. Such elusive behavior of these systems prompted us to study the Ce substitution in $NdCrO_3$, which is still unexplored. It is anticipated that the spin reorientation of the $Nd_{(1-x)}Ce_xCrO_3$ will be similarly rich, accounting for the modified R -Cr interactions and new magnetic states. As the Ce-based interaction can lead to the uncommon hysteresis below Neel temperature, it would be interesting to perturb the Nd site with Ce ions and observe its influence on EB-like features.

In this work, a systematic study based on XRD, Raman, XPS, and dc magnetization was performed to investigate the structure, valance state, and magnetic properties of $Nd_{(1-x)}Ce_xCrO_3$ ($x = 0.05-0.175$) samples. The process to obtain the two different magnetization states for the same external field in different directions is discussed.

5.2 Experimental Section

The samples of $Nd_{1-x}Ce_xCrO_3$ ($x = 0.05, 0.075, 0.10, 0.15, \text{ and } 0.175$) were made by the standard solid-state reaction route in polycrystalline form. The stoichiometric amount of Nd_2O_3 (99.9%), CeO_2 (99.9%), and Cr_2O_3 (99.6%) powders was well ground in an agate mortar pestle for several hours and pressed into pellets using a hydraulic press. The pellets were calcined at 1000 °C for 12 h, reground, and finally sintered at 1300 °C for 36 h in air. The structural analysis of the samples was done using the X-ray diffractometer (Rigaku, Smart Lab) with $Cu-K_\alpha$ radiation ($\lambda = 1.5406 \text{ \AA}$). For surface morphology, dispersive energy X-ray (EDX) (Sigma) and the field emission scanning electron microscope (FESEM) (Zeiss, Sigma 300) were used. The Raman spectra were collected using Raman

spectrometer (Horiba Jobin Yvon, LabRam HR) with a 514 nm wavelength. High-resolution X-ray photoelectron spectroscopy (XPS) was utilized to find the valance state of compositions by using an X-ray photoelectron spectrometer (ESCALAB Xi+, Thermo Fisher). Magnetization measurements in the 3-300 K temperature range were carried out with the help of the physical property measurement system (PPMS 9T, Quantum Design).

5.3 Results and discussions

5.3.1 X-ray diffraction (Rietveld refinement and Maximum Entropy Method)

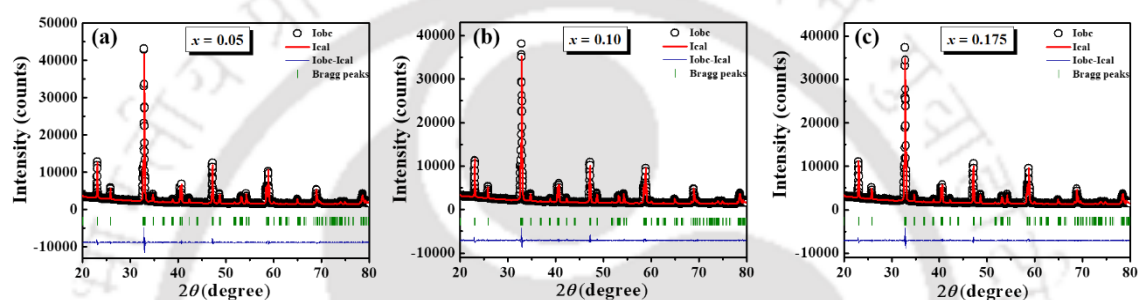


Fig. 5-1 The Rietveld refinement fitting of XRD data of the $Nd_{1-x}Ce_xCrO_3$ (a) $x = 0.05$ (b) $x = 0.10$ and (c) $x = 0.175$ compositions.

The $Nd_{(1-x)}Ce_xCrO_3$ ($x = 0.05-0.175$) samples were characterized with respect to phase purity by powder XRD. The peaks for each sample were indexed with distorted perovskite structure and matched with the parent compound. The analysis of XRD data shows the formation of single-phase samples up to $x = 0.175$ substitution, as the further increase of Ce resulted in the CeO_2 secondary phase. Reports suggest that the preparation of Ce-doped $RCrO_3$ using a solid-state reaction route is challenging due to the phase separation of CeO_2 driven by Ce^{3+} oxidation [174][128]. However, this is the first attempt to synthesize the Ce-substituted $NdCrO_3$ polycrystalline samples. The XRD data of all the samples were Rietveld refined by the orthorhombic symmetry (space group: $Pnma$). A representative Rietveld refined pattern of $x = 0.05, 0.10,$ and 0.175 samples are plotted in **Fig. 5-1**, which

shows the good agreement between the calculated and observed patterns by χ^2 values. The crystallographic parameters as the function of Ce content obtained from Rietveld refinement are listed in **Table 5-1**. We found that the lattice parameters a , b , and c and hence the cell volume V increases with x compared to the undoped compound [112] due to the substitution of Nd^{3+} (1.109 Å) site with Ce^{3+} (1.143 Å) ion having a larger ionic radius. Furthermore, the orthorhombic strain in the a - c plane (S_{ac}) for all the samples is estimated using the relation $S_{ac} = 2(a-c)/(a+c)$. We noticed the decrease in S_{ac} upon x variation, which accounts for the overall lattice expansion of $NdCrO_3$ with Ce doping. The observed variations in octahedral Cr-O1 bond length and Cr-O1-Cr bond angle for the samples are listed in **Table 5-1**. The refined atomic positions and site occupancies of Nd/Ce, Cr, O1, and O2 atoms are also mentioned, which shows that Ce occupies the Nd site. However, the decrease in refined O1 occupancy of $\sim 1\%$ ($x = 0.05$) to 4.8% ($x = 0.175$) may result from the O vacancy [177]. For the understanding of present compounds, we utilized the maximum entropy method (MEM), and the electron charge density distribution was determined using MEM.

The structure studies of several compounds have been effectively carried out using combined Rietveld refinement and MEM analysis [154]. The accuracy of the MEM lies in the fact that the charge density maps produced by the MEM are always consistent with the observed structural factor and least biased to the unobserved structure factors [178]. The MEM calculations were performed in $48 \times 72 \times 48$ pixels per orthorhombic lattice employing the computer program *Dysnomia* [154].

Table 5-1 The lattice parameters a , b , and c , cell volume (V), orthorhombic strain (S_{ac}), Cr-O1-Cr bond angle, Cr-O1 bond length, position coordinates, site occupancies obtained from Rietveld refinement and the electron charge density at the Cr-O1 bond mid and at central O1 atom obtained from MEM analysis.

Parameters		$x = 0.05$	$x = 0.075$	$x = 0.10$	$x = 0.15$	$x = 0.175$
a (Å)		5.4832(1)	5.4834(1)	5.4836(2)	5.4840(2)	5.4842(1)
b (Å)		7.6932(2)	7.6963(3)	7.6975(4)	7.6999(3)	7.7004(2)
c (Å)		5.4217(2)	5.4252(4)	5.4241(1)	5.4298(2)	5.4303(1)
V (Å ³)		228.70(5)	228.95(6)	228.95(7)	229.28(7)	229.32(6)
S_{ac} (10 ⁻³)		11.282	10.679	10.911	9.934	9.874
Cr-O1-Cr (°)		150.68(6)	151.08(5)	150.83(7)	151.81(7)	152.54(6)
Cr-O1 (Å)		1.977(3)	1.978(3)	1.979(4)	1.981(4)	1.982(3)
Nd/Ce	x	0.0404(1)	0.0402(1)	0.0399(1)	0.0396(1)	0.0394(1)
	z	0.0089(3)	0.0090(3)	0.0091(3)	0.0092(2)	0.0094(3)
	Occupancy(Nd)	0.475	0.462	0.449	0.425	0.412
	Occupancy(Ce)	0.024	0.035	0.049	0.073	0.087
Cr	Occupancy	0.500	0.502	0.500	0.501	0.501
O1	x	0.488(2)	0.488(1)	0.488(2)	0.489(1)	0.492(1)
	z	-0.093(2)	-0.092(2)	-0.091(2)	-0.088(2)	-0.086(2)
	Occupancy	0.495	0.493	0.490	0.481	0.476
O2	x	0.292(2)	0.291(1)	0.295(1)	0.301(2)	0.301(1)
	y	0.038(1)	0.038(1)	0.036(2)	0.033(1)	0.031(1)
	z	-0.282(2)	-0.280(2)	-0.280(2)	-0.278(2)	-0.277(2)
	Occupancy	1.004	1.001	1.003	1.002	1.001
Charge density	Cr-O1 (eÅ ⁻³)	0.71	0.74	0.75	0.83	0.87
	O1 (eÅ ⁻³)	24.7	24.4	22.3	21.9	20.2

Note: Space group: $Pnma$. Atomic positions: Nd/Ce, $4c$ ($x, 0.25, z$); Cr, $4b$ ($0, 0, 0.5$); O1, $4c$ ($x, 0.25, z$); and O2, $8d$ (x, y, z).

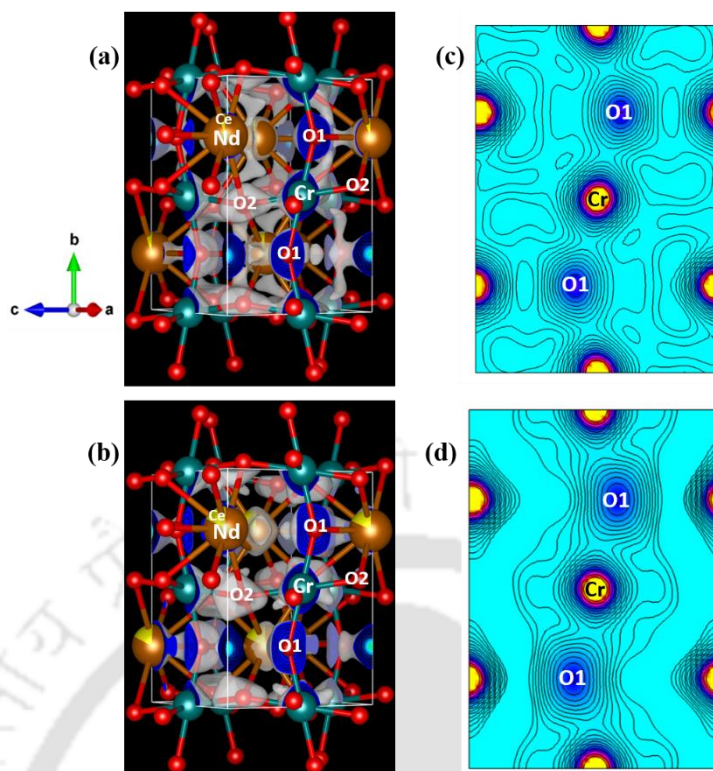


Fig. 5-2 The MEM charge density map of $Nd_{1-x}Ce_xCrO_3$ (a) $x = 0.05$ and (b) 0.175 samples at the iso surface level of $1 \text{ e}\text{\AA}^{-3}$. The charge density distribution of (c) $x = 0.05$ and (d) $x = 0.175$ samples for the (100) section. The contour range is from 0 to $1 \text{ e}\text{\AA}^{-3}$ with $0.1 \text{ e}\text{\AA}^{-3}$ intervals.

The density maps in **Fig. 5-2(a)(b)** demonstrate the electron clouds extending out from the respective Nd atoms (with Ce substitution shown by yellow color), Cr atoms (on the octahedral site), and O atoms (of two type, namely, O1 and O2) for $x = 0.05$ and 0.175 compounds. The increased Ce substitution results in the detachment of O electron clouds from Nd/Ce-O and CrO_6 bonding (**Fig. 5-2 (b)**). In **Fig. 5-2(c)-(d)**, the electron density distribution for (100) plane of $x = 0.05$ and 0.175 samples display the possible Cr-O1 covalent feature. It is observed that the localized ordering of charges [177] toward the Cr-O1-O-Cr bonding direction increases with Ce concentration in the NdO matrix. The values of electron charge density around the Cr-O1 bond midpoint are estimated and written in **Table 5-1**. The observed charge density of $\sim 0.653(4) \text{ e}/\text{\AA}^3$ for the parent compound is comparable with the charge density of $\sim 0.6 \text{ e}/\text{\AA}^3$ of Mn-O covalent bonding [150]. It is noticed that

the Cr-O1 charge density increases from $\sim 0.711(4) e/\text{\AA}^3$ for $x = 0.05$ to $0.878(3) e/\text{\AA}^3$ for $x = 0.175$ sample, which indicates a small improvement of the Cr-O1 covalent nature. **Table 5-1** also shows the decrease in the electron density at the central O1 atoms from $\sim 24.73(3) e/\text{\AA}^3$ ($x = 0.05$) to $20.20(3) e/\text{\AA}^3$ ($x = 0.175$). This value is in accordance with oxygen vacancies in a few oxides [179]. Therefore, the less occupied O1 sites may cause oxygen vacancies and slightly enhance the Cr-O1 covalent bonding for $Nd_{1-x}Ce_xCrO_3$ compositions.

5.3.2 Microstructural analysis

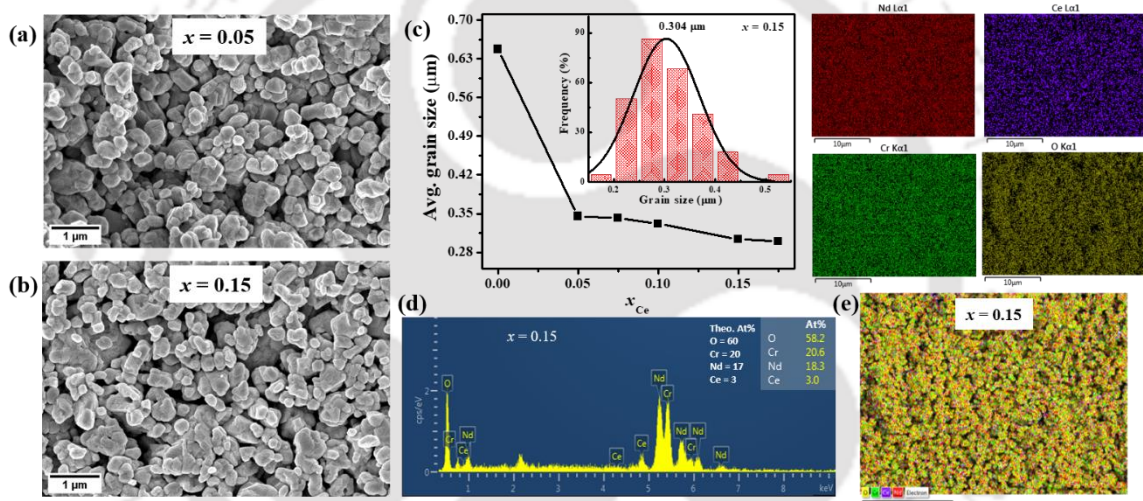


Fig. 5-3 FESEM images of the $Nd_{1-x}Ce_xCrO_3$ (a) $x = 0.05$ and (b) $x = 0.15$ composition (c) Average grain size as the function of Ce concentration and the inset shows the grain size distribution of $x = 0.15$ sample (d) EDX spectrum and (e) elemental mapping of $x = 0.15$ composition showing the presence of Nd, Ce, Cr, and O elements.

The FESEM micrographs in **Fig. 5-3(a)-(b)** elucidate the surface morphology of the $Nd_{1-x}Ce_xCrO_3$ ($x = 0.05, 0.15$) samples with uniform grain growth. The average grain size is estimated by Image-J software (linear intercept method), and its value ranges from 0.345 μm for $x = 0.05$ to 0.299 μm for $x = 0.175$ composition. It is observed from **Fig. 5-3(c)** that the substitution of Ce causes a smaller grain size than the undoped one, which may arise

from the reduced surface energy of the grains [160]. In **Fig. 5-3(d)-(e)**, the EDX spectrum and mapping for $x = 0.15$ compound detect the O, Cr, Nd, and Ce elements with uniform distribution.

5.3.3 Raman analysis

The subtle changes of the $NdCrO_3$ lattice due to the Ce substitutions are examined through Raman spectroscopy. The Raman spectra of $Nd_{(1-x)}Ce_xCrO_3$ ($x = 0.05-0.175$) compounds at room temperature are shown in **Fig. 5-4**. We know the group theory describes the 24 phonon modes of orthorhombic $RCrO_3$ with four formulas per unit cell as, $\Gamma = 7A_g + 5B_{1g} + 7B_{2g} + 5B_{3g}$ [46]. Thus, the eleven Raman active modes similar to the pristine sample and an additional hump are detected for Ce substitution, as depicted in **Fig. 5-4**. The available literature shows Raman behavior of Ce-based rare-earth chromites is limited. Hence, it is important to discuss Raman behavior of the present system in detail.

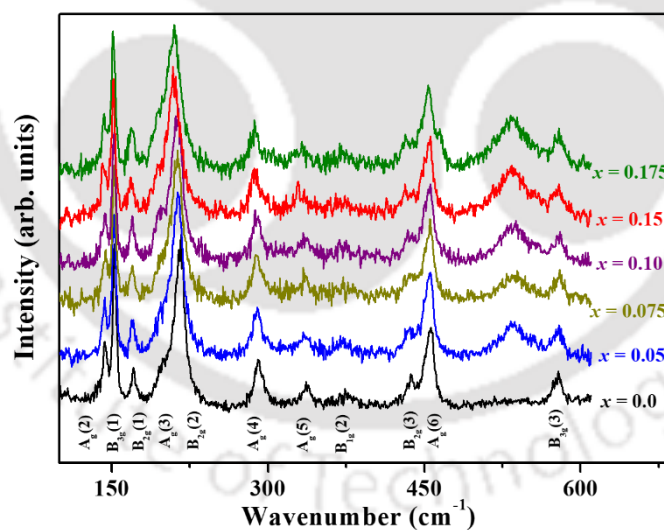


Fig. 5-4 Raman spectra acquired from the $Nd_{1-x}Ce_xCrO_3$ ($x = 0.05-0.175$) compositions.

The variation of wavenumber with Ce concentration for the modes having significant Raman shift is depicted in **Fig. 5-5(a)**. We found that the mode frequencies (values are written for $x = 0.05$ sample) $A_g(2) \sim 142.9 \text{ cm}^{-1}$, $B_{3g}(1) \sim 152.2 \text{ cm}^{-1}$ and $B_{2g}(1) \sim 169.9$

cm^{-1} related to Nd/Ce -ion (z)(y)(x) vibrations show the small shift toward low wavenumber (red shift) with increasing x . However, the noticeable redshift of $\sim 5\text{ cm}^{-1}$ is marked for the doublet of symmetry $A_g(3)$ at $\sim 200\text{ cm}^{-1}$ associated with in-phase CrO_6 (y) rotation and $B_{2g}(2)$ at 213.4 cm^{-1} related with Nd/Ce-O(z) vibration, displayed in **Fig. 5-5(a)**. We can expect such behavior of Raman modes related to the increase of A-site ionic radii introduced by Ce substitution. Other less intense modes $A_g(4) \sim 289.5\text{ cm}^{-1}$ related to Nd/Ce-O(x) vibration, $A_g(5) \sim 334.8\text{ cm}^{-1}$ (see **Fig. 5-5(a)**) and $B_{1g}(2) \sim 372.8\text{ cm}^{-1}$ associated with out of phase (x)(y) CrO_6 rotation also exhibit the red shift. Similarly, the doublet bands near $B_{2g}(3) \sim 435.8\text{ cm}^{-1}$ (see **Fig. 5-5(a)**) and $A_g(6) \sim 454.5\text{ cm}^{-1}$ corresponding to tilting and bending of CrO_6 octahedra shift to low wavenumber with increasing x . Only one phonon mode $B_{3g}(3) \sim 577.6\text{ cm}^{-1}$ related with the anti-stretching of CrO_6 octahedra shift $\sim 1.5\text{ cm}^{-1}$ to high wavenumber (blue shift) with increasing Ce percentage, which is plotted in **Fig. 5-5(a)**.

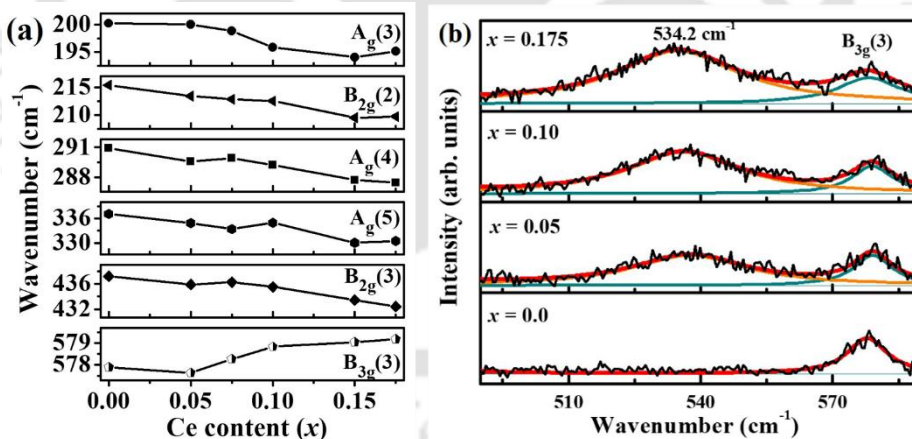


Fig. 5-5 The wavenumbers as a function of Ce content of selected phonon modes and (b) Fitting of Raman spectra of $Nd_{1-x}Ce_xCrO_3$ ($x = 0.05$ to 0.175) compositions in 490 to 590 cm^{-1} wavenumber range illustrating additional hump as compared to the undoped sample.

These changes are attributed to the change of CrO_6 octahedral distortion by substituting Nd with Ce ion. The profile fitting in **Fig. 5-5(b)** displays the broad hump centered around 537.4 cm^{-1} ($x = 0.05$) to 534.2 cm^{-1} ($x = 0.175$).

It is noticed that the hump does not correspond to the phonon modes of orthorhombic $RCrO_3$ ($R = Nd, Ce$) compounds [46]. Therefore, to assign it, we first checked the phonon frequencies of CeO_2 using the DFPT calculations by the Quantum espresso package [127]. The calculations confirm only one Raman active mode $F_{2g} \sim 421.5 \text{ cm}^{-1}$, comparable with the experimental value $\sim 464.5 \text{ cm}^{-1}$ and other reported results [180], eliminating the possibility of a secondary CeO_2 phase. Moreover, the Raman spectra of Ce-based oxides reveal an additional band around $540\text{-}600 \text{ cm}^{-1}$ related to oxygen vacancies through charge compensating defects [181][182]. Hence, the hump is assigned as the vibrational band related to the oxygen vacancies. The readjustment of the Ce oxidation number may induce oxygen vacancy in substituted samples, which will be probed with XPS measurement in the upcoming section.

5.3.4 XPS analysis

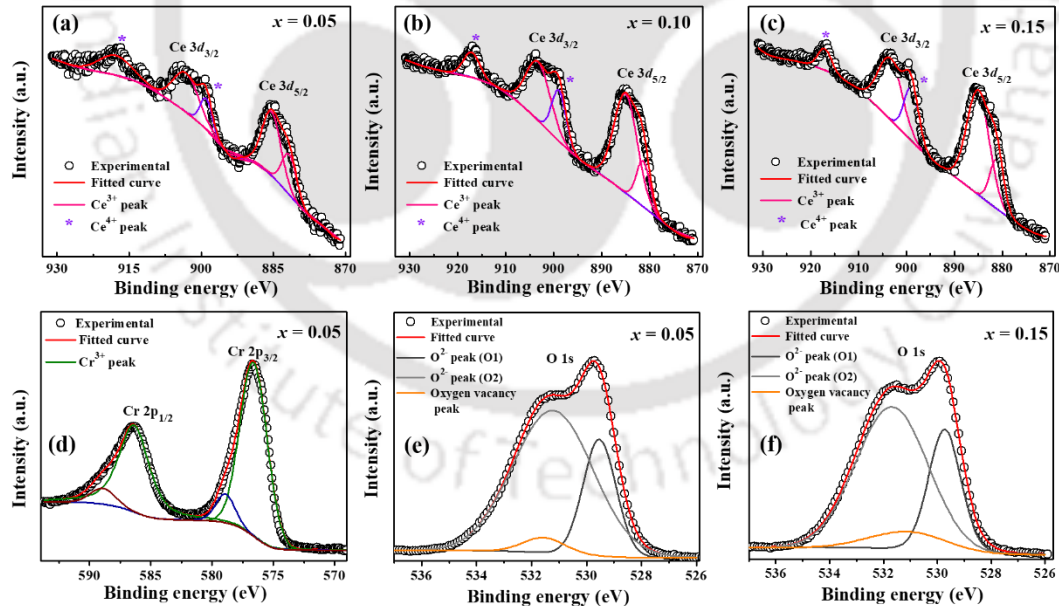


Fig. 5-6 The XPS results of $Nd_{1-x}Ce_xCrO_3$ for (a)-(c) The core-level Ce 3d of $x = 0.05, 0.10$ and 0.15 (d) The core-level Cr 2p spectra of $x = 0.05$ and (e)-(f) The O 1s spectra of $x = 0.05$ and 0.15 samples.

The XPS data of the present compositions were also recorded to verify the valence states of Nd/Ce and Cr ions, which might affect the magnetic behavior of the $Nd_{(1-x)}Ce_xCrO_3$

system. Here, **Fig. 5-6(a)-(c)** displays the high-resolution Ce 3d spectra for substituted ($x = 0.05, 0.10, \text{ and } 0.15$) samples. The existence of Ce^{3+} ($J = 5/2$) ion is confirmed with the spin-orbit resolved $Ce3d_{5/2}$ peaks at 881.7, 885.3 eV, and $Ce3d_{3/2}$ peak at 903.1 eV binding energies for $x = 0.05$ sample. In addition, the deconvoluted $Ce3d_{3/2}$ peak at 898.9 eV and extra peak at 917.7 eV indicate the presence of Ce^{4+} ($J = 0$) ion [183] for the $x = 0.05$ sample. The calculated percentage of Ce^{3+} and Ce^{4+} ions by quantitative analysis [184] are listed in **Table 5-2**. Interestingly, we found that the Ce^{3+}/Ce^{4+} ratio is nearly 2:1, which is constant while increasing Ce content. The Ce^{3+} and Ce^{4+} switching occurs during the oxidation-reduction process, where the Ce^{3+} ions bind to the defect and contributes to Ce^{4+} ions [185][186].

Table 5-2 The Ce ions percentage in 3+, 4+ oxidation states for the $Nd_{1-x}Ce_xCrO_3$ ($x = 0.05, 0.10, \text{ and } 0.15$) compositions.

% of ions	$x = 5 \%$	$x = 10 \%$	$x = 15 \%$
Ce^{3+}	3.17	6.66	9.64
Ce^{4+}	1.66	3.72	5.06

Fig. 5-6(d) displays the core level Cr 2p binding energy spectra of the $x = 0.05$ compound. The spin-orbit splitting of the 2p level into $2p_{3/2}$ peak situated at ~ 576.1 eV and $2p_{1/2}$ peak at ~ 585.7 eV binding energies confirm the Cr^{3+} ($S = 3/2$) ion agrees with the report [163]. The $Cr2p_{3/2}$ and $Cr2p_{1/2}$ levels were resolved into the peak at ~ 578.2 eV and 588.5 eV related to the multiplet of Cr^{3+} $2p_{3/2}$ and small shake-up contribution [163][162], respectively. Similar results were observed for the other samples.

Furthermore, the O 1s XPS spectra for the $x = 0.05$ and 0.15 samples are shown in **Fig. 5-6(e)-(f)** and deconvoluted into three peaks. The binding energy peaks (values are written for $x = 0.15$) at ~ 529.7 eV and 531.6 eV characterize the lattice oxygen $(O1)^{2-}$ and $(O2)^{2-}$

ions, and the resolved peak at 531.1 eV corresponds to the oxygen vacancies. [187]. Further, the area under the peaks in **Fig. 5-6(e)-(f)** reveals the oxygen vacancies of $\sim 2.20\%$ for $x = 0.05$ and $\sim 6.18\%$ for $x = 0.15$ compound. We find the oxygen vacancies through XPS are in accordance with MEM and Raman analysis. Thus, both Ce^{3+} and Ce^{4+} ions occupy the Nd^{3+} site, and the oxygen vacancies maintain the charge neutrality within $Nd_{1-x}Ce_xCrO_3$ compositions.

5.3.5 Magnetic characterization

Fig. 5-7(a) shows the temperature dependence of magnetization of the $Nd_{1-x}Ce_xCrO_3$ ($x = 0.05-0.175$) samples for the applied field of 100 Oe in field cooled (FC) mode. We observed a decrease in the magnetization below magnetic ordering with increasing Ce substitution.

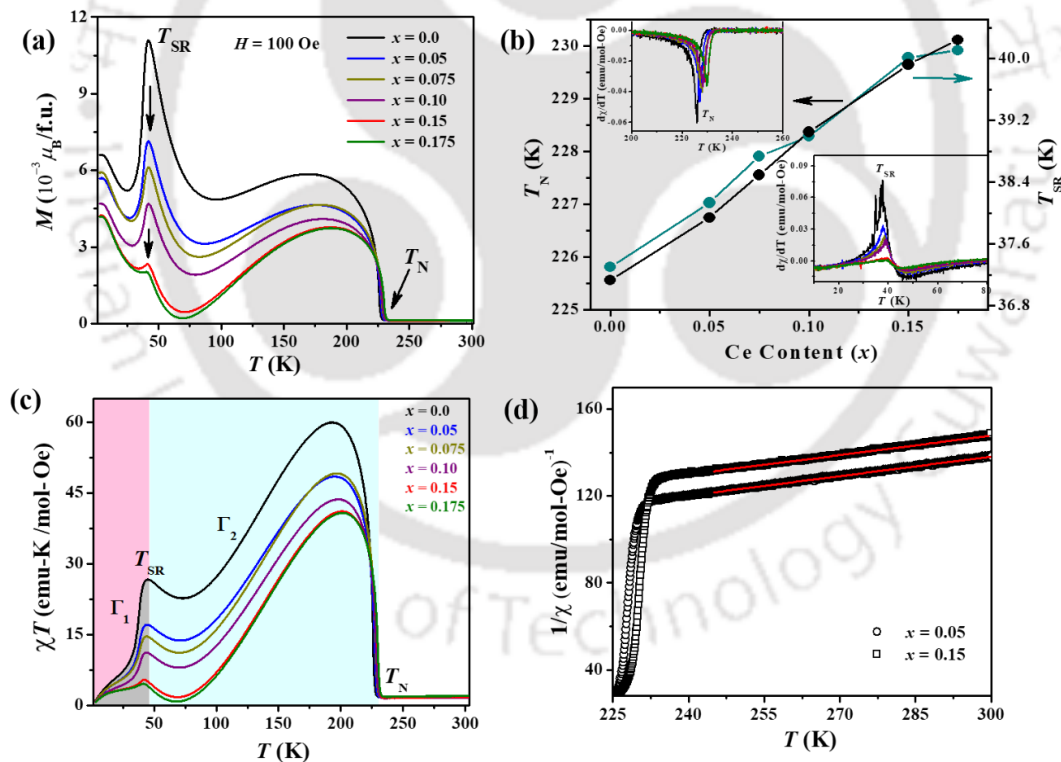


Fig. 5-7 (a) FC magnetization vs. temperature under an applied magnetic field of 100 Oe of $Nd_{1-x}Ce_xCrO_3$ ($x = 0.05-0.175$) samples (b) The value of T_N and T_{SR} as the function of Ce content where insets show extended $d\chi/dT$ vs. T curves of present samples (c) Temperature variation of the magnetic susceptibility times temperature (χT) using 100 Oe FC magnetization curves, demonstrating the magnetic phases and (d) Inverse susceptibility vs. temperature curves and the solid red lines are fit to the Curie-Weiss law for selected samples.

The derivative of magnetic susceptibility ($d\chi/dT$) in the inset of **Fig. 5-7(b)** determines the AFM ordering temperature (T_N) and spin-reorientation transition temperature (T_{SR}). **Fig. 5-7(b)** shows the increase in $T_N \sim 229.9$ K and $T_{SR} \sim 40.2$ K as compared to pure sample [111] and ascribed to the increased structural parameters with Ce substitution. We have plotted the magnetic susceptibility multiplied by temperature (χT) as the function of temperature [188] of $x = 0.0-0.175$ samples in **Fig. 5-7(c)**. The χT vs. T graph demonstrates the weak ferromagnetic $\Gamma_2(F_x, C_y, G_z)$ phase below T_N and the AFM $\Gamma_1(A_x, G_y, C_z)$ phase [16] below T_{SR} by the shaded areas in **Fig. 5-7(c)**. It is found that the reorientation of canted Cr^{3+} moments from Γ_2 to Γ_1 phase exhibits for each composition. However, the strength of spin reorientation significantly reduces due to the decreased Γ_1 phase. This can be related to the weakened Nd-Cr magnetic exchange interactions with the increase of Ce concentration. The detailed analysis of T_{SR} as the function of the applied magnetic field will be discussed later.

For quantitative interpretation of magnetization data, the temperature dependence of dc magnetic susceptibility data above T_N were fitted to the Curie-Weiss law,

$$\chi = \frac{C}{T - \Theta} \quad (5.1)$$

where, C and Θ are the Curie constant and Curie temperature respectively. The temperature dependence of inverse susceptibility and the fitting for $x = 0.05$ and 0.15 samples in paramagnetic region is shown in **Fig. 5-7(d)**. The $1/\chi$ vs T data fitted well to the Curie-Weiss law above long-range ordering and deviates from this behavior below T_N due to weak ferromagnets arising from canted Cr^{3+} antiferromagnetism. The fitted value of the C is used for the calculation of the effective paramagnetic moment (μ_{eff}) by using the relation,

$$\mu_{eff} = \sqrt{\frac{3K_B C}{N_A \mu_B^2}} \quad (5.2)$$

where, K_B , N_A and μ_B are the Boltzmann constant, Avogadro number and Bohr magneton respectively. Alternatively, the theoretical value of μ_{eff} for the samples is calculated using the relation,

$$\mu_{eff}^T = \sqrt{[(1-x)\mu_{Nd}^2 + x\mu_{Ce}^2 + \mu_{Cr}^2]} \quad (5.3)$$

We observed that the $\mu_{eff} \sim 5.167 \mu_B$ ($x = 0.05$) to $5.098 \mu_B$ ($x = 0.175$) were less than the corresponding $\mu_{eff}^T \sim 5.267 \mu_B$ ($x = 0.05$) to $5.188 \mu_B$ ($x = 0.175$) values. The decrease of μ_{eff} with increasing x is related to substituting Ce^{3+} ion ($2.54 \mu_B$) on the Nd^{3+} site ($3.62 \mu_B$). However, the slight difference between μ_{eff} and μ_{eff}^T values can be due to the certain amount of non-magnetic Ce^{4+} ions ($J = 0$) along with magnetic Ce^{3+} ions ($J = 5/2$). We found a good agreement between $\mu_{eff} \sim 5.15 \mu_B$ and $\mu_{eff}^T \sim 5.17 \mu_B$ ($x = 0.15$) using relative percentage of Ce^{3+} and Ce^{4+} ions from XPS analysis. The Curie temperature (Θ) obtained from the Curie-Weiss law fitting increases from ~ -161.5 K ($x = 0.05$) to -201.2 K ($x = 0.175$), showing the predominance of antiferromagnetic interactions.

Fig. 5-8(a) represents the magnetization hysteresis ($M-H$) loops of $x = 0.05-0.175$ samples. The $M-H$ loops were measured after cooling the samples from 300 K to 100 K in FC condition with a field of 50 kOe. These loops were found to be linear for the $T < T_N$ where the canted AFM ordering of Cr^{3+} spins related to antisymmetric Dzyaloshinsky-Moriya interaction is present [54]. The enlarged isotherms in **Fig. 5-8(b)-(e)** depict the unusual closure of the $M-H$ loop and its shifting along the negative field axis, evidencing the EB effect. The literature suggests a linear field dependency of magnetization without any

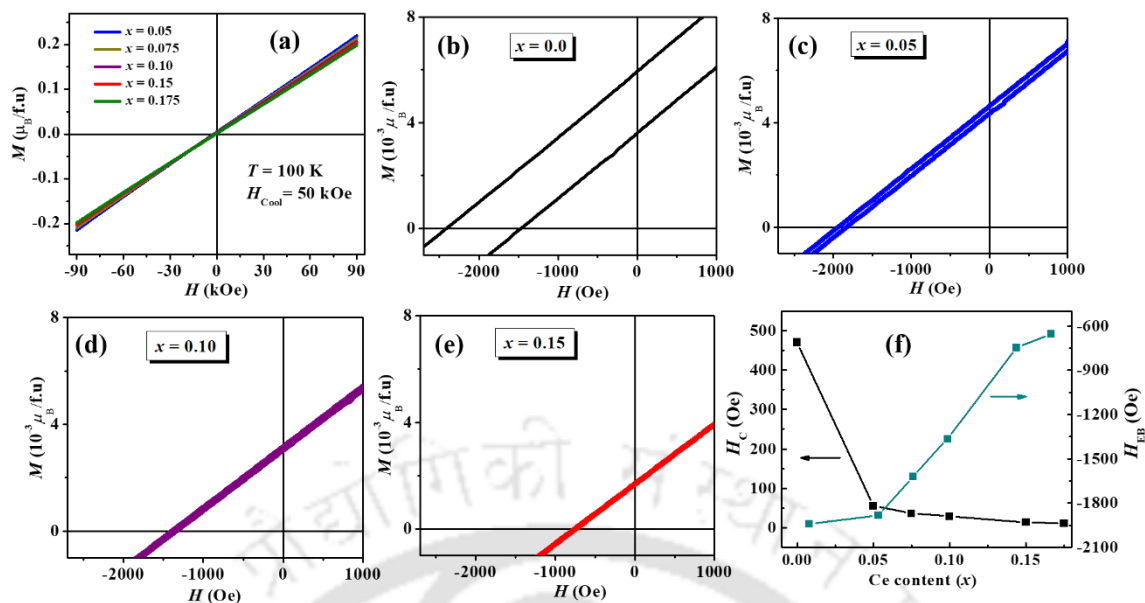


Fig. 5-8 (a) Field dependence of magnetization (M - H) of $Nd_{1-x}Ce_xCrO_3$ ($x = 0.05$ - 0.175) samples in -90 to $+90$ kOe field sweep at 100 K (b)-(e) Expanded view of exchange biased M - H loops of $x = 0.0, 0.05, 0.10,$ and 0.15 samples and (f) The variation of EB field (H_{EB}) and coercive field (H_C) with Ce content.

hysteresis only for the higher Ce substitution in $LaCrO_3$, however, no EB effect was seen in these compounds [174]. The EB field and the coercive field were obtained using the relation $H_{EB} = (H_+ + H_-)/2$ and $H_C = (H_+ - H_-)/2$ where H_+ and H_- are the ascending and descending branch field value across $M = 0$. From **Fig. 5-8(f)**, we observed the $H_{EB} \sim -1942$ Oe for $x = 0.0$ sample at the $H_C \sim 470$ Oe. However, for $x = 0.075$ - 0.175 samples the H_{EB} decreases monotonically to a value ~ -653 Oe. Only for the $x = 0.05$ sample, the H_{EB} decreases slightly from the parent compound to a value ~ -1890 Oe with a sharp decrease of $H_C \sim 55$ Oe. This sharp decrease of coercivity merges the M - H loop for Ce substituted samples, as shown in **Fig. 5-8(c)-(e)**. The correlations between EB and magnetization reversal are established in various single-phase compounds [165][7][189]. However, the small Ce substitution causing the EB through shifted paramagnetic type loop seems uncommon.

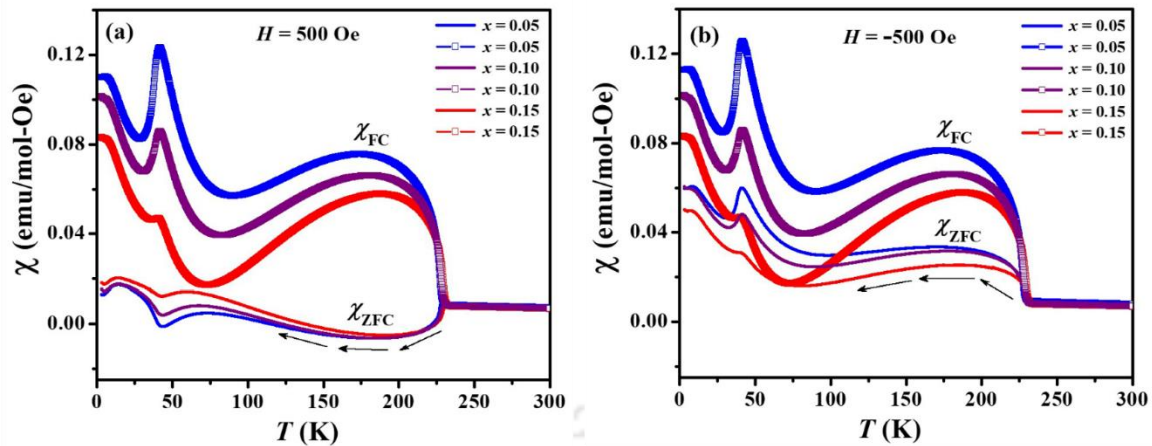


Fig. 5-9 The Magnetic susceptibility as the function of temperature, measured in ZFC mode (χ_{ZFC}) (solid line) and FC mode (χ_{FC}) (scatter line) at the magnetic field of (a) $H = +500$ Oe and (b) $H = -500$ Oe for the $Nd_{1-x}Ce_xCrO_3$ ($x = 0.05, 0.10$ and 0.15) samples. The arrow indicates the χ_{ZFC} direction for the positive and negative fields, respectively.

Hence, to find the possible correlations, we studied the temperature dependence of magnetic susceptibility under zero field cooled condition (χ_{ZFC}) and field cooled condition (χ_{FC}) at $H = 500$ Oe for $x = 0.05, 0.10$ and 0.15 samples shown in **Fig. 5-9(a)**. The large bifurcation between ZFC and FC magnetization below T_N results in the positive χ_{FC} at all temperatures. However, the negative χ_{ZFC} in **Fig. 5-9(a)** sign the negative magnetization (see arrows) for the samples. The negative magnetization occurs in Γ_2 state within the 100 K to 223 K T -range, where the G_z spin component aligns opposite to the applied field. The negative magnetization with diamagnetism-like characteristics is observed for the ZFC condition under low fields in polycrystalline $HoCrO_3$ [190] and $PrCr_{1-x}Cu_xO_3$ [191] orthochromite. However, these reports do not show any negative susceptibility to distinguish diamagnetism. Therefore, for further understanding of the ZFC and FC susceptibility, the above measurements have been repeated under the magnetic field of -500 Oe and depicted in **Fig. 5-9(b)**. From these curves, we found that the χ_{ZFC} flips to positive values (see arrows), while the χ_{FC} remains the same for all the samples. We observed the sign change of χ_{ZFC} for the same applied field of the magnitude of 500 Oe.

Such sign change in magnetic susceptibility is unexpected and beyond the diamagnetism-like description of negative magnetization.

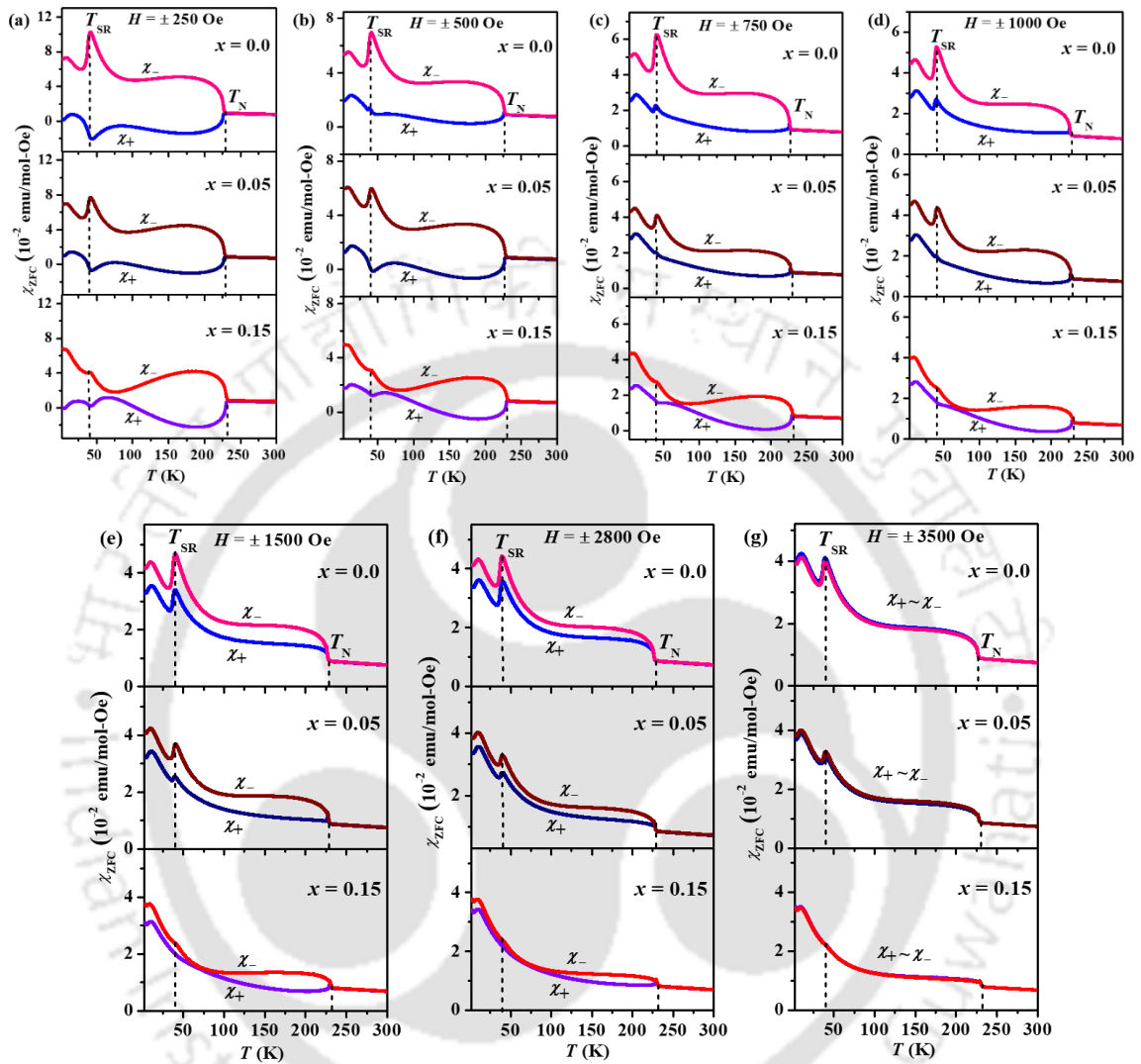


Fig. 5-10 Temperature dependence of magnetic susceptibility measured in ZFC mode (χ_{ZFC}) under the applied field of (a) ± 250 Oe (b) ± 500 Oe (c) ± 750 Oe (d) ± 1000 Oe (e) ± 1500 Oe (f) ± 2800 Oe and (g) ± 3500 Oe for the $\text{Nd}_{1-x}\text{Ce}_x\text{CrO}_3$ ($x = 0.0, 0.05$ and 0.15) compositions. Here, χ_+ (solid line in blue shades) is the ZFC susceptibility under the positive applied magnetic field, and χ_- (solid line in red shades) is the ZFC susceptibility under the negative applied magnetic field.

Therefore, it is crucial to examine the ZFC magnetic susceptibility at the same magnitude of positive and negative magnetic fields. For this, we measured the magnetic susceptibility under two conditions (1) the ZFC susceptibility at the positive applied magnetic field (χ_+)

and (2) the ZFC susceptibility at the negative applied magnetic field (χ_-). The plots of χ_+ vs. T for the applied field of +250 to +3500 Oe for $x = 0.0-0.15$ samples are shown by the blue curves in **Fig. 5-10(a)-(g)**. The plots of χ_- vs. T for the applied of -250 to -3500 Oe are shown by the red curves in the same **Fig. 5-10(a)-(g)**. These measurements show an interesting thermomagnetic history. Here, the χ_+ vs. T curves follow the different trend than χ_- vs. T ones. The χ_- in **Fig. 5-10(a)-(g)** show the increase below T_N and exhibits the spin reorientation transition across T_{SR} . This behavior of χ_- is similar to the temperature dependence of FC magnetization explained in **Fig. 5-7(a)**. However, the χ_+ at 250 Oe and 500 Oe in **Fig. 5-10(a)-(b)** decreases below T_N attaining the minimum value near T_{SR} and afterward it increases with lowering temperatures. From **Fig. 5-10(c)**, we noticed that the χ_+ changes its form at 750 Oe and shows a negligible reorientation of Cr^{3+} spins. For the fields > 1000 Oe in **Fig. 5-10(d)-(f)**, the deviation of χ_+ from χ_- gradually decreases due to the re-establishment of T_{SR} . It indicates the spin reorientation of the present system is soft in nature. Finally, the overlapping of χ_+ and χ_- occurs at 3500 Oe in **Fig. 5-10(g)**, where the thermo-magnetization history of $x = 0.0-0.15$ samples vanishes.

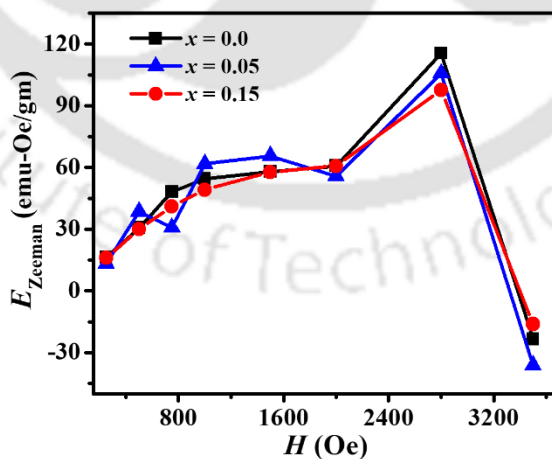


Fig. 5-11 Magnetic field dependence of Zeeman energy for the $Nd_{1-x}Ce_xCrO_3$ ($x = 0.0, 0.05, \text{ and } 0.15$) samples.

For further understanding, we have calculated the Zeeman energy ($-\Delta MH$) using the magnetization values obtained from **Fig. 5-10(a)-(g)**. In **Fig. 5-11**, we have shown the change in Zeeman energy as the function of the applied field for $x = 0.0$ - 0.15 samples at 150 K. The Zeeman energy of the samples increases with increasing magnetic field and becomes maximum at 2800 Oe, and afterward, it sharply decreases at 3500 Oe. We know the negative EB field is related to the additional Zeeman energy needed to overcome the internal coupling and align the spins along the magnetic field direction.

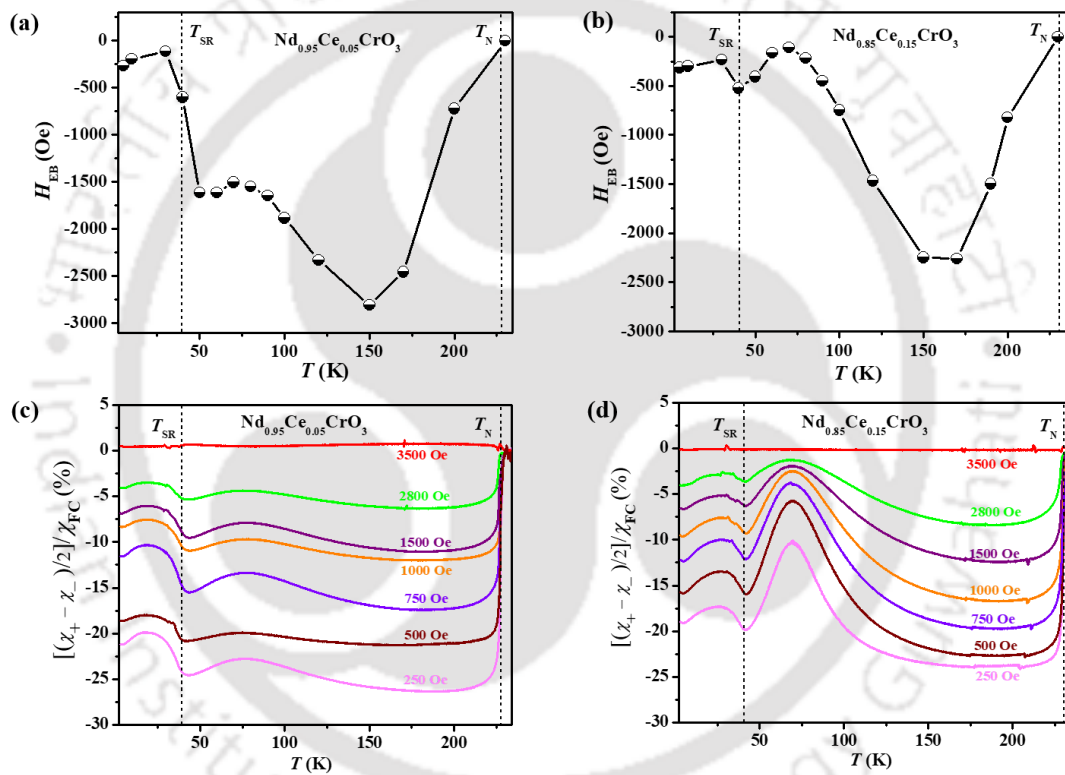


Fig. 5-12 The Temperature dependence of EB field (H_{EB}) for $Nd_{1-x}Ce_xCrO_3$ (a) $x = 0.05$ and (b) 0.15 samples. Temperature dependence of ZFC magnetic susceptibility difference normalized by FC susceptibility $\frac{(\chi_+ - \chi_-)/2}{\chi_{FC}}$ for (c) $x = 0.05$ and (d) 0.15 samples under the applied field of 250 Oe to 3500 Oe.

Therefore, the EB field as the function of temperature for $x = 0.05$ and 0.15 samples are analyzed in **Fig. 5-12(a)-(b)**. From these plots, we marked a maximum $H_{EB} \sim -2809$ Oe for $x = 0.05$ and -2260 Oe for $x = 0.15$ samples at 150 K. **Fig. 5-11** confirms both the

samples exhibit the maximum Zeeman energy at the magnetic field of 2800 Oe at that temperature. Thus, the maximum H_{EB} is comparable with the magnetic field emerging maximum Zeeman energy. It shows a correspondence between the Zeeman energy and the EB.

Furthermore, we calculated the ZFC susceptibility difference using χ_+ and χ_- values from **Fig. 5-10(a)-(g)** and normalized it by the FC susceptibility at the same field. In **Fig. 5-12(c)-(d)**, we have shown the temperature dependence of the ratio $\left[\frac{(\chi_+ - \chi_-)/2}{\chi_{FC}}\right]$ for $x = 0.05$ and 0.15 compounds. Interestingly, this ratio reveals the amount of the pinned Cr^{3+} spins below T_N . We found that a maximum $\sim 26\%$ and 24% pinning occurs for $x = 0.05$ and 0.15 samples. This means 1 spin out of 4 Cr^{3+} spins are unable to rotate and align to give the required magnetic structure for that direction of the magnetic field. Hence, it is not unusual to find that the maximum Zeeman energy for the doped samples is of a similar magnitude. The temperature variation of H_{EB} and $\left[\frac{(\chi_+ - \chi_-)/2}{\chi_{FC}}\right]$ in **Fig. 5-12(a)-(d)** shows the maximum H_{EB} lying in the region of maximum pinning of Cr^{3+} spins for both samples. This validates a common EB feature.

We know that at low temperatures (below T_{SR}) the Cr^{3+} spins are in complete AFM $\Gamma_1(A_x, G_y, C_z)$ phase. Our measurements depict the thermomagnetic history can maximally affect one-fourth of the Cr^{3+} spins. This means that 1 spin out of 4 Cr spins is unable to rotate. Here, the Cr^{3+} spins interact with the Nd^{3+} spins by the superexchange interactions. The asymmetric placement of the Nd atom in the distorted perovskite structure may cause an unequal influence on the neighboring Cr atoms. Because of the shift of the Nd atoms along the a -axis, the Cr atoms interacting with Nd atoms along this axis are mostly affected. It may be possible that the partial quenching of the Cr^{3+} spins happen in such a way that the magnitude of one Cr spin is frozen. Thus, it can generate a ferromagnetic component. This

results in a metastable magnetic state, which requires some energy to attain a stable spin configuration. It has been reported that oxygen vacancies restore the missing magnetic superexchange interactions, allowing unexpected magnetic states to stabilize [176]. With the Ce substitution, the oxygen vacancies are introduced in such a way that few of the mutual interactions via the O1 site are broken. This possibly allows the Cr^{3+} spins to return to the influence of the Nd^{3+} spins through the superexchange interaction and leads to the reduction of the EB. However, further microscopic measurements are required to confirm this proposition.

5.4 Summary

We synthesized single-phase orthorhombic $Nd_{1-x}Ce_xCrO_3$ ($x = 0.05-0.175$) compounds. Structural analysis suggests an enhanced covalency of Cr-O1 bonds with Ce substitution. The XPS analysis confirms a constant $\sim 2:1$ ratio of $Ce^{3+}:Ce^{4+}$ ions and charge neutralization through oxygen vacancies. The dc magnetization reveals the increase of T_N and T_{SR} up to ~ 229.9 K and 40.2 K and specifies soft spin-reorientation attributed to diluted superexchange interactions with Ce incorporation. The EB effect through an unusual closure of the $M-H$ loop is noticed for $x = 0.05-0.175$ samples in a different way to Eu^{3+} and Pr^{3+} substituted samples. We demonstrate for the first time that the magnitude of the magnetization is different for the same applied field in positive and negative directions, indicating the existence of two different magnetic states. The difference between these two magnetic states possibly arises from the pinning of Cr^{3+} spins, which requires an additional Zeeman energy for it to rotate. Such that a maximum $H_{EB} \sim -2809$ Oe is found to be comparable with the magnetic field of 2800 Oe, emerging maximum Zeeman energy. Importantly, the ratio $\left[\frac{(\chi_+ - \chi_-)/2}{\chi_{FC}} \right]$ obtained from normalized magnetic susceptibility reveals $\sim 25\%$ pinned Cr^{3+} spins and corroborates EB feature similar to H_{EB} . In these materials, the

pinned Cr^{3+} spins give rise to different magnetic states, which modify with the oxygen vacancies. However, the possible relations between unconventional EB and magnetic states need further exploration. The present work shows the two different states of magnetization at fields of the same magnitude as an alternative method to detect the sign change in small magnetic fields.



Chapter 6 : Conclusions

The results obtained from the present work for this thesis can be summarized as follows: Three distinct substitutions, namely Eu, Pr, and Ce, were introduced at Nd-site in NdCrO_3 . Detailed investigations were carried out to analyze the structural and magnetic properties of (i) $\text{Nd}_{1-x}\text{Eu}_x\text{CrO}_3$ (up to 100 % Eu substitution), (ii) $\text{Nd}_{1-x}\text{Pr}_x\text{CrO}_3$ (up to 30 % Pr substitution), and (iii) $\text{Nd}_{1-x}\text{Ce}_x\text{CrO}_3$ (up to 17.5 % Ce substitution) compounds. This chapter presents a summary of the key findings of the thesis and provides some future guidelines.

We prepared single-phase $\text{Nd}_{1-x}\text{Eu}_x\text{CrO}_3$ ($x = 0.0-1.0$) polycrystalline samples, where the gradual substitution of Nd^{3+} by Eu^{3+} resulted in a gradual change in the chemical pressure within these samples. The room temperature X-ray diffraction and Raman spectroscopy confirmed unit cell contraction and increased structural distortions due to Eu substitution. The microstructural analysis revealed the good quality of homogenous bulk samples. Notably, the substitution of Eu led to a decrease in T_N values, from ~ 225.4 K ($x = 0.0$) to 182.5 K ($x = 1.0$). The presence of T_{SR} from ~ 37.1 K for $x = 0.0$ to 13.3 K for $x = 0.90$ sample is observed. The x dependence of J_1 and J_2 indicated modifications in the Cr-Cr interactions. Overall, the observations of the structural and magnetic behavior across $x = 0.5$ suggest a chemical pressure boundary. We observed a negative exchange bias (EB) effect, and a decrease in the EB field (H_{EB}) from ~ -1945 Oe ($x = 0.0$) to -15 Oe ($x = 1.0$) is observed. Importantly, a non-monotonic behavior of the EB field with a maximum H_{EB} in range of ~ -1300 Oe was observed around $T^* \sim 90$ K and 80 K between T_N and T_{SR} for $x = 0.10-0.20$ samples. This behavior can be attributed to the competing antiferromagnetic interaction between the weak ferromagnetic component of canted Cr^{3+} moments and the paramagnetic moment of $\text{Nd}^{3+}/\text{Eu}^{3+}$ ions, along with lattice distortions, contributing to the

EB effect. The temperature dependence of phonon modes associated with the anti-stretching and bending of CrO_6 octahedra, as well as the vibration of $\text{Nd}^{3+}/\text{Eu}^{3+}$ ions below T_N , confirms the strong spin-phonon coupling up to the $x = 0.20$ sample. The non-monotonicity of the EB effect is correlated with an additional phonon anomaly near T^* . The Raman results were further supported by density functional theory-based calculations. Moreover, the temperature-dependent lattice parameters, CrO_6 deformations, and Nd/Eu positions confirmed strong magnetoelastic coupling below T_N up to $x = 0.20$ sample. Analysis of the electron density distribution using the maximum entropy method revealed that the centrosymmetric ($Pnma$) phase alone was inadequate to explain the crystal structure of the $\text{Nd}_{1-x}\text{Eu}_x\text{CrO}_3$ system near $T^* \sim 80$ K in between T_N and T_{SR} . Interestingly, we observed a structural reorientation across T^* that resolved the anomalous electron density jump of Nd/Eu ions within the $Pnma$ structure, resulting in a stable electron density of $\sim 41.79 \text{ e}/\text{\AA}^3$ for the $Pna2_1$ structure. However, further microscopic investigations are necessary to validate this proposition. This study provides novel insights into lattice modulations around T^* between T_N and T_{SR} in NdCrO_3 -based compounds, elucidating the spin-phonon-induced exchange bias and magneto-structural imprints for the first time.

With such interesting results of Eu substitution in NdCrO_3 , we have chosen the magnetic rare-earth element Pr^{3+} with a larger ion size in contrast with the Eu^{3+} ion. We prepared $\text{Nd}_{1-x}\text{Pr}_x\text{CrO}_3$ ($x = 0.0-0.30$) samples with perovskite-type structure. The Rietveld refinement and Raman analysis indicate that the samples exhibit unit cell expansion and reduced structural distortions as the concentration of Pr increases. By examining the EDX and FESEM micrograph, we observed that the Pr doping results in polycrystalline samples with smaller grain sizes. The semiconductor behavior of the samples was confirmed through UV-Vis spectroscopy. XPS analysis confirmed the presence of Pr ions in the desired (3+) valence states. The dc magnetization measurements demonstrated higher

magnetization than the parent compound and an increase in $T_N \sim 227.5$ K ($x = 0.30$). Further, the Pr substitution increases the weak ferromagnetic phase by diluting the antisymmetric Nd/Pr and Cr interactions. This gradual dilution causes a decrease in the T_{SR} up to ~ 31.8 K and ultimately eliminates the spin-reorientation in the $x = 0.30$ sample. Importantly, we observed the emergence of a Griffiths phase in the substituted samples, attributed to the existence of short-range weak ferromagnetic clusters above T_N . The shift in the $M-H$ loops provided evidence of the EB effect for all samples. In comparison to the Eu substitution, we have achieved a higher value of the EB field for Pr substitution. For temperatures below T_{SR} , a significant increase in the coercive field $H_C \sim 6186$ Oe and EB field $H_{EB} \sim -1285.8$ Oe was observed with Pr substitution. The $x = 0.3$ sample exhibited the maximum $H_{EB} \sim -1991.8$ Oe at $T = 150$ K. Interestingly, for the temperatures above T_{SR} , the behavior of the EB field of the $x = 0.0-0.30$ samples correlated with the trend observed in the Cr-O2 bond length. Further, the anomalous softening of the CrO_6 bending mode and the hardening of the anti-stretching mode confirmed spin-phonon coupling. The magnetic phase diagram of the samples exhibits various magnetic phases as a function of Pr content. These findings highlight the interplay of spin reorientation and EB in $\text{Nd}_{1-x}\text{Pr}_x\text{CrO}_3$ compounds.

Compared with the two previous substitutions, this work selects the redox-active rare earth Ce ion as our final substitute, allowing a mixed Ce valency at the Nd site. We successfully synthesized single-phase $\text{Nd}_{1-x}\text{Ce}_x\text{CrO}_3$ ($x = 0.0-0.175$) compounds and studied systematic structural and magnetic properties for the first time. XPS analysis provides evidence of a consistent ratio between Ce^{3+} and Ce^{4+} ions, approximately 2:1, and reveal charge neutralization through oxygen vacancies. Examining the electron density profile shows that the introduction of Ce enhances the covalency of Cr-O1 bonds. Magnetization measurements demonstrate that T_N and T_{SR} increase to ~ 229.9 K and 40.2 K, respectively,

while also revealing a soft spin reorientation resulting from diluted superexchange interactions upon incorporating Ce. The presence of Ce substitution leads to an unusual closure of the M - H loop manifesting exchange bias (EB) effect. We demonstrate for the first time the distinct magnetization magnitudes under the same applied magnetic field in the positive and negative directions, implying the presence of two distinct magnetic states. The difference between these states may be attributed to the pinning of Cr^{3+} spins, which requires an additional Zeeman energy for it to rotate. For example, the maximum EB field H_{EB} is ~ -2809 Oe is found to be comparable with the magnetic field of 2800 Oe inducing maximum Zeeman energy. Importantly, the normalized magnetic susceptibility ratio $\left[\frac{(\chi_+ - \chi_-)/2}{\chi_{\text{FC}}}\right]$ provides the presence of $\sim 25\%$ pinned Cr^{3+} spins and corroborates EB feature similar to H_{EB} . In these materials, the pinned Cr^{3+} spins contribute to distinct magnetic states that are influenced by the presence of oxygen vacancies. However, the underlying relationships between the unconventional EB and magnetic states require further investigation. This study demonstrates that, at fields of the same magnitude, the detection of two different magnetization states offers an alternative approach for identifying sign changes in small magnetic fields.

This thesis has resulted in the discovery of the spin-phonon induced exchange bias effect, structural-reorientations, and different magnetic states in $\text{Nd}_{1-x}\text{R}_x\text{CrO}_3$ ($\text{R} = \text{Eu}, \text{Pr}, \text{and Ce}$) compounds. It also indicates that the magnetic transition can be coupled to the crystalline lattice modulations in similar systems.

Such interesting findings of perovskite-type rare earth substituted NdCrO_3 samples enhance the multifunctionality of the system. There are some remarks and potential extensions of the current thesis work. For instance, the exploration of the Griffith phase in the case of Pr substituted samples is required. Whereas in the case of Ce substitution, the exact nature of magnetic states and their correlation with exchange bias can be explored. Further, Neutron

diffraction and synchrotron X-ray diffraction are recommended to confirm these proportions. In the present thesis, we have systematically examined the NdCrO_3 -based materials in polycrystalline form. This can be a starting point for preparing single crystals and thin films for future investigations.



References

- [1] Rajeswaran B, Khomskii D I, Zvezdin A K, Rao C N R and Sundaresan A 2012 Field-induced polar order at the Néel temperature of chromium in rare-earth orthochromites: Interplay of rare-earth and Cr magnetism *Phys. Rev. B - Condens. Matter Mater. Phys.* **86** 1–5
- [2] Cao Y, Cao S, Ren W, Feng Z, Yuan S, Kang B, Lu B and Zhang J 2014 Magnetization switching of rare earth orthochromite CeCrO₃ *Appl. Phys. Lett.* **104** 1–5
- [3] Kimura T, Goto T, Shintani H, Ishizaka K, Arima T and Tokura Y 2003 Magnetic control of ferroelectric polarization *Nature* **426** 55–8
- [4] Kools J C S 1996 Exchange-biased spin-valves for magnetic storage *IEEE Trans. Magn.* **32** 3165–84
- [5] Meiklejohn W H and Bean C P 1956 New magnetic anisotropy [1] *Phys. Rev.* **102** 1413–4
- [6] Nogués J and Schuller I K 1999 Exchange bias *J. Magn. Magn. Mater.* **192** 203–32
- [7] Giri S, Patra M and Majumdar S 2011 Exchange bias effect in alloys and compounds *J. Phys. Condens. Matter* **23**
- [8] Yoshii K 2011 Positive exchange bias from magnetization reversal in La 1-xPrxCrO₃ (x ~ 0.7-0.85) *Appl. Phys. Lett.* **99** 97–100
- [9] Fita I, Markovich V, Moskvina A S, Wisniewski A, Puzniak R, Iwanowski P, Martin C, Maignan A, Carbonio R E, Gutowska M U, Szewczyk A and Gorodetsky G 2018 Reversed exchange-bias effect associated with magnetization reversal in the weak

- ferrimagnet $\text{LuFe}_{0.5}\text{Cr}_{0.5}\text{O}_3$ *Phys. Rev. B* **97** 104416
- [10] Laverdière J, Jandl S, Mukhin A A, Ivanov V Y, Ivanov V G and Iliev M N 2006 Spin-phonon coupling in orthorhombic RMnO_3 ($\text{R}=\text{Pr}, \text{Nd}, \text{Sm}, \text{Eu}, \text{Gd}, \text{Tb}, \text{Dy}, \text{Ho}, \text{Y}$): A Raman study *Phys. Rev. B - Condens. Matter Mater. Phys.* **73** 1–5
- [11] Granado E, García A, Sanjurjo J A, Rettori C, Torriani I, Prado F, Sánchez R D, Caneiro A and Oseroff S B 1999 Magnetic ordering effects in the Raman spectra of $\text{La}_{1-x}\text{Mn}_{1-x}\text{O}_3$ *Phys. Rev. B - Condens. Matter Mater. Phys.* **60** 11879–82
- [12] Srinu Bhadram V, Rajeswaran B, Sundaresan A and Narayana C 2013 Spin-phonon coupling in multiferroic RCrO_3 ($\text{R}=\text{Y}, \text{Lu}, \text{Gd}, \text{Eu}, \text{Sm}$): A Raman study *Epl* **101**
- [13] Mahana S, Rakshit B, Basu R, Dhara S, Joseph B, Manju U, Mahanti S D and Topwal D 2017 Local inversion symmetry breaking and spin-phonon coupling in the perovskite GdCrO_3 *Phys. Rev. B* **96** 1–9
- [14] Taheri M, Razavi F S, Yamani Z, Flacau R, Reuvekamp P G, Schulz A and Kremer R K 2016 Magnetic structure, magnetoelastic coupling, and thermal properties of EuCrO_3 nanopowders *Phys. Rev. B* **93** 1–13
- [15] Hornreich R M 1978 Magnetic interactions and weak ferromagnetism in the rare-earth orthochromites *J. Magn. Magn. Mater.* **7** 280–5
- [16] Shamir N, Shaked H and Shtrikman S 1981 Magnetic structure of some rare-earth orthochromites *Phys. Rev. B* **24** 6642–51
- [17] Bertaut E F and Mareschal J 1967 Etude de la structure magnetique des chromites d'erbium et de neodyme par diffraction neutronique *Solid State Commun.* **5** 93–7
- [18] Indra A, Dey K, Midya A, Mandal P, Gutowski O, Rütt U, Majumdar S and Giri S

- 2016 Magnetoelectric coupling and exchange bias effects in multiferroic NdCrO₃ *J. Phys. Condens. Matter* **28**
- [19] Baibich M N, Broto J M, Fert A, Van Dau F N, Petroff F, Eitenne P, Creuzet G, Friederich A and Chazelas J 1988 Giant magnetoresistance of (001)Fe/(001)Cr magnetic superlattices *Phys. Rev. Lett.* **61** 2472–5
- [20] Mancoff F B, Hunter Dunn J, Clemens B M and White R L 2000 A giant magnetoresistance sensor for high magnetic field measurements *Appl. Phys. Lett.* **77** 1879–81
- [21] Anderson P W and Matthias B T 2005 Superconductivity *Career Theor. Physics, A (2nd Ed.* **193** 209–17
- [22] Hull J R and Murakami M 2004 Applications of bulk high-temperature superconductors *Proc. IEEE* **92** 1705–17
- [23] Nagaev E L 2001 Colossal-magnetoresistance materials: Manganites and conventional ferromagnetic semiconductors *Phys. Rep.* **346** 387–531
- [24] Yu B F, Gao Q, Zhang B, Meng X Z and Chen Z 2003 Review on research of room temperature magnetic refrigeration *Int. J. Refrig.* **26** 622–36
- [25] Hasan M Z and Kane C L 2010 Colloquium: Topological insulators *Rev. Mod. Phys.* **82** 3045–67
- [26] Fert A, Reyren N and Cros V 2017 Magnetic skyrmions: Advances in physics and potential applications *Nat. Rev. Mater.* **2**
- [27] Wolf S A, Awschalom D D, Buhrman R A, Daughton J M, Von Molnár S, Roukes M L, Chtchelkanova A Y and Treger D M 2001 Spintronics: A spin-based electronics vision for the future *Science (80-.).* **294** 1488–95

- [28] Chen X, Hochstrat A, Borisov P and Kleemann W 2006 Magnetoelectric exchange bias systems in spintronics *Appl. Phys. Lett.* **89** 1–4
- [29] Eerenstein W, Mathur N D and Scott J F 2006 Multiferroic and magnetoelectric materials *Nature* **442** 759–65
- [30] Béa H, Bibes M, Cherifi S, Nolting F, Warot-Fonrose B, Fusil S, Herranz G, Deranlot C, Jacquet E, Bouzheouane K and Barthélémy A 2006 Tunnel magnetoresistance and robust room temperature exchange bias with multiferroic BiFeO₃ epitaxial thin films *Appl. Phys. Lett.* **89** 87–90
- [31] Fusil S, Garcia V, Barthélémy A and Bibes M 2014 Magnetoelectric devices for spintronics *Annu. Rev. Mater. Res.* **44** 91–116
- [32] Nan C W, Bichurin M I, Dong S, Viehland D and Srinivasan G 2008 Multiferroic magnetoelectric composites: Historical perspective, status, and future directions *J. Appl. Phys.* **103**
- [33] Heisenberg W 1926 Mehrkörperproblem und Resonanz in der Quantenmechanik *Zeitschrift für Phys.* **38** 411–26
- [34] Stephen Blundell 2001 Magnetism in Condensed Matter *Oxford Univ. Press* 80–1
- [35] Moshinsky M 1959 *No Title* □□□□ vol 13
- [36] Rödl C, Fuchs F, Furthmüller J and Bechstedt F 2009 Quasiparticle band structures of the antiferromagnetic transition-metal oxides MnO, FeO, CoO, and NiO *Phys. Rev. B - Condens. Matter Mater. Phys.* **79** 1–8
- [37] Zysler R, Fiorani D, Dormann J L and Testa A M 1994 Magnetic properties of ultrafine α -Fe₂O₃ antiferromagnetic particles *J. Magn. Magn. Mater.* **133** 71–3
- [38] Makhoulouf S A 2004 Magnetic properties of Cr₂O₃ Nanoparticles *J. Magn. Magn.*

- Mater.* **272–276** 1530–2
- [39] Huang Y H, Fjellvåg H, Karppinen M, Hauback B C, Yamauchi H and Goodenough J B 2006 Crystal and magnetic structure of the orthorhombic perovskite YbMnO_3 *Chem. Mater.* **18** 2130–4
- [40] Abe S, Atsumi Y, Kaneko T and Yoshida H 1992 Magnetic properties of RCu_4In (R=Gd-Er) intermetallic compounds *J. Magn. Magn. Mater.* **104–107** 1397–8
- [41] Melot B C, Drewes J E, Seshadri R, Stoudenmire E M and Ramirez A P 2009 Magnetic phase evolution in the spinel compounds $\text{Zn}_{1-x}\text{Co}_x\text{Cr}_2\text{O}_4$ *J. Phys. Condens. Matter* **21**
- [42] Suzuyama T, Awaka J, Yamamoto H, Ebisu S, Ito M, Suzuki T, Nakama T, Yagasaki K and Nagata S 2006 Ferromagnetic-phase transition in the spinel-type CuCr_2Te_4 *J. Solid State Chem.* **179** 140–4
- [43] Abramov Y A, Tsirelson V G, Zavodnik V E, Ivanov S A and Brown I D 1995 The chemical bond and atomic displacements in SrTiO_3 from X-ray diffraction analysis *Acta Crystallogr. Sect. B* **51** 942–51
- [44] Goldschmidt V 1926 The laws of crystal chemistry *Nat. Sci.* **14** 477–85
- [45] Geller S 1957 Crystallographic studies of perovskite-like compounds. IV. Rare earth scandates, vanadites, galliates, orthochromites *Acta Crystallogr.* **10** 243–8
- [46] Weber M C, Kreisel J, Thomas P A, Newton M, Sardar K and Walton R I 2012 Phonon Raman scattering of RCrO_3 perovskites (R=Y, La, Pr, Sm, Gd, Dy, Ho, Yb, Lu) *Phys. Rev. B - Condens. Matter Mater. Phys.* **85** 1–9
- [47] Wollan E O and Koehler W C 1955 Neutron diffraction study of the magnetic properties of the series of perovskite-type compounds $[(1-x)\text{La},x\text{Ca}]\text{MnO}_3$ *Phys.*

Rev. **100** 545–63

- [48] Koehler W C and Wollan E O 1957 Neutron-diffraction study of the magnetic properties of perovskite-like compounds LaBO_3 *J. Phys. Chem. Solids* **2** 100–6
- [49] Picozzi S, Yamauchi K, Sanyal B, Sergienko I A and Dagotto E 2007 Dual nature of improper ferroelectricity in a magnetoelectric multiferroic *Phys. Rev. Lett.* **99** 1–4
- [50] Lee J H, Jeong Y K, Park J H, Oak M A, Jang H M, Son J Y and Scott J F 2011 Spin-canting-induced improper ferroelectricity and spontaneous magnetization reversal in SmFeO_3 *Phys. Rev. Lett.* **107** 1–5
- [51] Goodenough J B 2004 Electronic and ionic transport properties and other physical aspects of perovskites *Reports Prog. Phys.* **67** 1915–93
- [52] Zener C 1951 Interaction between the d-shells in the transition metals. II. Ferromagnetic compounds of manganese with Perovskite structure *Phys. Rev.* **82** 403–5
- [53] Dvořák V 1971 A Thermodynamic Theory of Gadolinium Molybdate *Phys. Status Solidi* **46** 763–72
- [54] Moriya T 1960 Anisotropic superexchange interaction and weak ferromagnetism *Phys. Rev.* **120** 91–8
- [55] Sergienko I A and Dagotto E 2006 Role of the Dzyaloshinskii-Moriya interaction in multiferroic perovskites *Phys. Rev. B - Condens. Matter Mater. Phys.* **73** 1–5
- [56] Symmetry M 1957 3 it amounts, according **5** 1259–72
- [57] Morrish A H 2001 *The physical principles of magnetism*
- [58] Heinze S, Von Bergmann K, Menzel M, Brede J, Kubetzka A, Wiesendanger R,

- Bihlmayer G and Blügel S 2011 Spontaneous atomic-scale magnetic skyrmion lattice in two dimensions *Nat. Phys.* **7** 713–8
- [59] Niebieskikwiat D and Salamon M B 2005 Intrinsic interface exchange coupling of ferromagnetic nanodomains in a charge ordered manganite *Phys. Rev. B - Condens. Matter Mater. Phys.* **72** 1–6
- [60] Ding J F, Lebedev O I, Turner S, Tian Y F, Hu W J, Seo J W, Panagopoulos C, Prellier W, Van Tendeloo G and Wu T 2013 Interfacial spin glass state and exchange bias in manganite bilayers with competing magnetic orders *Phys. Rev. B - Condens. Matter Mater. Phys.* **87** 1–7
- [61] Tang Y K, Sun Y and Cheng Z H 2006 Exchange bias associated with phase separation in the perovskite cobaltite $\text{La}_{1-x}\text{Sr}_x\text{CoO}_3$ *Phys. Rev. B - Condens. Matter Mater. Phys.* **73** 1–6
- [62] Tsang C H, Fontana R E, Lin T, Heim D E, Gurney B A and Williams M L 1998 Design, fabrication, and performance of spin-valve read heads for magnetic recording applications *IBM J. Res. Dev.* **42** 103–15
- [63] Lage E, Kirchof C, Hrkac V, Kienle L, Jahns R, Knöchel R, Quandt E and Meyners D 2012 Exchange biasing of magnetoelectric composites *Nat. Mater.* **11** 523–9
- [64] Nordblad P 2015 Tuning exchange bias Diffusive origins *Nat. Publ. Gr.* **14** 0–1
- [65] Parkin S S P, Roche K P, Samant M G, Rice P M, Beyers R B, Scheuerlein R E, O’Sullivan E J, Brown S L, Bucchigano J, Abraham D W, Lu Y, Rooks M, Trouilloud P L, Wanner R A and Gallagher W J 1999 Exchange-biased magnetic tunnel junctions and application to nonvolatile magnetic random access memory (invited) *J. Appl. Phys.* **85** 5828–33
- [66] Nogues J, Lederman D, Moran T J and Schuller I K 1996 Positive Exchange Bias

in FeF₂-Fe Bilayers **1**

- [67] Maat S, Takano K, Parkin S S P and Fullerton E E 2001 Perpendicular Exchange Bias of Co/Pt Multilayers 8–11
- [68] P. D. Kulkarni¹, A. Thamizhavel¹, V. C. Rakhecha¹, A. K. Nigam¹, P. L. Paulose¹ S R and A K G 2009 Magnetic compensation phenomenon and the sign reversal in the exchange bias field in a single crystal of Nd_{0.75}Ho_{0.25}Al₂ *Europhys. Lett.* **86** 47003
- [69] Padam R, Pandya S, Ravi S, Ramakrishnan S, Nigam A K, Grover A K and Pal D 2017 Study of the sign change of exchange bias across the spin reorientation transition in Co(Cr_{1-x}Fe_x)₂O₄ (x = 0.00-0.125) *J. Phys. Condens. Matter* **29**
- [70] Kumar R, Padam R, Rayaprol S, Siruguri V and Pal D 2016 Correlation of exchange bias with magneto-structural effects across the compensation temperature of Co(Cr_{1-x}Fe_x)₂O₄ (x = 0.05 and 0.075) *J. Appl. Phys.* **119** 0–6
- [71] Hong F, Cheng Z, Wang J, Wang X and Dou S 2012 Positive and negative exchange bias effects in the simple perovskite manganite NdMnO₃ *Appl. Phys. Lett.* **101** 1–6
- [72] Zhao Y T, Yu G B, Zhu C M, Wang L G and Yao M W 2021 Evolution of structure and the exchange bias behavior with annealing temperature in nanoscale NiCr₂O₄ *J. Alloys Compd.* **858**
- [73] Dalal B, Sarkar B, Rayaprol S, Das M, Siruguri V, Mandal P and De S K 2020 Unveiling ferrimagnetic ground state, anomalous behavior of the exchange-bias field around spin reorientation, and magnetoelectric coupling in YbCr_{1-x}Fe_xO₃ (0.1 ≤ x ≤ 0.6) UNVEILING FERRIMAGNETIC GROUND STATE, ... BISWAJIT DALAL et al. *Phys. Rev. B* **101** 144418
- [74] Wang L, Wang S W, Zhang X, Zhang L L, Yao R and Rao G H 2016 Reversals of

- magnetization and exchange-bias in perovskite chromite YbCrO₃ *J. Alloys Compd.* **662** 268–71
- [75] Mendivil L F, Alvarado-Rivera J, Verdín E, Díaz J A, Mata J, Conde A and Durán A 2020 Reversal magnetization and exchange bias effect of the nanocrystalline Yb_{1-x}Pr_xCrO₃ solid solution *Appl. Phys. A Mater. Sci. Process.* **126** 1–12
- [76] Patra M, Thakur M, Majumdar S and Giri S 2009 The exchange bias effect in phase separated Nd_{1-x}Sr_xCoO₃ at the spontaneous ferromagnetic/ferrimagnetic interface *J. Phys. Condens. Matter* **21**
- [77] Liu W, Shi L, Zhou S, Zhao J, Li Y and Guo Y 2014 Griffiths phase, spin-phonon coupling, and exchange bias effect in double perovskite Pr₂CoMnO₆ *J. Appl. Phys.* **116**
- [78] Sahoo R C, Takeuchi Y, Ohtomo A and Hossain Z 2019 Exchange bias and spin glass states driven by antisite disorder in the double perovskite compound LaSrCoFeO₆ *Phys. Rev. B* **100** 1–9
- [79] Cheng Z X, Wang X L, Dou S X, Kimura H and Ozawa K 2010 A novel multiferroic system: Rare earth chromates *J. Appl. Phys.* **107** 8–11
- [80] Serrao C R, Kundu A K, Krupanidhi S B, Waghmare U V. and Rao C N R 2005 Biferroic YCrO₃ *Phys. Rev. B - Condens. Matter Mater. Phys.* **72** 2–5
- [81] Alonso J A, Martínez-Lope M J, Casais M T and Fernández-Díaz M T 2000 Evolution of the Jahn-Teller distortion of MnO₆ octahedra in RMnO₃ perovskites (R = Pr, Nd, Dy, Tb, Ho, Er, Y): A neutron diffraction study *Inorg. Chem.* **39** 917–23
- [82] Zhou J S and Goodenough J B 2008 Intrinsic structural distortion in orthorhombic perovskite oxides *Phys. Rev. B - Condens. Matter Mater. Phys.* **77** 2–5

- [83] Yin L H, Yang J, Tong P, Luo X, Park C B, Shin K W, Song W H, Dai J M, Kim K H, Zhu X B and Sun Y P 2016 Role of rare earth ions in the magnetic, magnetocaloric and magnetoelectric properties of RCrO₃ (R = Dy, Nd, Tb, Er) crystals *J. Mater. Chem. C* **4** 11198–204
- [84] Yamaguchi T 1974 Theory of spin reorientation in rare-earth orthochromites and orthoferrites *J. Phys. Chem. Solids* **35** 479–500
- [85] Oliveira G N P, Teixeira R C, Moreira R P, Correia J G, Araújo J P and Lopes A M L 2020 Local inhomogeneous state in multiferroic SmCrO₃ *Sci. Rep.* **10** 1–12
- [86] Schmidt R, Romero J, David A, Amador U and Mora E 2013 Microwave-Assisted Synthesis , Microstructure , and Physical Properties of Rare-Earth Chromites *J. Phys. Chem. C* **117** 10450–10458
- [87] Hornreich R M, Komet Y, Nolan R, Wanklyn B M and Yaeger I 1975 Magneto-optical and magnetization studies in the rare-earth orthochromites. VI. NdCrO₃ *Phys. Rev. B* **12** 5094–104
- [88] Li H, Liu Y Z, Xie L, Guo Y Y, Ma Z J, Li Y T, He X M, Liu L Q and Zhang H G 2018 The spin-reorientation magnetic transitions in Ga-doped SmCrO₃ *Ceram. Int.* **44** 18913–9
- [89] Cooke A H, Martin D M and Wells M R 1974 Magnetic interactions in gadolinium orthochromite, GdCrO₃ *J. Phys. C Solid State Phys.* **7** 3133–44
- [90] Zhou J S, Alonso J A, Pomjakushin V, Goodenough J B, Ren Y, Yan J Q and Cheng J G 2010 Intrinsic structural distortion and superexchange interaction in the orthorhombic rare-earth perovskites R CrO₃ *Phys. Rev. B - Condens. Matter Mater. Phys.* **81** 1–5
- [91] Yoshii K 2012 Magnetization reversal in TmCrO₃ *Mater. Res. Bull.* **47** 3243–8

- [92] Su Y, Zhang J, Feng Z, Li L, Li B, Zhou Y, Chen Z and Cao S 2010 Magnetization reversal and Yb³⁺/Cr³⁺ spin ordering at low temperature for perovskite YbCrO₃ chromites *J. Appl. Phys.* **108** 1–6
- [93] Khomchenko V A, Troyanchuk I O, Szymczak R and Szymczak H 2008 Negative magnetization in La_{0.75}Nd_{0.25}CrO₃ perovskite *J. Mater. Sci.* **43** 5662–5
- [94] Shukla R, Bera A K, Yusuf S M, Deshpande S K, Tyagi A K, Hermes W, Eul M and Pöttgen R 2009 Multifunctional nanocrystalline CeCrO₃: Antiferromagnetic, relaxor, and optical properties *J. Phys. Chem. C* **113** 12663–8
- [95] Manna P K, Yusuf S M, Shukla R and Tyagi A K 2010 Coexistence of sign reversal of both magnetization and exchange bias field in the core-shell type La_{0.2} Ce_{0.8} CrO₃ nanoparticles *Appl. Phys. Lett.* **96** 1–4
- [96] Gupta P, Bhargava R and Poddar P 2015 Colossal increase in negative magnetization, exchange bias and coercivity in samarium chromite due to a strong coupling between Sm³⁺ – Cr³⁺ spins sublattices
- [97] Zhao Y, Li C, Liu X, Gu F, Jiang H, Shao W, Zhang L and He Y 2007 Synthesis and optical properties of TiO₂ nanoparticles *Mater. Lett.* **61** 79–83
- [98] Singh K D, Pandit R and Kumar R 2018 Effect of rare earth ions on structural and optical properties of specific perovskite orthochromates; RCrO₃ (R = La, Nd, Eu, Gd, Dy, and Y) *Solid State Sci.* **85** 70–5
- [99] Gupta P and Poddar P 2015 Using Raman and dielectric spectroscopy to elucidate the spin phonon and magnetoelectric coupling in DyCrO₃ nanoplatelets *RSC Adv.* **5** 10094–101
- [100] Boudad L, Taibi M, Belayachi W and Abd-lefdil M 2022 Journal of Solid State Chemistry Investigation of magnetic, dielectric, optical, and electrical properties

- of Fe half-doped PrCrO₃ perovskite *J. Solid State Chem.* **309** 122933
- [101] Yin S, Seehra M S, Guild C J, Suib S L, Poudel N, Lorenz B and Jain M 2017 Magnetic and magnetocaloric properties of HoCrO₃ tuned by selective rare-earth doping *Phys. Rev. B* **95** 1–12
- [102] Fiebig M 2005 Revival of the magnetoelectric effect *J. Phys. D: Appl. Phys.* **38**
- [103] Sahu J R, Serrao C R, Ray N, Waghmare U V. and Rao C N R 2007 Rare earth chromites: A new family of multiferroics *J. Mater. Chem.* **17** 42–4
- [104] Yin L H, Yang J, Zhang R R, Dai J M, Song W H and Sun Y P 2014 Multiferroicity and magnetoelectric coupling enhanced large magnetocaloric effect in DyFe_{0.5}Cr_{0.5}O₃ *Appl. Phys. Lett.* **104** 1–6
- [105] Kenzelmann M, Harris A B, Jonas S, Broholm C, Schefer J, Kim S B, Zhang C L, Cheong S W, Vajk O P and Lynn J W 2005 Magnetic inversion symmetry breaking and ferroelectricity in TbMnO₃ *Phys. Rev. Lett.* **95** 27–30
- [106] Weber M C, Guennou M, Evans D M, Toulouse C, Simonov A, Kholina Y, Ma X, Ren W, Cao S, Carpenter M A, Dkhil B, Fiebig M and Kreisel J 2022 Emerging spin–phonon coupling through cross-talk of two magnetic sublattices *Nat. Commun.* **13**
- [107] Sharma Y, Sahoo S, Perez W, Mukherjee S, Gupta R, Garg A, Chatterjee R and Katiyar R S 2014 Phonons and magnetic excitation correlations in weak ferromagnetic YCrO₃ *J. Appl. Phys.* **115**
- [108] Amrani M El, Zaghrioui M, Phuoc V T, Gervais F and Massa N E 2014 Journal of Magnetism and Magnetic Materials Local symmetry breaking and spin – phonon coupling in SmCrO₃ orthochromite *J. Magn. Magn. Mater.* **361** 1–6

- [109] Kotnana G, Sathe V G and Narayana Jammalamadaka S 2018 Spin–phonon coupling in $\text{HoCr}_{1-x}\text{Fe}_x\text{O}_3$ ($x = 0$ and 0.5) compounds *J. Raman Spectrosc.* **49** 764–70
- [110] Treves D 1962 Magnetic studies of some orthoferrites *Phys. Rev.* **125** 1843–53
- [111] Bartolomé F, Bartolomé J, Castro M and Melero J J 2000 Specific heat and magnetic interactions *Phys. Rev. B - Condens. Matter Mater. Phys.* **62** 1058–66
- [112] Lufaso M W, Mugavero S J, Gemmill W R, Lee Y, Vogt T and zur Loye H C 2007 Pressure- and temperature-dependent X-ray diffraction studies of NdCrO_3 *J. Alloys Compd.* **433** 91–6
- [113] Iliev M N, Litvinchuk A P, Hadjiev V G, Wang Y Q, Cmaidalka J, Meng R L, Sun Y Y, Kolev N and Abrashev M V. 2006 Raman spectroscopy of low-temperature (Pnma) and high-temperature ($R\bar{3}c$) phases of LaCrO_3 *Phys. Rev. B - Condens. Matter Mater. Phys.* **74** 1–7
- [114] Chakraborty K R, Mukherjee S, Kaushik S D, Rayaprol S, Prajapat C L, Singh M R, Siruguri V, Tyagi A K and Yusuf S M 2014 Low temperature neutron diffraction study of $\text{Nd}_{1-x}\text{Sr}_x\text{CrO}_3$ ($0.05 \leq x \leq 0.15$) *J. Magn. Magn. Mater.* **361** 81–7
- [115] Shen Y, Liu M, He T and Jiang S P 2009 Preparation, electrical conductivity, and thermal expansion behavior of dense $\text{Nd}_{1-x}\text{Ca}_x\text{CrO}_3$ solid solutions *J. Am. Ceram. Soc.* **92** 2259–64
- [116] Du Y, Cheng Z X, Wang X L and Dou S X 2010 Structure, magnetic, and thermal properties of $\text{Nd}_{1-x}\text{La}_x\text{CrO}_3$ ($0 \leq x \leq 1.0$) *J. Appl. Phys.* **108** 0–9
- [117] Sharannia M P, De S, Singh R, Das A, Nirmala R and Santhosh P N 2017 Observation of magnetization and exchange bias reversals in $\text{NdFe}_{0.5}\text{Cr}_{0.5}\text{O}_3$ *J. Magn. Magn. Mater.* **430** 109–13

- [118] McDannald A, Dela Cruz C R, Seehra M S and Jain M 2016 Negative exchange bias in single-phase $Dy_{1-x}Nd_xCrO_3$ induced by Nd doping *Phys. Rev. B* **93** 1–8
- [119] Schwarz R B and Johnson W L 1983 Formation of an amorphous alloy by solid-state reaction of the pure polycrystalline metals *Phys. Rev. Lett.* **51** 415–8
- [120] Kittel C 1957 *Introduction to solid state physics* vol 6
- [121] Rodríguez-Carvajal J 1993 Recent advances in magnetic structure determination by neutron powder diffraction *Phys. B Phys. Condens. Matter* **192** 55–69
- [122] Anon 2016 Introduction to Raman Spectroscopy 1–50
- [123] Men S, Lovelock K R J and Licence P 2011 X-ray photoelectron spectroscopy of pyrrolidinium-based ionic liquids: Cation-anion interactions and a comparison to imidazolium-based analogues *Phys. Chem. Chem. Phys.* **13** 15244–55
- [124] Tsushima K, Takemura I and Osaka S 1969 Weak-Ferromagnetism in $EuCrO_3$ *Solid State Commun.* **7** 71–3
- [125] Dieny B, Speriosu V S, Parkin S S P, Gurney B A, Wilhoit D R and Mauri D 1991 Giant magnetoresistive in soft ferromagnetic multilayers *Phys. Rev. B* **43** 1297–300
- [126] El Amrani M, Zaghrioui M, Ta Phuoc V, Gervais F and Massa N E 2014 Local symmetry breaking and spin-phonon coupling in $SmCrO_3$ orthochromite *J. Magn. Magn. Mater.* **361** 1–6
- [127] Giannozzi P, Baroni S, Bonini N, Calandra M, Car R, Cavazzoni C, Ceresoli D, Chiarotti G L, Cococcioni M, Dabo I, Dal Corso A, De Gironcoli S, Fabris S, Fratesi G, Gebauer R, Gerstmann U, Gougoussis C, Kokalj A, Lazzeri M, Martin-Samos L, Marzari N, Mauri F, Mazzarello R, Paolini S, Pasquarello A, Paulatto L, Sbraccia C, Scandolo S, Sclauzero G, Seitsonen A P, Smogunov A, Umari P and Wentzcovitch

- R M 2009 QUANTUM ESPRESSO: A modular and open-source software project for quantum simulations of materials *J. Phys. Condens. Matter* **21**
- [128] Taheri M, Razavi F S, Yamani Z, Flacau R, Ritter C, Bette S and Kremer R K 2019 Structural, magnetic, and thermal properties of $\text{Ce}_{1-x}\text{Eu}_x\text{CrO}_3$ orthochromite solid solutions *Phys. Rev. B* **99**
- [129] Martínez-Lope M J, Alonso J A, Retuerto M and Fernández-Díaz M T 2008 Evolution of the crystal structure of RVO_3 (R = La, Ce, Pr, Nd, Tb, Ho, Er, Tm, Yb, Lu, Y) perovskites from neutron powder diffraction data *Inorg. Chem.* **47** 2634–40
- [130] Zhao Y, Weidner D J, Parise J B and Cox D E 1993 Critical phenomena and phase transition of perovskite - data for NaMgF_3 perovskite. Part II *Phys. Earth Planet. Inter.* **76** 17–34
- [131] Zhou J S, Alonso J A, Muñoz A, Fernández-Díaz M T and Goodenough J B 2011 Magnetic structure of LaCrO_3 perovskite under high pressure from in situ neutron diffraction *Phys. Rev. Lett.* **106** 1–4
- [132] Terkhi S, Bentata R, Bendahma F, Lantri T, Bentata S, Aziz Z and Abbar B 2021 Half-metallic ferromagnetic behavior of cubic lanthanide based on perovskite-type oxide NdCrO_3 : first-principles calculations *Indian J. Phys.* **95** 833–9
- [133] Ross N L, Zhao J, Burt J B and Chaplin T D 2004 Equations of state of GdFeO_3 and GdAlO_3 perovskites *J. Phys. Condens. Matter* **16** 5721–30
- [134] Liu X, Hao L, Ma X, Wang C W, Klose F, Liu Y, Sun K, Li Y and Chen D 2017 Magnetic interactions in $\text{HoCr}_{1-x}\text{Fe}_x\text{O}_3$ ($x = 0, 0.2$) investigated by neutron powder diffraction *J. Magn. Magn. Mater.* **433** 84–90
- [135] Bhadram V S, Swain D, Dhanya R, Polentarutti M, Sundaresan A and Narayana C 2014 Effect of pressure on octahedral distortions in RCrO_3 (R= Lu, Tb, Gd, Eu,

- Sm): The role of R-ion size and its implications *Mater. Res. Express* **1**
- [136] Iliev M and Abrashev M 1998 Raman spectroscopy of orthorhombic perovskitelike and *Phys. Rev. B - Condens. Matter Mater. Phys.* **57** 2872–7
- [137] Camara N R, Ta Phuoc V, Monot-Laffez I and Zaghrioui M 2017 Polarized Raman scattering on single crystals of rare earth orthochromite RCrO₃ (R = La, Pr, Nd, and Sm) *J. Raman Spectrosc.* **48** 1839–51
- [138] Tsushima K, Aoyagi K and Sugano S 1970 Magnetic and magneto-optical properties of some rare-earth and yttrium orthochromites *J. Appl. Phys.* **41** 1238–40
- [139] Harres A, Mikhov M, Skumryev V, De Andrade A M H, Schmidt J E and Geshev J 2016 Criteria for saturated magnetization loop *J. Magn. Magn. Mater.* **402** 76–82
- [140] Taheri M, Kremer R K, Trudel S and Razavi F S 2015 Exchange bias effect and glassy-like behavior of EuCrO₃ and CeCrO₃ nano-powders *J. Appl. Phys.* **118**
- [141] Wu S M, Cybart S A, Yu P, Rossell M D, Zhang J X, Ramesh R and Dynes R C 2010 Reversible electric control of exchange bias in a multiferroic field-effect device *Nat. Mater.* **9** 756–61
- [142] Dey J K, Majumdar S and Giri S 2018 Coexisting exchange bias effect and ferroelectricity in geometrically frustrated ZnCr₂O₄ *J. Phys. Condens. Matter* **30** aac0b7
- [143] Balkanski M, Wallis R F and Haro E 1983 Anharmonic effects in light scattering due to optical phonons in silicon *Phys. Rev. B* **28** 1928–34
- [144] Mandal P, Bhadram V S, Sundarayya Y, Narayana C, Sundaresan A and Rao C N R 2011 Spin-reorientation, ferroelectricity, and magnetodielectric effect in YFe_{1-x}MnxO₃ (0.1 ≤ x ≤ 0.40) *Phys. Rev. Lett.* **107** 1–5

- [145] Anon MES1_Strong magnetoelastic coupling in orthorhombic $\text{Eu}_{1-x}\text{Y}_x\text{MnO}_3$ manganite.pdf
- [146] Raut S, Mahapatra S and Panigrahi S 2021 Spin–phonon interaction and magnetoelastic coupling associated with unusual cluster-glass states in $\text{YFe}_{0.9}\text{Cr}_{0.1}\text{O}_3$ *J. Magn. Magn. Mater.* **529** 167887
- [147] Sands D E 1993 Introduction to crystallography
- [148] Streltsov V A and Ishizawa N 1999 Synchrotron X-ray study of the electron density in RFeO_3 (R = Nd, Dy) *Acta Crystallogr. Sect. B Struct. Sci.* **55** 1–7
- [149] Chaturvedi S, Shyam P, Apte A, Kumar J, Bhattacharyya A, Awasthi A M and Kulkarni S 2016 Dynamics of electron density, spin-phonon coupling, and dielectric properties of SmFeO_3 nanoparticles at the spin-reorientation temperature: Role of exchange striction *Phys. Rev. B* **93** 1–12
- [150] Takata M, Nishibori E and Sakata M 2001 Charge density studies utilizing powder diffraction and MEM. Exploring of high T_c superconductors, C60 superconductors and manganites *Zeitschrift fur Krist.* **216** 71–86
- [151] Netzel J, Hofmann A and Van Smaalen S 2008 Accurate charge density of α -glycine by the maximum entropy method *CrystEngComm* **10** 335–43
- [152] Im W Bin, Page K, Denbaars S P and Seshadri R 2009 Probing local structure in the yellow phosphor $\text{LaSr}_2\text{AlO}_5:\text{Ce}^{3+}$, by the maximum entropy method and pair distribution function analysis *J. Mater. Chem.* **19** 8761–6
- [153] Petříček V, Dušek M and Palatinus L 2014 Crystallographic computing system JANA2006: General features *Zeitschrift fur Krist.* **229** 345–52
- [154] Momma K, Ikeda T, Belik A A and Izumi F 2013 Dysnomia, a computer program

- for maximum-entropy method (MEM) analysis and its performance in the MEM-based pattern fitting *Powder Diffr.* **28** 184–93
- [155] Dong S, Yamauchi K, Yunoki S, Yu R, Liang S, Moreo A, Liu J M, Picozzi S and Dagotto E 2009 Exchange bias driven by the dzyaloshinskii-moriya interaction and ferroelectric polarization at G-type antiferromagnetic perovskite interfaces *Phys. Rev. Lett.* **103** 1–4
- [156] Sasani A, Iñiguez J and Bousquet E 2021 Magnetic phase diagram of rare-earth orthorhombic perovskite oxides *Phys. Rev. B* **104** 1–15
- [157] Gordon J D, Hornreich R M, Shtrikman S and Wanklyn B M 1976 Magnetization studies in the rare-earth orthochromites. V. TbCrO₃ and PrCrO₃ *Phys. Rev. B* **13** 3012–7
- [158] Gupta P and Pal D 2023 Exploration of low field magnetic states in Nd_{1-x}Ce_xCrO₃ *J. Phys. Condens. Matter* **35** 345803
- [159] Yoshii K, Nakamura A, Ishii Y and Morii Y 2001 Magnetic properties of La_{1-x}Pr_xCrO₃ *J. Solid State Chem.* **162** 84–9
- [160] Mori M, Yamamoto T, Itoh H and Watanabe T 1997 Compatibility of alkaline earth metal (Mg, Ca, Sr)-doped lanthanum chromites as separators in planar-type high-temperature solid oxide fuel cells *J. Mater. Sci.* **32** 2423–31
- [161] Pomiro F J, Gaviría J P, Fougá G G, Vega L D and Bohé A E 2019 Chlorination of Pr₂O₃ and Pr₆O₁₁. Crystal structure, magnetic and spectroscopic properties of praseodymium oxychloride *J. Alloys Compd.* **776** 919–26
- [162] Briggs D 2005 X-ray photoelectron spectroscopy (XPS) *Handb. Adhes. Second Ed.* 621–2

- [163] Aronniemi M, Sainio J and Lahtinen J 2005 Chemical state quantification of iron and chromium oxides using XPS: The effect of the background subtraction method *Surf. Sci.* **578** 108–23
- [164] Venugopal R B, Vittal P B, Narsinga R G, Chou F C and Suresh B D 2015 Magnetization Reversal in PrCrO₃ *Adv. Mater. Res.* **1086** 96–100
- [165] Durán A, Escamilla R, Escudero R, Morales F and Verdín E 2018 Reversal magnetization, spin reorientation, and exchange bias in YCr O₃ doped with praseodymium *Phys. Rev. Mater.* **2** 1–13
- [166] Salamon M B, Lin P and Chun S H 2002 Colossal magnetoresistance is a Griffiths singularity *Phys. Rev. Lett.* **88** 1972031–4
- [167] Bray A J 1987 Nature of the Griffiths phase *Phys. Rev. Lett.* **59** 586–9
- [168] Salamon B and Chun H 2003 Griffiths singularities and magnetoresistive manganites *Phys. Rev. B - Condens. Matter Mater. Phys.* **68** 1–8
- [169] Pramanik A K and Banerjee A 2010 Griffiths phase and its evolution with Mn-site disorder in the half-doped manganite Pr 0.5 Sr 0.5 Mn 1-y Ga y O₃ (y=0.0, 0.025, and 0.05) *Phys. Rev. B - Condens. Matter Mater. Phys.* **81** 1–5
- [170] Mali B, Nair H S, Heitmann T W, Nhalil H, Antonio D, Gofryk K, Bhandari S R, Ghimire M P and Elizabeth S 2020 Re-entrant spin reorientation transition and Griffiths-like phase in antiferromagnetic TbFe_{0.5}Cr_{0.5} O₃ *Phys. Rev. B* **102** 1–10
- [171] Zhang H, Qian H, Xie L, Guo Y, Liu Y and He X 2021 The spin reorientation and improvement of magnetocaloric effect in HoCr_{1-x}Ga_xO₃ (0 ≤ x ≤ 0.5) *J. Alloys Compd.* **885**
- [172] Gupta P and Pal D 2021 Spin induced exchange bias and lattice modulation in

- Nd_{1-x}Eu_xCrO₃ *J. Phys. Condens. Matter* **33** 135806
- [173] Du Y, Cheng Z X, Wang X L and Dou S X 2010 Structure, magnetic, and thermal properties of Nd_{1-x}La_xCrO₃ (0 ≤ x ≤ 1.0) *J. Appl. Phys.* **108**
- [174] Shukla R, Manjanna J, Bera A K, Yusuf S M and Tyagi A K 2009 La_{1-x}Ce_xCrO₃ (0.0 ≤ x ≤ 1.0): A new series of solid solutions with tunable magnetic and optical properties *Inorg. Chem.* **48** 11691–6
- [175] Wexler R B, Gautam G S, Stechel E B and Carter E A 2021 Factors Governing Oxygen Vacancy Formation in Oxide Perovskites *J. Am. Chem. Soc.* **143** 13212–27
- [176] Menéndez C, Chu D and Cazorla C 2020 Oxygen-vacancy induced magnetic phase transitions in multiferroic thin films *npj Comput. Mater.* **6**
- [177] Shoko E, Smith M F and McKenzie R H 2010 Charge distribution near bulk oxygen vacancies in cerium oxides *J. Phys. Condens. Matter* **22** 223201
- [178] Noritake T, Aoki M, Towata S, Seno Y, Hirose Y, Nishibori E, Takata M and Sakata M 2002 Chemical bonding of hydrogen in MgH₂ *Appl. Phys. Lett.* **81** 2008–10
- [179] Park J H, Lee Y J, Bae J S, Kim B S, Cho Y C, Moriyoshi C, Kuroiwa Y, Lee S and Jeong S Y 2015 Analysis of oxygen vacancy in Co-doped ZnO using the electron density distribution obtained using MEM *Nanoscale Res. Lett.* **10** 1–7
- [180] Wheeler D W and Khan I 2014 A Raman spectroscopy study of cerium oxide in a cerium-5 wt.% lanthanum alloy *Vib. Spectrosc.* **70** 200–6
- [181] Dohević-Mitrović Z D, Grujić-Brojin M, Čepanović M, Popović Z V., Boković S, Matović B, Zinkevich M and Aldinger F 2006 Ce_{1-x}Y(Nd)_xO_{2-δ} nanopowders: Potential materials for intermediate temperature solid oxide fuel cells *J. Phys. Condens. Matter* **18**

- [182] You A, Be M A Y and In I 2005 where RE = La , Pr , Nd , Eu , Gd , and Tb **2435**
- [183] Rojas-Buzo S, Concepción P, Olloqui-Sariego J L, Moliner M and Corma A 2021 Metalloenzyme-Inspired Ce-MOF Catalyst for Oxidative Halogenation Reactions *ACS Appl. Mater. Interfaces* **13** 31021–30
- [184] Nicolini V, Gambuzzi E, Malavasi G, Menabue L, Menziani M C, Lusvardi G, Pedone A, Benedetti F, Luches P, D’Addato S and Valeri S 2015 Evidence of catalase mimetic activity in Ce³⁺/Ce⁴⁺ doped bioactive glasses *J. Phys. Chem. B* **119** 4009–19
- [185] Orera V M, Merino R I and Peña F 1994 Ce³⁺↔Ce⁴⁺ conversion in ceria-doped zirconia single crystals induced by oxido-reduction treatments *Solid State Ionics* **72** 224–31
- [186] Sun L, Huang X, Wang L and Janotti A 2017 Disentangling the role of small polarons and oxygen vacancies in Ce O₂ *Phys. Rev. B* **95** 1–8
- [187] Park J H, Kim Y G, Yoon S, Hong S and Kim H J 2014 Simple method to enhance positive bias stress stability of In-Ga-Zn-O thin-film transistors using a vertically graded oxygen-vacancy active layer *ACS Appl. Mater. Interfaces* **6** 21363–8
- [188] Gálisová L 2013 Magnetic properties of the spin-1/2 Ising-Heisenberg diamond chain with the four-spin interaction *Phys. Status Solidi Basic Res.* **250** 187–95
- [189] Kumar R, Rayaprol S, Xiao Y, Babu P D, Siruguri V and Pal D 2018 Tuning of magnetic structure and its effect on magnetic properties in Co(Cr_{1-x}Mn_x)₂O₄ (x = 0-0.3) *J. Appl. Phys.* **124** 0–13
- [190] Su Y, Zhang J, Feng Z, Li Z, Shen Y and Cao S 2011 Magnetic properties of rare earth HoCrO₃ chromites *J. Rare Earths* **29** 1060–5

- [191] Mendivil L F, Alvarado-Rivera J, Tavizón G, Verdín E, Arenas-Alatorre J and Durán A 2021 Negative magnetization in the zero field-cooled and exchange-bias effect in Cu-doped PrCrO₃ *J. Mater. Sci. Mater. Electron.* **32** 24484–95



Vitae

Pragya Gupta was born on 06th December, 1994 in Uttar Pradesh state, India. She completed her Bachelors in Physics from Dr. R.M.L Avadh University, Ayodhya, Uttar Pradesh. She obtained her Masters in Physics from Banaras Hindu University, Banaras, Uttar Pradesh. She pursued her Doctoral research career with experimental condensed matter physics, at the Department of Physics, IIT Guwahati under the supervision of Prof. Dilip Pal. Her current research interests include Multiferroics, Magnetism, Strongly correlated electron systems, Magnetic, and structural studies of orthochromites.